Experimental measurements of break-up reactions to study alpha clustering in carbon-12 and beryllium-9

by

Robin Smith

A thesis submitted to
The University of Birmingham
for the degree of
DOCTOR OF PHILOSOPHY

School of Physics and Astronomy
College of Engineering and Physical Sciences
University of Birmingham
July 2017

Abstract

Due to the high binding energy of the α-particle, this object can preform in heavier atomic nuclei. This work explores α-clustering in ^{9}Be and ^{12}C by measuring their nuclear break-up. For ^{9}Be, it has been proposed that the two α-particles of the unstable ^{8}Be nucleus are bound together by a covalently shared neutron. This thesis reports the observation of a state in ^{9}Be at 3.8 MeV through the ^{9}Be(^{4}He,α)$\alpha\alpha n$ reaction. By comparing its reduced width with that of a potential mirror analogue in ^{9}B, its angular momentum was shown to be $J < 7/2$. This is consistent with a hitherto unmeasured $3/2^{+}$ molecular binding configuration state. The ^{12}C nucleus is thought to consist of three α-clusters and its famous Hoyle state has been shown to possess an unusually large volume. Due to its low density, this state may behave like a Bose-Einstein condensate, where the fermonic structures of the constituent α-particles are no longer important. By precisely measuring the decay of the Hoyle state into three α-particles, through the ^{12}C(^{4}He,α)3α reaction, an upper limit for the direct 3α decay branch of 0.047% was obtained. This lies below predictions for the decay of a condensate state, casting doubt on this interpretation.

To my Mom and Dad, Jane and Ray Smith,

for your support, encouragement

and belief in me.

Acknowledgements

As well as being a beautiful example of knot theory, the Borromean rings, and more generally Brunnian links, are an excellent metaphor for good team work: If one element of a team is missing, the remaining members will struggle without them. The Borromean ring structure in the left panel of figure 1 forms an nice analogy for the ^{9}Be and ^{12}C nuclei I've studied over the course of my PhD. In a similar way, I've used the four-component Brunnian link shown in the right panel of figure 1, as a metaphor for myself and the other students I've been fortunate enough to work with over the past few years. I believe that Jack, Sam, Joe and myself worked together as an excellent team. I'd like to thank Joe for making a big effort to welcome me to the group four years ago. I'd like to thank Sam for being a constant source of wisdom who was always happy to help me to understand various aspects of nuclear theory. Finally, I'd like to thank Jack for all of his help towards the work that we performed on the MC40 cyclotron; his hard work, technical aptitude and cheerful company were very welcome in the medical physics basement.

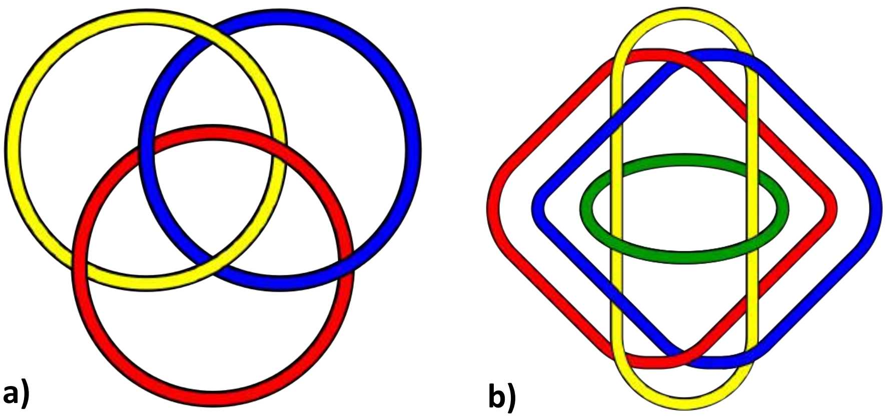

Figure 1: a) Borromean rings. b) Four-component Brunnian link (Jack, Sam, Joe, Robin).

Of course, there are so many more people who have made my experience as a PhD student at Birmingham so memorable. Many thanks to Carl and Martin for being excellent supervisors, providing me with the space to exercise my own creativity but always making time to help me out and proof-read work. To Tzany for her nuclear physics help, general support and continual supply of vegan sweets. To Neil for his climbing help and for all of his assistance with `RES8` and other aspects of my analysis. Thank you to Peter Jones, Garry Tungate, Dave Forest, Gordon Squier and various other group members for their useful feedback to practice talks and excellent support and guidance as teaching colleagues. Thank you to David Parker and other members of the Birmingham cyclotron staff for their hard work and patience during the experiments. Thank you to Paul Jagpal for his expertise in nuclear electronics and advice. Thank you to Mark Caprio, Pieter Maris and James Vary for a number of illuminating discussions about *ab initio* nuclear theory, which taught me a lot. Finally, thank you to the staff in the physics workshop and stores, who have been very helpful in sourcing materials and building equipment needed for this research. If I wished to include everybody in this kind of Brunnian link, then you end up with something similar to, but more complicated than, figure 2. Thank you; it has been wonderful to work with you all over the past few years.

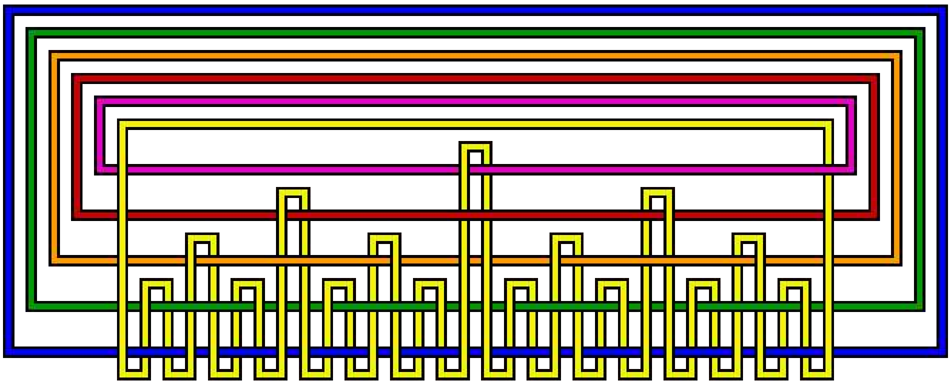

Figure 2: Six component Brunnian link (more complicated with extra people).

Author contribution

The skills and efforts of many people have come together to lead to the research outcomes detailed in this thesis. This is particularly pertinent when considering the set-up of the experiments and the acquisition of data. My own role in this research is detailed below.

Regarding the structure of ^{9}Be, which is detailed in chapter 4, I did not attend the experiment used to obtain this data set. I retrieved the calibrated data upon starting my PhD. However, the data analysis is my own. This involved writing sort codes to perform the primary data analysis, in order to generate clean excitation spectra for ^{9}Be. I performed Monte-Carlo simulations and wrote a Voigt curve fitting code in order to extract information from these spectra. The calculation of reduced widths, the comparison with the ^{9}B mirror nucleus and theoretical interpretation were performed by me. I wrote the papers that were published on this research.

I was the lead investigator into the structure of the ^{12}C Hoyle state detailed in chapter 5. I performed Monte-Carlo simulations in order to optimise the experimental set-up, lead the physical construction of the apparatus, calibrated the data and was in attendance as the data were being acquired during a long experimental campaign. In addition to this, I performed the entirety of the data analysis. This included writing the main primary analysis sort code to generate the Dalitz plots. The Monte-Carlo simulations of the sequential and direct decay processes were also performed by me, along with the statistical analysis used to determine upper limits for the direct decay contributions. Calculations of the expected direct decay branching ratio, based on phase space and Coulomb barrier penetrabilities, were also my work. I wrote the paper that was published on this research.

List of publications

Experimental

R. Smith, Tz. Kokalova, et al. *New Measurement of the Direct 3*α *Decay from the* ^{12}*C Hoyle State*, Phys. Rev. Lett. **119** (2017).

R. Smith, M. Freer, C. Wheldon, N. Curtis, Tz. Kokalova, et al. *Disentangling unclear nuclear breakup channels of beryllium-9 using the three-axis Dalitz plot.* Journal of Physics: Conf. Series **863** (2017).

R. Smith, C. Wheldon, M. Freer, N. Curtis, Tz. Kokalova, et al. *Evidence for a 3.8 MeV state in* ^{9}*Be.* Physical Review C **94** (2016).

S. Bailey, M. Freer, Tz. Kokalova, C. Wheldon, R. Smith, J. Walshe, et. al. *Alpha clustering in Ti isotopes:* ^{40,44,48}*Ca +* α *resonant scattering.* In EPJ Web of Conferences **113** 08002 (2016).

R. Smith, C. Wheldon, M. Freer, N. Curtis, Tz. Kokalova, et al. *Breakup branches of Borromean beryllium-9.* Proceedings of Nuclear Structure and Dynamics 15. Vol. **1681**. AIP Publishing, (2015).

Theoretical

M. A. Caprio, P. Maris, J. P. Vary, and R. Smith, *Collective rotation from ab initio theory*, Int. J. Mod. Phys. E **24**, 1541002 (2015).

M. A. Caprio, P. Maris, J. Vary, and R. Smith, *Emergence of rotational bands in ab initio no-core configuration interaction calculations*, Rom. J. Phys. **60**, 5-6 (2015).

J. P. Vary, P. Maris, H. Potter, M. A. Caprio, R. Smith, S. Binder, A. Calci, J. Langhammer, R. Roth, H. M. Aktulga et. al. *Ab Initio No Core Shell Model - Recent Results and Further Prospects*, Proceedings of International Conference "Nuclear Theory in the Supercomputing Era 2014" (NTSE-2014), Pacific National University, Khabarovsk, Russia, June 23-27, 2014 (2015).

Have you ever noticed that the words

“nuclear” and “unclear” are so similar?

– trad.

Contents

Contents

List of figures

List of tables

1 Introduction **1**

2 Nuclear structure **5**

2.1 The liquid drop model 5

2.2 The spherical shell model 8

2.3 Nuclear deformation 11

2.4 Collective rotation 15

2.5 α-clustering 19

3 Nuclear reactions **25**

3.1 Nuclear resonances 25

3.2 Introduction to R-Matrix theory 28

4 Molecular structures in the mirror nuclei, beryllium-9 and boron-9 **34**

4.1 Review of the beryllium-9 nucleus 36

4.1.1 Two-centre shell model 36

4.1.2 Molecular model 38

4.1.3 Shell model and no-core shell model calculations 41

4.1.4 Experimental review of ^{9}Be 42

4.1.5 Mirror nuclei 44

4.2 Experimental details and apparatus . . . 47
4.2.1 Notre Dame tandem Van De Graaff accelerator . . . 47
4.2.2 Basic reaction dynamics . . . 51
4.2.3 Detector set-up . . . 52
4.2.4 Electronics and data acquisition . . . 57
4.3 Primary analysis . . . 62
4.3.1 Determining the direction and momenta of the detected particles . . . 62
4.3.2 Detector front and rear face energy matching . . . 63
4.3.3 Kinematic lines . . . 64
4.3.4 Q-value spectra . . . 65
4.3.5 Target energy losses correction . . . 67
4.3.6 Decay channel selection . . . 71
4.3.7 Excitation energy calculation . . . 74
4.3.8 Further contaminant reaction channels . . . 76
4.4 Secondary analysis . . . 79
4.4.1 Monte-Carlo simulations . . . 79
4.4.2 Peak fitting . . . 90
4.4.3 Reduced width calculations . . . 100
4.5 Interpretation of results . . . 104
4.6 Outlook . . . 106

5 Investigating the 3α break-up modes of the ^{12}C Hoyle state 109

5.1 Introduction . . . 111
5.2 The Hoyle state in stellar nucleosynthesis . . . 115
5.3 Theoretical models of ^{12}C and the Hoyle state . . . 117
5.3.1 Mean field models of ^{12}C . . . 117
5.3.2 *Ab initio* approaches to ^{12}C . . . 118
5.3.3 Antisymmetrised molecular dynamics (AMD) and fermionic molecular dynamics (FMD) . . . 120
5.3.4 Cluster models and dynamical symmetries . . . 122
5.3.5 Bose-Einstein Condensates . . . 125

5.4 The 3α decay of the Hoyle state 129
    5.4.1 Structures and 3α decay signatures 130
    5.4.2 Full three-body calculations 132
    5.4.3 Decay signatures of an α-condensed state 134
5.5 Sequential and direct decay calculations 135
    5.5.1 Semi-classical approach to barrier transmission 136
    5.5.2 Phase space calculations 142
5.6 Experimental details and apparatus 146
    5.6.1 Birmingham MC40 cyclotron accelerator 146
    5.6.2 Detector set-up 149
    5.6.3 Electronics and data acquisition 151
5.7 Monte-Carlo simulations 153
5.8 Primary analysis and data reduction 158
    5.8.1 Detector energy and position calibration 159
    5.8.2 Detector energy resolution 163
    5.8.3 Particle identification telescope, hit multiplicities and hit patterns 167
    5.8.4 Excitation, total energy, and total momentum spectra 172
    5.8.5 Break-up channel visualisation 181
    5.8.6 Dalitz Plots 183
    5.8.7 Simulated Dalitz plots 191
    5.8.8 Kinematic fitting 197
5.9 Secondary analysis 202
    5.9.1 Dalitz plot projections 202
    5.9.2 Frequentist statistical analysis 205
    5.9.3 Bayesian statistical analysis 210
    5.9.4 Summary of results 215
5.10 Interpretation of Results 216
5.11 Outlook 218

6 Resistive strip detector improvements **221**

7 Summary **236**

Appendices **242**

A Rotational wave functions **243**

B Calculation of the angle of each detected particle **246**

C Two-body kinematics **248**

D Dalitz plots **251**

D.1 Deriving the Dalitz plot coordinates 251

D.2 Deriving the bounded area of the Dalitz plot 253

E Kinematic fitting **256**

E.1 Kinematic fitting example 256

E.2 Kinematic fitting theory 261

F Lead author publications **264**

References **287**

List of Figures

2.1 a) The binding energy per nucleon, BE/A, as a function of mass number, A (for odd-A isotopes only). The points show experimental data and the red line gives the prediction of the SEMF. The inset shows the fit residuals. b) The process of fission through a liquid-drop picture. 1. The configuration with the least surface energy and the greatest Coulomb energy, 2. & 3. More surface energy and less Coulomb energy. 4. If the surface + Coulomb energy is greater for the deformed system, the nucleus will split/fission. Image in b) is modified from reference [12]. 7

2.2 The single-particle energy levels of a Woods-Saxon potential, with (right) and without (left) the inclusion of spin-orbit splitting. The levels are labelled $N\ell_j$, with N as the principal quantum number, ℓ as the orbital angular momentum, and j as the total angular momentum. The numbers to the right of the levels show the proton/neutron degeneracies. The levels are shown within a Woods-Saxon potential with the form of equation 2.3. 9

2.3 The intrinsic shape of an axially-symmetric deformed nucleus as a function of the deformation parameter, β_2. Image modified from reference [20]. 11

2.4 The Nilsson single-particle levels as a function of the deformation parameter, ϵ_2 [6] 13

2.5 a) Definition of the coordinate system and Ω quantum number used in the Nilsson model (adapted from [22]). b) Schematic level splitting as a function of the deformation parameter, ϵ. 14

2.6 The coupling of intrinsic and collective angular momenta and their projections onto the deformation (symmetry) axis. 17

2.7 a) The Coriolis force as an artefact of the Earth's rotation, deflects an object either in the direction of, or against the direction of, the Earth's rotational angular momentum. Image adapted from reference [27]. b) A classical picture of a nucleon with intrinsic angular momentum, $\boldsymbol{j}$, coupling to a total angular momentum $\boldsymbol{J}$, with a strength $(\boldsymbol{J} \cdot \boldsymbol{j})$. 18

2.8 The excitation of a spherical shoal of mackerel into a two 'cluster' structure. Images from reference [30]. 19

2.9 The Ikeda diagram, which links accessible cluster structures with excitation energy. Clusters are labelled except for α-particles, which are denoted by the green circles. Image created by Tz. Kokalova and taken from reference [28]. 20

2.10 The binding energy per nucleon (BEPN) as a function of the nucleon number, A, for a selection of even-A naturally occurring isotopes. Images from reference [32]. 21

2.11 Left: The energy levels of the SHO as a function of the deformation parameter ϵ_2. Right: Approximate ^{8}Be nuclear density projections calculated in the HO basis. Image from reference [6]. 22

3.1 The production of unbound resonances in the $n +^A_Z$ X system. Image modified from reference [38]. 26

3.2 Penetration into the internal nuclear region for different values of the phase shift, ζ. The top panel shows the system far away from resonance, and the bottom panel shows the system on resonance (wave function derivative is zero at the boundary). The centre panel shows the system for an intermediate value of ζ. Image from reference [39]. 27

3.3 The functional form of the potential for varying centrifugal barriers in the ^{16}O + ^{208}Pb system. Image from reference [43]. 29

4.1 The energy levels of the two-centre shell model as a function of the α-cluster separation distance r. Figure from references [54] and [55]. 37

4.2 The relative alignments of the two $p_{3/2}$ orbitals with respect to the ^{9}Be deformation axis for the σ- and π-type bonding. Images from reference [6]. 38

4.3 Left: energy levels of the two centre shell model. Right: the σ- and π-type molecular orbital wave functions associated with the valence neutron in ^{9}Be. These correspond to superpositions of [1,0,0] and [0,0,1] ([n_x, n_y, n_z]) harmonic oscillator wave functions. Images from references [55] and [6]. 39

4.4 The valence neutron density calculated from generator coordinate method α + α + n molecular calculations. Images from references [57, 58]. 40

4.5 Nucleon densities (left: proton, centre: neutron, right: neutron − proton) for the ^{9}Be ground state in the intrinsic frame, from large-basis, no-core shell-model calculations. Images from references [63] and [64]. 41

4.6 The known rotational bands of ^{9}Be based on the level compilation in reference [52]. Some angular momentum assignments are tentative and have been changed on this plot in order for the levels to exhibit the correct rotational trends. Please refer to table 4.1 for the J^{π} assignments of the most recent ^{9}Be level compilation. 43

4.7 The level schemes of the ^{9}Be/^{9}B mirror pair [52]. The different colours highlight proposed rotational bands. 45

4.8 a) Expanded view of a generic Van de Graaff generator with the main components labelled. b) Schematic diagram illustrating the ‘tandem’ acceleration principle and how ions are accelerated practically using a Van de Graaff generator. Image in a) from reference [80]. 47

4.9 Controlling the electric field gradient of the Van de Graaff accelerator using metal electrodes and resistors along the length of the beam pipe. a) Schematic diagram illustrating the principle. b) Photograph of the set-up at the FN tandem accelerator at Notre Dame from reference [81]. 49

4.10 Overview of the helium ion source and its various component stages. Image from reference [81]. 50

4.11 Microscopic, pictorial representation of the inelastic scattering and break-up of ^{9}Be. The α particle beam strikes a stationary ^{9}Be nucleus in the target, raising it into an excited state. This then breaks apart into its cluster constituents. The energies and angles of the charged particles in the final state were measured by an array of silicon detectors. 51

4.12 a) The positions of the detectors and target inside the vacuum chamber along with an illustration of the ^{9}Be break-up process. The bottom right image shows the detector array as viewed from the target position. b) A photograph of the detector array inside the experimental chamber. 52

4.13 The formation of the depletion region at a P-N junction [82]. 53

4.14 Schematic diagram of a double-sided silicon strip detector. The upper image shows the face of the detector and the lower image shows the cross section through the detector. When two particles hit the detector, four strips collect charge (two vertical on the front and two horizontal on the rear) which are highlighted in a darker shade. The crossing points in black mark the possible hit points. 55

4.15 Notation for assigning the angle of the particle detection with respect to the initial beam direction and the target. Image from reference [90]. 56

4.16 Simplified block diagram showing the ordering of the pulse processing electronics and data acquisition system. 57

4.17 Diagram of a basic charge-sensitive preamplifier. 58

4.18 Triggering logic block diagram. 60

4.19 Plot of the energies collected by the front detector strips *vs.* the energies collected by the rear detector strips, on a single DSSD. ‘Good’ events lie on the diagonal line. 63

4.20 Plot of the energies of the detected particles as a function of the scattering angle (θ_{tot} in figure 4.15) for the 26 MeV beam energy data. The theoretical kinematic lines are overlaid. 64

4.21 The calculated Q-value for ^{9}Be break-up plotted against the calculated Q-value for ^{12}C break-up. Plot from reference [94]. 66

4.22 The energy losses of the beam and the reaction products in the cases where the reaction happens on the rear (left panel) or front (right panel) face of the target. 67

4.23 Diagram used to numerically calculate the energy losses of the particles in the target. 68

4.24 Q-value spectra before (line) and after (filled) the energy-loss correction routine was applied. 22 MeV and 26 MeV data occupy the upper and lower panels, respectively. 69

4.25 Simulated ^{9}Be excitation spectrum for a narrow state at 6 MeV, with and without target energy-loss correction. 70

4.26 Relative energy spectrum between final state α-particles. The narrow peak at 92 keV corresponds the ^{8}Be ground state. The bump at ≈ 0.6 MeV corresponds to decays from the 2.43 MeV $5/2^-$ state in ^{9}Be to the tail of the ^{8}Be$_{2+}$ level. The dashed line shows the simulated decay of the $5/2^-$ state in ^{9}Be and the solid line shows experimental data. 72

4.27 Two dimensional plot of α-particle relative energies from the 26 MeV data set. The 22 MeV data set produced an almost identical plot. 73

4.28 Excitation spectra for ^{9}Be, subject to the condition of a ^{8}Be$_{\text{g.s.}}$ intermediate state. The 22 MeV beam data are shown by the dot-dashed line and the 26 MeV data are shown by the solid line. Some key levels in ^{9}Be are marked by the vertical arrows. 75

4.29 Excitation energy of a proposed ^{9}Be $(\alpha + \alpha + n)$ *vs.* the excitation energy of a proposed ^{12}C $(\alpha + \alpha + \alpha)$ (26 MeV beam data only). Broad horizontal lines correspond to states in ^{9}Be and the vertical lines correspond to the known natural parity states in ^{12}C. The diagonal band corresponds to the neutron transfer reaction and break-up of ^{5}He. The dashed and dot-dashed lines mark the regions occupied by contaminant reactions. See text for details. 76

4.30 Excitation spectra for ^{9}Be, subject to the condition of a ^{8}Be$_{\text{g.s.}}$ intermediate state, and after all software cuts were placed. The 22 MeV beam data are shown by the dot-dashed line and the 26 MeV data are shown by the solid line. 78

4.31 A sequential break-up reaction generated in `RES8`. $A + B \rightarrow C^* + D$ then $C^* \rightarrow E + F*$ etc. 79

4.32 Efficiencies, as a function of ^{9}Be excitation energy, for the various angular distributions used in the simulations. A beam energy of 26 MeV was used in these simulations. 82

4.33 Angular distributions of the simulated inelastic scattering. A uniform angular distribution between $0° - 180°$ was used in the final analysis. 82

4.34 The maximum percentage difference between the efficiencies at each value of the excitation energy, calculated over all possible angular distributions used in the simulations. The red and blue lines show the average difference over the entire excitation range and the $0-8$ MeV range, respectively. Shown for 26 MeV beam data, though similar differences were seen for the 22 MeV data set. 83

4.35 The calculated ^{9}Be excitation spectra, normalised by the efficiency at each energy. The 22 MeV beam data (scaled by a factor of 0.8) are shown by the dot-dashed line and the 26 MeV data are shown by the solid line. 84

4.36 Plots showing the effect of increasing experimental Gaussian smearing, σ, on the appearance of a Lorentzian peak of intrinsic width γ, in the measured excitation spectrum 86

4.37 Plot of the excitation energy resolution ($\sigma \approx$ FWHM/2.35 for Gaussian peaks and Γ for Lorentzian peaks) for the 22 MeV beam energy, as a function of the ^{9}Be excitation energy. These results were derived from Monte-Carlo simulations. 87

4.38 Plot of the excitation energy resolution ($\sigma \approx$ FWHM/2.35 for Gaussian peaks and Γ for Lorentzian peaks) for the 26 MeV beam energy, as a function of the ^{9}Be excitation energy. These results were derived from Monte-Carlo simulations. 87

4.39 Fit to the 2.43 MeV $5/2^-$ state in ^{9}Be for the 22 MeV beam energy data. The red and green lines show the fit with and without a linear background, respectively. 88

4.40 Fit to the 2.43 MeV $5/2^-$ state in ^{9}Be for the 26 MeV beam energy data. The red and green lines show the fit with and without a linear background, respectively. 89

4.41 Predicted excitation function for the $1/2^+$ state at 1.684 MeV in ^{9}Be using R-Matrix theory ($\ell = 0$). The lighter histogram shows the peak shape after the data were blurred by a Gaussian spectral response function (FWHM 630 keV). 91

4.42 Predicted excitation function for the $5/2^+$ state at 3.05 MeV in ^{9}Be using R-Matrix theory ($\ell = 2$). The lighter histogram shows the peak shape after the data were blurred by a Gaussian spectral response function (FWHM 630 keV). . 91

4.43 Fit of the known levels in ^{9}Be to the 22 MeV beam energy excitation spectrum. The lower panel shows the fit residuals, indicating an extra feature in the 4 MeV region. 92

4.44 Fit of the known levels in ^{9}Be to the 26 MeV beam energy excitation spectrum. The lower panel shows the fit residuals, indicating an extra feature in the 4 MeV region. 93

4.45 Fit of the known levels in ^{9}Be to the 22 MeV beam energy excitation spectrum, with the modelled quadratic background profile subtracted. 94

4.46 Fit of the known levels in ^{9}Be to the 26 MeV beam energy excitation spectrum, with the modelled cubic background profile subtracted. 95

4.47 Fit of the known levels in ^{9}Be, and a new level at 3.8 MeV, to the 22 MeV beam energy excitation spectrum. The lower panel shows the fit residuals. See text for details. 96

4.48 Fit of the known levels in ^{9}Be, and a new level at 3.8 MeV, to the 26 MeV beam energy excitation spectrum. The lower panel shows the fit residuals. See text for details 97

4.49 Fit of the known levels in ^{9}Be, and a new level at 3.8 MeV, to the 22 MeV beam energy excitation spectrum, with the modelled quadratic background profile subtracted. 98

4.50 Fit of the known levels in ^{9}Be, and a new level at 3.8 MeV, to the 26 MeV beam energy excitation spectrum, with the modelled cubic background profile subtracted. 98

4.51 The change in the value of χ^2 for the fits, as the value of the energy and width of the state are varied close to their optimal values. 99

4.52 Reduced-width-to-Wigner-limit ratios (θ^2) were calculated for the two decay scenarios shown, for various values of orbital angular momentum ℓ. Each ℓ would correspond to the decay of a state in ^{9}Be/^{9}B of a particular J^{π}. If consistent θ^2 values are calculated for both nuclei, for a particular ℓ, limits on J^{π} can be inferred. 101

4.53 The possible rotational bands in the ^{9}Be/^{9}B mirror pair, with the inclusion of the newly measured states near to 4 MeV. Image from reference [114]. 104

4.54 Excitation spectrum of ^{9}Be reconstructed from the decay of ^{13}C. Image adapted from reference [115]. 107

5.1 Organic molecules: a) carbon tetrahedral bonds b) methane c) ethane. Various carbon-carbon bonds: d) single bonding e) double bonding f) triple bonding. Images adapted from reference [119]. 111

5.2 The proposed nuclear reaction chain for Big Bang Nucleosynthesis. Image from reference [122]. 112

5.3 Triple-α process: The sequential capture of three α-particles to form ^{12}C in its ground state. 113

5.4 Schematic plot of a Gamow peak from reference [135] showing the contributions from the Maxwell Boltzmann distribution of particle energies and the Coulomb barrier tunnelling probability. 115

5.5 The results of mean field calculations of ^{12}C from reference [141]. The experimental levels are given in the leftmost column, and shell-model calculations using the various NN interactions are shown in the remaining three columns. Blue lines show the ground-state energies and the red lines show the energies of the first excited 2^+ state. The magenta lines give the energies of the Hoyle state, which differ significantly between calculations and experiment. 118

5.6 The results of no-core symplectic model (NCSpM) calculations utilising a symmetry-guided basis [143]. 119

5.7 The arrangement of the three α-particles in ^{12}C from calculations in reference [144]. 120

5.8 The energy levels and intrinsic nucleon densities of ^{12}C predicted by AMD calculations [146]. 121

5.9 Explaining the angular momenta and parities of the ground state rotational band based on an equilateral triangle configuration of α-particles. 123

5.10 The a) *breathing* and b) *bending* mode vibrations that give rise to the 0^+ Hoyle state and the 1^- state in ^{12}C, respectively. 124

5.11 The rotational bands of ^{12}C. The points depict experimental measurements and the lines show the predictions from the ACM. Image from reference [158]. 124

5.12 Pictorial representation of the THSR wave function of reference [160]. 127

5.13 Contour plot for ^{12}C of the calculated $E(R_0, b)$ energy surface from reference [160]. 127

5.14 Schematic diagram of the types of α-particle emissions expected for various structures. 130

5.15 The ratios of the adiabatic components of the Hoyle state (upper panel) and 0_3^+ resonance (lower panel) in ^{12}C. The ratio of f_2 to f_3 varies during the decay of the Hoyle state, but the f_1 component remains dominant over all hyperradii. Here, E is the energy above the α-particle decay threshold. Image from reference [176]. . 133

5.16 Various geometric configurations of a three-body decay. The situations are labelled from left to right as *other collinear*, *extreme collinear* and *equal energies.* Other collinear: particles 1 and 2 remain close during the decay (similar to a sequential decay). Extreme collinear: the decay is collinear and one particle remains stationary. Equal energies: the particles are emitted with equal energies and with equal angles between them. Image from reference [182]. 135

5.17 The ^{8}Be + α Coulomb barrier as a function of the separation of the two fragments. 137

5.18 The relative coordinates between the three particles in a direct decay. 138

5.19 The three-body $\alpha + \alpha + \alpha$ Coulomb barrier as a function of the *hyperradius*, ρ. The lines depict three extreme situations: the three particles are emitted with the same energy and at equal angles to each other (blue line); a collinear decay where one particle is given the maximum 2/3 of the total decay energy and the others are emitted perpendicular to this particles direction (yellow line); a collinear decay where one α particle remains at rest (red line). 140

5.20 Decay from a single state into three particles. 143

5.21 The basic operation of a cyclotron accelerator. The images are adapted from [194]. In reality, the RF signal has a sinusoidal form and the cyclotron orbits become closer together at larger radii. 146

5.22 a) The positions of the detectors and target inside the vacuum chamber along with an illustration of the ^{12}C break-up process. b) A photograph of the full detector set-up inside the reaction vacuum chamber. 149

5.23 Chain of electronics used in the experiment. It is broadly the same as that used in the ^{9}Be experiment (figure 4.16). The main difference is the number of data channels, and that the signals from the telescope and Quad array of DSSDs are used separately in a more complicated trigger. 151

5.24 Triggering circuit for the experiment. The aim was to demand three hits in the quad arrangement of DSSDs, in coincidence with a single hit in the $\Delta E - E$ telescope. In addition to triggering, the *or* outputs from the discriminators were input to the TDC. 152

5.25 Plot of the total Hoyle state peak-to-background ratio for the ^{12}C excitation spectrum (see figure 5.36 later for a spectrum). Extrapolating to zero beam current does not give zero background. Therefore, a small background source, around 1/3 of the amount at 6 enA beam energy, remains. 155

5.26 Figure relating to table 5.1. Illustrating how the deduced hit position of two particles changes if the energies detected by the front and rear strips change order between the two particles, α and β. Panels: a) The correct hit positions; b) If the rear energies become switched; c) if the front energies become switched; d) If front and rear energies become switched. 157

5.27 a) A total of seven Gaussian peaks fitted to a raw α-particle calibration spectrum from a single detector channel. b) A plot of peak centroid *vs* α-particle energy. . 159

5.28 a) Schematic diagram of the set-up used to measure the energy losses of the calibration α-particles in the source. b) A plot of the average α energy *vs.* the angle of emission from the source. The points show experimental data and the line shows the Bethe formula prediction for ^{4}He ions travelling through a 0.55 μm-thick even mixture of ^{239}Pu, ^{241}Am and ^{244}Cu. To obtain plot b), the detector strips were calibrated in energy at zero degrees, since this is where the energy losses are minimal. The calculations assumed a linear energy loss through the source material, which causes the disagreement between the experimental data and the Bethe formula prediction at large angles. 161

5.29 The energies the scattered α-particles as a function of their angles for a beam energy of 12.3 MeV. The position of the telescope was calibrated with a 40 MeV beam energy and the Quad array was calibrated with a 12.3 MeV beam energy. The positions of the detectors were slightly adjusted so that the kinematic predictions (black lines) best overlaid the experimental kinematic lines. The calculated kinematic lines correspond to populating the recoiling ^{12}C in its ground state, 4.4 MeV 2^{+} state and 7.65 MeV 0^{+} Hoyle state. 162

5.30 Normalised distributions of the ΔE quantity for various values of the beam current. 163

5.31 The average detector resolution as a function of the beam current. The points with error bars show the beam data, the circular point shows the resolution for the α-source, and the line shows a linear least squares fit to the first 4 points. . . 164

5.32 The measured resolution as a function of the particle energy, for the rear detector in the $\Delta E - E$ telescope. 165

5.33 Plot of ΔE *vs.* E for the particles scattered into the telescope arrangement. Data are shown with a linear intensity colour scale. Since there was a high beam current of ^{4}He ions, the most intense band corresponds to these particles. 168

5.34 Plot of ΔE *vs* E for the particles scattered into the telescope arrangement, with a logarithmic (base 10) colour scale. The predictions of the Bethe formula (equation 5.41) are shown for various ions by the black lines. 169

5.35 The relative frequencies of hit multiplicities measured across the quad array. Since the Hoyle state breaks up into three α particles, the frequency is expected to drop sharply beyond this multiplicity. 170

5.36 Histogram of the excitation energies of the recoiling ^{12}C, for the case that the three break-up α particles strike separate DSSDs. The Histogram shows 50,368 events. 173

5.37 Histogram of the excitation energies of the recoiling ^{12}C, for the case that the two break-up α particles strike the same DSSD. The Histogram shows 194,095 events. 173

5.38 Histogram of the total energy of the particles measured in the final state, subject to the constraint that the three break-up α particles strike separate DSSDs. The histogram shows 28,252 experimental events and the (red) line shows 146,238 scaled Monte-Carlo events. Data are plotted on a logarithmic vertical scale. . . . 175

5.39 Histogram of the total energy of the particles measured in the final state, subject to the constraint that two break-up α particles strike the same DSSD. The histogram shows 109,004 experimental events and the (red) line shows scaled 161,583 Monte-Carlo events. Data are plotted on a logarithmic vertical scale. 175

5.40 Excitation energy spectrum of ^{12}C calculated from the three break-up α-particles. Events are chosen where each α-particle is detected in a separate DSSD. A total of 2.4×10^4 events are plotted. The histogram depicts experimental data and the solid (red) line shows the results of Monte-Carlo simulations. The main panel shows the data on a linear scale and the inset uses a logarithmic scale for a closer examination of the background. 177

5.41 Excitation energy spectrum of ^{12}C calculated from the three break-up α-particles. Events are chosen where two α-particles are detected in the same DSSD. A total of 8.5×10^4 events are plotted. The histogram depicts experimental data and the solid (red) line shows the results of Monte-Carlo simulations. The main panel shows the data on a linear scale and the inset uses a logarithmic scale for a closer examination of the background. 177

5.42 Distribution of the total momenta in the x, y and z directions. This plot shows data subject to the condition that the three break-up α-particles hit different DSSDs. 179

5.43 Distribution of the total momenta in the x, y and z directions. This plot shows data where two break-up α-particles hit the same DSSD. 179

5.44 Level scheme for the sequential decay of ^{12}C into three α-particles, through the intermediate ^{8}Be ground state. 181

5.45 Histograms of the fractional energies of each α-particle in the CoM of the decaying ^{12}C. The histogram shows experimental data and the red line shows the Monte-Carlo simulations of the sequential decay process. A peak at $\epsilon = 1/2$ in these spectra corresponds to the case where that α-particle is emitted first, in a sequential decay through the ^{8}Be ground state. 182

5.46 The construction of a symmetric Dalitz plot. Panel a) Illustrates that data must lie on a plane when plotted in 3-dimensional space if ϵ_1, ϵ_2 and ϵ_3 sum to a constant value. Panel b) depicts the projection of this diagram into 2-dimensional space. Panel c) shows the bounds of the Dalitz plot due to energy and momentum conservation. See text for details. Image from reference [198]. 183

5.47 Depiction of the sequential break-up of ^{12}C along with where on the Dalitz plot these points will lie. 184

5.48 Symmetric Dalitz plot showing the fractional energies of the three break-up α-particles. This shows 2.4×10^4 Hoyle state break-up events, corresponding to the case where each α-particle was detected by a separate DSSD. Sequential decay events are forced to lie on the triangular locus. 186

5.49 Symmetric Dalitz plot showing the fractional energies of the three break-up α-particles. This shows 6.9×10^4 Hoyle state break-up events, corresponding to the case where two α-particles were detected by the same DSSD. 187

5.50 Symmetric Dalitz plot showing the fractional energies of the three break-up α-particles. This shows 6.0×10^4 Hoyle state break-up events, corresponding to the case where two α-particles were detected by the DSSD array, and the third was reconstructed. 187

5.51 Dalitz plots folded so that the data occupy one sextant of the plot. Panel a) shows the case where each break-up α-particle is detected by a separate DSSD (2.4×10^4 events) and panel b) shows the case where two α-particles hit the same DSSD (6.9×10^4 events). 189

5.52 Folded Dalitz plots from two previous measurements of the Hoyle state break-up. Panel a) shows data from reference [139] and depicts around 5×10^3 events. Panel b) shows data from reference [140] and depicts around 2×10^4 events. . . 189

5.53 Symmetric Dalitz plot showing the fractional energies of the three break-up α-particles from the sequential decay Monte-Carlo simulations. This corresponds to the case where each α-particle strikes a separate DSSD, and shows 1.09×10^5 Hoyle state break-up events. Sequential decay events are forced to lie on the triangular locus. The analogous experimental data are shown in figure 5.48. . . . 191

5.54 Symmetric Dalitz plot showing the fractional energies of the three break-up α-particles from the sequential decay Monte-Carlo simulations. This corresponds to the case where two α-particles hit the same DSSD, and shows 4.2×10^5 Hoyle state break-up events. Sequential decay events are forced to lie on the triangular locus. The analogous experimental data are shown in figure 5.49. 192

5.55 Simulated Dalitz plots folded so that the data occupy one sextant of the plot. Panel a) shows the case where each of the break-up α-particles hit a separate DSSD and panel b) shows the case where two α-particles hit the same DSSD. The analogous experimental data are shown in figure 5.51. 192

5.56 Simulated Dalitz plots for each of the direct decay models, folded so that the data occupy one sextant of the plot. The left panels show data that satisfy the strict hit pattern of one α-particle in each DSSD. The right panel shows data that correspond to the case where two break-up α-particles hit the same DSSD. The top, middle and bottom rows show the DDΦ, DDE and DDL break-up models, respectively. 194

5.57 a) Simulated Dalitz plot for the DDP^2 direct decay. This is DDΦ uniform phase space decay but accounts for how the Coulomb barrier transmission probability depends on the emission angles of the three break-up α-particles. b) Folded DDP^2 Dalitz plot. The plots show 500,000 simulated events and do not include experimental effects. 195

5.58 Dalitz plot showing the fractional energies of the three break-up α-particles. This shows 6.0×10^4 Hoyle state break-up events, corresponding to the case where two α-particles were detected by the DSSD array, and the third was reconstructed. The left panel shows the data before kinematic fitting, and the right shows data after kinematic fitting. 200

5.59 Histograms of the projected Dalitz plot, before and after kinematic fitting. 201

5.60 One-dimensional projections of the folded Dalitz plots onto the vertical axis. The black histogram depicts experimental data and the red lines show the Monte-Carlo simulations. Panel a) shows the case where each break-up α-particle is detected by a separate DSSD and panel b) shows the case where two α-particles hit the same DSSD. The main panel of each plot shows the data plotted on a logarithmic scale in order to examine the tails of the distributions. The insets show the same data plotted with linear scales. 202

5.61 One-dimensional projection of the Dalitz plot, corresponding to when each α-particle strikes a separate DSSD. The sequential decay profile has a 100% branching ratio. The three direct decay profiles are shown at the level of 0.1%. 204

5.62 One-dimensional projection of the Dalitz plot, corresponding to where two α-particles strike the same DSSD. The sequential decay profile has a 100% branching ratio. The three direct decay profiles are shown at the level of 0.1%. 204

5.63 The normalised likelihood of reproducing the experimental data as a function of the direct decay branching ratio parameter. The dashed line shows the distribution for a DDE/DDP^2 direct decay contribution and the solid line shows the distribution for the DDΦ decay. The likelihood distribution for the DDL decay was much narrower and could not be plotted on the same scale. Upper limits on the direct decay contributions were calculated by evaluating the 95% confidence intervals of these distributions (P-value = 0.05), and are marked by the vertical lines. 206

5.64 DDΦ direct decay mechanism: Fit of Monte-Carlo simulations to the experimental data for DDΦ branching ratios 0% (solid blue line), 0.047% (dot-dashed red line) and 0.1% (dotted black line). 207

5.65 DDE/DDP^2 direct decay mechanism: Fit of Monte-Carlo simulations to the experimental data for DDE/DDP^2 branching ratios 0% (solid blue line), 0.035% (dot-dashed red line) and 0.1% (dotted black line). 208

5.66 DDL direct decay mechanism: Fit of Monte-Carlo simulations to the experimental data for DDL branching ratios 0% (solid blue line), 0.02% (dot-dashed red line) and 0.1% (dotted black line). 208

5.67 Three prior distributions chosen to reflect the present experimental knowledge about the direct decay branching ratio. The vertical line marks the known upper limit on the branching ratio (2σ confidence) from reference [140]. 213

5.68 A O-TPC image of the ^{12}C(γ,α)^{8}Be reaction from reference [203]. 218

B.1 Diagram showing the notation for the various parameters used to calculate the detection angles of the particles. 247

B.2 Diagram showing the horizontal and vertical angles required to fully label the position of a particle detection within the detector array with respect to the initial beam direction. 247

C.1 Diagram used when deriving the form of the kinematic lines for two-body scattering. 249

D.1 Diagrams used in deriving the Dalitz plot coordinates X and Y from the three fractional energies ϵ_i. 251

D.2 The general bounds of the Dalitz plot, due to energy and momentum conservation, for the case of unequal masses. Image adapted from reference [198]. 255

E.1 The distribution of particle energies before (clear histogram) and after (filled histogram) the kinematic fitting was performed, using one constraint equation. The plot is layered such that the distribution after kinematic fitting can be seen through the initial distribution. The uncertainty on each of the measured energies decreases after the fit was performed, illustrated by the narrower distribution of energies. 257

E.2 The distribution of particle energies before (clear histogram) and after (filled histogram) the kinematic fitting was performed, using both constraint equations. The uncertainty on each of the measured energies decreases further when the second constraint equation is applied. 258

E.3 The effects of kinematic fitting (single constraint) when E_2 (centre peak) is subject to a systematic offset from its true value. The initial distribution is centred on 10 MeV, rather than 9 MeV. The kinematic fitting procedure brings the E_2 distribution closer to its true value of 9 MeV, but the other two quantities move further from their true values. 259

E.4 The effects of kinematic fitting (both constraints) when E_2 (centre peak) is subject to a systematic offset from its true value. The kinematic fitting procedure brings the E_2 distribution closer to its true value of 9 MeV, and since the system is now better-constrained, the other two parameters do not move far from their true values. 259

E.5 The effects of kinematic fitting (single constraint) when E_2 (centre peak) is subject to a systematic offset from its true value, but has a significantly larger statistical uncertainty than the other parameters, $(\sigma_1, \sigma_2, \sigma_3) = (0.5, 1.5, 0.5)$ MeV. 260

List of Tables

4.1 Comparison of ^{9}B and ^{9}Be experimental levels [52]. The horizontal lines highlight a newly-measured state in ^{9}B, which could correspond to the π-antibinding molecular configuration. ^{1} Tentative assignment from reference [65]. ^{2} Weighted average of references [65, 66]. 42

4.2 Calculation of $\theta^2 = \gamma^2/\gamma_{\mathrm{w}}^2$ for the ^{8}Be$_{\mathrm{g.s.}}$ + n/p decay channel of the $5/2_1^-$ state. 102

4.3 The reduced-width-to-Wigner-limit ratios (^{8}Be$_{\mathrm{g.s.}}+n/p$ channel) for the 3.9 MeV state in ^{9}B and the 3.8 MeV state in ^{9}Be for various values of the branching ratio. 103

5.1 Illustration of the mis-assignment of hit positions of particles on the same DSSD. Particles α and β have simulated energies E. They each deposit a signal in a front and back strip. The energy orders of the two front, or two back strips that fire are given by ord. f and ord. b. The front and rear strip energies are smeared by σE_f and σE_b to give new energies E_f' and E_b'. These may have a new energy order (ord. f and ord. b). If this is the case, their hit positioned are switched horizontally, vertically, or both. Rows separated by horizontal lines from top to bottom are depicted in figure 5.26 panels a) − d). 156

5.2 Comparing the number of generated Monte-Carlo events N, with the number that reach the final Dalitz plots i. This provides a measure of the experimental efficiency ϵ. Separate results are shown for the cases where each α-particle hits a separate DSSD (hit pattern 1) and where two hit the same DSSD (hit pattern 2). 193

5.3 The values of branching ratio upper limits for each of the direct decay mechanisms. 206

5.4 The values of the DDΦ branching ratio limits to 95% and 99.5% credible intervals based on the Bayesian analysis. Uncertainties are systematic due to the choice of prior. 214

5.5 The values of branching ratio upper limits for each of the direct decay mechanisms. The left columns of data correspond to the frequentist analysis and the right columns correspond to the Bayesian analysis. The quoted systematic uncertainties are due to the choice of prior distribution in the Bayesian analysis. 215

Chapter 1

Introduction

> *"Begin at the beginning," the King said gravely,*
>
> *"and go on till you come to the end: then stop."*
>
> – Lewis Carroll, Alice in Wonderland

Atomic nuclei are self-bound objects that lie at the heart of every atom. Atoms have a size around 1 Å(10^{-10} m), whereas the atomic nucleus is 100,000 times smaller around 1 fm (10^{-15} m). Within nuclei, sub-atomic particles called *nucleons* can move both independently of each other and collectively, giving rise to varied and interesting excitations of these systems.

To a nuclear physicist, these nucleons, called *protons* and *neutrons*, are the building blocks of atomic nuclei. From more fundamental studies in particle physics, it is known that nucleons are composite systems, consisting of quarks and gluons. A proton consists of *uud* quarks and a neutron has an *udd* quark composition. However, to excite a proton (rest mass $\approx$938 MeV/c^2) into an excited Δ^+ state (rest mass $\approx$1232 MeV/c^2) takes several hundred MeV of energy. In contrast, a typical nuclear excitation, based on the relative motion of the constituent nucleons, typically occurs over an energy range of $0.1-10$ MeV. Therefore, in low-energy nuclear physics, protons and neutrons are treated as fundamental particles whose properties and interactions give rise to observed nuclear properties.

Despite their small size, nuclei carry $> 99\%$ of the mass of the atom, so possess an incredibly high average density around 2×10^{17} kg/m^3. At the same time, they are also extremely dynamic objects. A quantum mechanical particle such as a nucleon, trapped in a small, $\approx$fm sized, space such as a nucleus, must have a high momentum, due to Heisenberg's position-momentum uncertainty principle. In some cases, the motion of individual nucleons may amount to an appreciable fraction of the speed of light. In this sense, atomic nuclei are incredibly exciting entities, far removed from the macroscopic objects in the world around us. Some nuclei are spherical in shape, but others possess a variety of interesting deformations and structures, which can rotate like nuclear spinning-tops.

One of the most fundamental problems in nuclear physics is understanding the exact nature of the nuclear force, which binds the nucleus together [1]. Much progress has been made in fundamental physics to understand the strong interaction between quarks and gluons, which will underpin the residual nuclear force between nucleons. At incredibly high energies (TeV) and densities, perturbation theory may successfully be applied to the strong interaction, due to the behaviour of the strong coupling constant with energy [2]. At lower energies, recent advances in chiral effective field theory have provided a way to realistically model the interactions between nucleons. Through *ab initio* calculations, where the various interactions between all constituent nucleons are considered, many properties of light nuclei have been successfully calculated with these realistic nucleon-nucleon interactions [3].

Due to the computationally intensive nature of calculating the properties of a many-body system *ab initio*, part of the work of a nuclear physicist is to extract simpler descriptions of nuclear systems. Therefore, a key feature in the study of nuclear physics is the application of phenomenological models as a way of understanding observed phenomena [4]. Within each description, the ability to interpret experimental data and make predictions based on the various phenomenological models is often fairly complete. However, nuclear physics does lack an overriding theoretical formulation that would allow the analysis of all measured phenomena in a consistent way.

One phenomenon that may add a great deal to our understanding of nuclear structure is the idea of nuclear clustering. Clustering is the concept that groups of nucleons may preferentially form in the nucleus, organising themselves into coherent crystal-like structures. The A-nucleon many-body problem may then reduce down to a smaller configuration space where the effective interactions between clusters of nucleons need only be considered. The subject of clustering is by no means a new idea, and has been discussed throughout the history of nuclear physics [5, 6]. Clustering is a recurrent feature, especially in light nuclei, and there are many documented cases. In relation to this thesis, ^{9}Be is thought to have an $\alpha + n + \alpha$ molecular structure, where the two α-particles are bound together through the exchange of the neutron. Furthermore, ^{12}C is well-described by the relative motion of three interacting α-particles.

Despite the experimental and theoretical attention that nuclear clustering has attracted, the mechanism of cluster formation is not properly understood. Some studies have proposed that the origin of clustering may be traced back to the depth of the confining nuclear potential, so cluster formation should be a sensitive probe of the nuclear force [7]. Other questions arise regarding to what extent the clusters maintain their identities in the nucleus. In ^{12}C, for example, the bosonic α-particles may form a Bose-Einstein-condensate-type state, if the fermonic structures of the α-clusters can be ignored, e.g. in diffuse arrangements. The cluster structures of various nuclei and their excited states are also predicted to have a significant role in stellar nucleosynthesis, which plays a crucial part in the evolution of the universe. The present thesis uses the experimental technique of break-up reactions in order to explore the potential cluster structures of ^{9}Be and ^{12}C.

The following theory chapters describe some ways in which the nuclear many-body problem has been simplified over the years and the progress that has been made towards understanding the complex behaviour of atomic nuclei. The famous liquid-drop model and shell model are initially discussed before a more in-depth discussion on nuclear deformation and clustering. The basic theory of nuclear reactions is then covered before moving on to detailing three experiments. The first explores the possible molecular structure of ^{9}Be and the second answers the question of whether the excited “Hoyle state” of ^{12}C is an α-particle-condensate state. The third study details improvements in the performance of resistive charge division strip detectors.

Chapter 2

Nuclear structure

2.1 The liquid drop model

An early attempt to understand the properties of atomic nuclei, by German physicist Carl Friedrich von Weizsäcker, was called the *liquid drop model* [8]. A nucleus has a constant binding energy per nucleon, which is analogous to the latent heat of vaporisation of a fluid. Furthermore, surface tension effects of a nucleus were thought to be similar to those of a liquid drop. Therefore, by modelling the atomic nucleus as a liquid drop, a quantitative, empirical model was developed that approximated the mass and binding energy of nuclei.

The latent heat of vaporisation of a fluid denotes the amount of energy required to convert molecules from a liquid to a gas phase. Empirically, the latent heat of vaporisation was seen to be proportional to the number of molecules making up the liquid (the total number of bonds) [9]. In a similar way, the binding energy of a nucleus was also observed to be approximately proportional to the total number of nucleons. Using this analogy, the *semi-empirical mass formula* (SEMF) − known also as the *Bethe-Weizäcker formula* − was derived.

In this liquid-drop picture, there are five terms that contribute to the binding energy of a nucleus. The so-called *volume term* is directly proportional to the total number of nucleons, A, as $a_v A$. Here, a_v is a proportionality constant, which is empirically-derived. This encapsulates the idea that each nucleon in the nucleus interacts exclusively with its nearest neighbours, due to the short-range nuclear interaction. The *surface term* accounts for the fact the nucleons on the surface of the nucleus have fewer neighbouring nucleons compared with those in the nuclear interior. This term is analogous to formulation of the surface tension of a liquid drop. Treating the nucleus as a sphere, if the volume is proportional to the total number of nucleons, then the surface area is proportional to $A^{2/3}$. Therefore, a reduction in the binding energy of $a_s A^{2/3}$ is expected. The *Coulomb term* accounts for the electrostatic repulsion between protons in a nucleus, which does not only act between nearest neighbours. The electrostatic repulsion between two protons is inversely proportional to their separation. Therefore, the average reduction in the binding energy in a nucleus with Z protons is $a_c {}^{Z(Z-1)}/_{A^{1/3}}$. The $Z(Z-1)$, as opposed to Z^2, accounts for the fact that each proton can only interact with $Z-1$ other protons.

The final two terms are not analogous with a liquid drop and are exclusive to the quantum mechanical nuclear system. The *asymmetry term* accounts for the difference in the number of protons and neutrons in the nucleus, $a_{\text{asym.}} {}^{(N-Z)^2}/_{A}$. This term corrects for the energy associated with the Pauli exclusion principle, which states that two fermions can not occupy exactly the same quantum state. Therefore, as more nucleons are added to the nucleus, they must occupy higher energy levels, decreasing the overall binding energy. Since protons and neutrons are distinct types of particles, they occupy different quantum states, meaning that the lowest energy configuration corresponds to when there are equal numbers of each. The final *pairing term* accounts for the spin-coupling effects between like nucleons. The nucleus has a lower energy when the number of "spin-up" protons/neutrons equals the number of "spin-down" protons/neutrons. Only in the case where both Z and N are even, can this be the case for both the protons and neutrons. This term takes the form $-{}^{\delta}/_{A^{1/2}}$ where δ changes value between negative, zero, and positive, if the nucleus is *even-even*, *even-odd* or *odd-odd*. The total semi-empirical mass formula is given by equation 2.1.

$$BE = a_v A - a_s A^{2/3} - a_c {}^{Z(Z-1)}/_{A^{1/3}} - a_{\text{asym.}} {}^{(N-Z)^2}/_{A} - {}^{\delta}/_{A^{1/3}} \quad \text{where,} \tag{2.1}$$

$$\delta \approx -12 \text{ MeV for } \textit{even-even},\ 0 \text{ MeV for } \textit{even-odd},\ +12 \text{ MeV for } \textit{odd-odd}. \tag{2.2}$$

As shown in figure 2.1 a), when the parameters a_v through to $a_{\text{asym.}}$ are fit to the experimentally measured binding energies, the general trend is successfully reproduced by the SEMF.

Another success of the SEMF is that it correctly predicts the natural limit for spontaneous fission in nuclei of $^{Z^2}/_{A} = 48$ [10, 11]. If a "liquid drop" nucleus is deformed from its initial spherical shape, the surface energy, U_s, will increase due to the increased surface area. At the same time, the Coulomb energy, U_C, decreases because the nuclear charge becomes more diffuse. Bohr and Wheeler noted that if $U_s + U_C$ for the deformed system is greater than for the spherical configuration, the nucleus will be unstable against fission. This is depicted in figure 2.1 b).

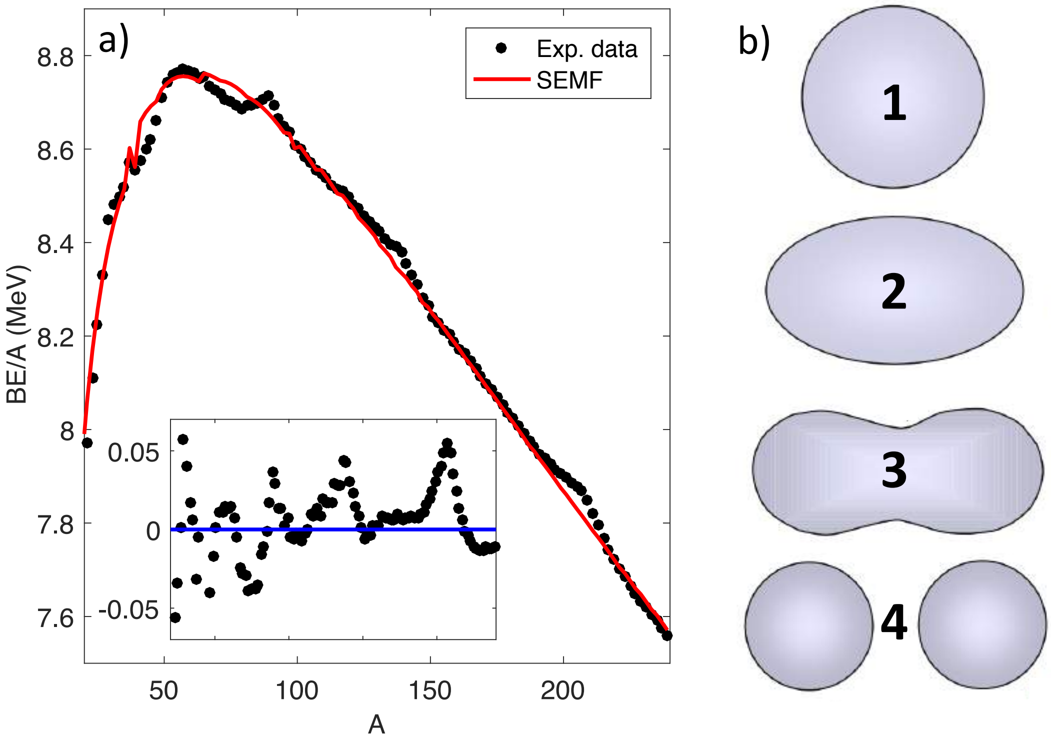

Figure 2.1: a) The binding energy per nucleon, BE/A, as a function of mass number, A (for odd-A isotopes only). The points show experimental data and the red line gives the prediction of the SEMF. The inset shows the fit residuals. b) The process of fission through a liquid-drop picture. 1. The configuration with the least surface energy and the greatest Coulomb energy, 2. & 3. More surface energy and less Coulomb energy. 4. If the surface + Coulomb energy is greater for the deformed system, the nucleus will split/fission. Image in b) is modified from reference [12].

On the other hand, sharp increases in binding energy, compared with the SEMF prediction, at certain *magic numbers* of protons and neutrons, can be seen in figure 2.1 a), which cannot be explained by the liquid drop model. To describe this behaviour, a fully quantum mechanical approach is needed, which is described next.

2.2 The spherical shell model

An electronic theory of the atom, based on the idea that electrons occupy a variety of single-particle orbitals, has been very successful in describing the observed properties of atomic systems [13]. In this *atomic shell model*, discrete single-particle levels are systematically filled in order of energy, as dictated by the Pauli exclusion principle. In doing so, it is possible to obtain atomic systems that consist of completely filled orbitals − *closed shells* − along with extra valence electrons that lie beyond the closed shells. Under the assumption that the electrons contained within the closed shells are inert, or non-interacting, the bulk of atomic properties can be understood by considering the motion and interactions of valence electrons alone. A key feature is that, as more electrons are added to a system, moving left to right across the periodic table of the elements, the observed properties vary smoothly. However, at certain numbers of electrons, the properties of the atoms, such as their binding energies and radii, can be seen to undergo an abrupt change. This corresponds to the case where an electronic shell has been filled. This is analogous to the sudden increase in nuclear binding energies at certain magic numbers of protons and neutrons.

Given the success of the atomic shell model, and the somewhat similar behaviour that atoms and nuclei exhibit, it seems natural to apply a similar shell-model approach to atomic nuclei. However, there are some major differences between the two systems that make the nuclear system more challenging to analyse in this manner. Foremost, the central *Coulomb* interaction set up by the atomic nucleus, which forms the confining potential for the electrons in an atom, is common between all of the electrons. On the other hand, nuclei are self-bound systems. Protons and neutrons are bound together, without some central potential common to the whole system. Secondly, atomic electrons interact with each other and the central potential by the Coulomb interaction alone. The interaction between nucleons is far more complicated.

In the first half of the 20th century a breakthrough model was introduced to explain the observed magic numbers in nuclei. The motion of individual nucleons was approximated to be defined by a potential that is caused by the average interaction of a nucleon with each of the other nucleons. This *mean-field* approach was named the spherical shell-model of the nucleus

[14]. Nucleon-nucleus scattering experiments indicated that the charge distribution of a nucleus was fairly constant within the nuclear interior, with a diffuseness at the nuclear surface [15]. Assuming that the spatial variation of the nuclear interaction was proportional to the density of nuclear matter throughout the nucleus, the confining potential was considered to follow a Woods-Saxon profile [15] as

$$V(r) = -\frac{V_0}{1 + e^{(r-R_0)/a}}, \tag{2.3}$$

where R_0 is the nuclear radius (the point at which the nuclear density drops to 1/2 of its interior value, and a is a diffuseness parameter, which dictates how sharply the nuclear density drops at the surface. By solving this potential, the energy level scheme shown by the left side of figure 2.2 is obtained.

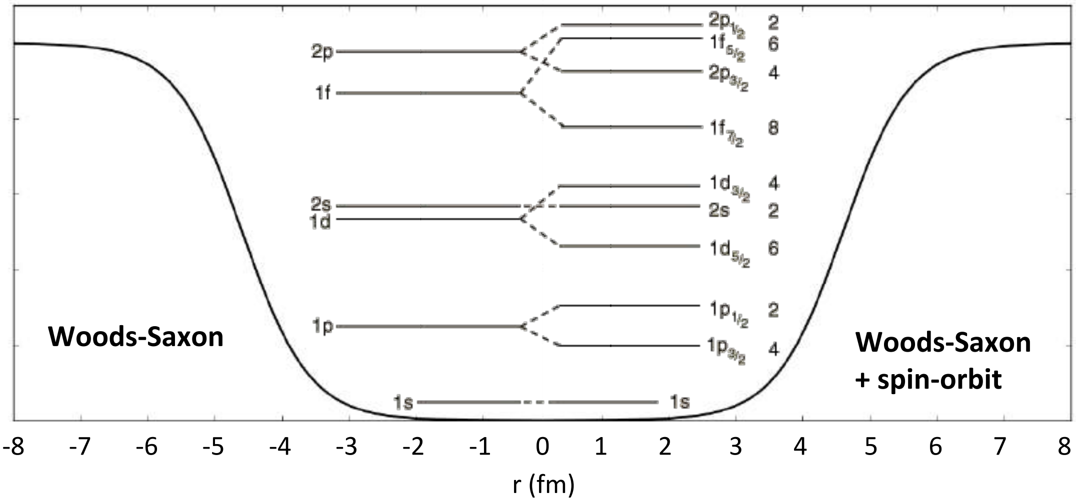

Figure 2.2: The single-particle energy levels of a Woods-Saxon potential, with (right) and without (left) the inclusion of spin-orbit splitting. The levels are labelled $N\ell_j$, with N as the principal quantum number, ℓ as the orbital angular momentum, and j as the total angular momentum. The numbers to the right of the levels show the proton/neutron degeneracies. The levels are shown within a Woods-Saxon potential with the form of equation 2.3.

In this picture, systematically filling the levels with $(2\ell + 1)$ protons and $(2\ell + 1)$ neutrons gives the correct closed shells at magic numbers of 2, 8 and 20, but higher magic numbers do not match the 28, 50, 82 and 126 pattern known from experiment. This can be corrected through the inclusion of a *spin-orbit* interaction [14, 16]. The spin-orbit energy arises due to a coupling between the intrinsic spin of the nucleons, s, and their orbital angular momentum, ℓ, such that the total angular momentum is defined by the vector sum $\boldsymbol{j} = \boldsymbol{\ell} + \mathbf{s}$. In atomic physics, there is also a spin-orbit interaction for electrons due to the interaction between their magnetic moment and the field generated due to their orbital motion in the atom. The nuclear spin-orbit interaction has the same general form as for electrons, $V_{\mathrm{so}}(\boldsymbol{\ell} \cdot \mathbf{s})$, but cannot have an electromagnetic origin, because its effect is too strong.

Consider the states on the left side of figure 2.2. The $\ell = 1$, $1p$ level has a total degeneracy of $2(2\ell + 1) = 6$. Coupling this angular momentum to the nucleon spins gives possible j values of $\ell \pm 1/2 = 1/2$ or $3/2$. Since these two situations correspond to different alignments of the orbital angular momentum and spin, the spin-orbit interaction energy ensures that they are no longer degenerate in energy, i.e. the level splits. Due to the $(\boldsymbol{\ell} \cdot \mathbf{s})$ nature of the interaction, the energy splitting is greater for higher ℓ. Inclusion of the spin-orbit term gives the energy levels on the right hand side of figure 2.2 and generates the correct magic numbers.

Perhaps surprisingly, given the simplifications made during its formulation, this final shell-model description is very powerful in predicting many properties of nuclei. For example, even-even nuclei are always $J^{\pi} = 0^{+}$ in their ground states, which is obtained when systematically filling these shell-model levels. Here J is the total angular momentum of the nucleus and π is the parity. Likewise, the levels structures of nuclei with one or two nucleons beyond a closed shell can be successfully examined through an m-scheme angular momentum coupling. In cases where there are a higher number of nucleons beyond a closed shell, the interactions between them can no longer be ignored, and the *interacting particle shell-model* must be employed [17].

2.3 Nuclear deformation

Some nuclei are non-spherical and are not best described by the spherical shell model. Under the assumption of the conservation of volume – if the nucleus is deformed away from a spherical shape it maintains the same volume – then the shape can be described by a sum of spherical harmonics, $Y_\lambda^\mu(\theta,\phi)$ as

$$R(\theta,\phi) = R_{\text{av}} \left[1 + \sum_{\lambda=2}^{\infty} \sum_{\mu=-\lambda}^{+\lambda} \alpha_{\lambda\mu} Y_\lambda^\mu(\theta,\phi) \right] , \tag{2.4}$$

where $\alpha_{\lambda\mu}$ are coefficients determining the contribution of each spherical harmonic to the shape [18, 19]. The monopole term involving $Y_0^\mu(\theta,\phi)$ is given by the 1 in the series and the dipole term $Y_1^\mu(\theta,\phi)$ is omitted since it just causes a translation in the centre-of-mass. Terms involving $Y_2^\mu(\theta,\phi)$ provide *quadrupole* deformation, $Y_3^\mu(\theta,\phi)$ provides octupole (pear-shape) deformations, and $Y_4^\mu(\theta,\phi)$ provides hexadecapole-type deformations. For a spheroidal nucleus possessing only a quadrupole deformation, the shape may be approximated as

$$R(\theta,\phi) = R_{\text{av}} \left[1 + \beta_2 Y_2^0(\theta) \right] . \tag{2.5}$$

The $\mu = 0$ means that these nuclei are axially-symmetric (cylindrically-symmetric) and can be depicted as a function of the deformation parameter, β_2, as in figure 2.3.

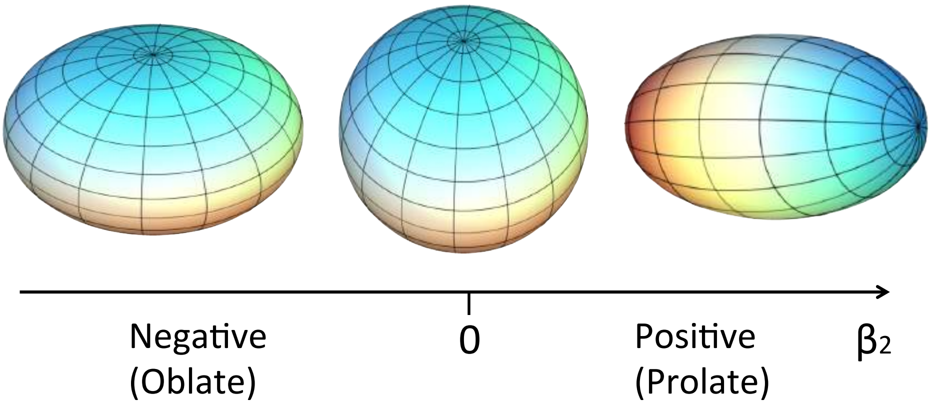

Figure 2.3: The intrinsic shape of an axially-symmetric deformed nucleus as a function of the deformation parameter, β_2. Image modified from reference [20].

Negative values of β_2 correspond to oblate (pumpkin) shaped nuclei, and positive values correspond to prolate (rugby ball) shaped nuclei. The deformation parameter, β_2, is physically related to the dimensions of the nucleus and to various other deformation parameters/notations by [19]

$$\begin{aligned}
\beta_2 &= \frac{4}{3}\sqrt{\frac{\pi}{5}}\frac{\Delta R}{R_{av}} && (2.6)\\
\delta &= \frac{\Delta R}{R_{r.m.s}} && (2.7)\\
\epsilon_2 &= \delta + \frac{1}{6}\delta^2 + \frac{5}{18}\delta^3 + ... && (2.8)\\
\beta_2 &= \sqrt{\frac{\pi}{5}}\left[\frac{4}{3}\epsilon_2 + \frac{4}{9}\epsilon_2^2 + \frac{4}{27}\epsilon_2^3 + ...\right]. && (2.9)
\end{aligned}$$

Here, ΔR is the difference between the lengths of the semi-major and semi-minor axes and $R_{\mathrm{r.m.s}}$ is the root-mean-squared radius. A key indicator of a deformed nucleus is its electric quadrupole moment, essentially a measure of the charge distribution of a nucleus. The relationship between the deformation parameter, β_2, and the intrinsic electric quadrupole moment, Q_0, of a nucleus with charge, Z, is given as

$$Q_0 = \frac{3}{\sqrt{5\pi}} R_{\mathrm{av}}^2 Z \beta_2 \left(1 + 0.16\beta_2\right). \qquad (2.10)$$

The intrinsic quadrupole moment, Q_0, is very different to the measured quadrupole moment in the laboratory frame. A nuclear state of good angular momentum J and projection m_j should have an angular wave function relative to some quantisation axis of $Y_j^{m_j}(\theta, \phi)$. Therefore, the intrinsic shape must be rotated around all axes to produce this distribution in the laboratory frame and the measured quadrupole moment will be a signature of the rotated nucleus. To extract the intrinsic quadrupole moment from this, a complicated deconvolution is required.

Deformed nuclei are described by a version of the shell-model, called the *Nilsson model* [21]. As opposed to using a spherically-symmetric Woods-Saxon potential, an axially-symmetric deformed harmonic oscillator potential is used along with additional centrifugal and spin-orbit terms. The result of solving this Hamiltonian is the famous Nilsson diagram as shown for the lowest single-particle orbitals in figure 2.4, as a function of the ϵ_2 parameter (equation 2.8). This is not a universal solution and the diagram changes depending on the mass of the nucleus in question.

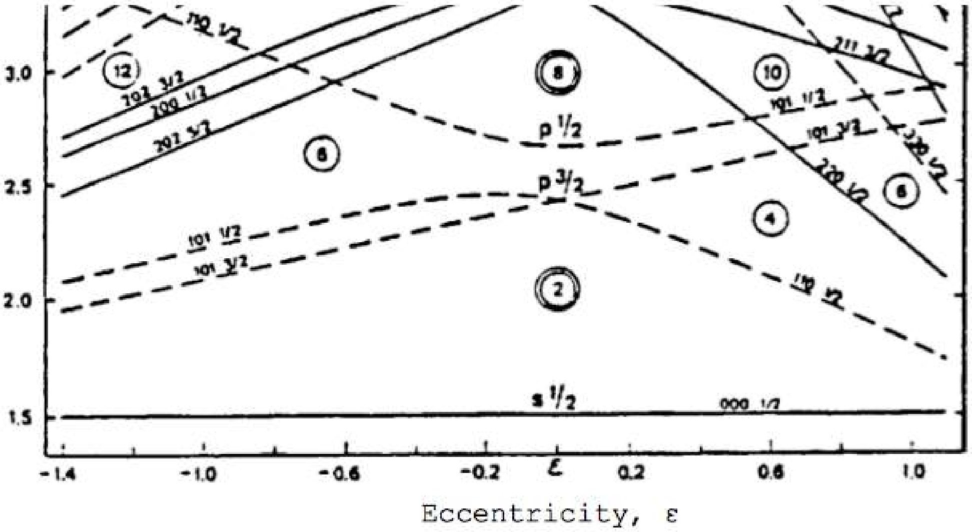

Figure 2.4: The Nilsson single-particle levels as a function of the deformation parameter, ϵ_2 [6]

At $\epsilon_2 = 0$, the levels reproduce those of the spherical shell-model. As the nucleus is deformed, the levels split and shift in energy, creating new shell structures. The magic numbers and closed shells depend on the deformation of the system. In the absence of a full derivation, a qualitative justification for this level splitting requires only two considerations: the short range, attractive nature of the nuclear force and two-state mixing. In the absence of nuclear rotation which is discussed in section 2.4, figure 2.5 shows that a single nucleon with total angular momentum, j, has some projection onto the deformation axis, Ω. It follows from this that in the case of oblate nuclei, high Ω states correspond to when the single-particle orbital has maximal overlap with the nuclear volume, increasing the binding energy. Low Ω projections have minimal overlap and, therefore, have a lower binding energy. The opposite occurs for prolate deformations as depicted in figure 2.5 a). It is this interaction with the nuclear volume that leads to the splitting of otherwise degenerate magnetic substates. Some levels on the diagram are permitted to cross because only states with the same Ω will mix. The lines sometimes curve if two Nilsson orbits with the same Ω approach each other in energy. Two-state mixing ensures that they will not cross, but will 'deflect' each other.

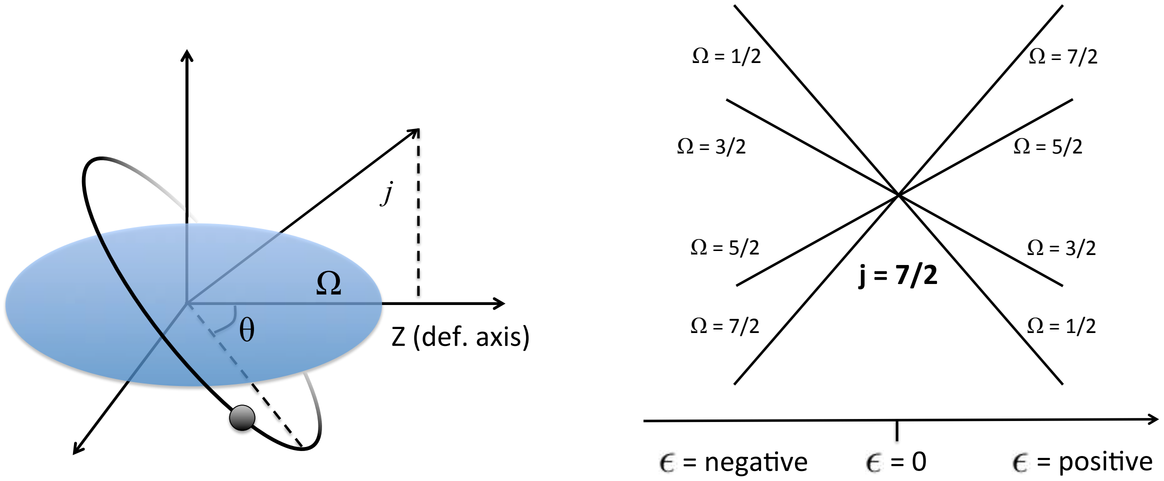

Figure 2.5: a) Definition of the coordinate system and Ω quantum number used in the Nilsson model (adapted from [22]). b) Schematic level splitting as a function of the deformation parameter, ϵ.

2.4 Collective rotation

Despite the successes of the spherical shell model and the deformed Nilsson model, to describe a range of nuclei, the possibility of the collective motion of nucleons must also be considered. In the shell-model picture, protons and neutrons systematically fill single-particle levels to form the lowest (ground) state. In this picture, to form an excited state of a closed-shell even-even nucleus, a pair of protons or neutrons must be broken and one promoted to a higher oscillator shell. As such, the large shell-gap energy should mean that the first excited state is found at a particularly high excitation energy. Additionally, this first excited state may have the opposite parity to the ground state. In many cases, such behaviour is not observed. In fact, a key indicator of collective behaviour in an even-even nucleus with a 0^+ ground state, is the existence of a relatively low-energy 2^+ first excited state.

One form of collectivity, exclusive to deformed nuclei, is rotation. Since clustered nuclei are inherently deformed and non-spherical, the experimental observation of rotation in these systems is key evidence for the existence of clusters. Such rotational behaviour has also been observed in many deformed poly-atomic molecular systems [23]. A deformed nucleus can generate angular momentum collectively via rotation (or vibration) or by single-particle excitations in which unpaired nucleons generate angular momentum. In practice, many states are a mixture of these two cases. Firstly, consider the case of an inert, rotating nucleus, while ignoring the motion of valence nucleons. In classical mechanics, the kinetic energy of a rotating object with a moment of inertia, $\mathcal{I}$, at an angular frequency of ω is given by

$$E(\omega) = \frac{1}{2}\mathcal{I}\omega^2. \tag{2.11}$$

Since the angular momentum of an object is $J = \mathcal{I}\omega$, the rotational kinetic energy can be rewritten as $E = {}^{J^2}/_{2\mathcal{I}}$. Since a nucleus is a quantum mechanical object, the angular momentum is replaced with the angular momentum operator $\widehat{J^2}$, which has eigenvalues of $\hbar^2 J(J+1)$. This gives a quantum mechanical rotational energy of

$$E(J) = \frac{\hbar^2}{2\mathcal{I}} J\,(J+1)\,. \tag{2.12}$$

Therefore, the quantum mechanical energy levels of a rotating nucleus are proportional to $J(J+1)$. By increasing the J quantum number, the excited states follow a pattern known as a *rotational band*. By plotting the excitation energies of a rotating system against $J(J+1)$ of the levels, a linear relationship should be found. In some cases where nuclear rotation is built upon an excited state, the *band head*, the lowest energy state in the band, lies at a higher excitation, E_0, than the ground state, hence, equation 2.12 becomes

$$E(J) = E_0 + \frac{\hbar^2}{2\mathcal{I}} J\,(J+1)\,. \tag{2.13}$$

In the case where the motion of valence nucleons within the rotating nucleus cannot be ignored, the angular momentum coupling scheme of figure 2.6 must be considered. Here, the total angular momentum of the nucleus, J, comes from several sources, not just the collective rotation. The orbital angular momentum and spin of an individual nucleon, $\boldsymbol{\ell}$ and $\boldsymbol{s}$, couple to a single-particle angular momentum of $\boldsymbol{j}$. This has a projection onto the deformation (symmetry axis) of Ω. A rotating nucleus will also have a component, $\boldsymbol{R}$, due to the collective rotation, which will couple with $\boldsymbol{j}$ to give a total angular momentum of $\boldsymbol{J}$, such that $\boldsymbol{J} = \sum_i \boldsymbol{j}_i + \boldsymbol{R}$. The projection of $\boldsymbol{J}$ onto the deformation axis is denoted by K, and it is this quantity that labels the rotational band. For most band heads, $J = K = \sum_i \Omega_i$, i.e. the angular momenta are aligned along the deformation axis, because of something called *collective back rotation.* It can be shown that, in order to minimise the rotational energy, the collective angular momentum of the core is equal and opposite to the component of the single-particle angular momentum.

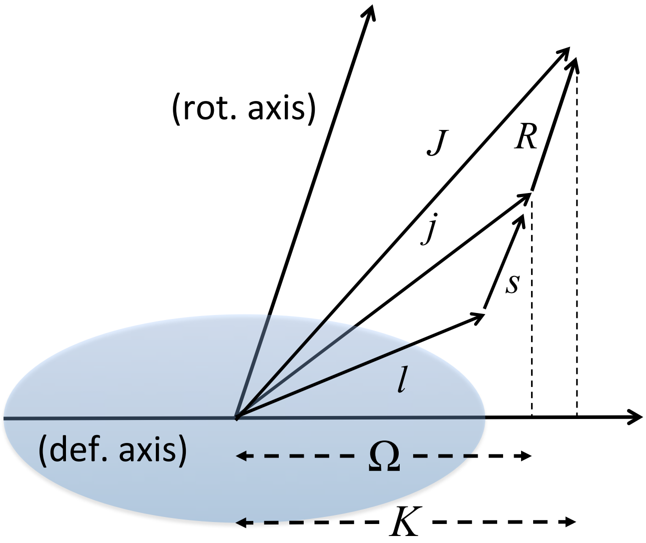

Figure 2.6: The coupling of intrinsic and collective angular momenta and their projections onto the deformation (symmetry) axis.

Under the assumption of an axially-symmetric rotating nucleus, K and Ω are good quantum numbers. As discussed in appendix A, a $K = 0$ rotational band is highlighted by a pattern of angular momenta that increase in steps of two units. These are 0, 2, 4 ... for $K^{\pi} = 0^{+}$ and 1, 3, 5 ... for $K^{\pi} = 0^{-}$. This is because the symmetrised wave functions of the systems vanish unless these conditions are met. For other values of K the angular momenta along a rotational band will increase by single units.

In a system where a deformed rotating core nucleus couples to an unpaired nucleon, the interaction between this particle and the core will cause an additional *Coriolis* effect. Similarly to the effects of an object on the surface of the Earth as it rotates, as shown by figure 2.7 a), the nuclear Coriolis interaction aligns the intrinsic angular momentum of an unpaired particle, j, with the nuclear rotation axis (figure 2.7 b)) [24–26]. The result, discussed further in appendix A, is that the energy-spin relationship deviates away from the linear relationship indicated by equation 2.13, to give

$$E(J) = E_0 + \frac{\hbar^2}{2\mathcal{I}} \left[J\left(J+1\right) + a(-1)^{J+1/2}\left(J + 1/2\right) \right]. \tag{2.14}$$

Here a is called the Coriolis decoupling parameter and $(-)$ changes sign as $J + {}^1\!/_2$ alternates between odd and even values. This gives a zig-zagged relationship between excitation energy and $J(J+1)$, rather than a linear one. An example of this behaviour can be seen in the $K = {}^1\!/_2$ rotational bands of ^{9}Be, which are exhibited in figure 4.6.

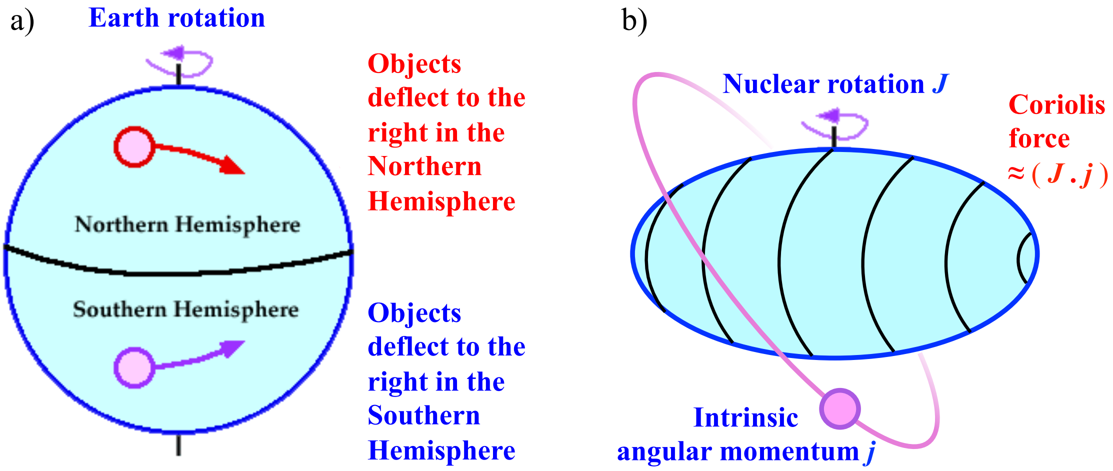

Figure 2.7: a) The Coriolis force as an artefact of the Earth's rotation, deflects an object either in the direction of, or against the direction of, the Earth's rotational angular momentum. Image adapted from reference [27]. b) A classical picture of a nucleon with intrinsic angular momentum, $\boldsymbol{j}$, coupling to a total angular momentum $\boldsymbol{J}$, with a strength $(\boldsymbol{J} \cdot \boldsymbol{j})$.

2.5 α-clustering

The preceding discussions of the shell model, deformation and rotational collectivity assume that for a few nucleons outside of a closed shell, the system is best modelled as an inert core, spherical or deformed, and that the valence nucleons move in a mean-field-type potential. However, another theory of nuclear structure exists based on the notion of *clustering*. This is the assertion that groups of nucleons may cluster together in the nucleus. Review articles on this topic may be found in references [6] and [28]. This theory was in part motivated in the early days of nuclear physics by the observation of α decaying heavy nuclei, leading to the idea that the α-particle, a quartet of two protons and two neutrons, may be preformed in the nucleus. Additionally, there are a number of cases where shell-model type approaches have failed to reproduce the properties of certain nuclei, leading to the idea of more exotic structures. This is discussed in more detail for the ^{9}Be and ^{12}C nuclei in the following chapters.

Such clustering behaviour is not surprising, and in fact is to be expected, given that clustering phenomena are observed throughout the universe. On the cosmological scale, galaxies cluster into filament-like structures, diverging away from the initial density field of the universe to minimise the gravitational energy [29]. Likewise, figure 2.8 illustrates that, when under attack from predators, shoals of mackerel will deform away from their initial spherical configuration into two or more clusters, to maximise their chances of survival.

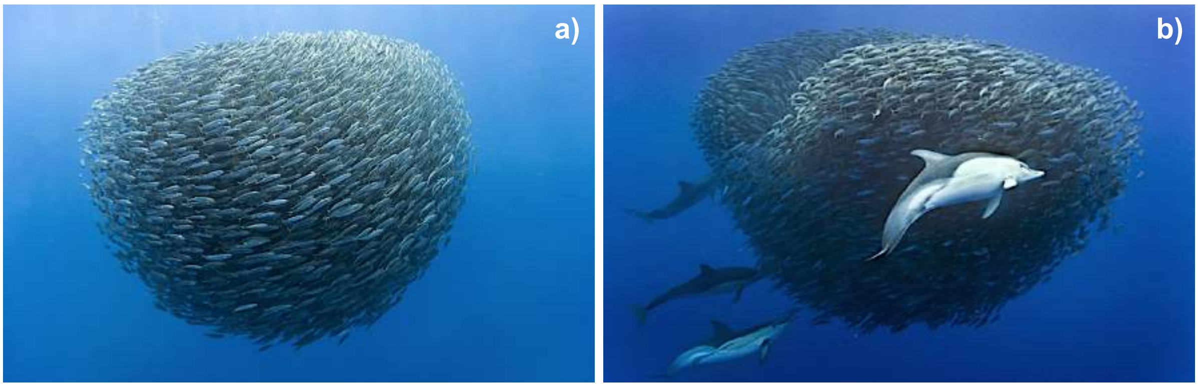

Figure 2.8: The excitation of a spherical shoal of mackerel into a two 'cluster' structure. Images from reference [30].

Given the clustering in the universe, and the reasons behind it, this begs the question of why clustering in nuclei happens in the first place. In general, bound systems of nucleons (nuclei) exist due to the fact that the bound system has a lower mass than the sum of its constituent parts. The difference in mass equals the binding energy of the system. Similarly, energy must be given to a nucleus in order for it to be disassembled. For a mass-A nucleus, it is observed, by examining the binding energies of the nucleus and its constituents, that clusters of nucleons are preferentially formed at lower energies than is required to completely disassemble the nucleus. For example, ^{20}Ne, when given an excitation energy of 4.7 MeV, may decay into ^{16}O + α. A further 7.2 MeV may liberate a further α-particle leading to ^{12}C + 2α decay. A far higher energy is required to liberate individual protons and neutrons. This suggests that at excitation energies above 4.7 MeV, the ^{20}Ne nucleus may possess a ^{12}C + α structure, and at higher energies still, more complicated cluster structures may emerge. This proposal is encapsulated within the famous Ikeda diagram, which links accessible cluster structures with the excitation energy of the nucleus [31], and is given in figure 2.9.

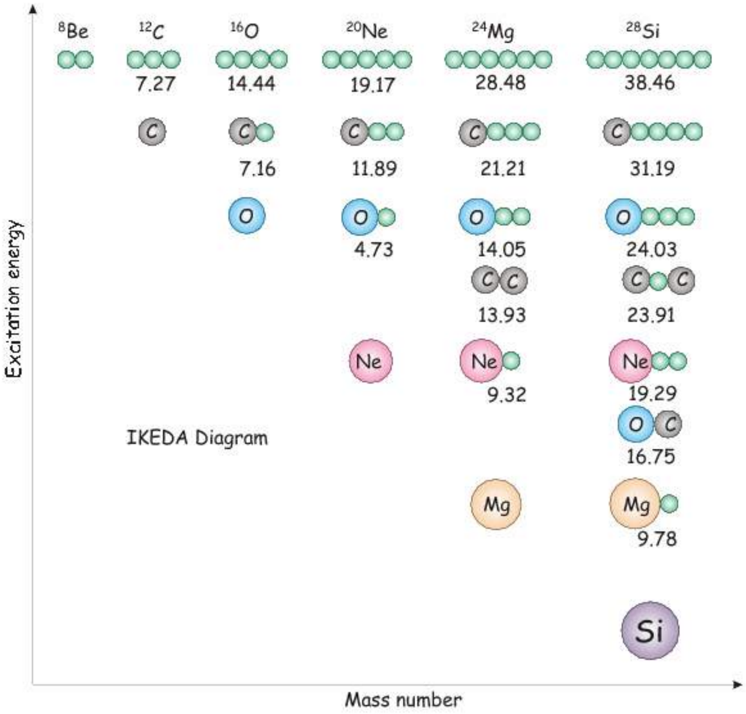

Figure 2.9: The Ikeda diagram, which links accessible cluster structures with excitation energy. Clusters are labelled except for α-particles, which are denoted by the green circles. Image created by Tz. Kokalova and taken from reference [28].

A common theme throughout the Ikeda diagram is that the ^{4}He nucleus (α-particle) is consistently the first cluster to be liberated from the nucleus. This is due to its rather high binding energy per nucleon as shown in figure 2.10. In the shell model, presented in section 2.2, ^{4}He corresponds to the first doubly-magic closed shell, where all the nucleons reside in the $0s$ orbital. Since all of the nucleons have the same wave function, there is a maximal overlap, leading to a particularly high binding energy. Therefore, the unique α-particle is considered to be an ideal cluster and the remainder of this thesis will focus on this possibility.

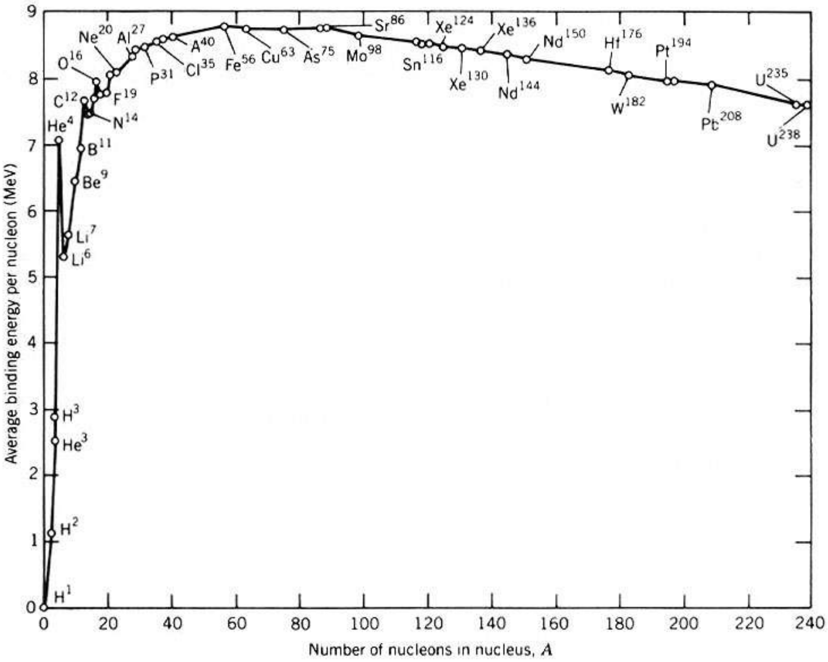

Figure 2.10: The binding energy per nucleon (BEPN) as a function of the nucleon number, A, for a selection of even-A naturally occurring isotopes. Images from reference [32].

Cluster formation is a key part of nuclear many-body dynamics, which must exist simultaneously with the formation of a mean-field potential. Therefore, since mean-field states and cluster states should coexist, the nuclear shell model should play an important role in the emergence of clustering. This connection between collective and single particle motion earned Bohr, Mottleson and Rainwater the Nobel Prize in Physics in 1975. The connection between the mean field and clustering can be basically illustrated from a harmonic oscillator (HO) perspective, where individual nucleons are assumed to move independently in a 3D quadratic potential [18]. Deforming the potential along the z-axis and implementing the conservation of nuclear volume causes a directional dependence of the oscillator frequency. These new characteristic frequencies are related to the degree of quadrupole deformation, ϵ as follows [6]

$$\begin{aligned} \epsilon &= (\omega_\perp - \omega_z)/\omega_0 && (2.15) \\ \omega_0 &= (2\omega_\perp + \omega_z). && (2.16) \end{aligned}$$

Here, $\omega_\perp$ is the oscillator frequency perpendicular to the deformation axis. This in turn perturbs the standard SHO energy levels and introduces new oscillator quantum numbers, $n_\perp$ and n_z

$$E = \hbar\omega_\perp n_\perp - \hbar\omega_z n_z + \frac{3}{2}\hbar\omega_0. \qquad (2.17)$$

The resulting energy level structure is found to vary as a function of the deformation parameter ϵ as shown in figure 2.11 a).

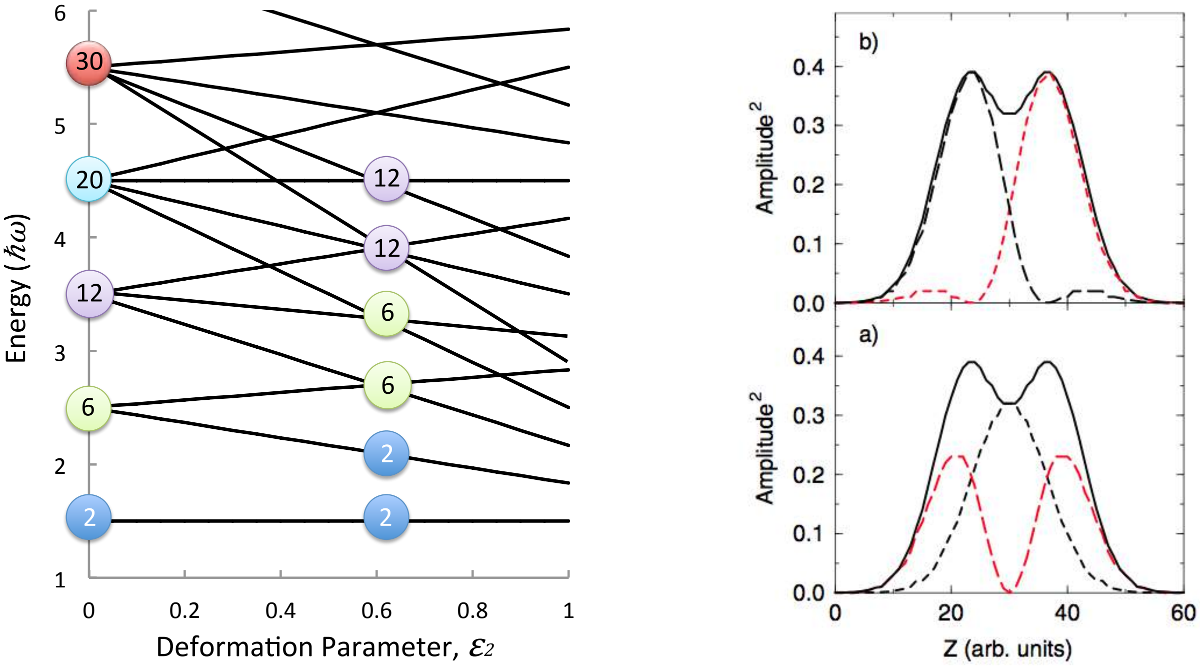

Figure 2.11: Left: The energy levels of the SHO as a function of the deformation parameter ϵ_2. Right: Approximate ^{8}Be nuclear density projections calculated in the HO basis. Image from reference [6].

As expected, $\epsilon = 0$ reproduces the standard HO levels. The key feature to note is the crossing of the levels at a deformation of 2:1 ($\epsilon = 0.63$). The new degeneracies demonstrate that the shell structure has evolved. At 2:1 deformation, the sequence of standard HO degenerate levels are repeated twice, indicative of two interacting spherical HO potentials and suggestive of clustering behaviour. These symmetries in the magic numbers emerge at additional deformations of 3:1, 4:1 etc and establish a link between deformed shell closures and cluster formation.

Inspection of the densities of the nucleons that occupy the deformed orbitals provides further indications of clustering. Consider the proposed 2α structure of ^{8}Be, which would correspond to a 2:1 deformation. The levels shown in figure 2.11 a) are systematically filled with 4 protons and 4 neutrons where pairs of particles couple to spin zero. The levels corresponding to $[n_\perp, n_z] = [0, 0]$ and $[0, 1]$ are occupied and the corresponding ^{8}Be density is given as $|\phi_{0,0}|^2 + |\phi_{0,1}|^2$. This has previously been evaluated and is plotted as a function of distance along the deformation axis in figure 2.11 b). A double-humped distribution is formed, indicative of a 2α cluster structure. Furthermore, it has been calculated that the density distribution has a greater than 90% overlap with the wave function of a free α-particle [33]. Clearly, the clustering that naturally emerges acts to deform the mean field that produced it in the first place. Herein lies the problem with a mean-field approach in the context of clustering.

Since each chapter of this thesis, relating to experimental studies of ^{9}Be and ^{12}C, gives detailed theoretical introductions to clustering in each of these nuclei, any further theoretical discussion of α-clustering is left until then. However, it is useful to consider what the experimental signatures for α-clustered states may be. Since clustering indicates a departure from a spherical shape, clustered nuclei will rotate, meaning that the discussion in section 2.4 is quite pertinent. By examining the energy-spin systematics of states in a clustered nucleus, the nuclear moment of inertia may be extracted and inferences about its shape can be made. Further, if the nuclear charge distribution deviates away from a spherical shape, the measured electric quadrupole moment will be non-zero. Finally, if a nuclear state is clustered, then it is reasonable to assume that when it decays, it will preferentially do so by emission of the cluster. To fully understand this, the discussion of resonances and nuclear reactions in chapter 3 must be considered.

Chapter 3

Nuclear reactions

3.1 Nuclear resonances

The aim of this thesis is to examine the excited states in ^{9}Be and ^{12}C in order to understand elements of their *structure*. The nuclear states under investigation lie at sufficiently high energy that they will preferentially choose to decay through particle emission, rather than electromagnetic decays to the ground state. These states appear as resonances in the reaction cross section, and their manifestation will depend on the *reaction* chosen to populate them, and the way in which they decay. As such, a general discussion about nuclear resonances will be useful.

In the 1930's, several experimental studies measured $n +^{A}_{Z}\mathrm{X}$ reactions, and by measuring the resulting decay radioactivity of the sample, were able to assess the probability of neutron absorption, or the reaction *cross section* [34, 35]. It was observed that the cross section was strongly energy dependent, which led to the idea of unbound, long-lived states in the $n +^{A}_{Z}\mathrm{X}$ system, at an energy defined by the centre-of-mass energy of the collision. A simple mathematical form for the reaction cross section was derived by Breit and Wigner [36, 37] as

$$\sigma(E) = \frac{\Lambda^2}{\pi} S \frac{\Gamma_s \Gamma_r}{(E - E_0)^2 + \Gamma^2}, \tag{3.1}$$

where Λ is the de Broglie wavelength of the projectile, E_0 is the frequency of the resonance, $S = 2J + 1$ (with J as the total angular momentum of the resonance), Γ is the total width of the resonance (full width at half maximum FWHM) and Γ_s and Γ_r are called the partial widths for the entrance and exit reaction channels.

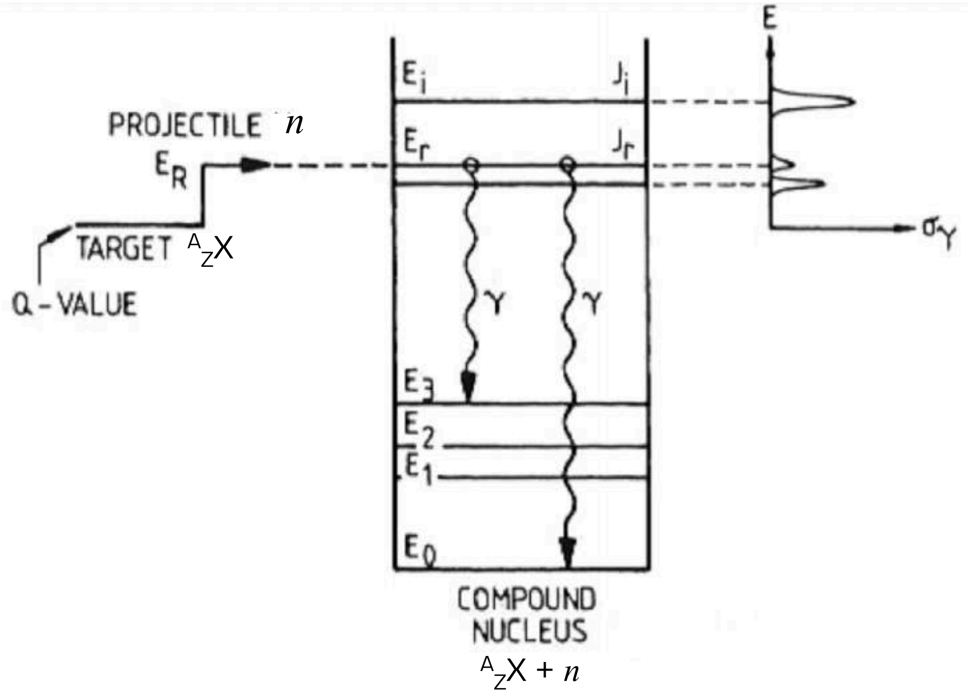

Figure 3.1: The production of unbound resonances in the $n + ^A_Z$ X system. Image modified from reference [38].

The idea of resonances in the $n + ^A_Z$ X system is straightforward to justify. In the one-dimensional toy model presented in reference [39], where the nuclear potential $V(r)$ is zero for $r > a$ and $-V$ for $r < a$, by solving the Schrödinger equation in each region, one obtains a wave function for the outgoing flux as

$$\psi_{\text{out}} = a\left[e^{-ikr} + e^{i(kr+2\zeta)}\right] = Acos(kr + \zeta). \tag{3.2}$$

The incoming wave function may be written as

$$\psi_{\text{in}} = Bsin(Kr + \delta). \tag{3.3}$$

Here, k and K are the wave numbers for each region ($k/K = \sqrt{2\mu(E - V)}/\hbar$). The symbols ζ and δ are phase shifts of the outgoing and incoming waves. The phase shift ζ is energy dependent and is caused by the interaction between the incoming particle and the nuclear potential. By demanding continuity of the wave function and its derivative at the boundary (nuclear radius $r = a$) a solution may be obtained for given values of k, K and ζ. As was demonstrated in reference [39], for some values of ζ (some values of energy) the incoming wave function is permitted to penetrate with a large amplitude into the interior of the nucleus. This penetration, as a function of ζ, is shown in figure 3.2. Although this simple picture does not elucidate the nature of nuclear resonances, it does highlight the idea that penetration into the nuclear volume – a necessity for nuclear excitation – is energy dependent.

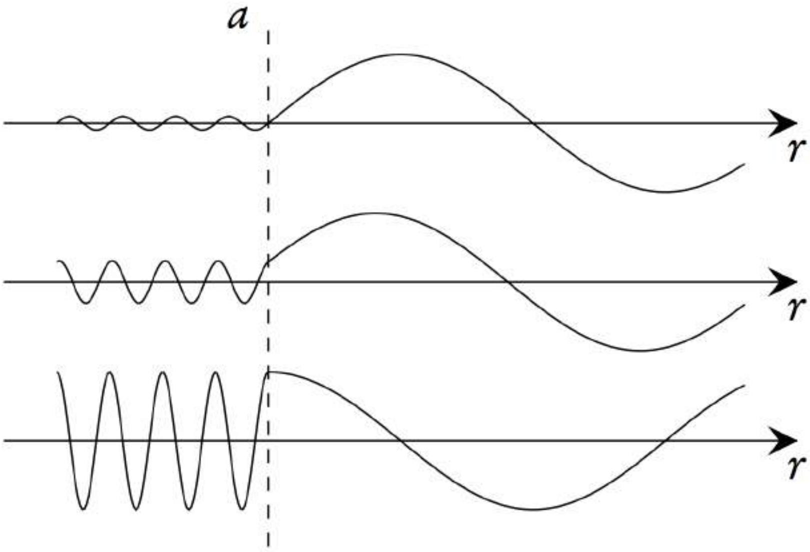

Figure 3.2: Penetration into the internal nuclear region for different values of the phase shift, ζ. The top panel shows the system far away from resonance, and the bottom panel shows the system on resonance (wave function derivative is zero at the boundary). The centre panel shows the system for an intermediate value of ζ. Image from reference [39].

3.2 Introduction to R-Matrix theory

A key feature that has not yet been discussed is the repulsive potential barrier from Coulomb and angular momentum between the two reacting nuclei. The existence of these barriers produce a classically-forbidden region outside of the nuclear volume, which modifies the coupling between states in the core and in the continuum. Hence, the simple Breit-Wigner cross section presented by equation 3.1 does not tell the full story.

In order to interpret nuclear cross sections, R-Matrix theory is required. A detailed review of this analysis framework can be found in reference [40] and a pedagogical text on the subject is given by reference [41]. This section aims to provide an introductory overview of the topic and provides some key results. In R-Matrix theory, the nucleus is treated as a compound system, which may be excited or de-excited through various *channels*. The channels correspond to different projectile-target combinations, channel spins, and relative angular momenta. For example, ^{16}O may be excited, or may decay, through a variety of channels. These include, but are not limited to, the ^{12}C + ^{4}He channel, the ^{8}Be + ^{8}Be channel, or through excited states in these nuclei, which may correspond to different angular momenta. The aim of an R-matrix analysis is to calculate the reaction cross section, $\sigma_{c'c}$, given an entrance channel, c', and an exit channel, c.

Using this method, the compound nuclear system is separated into two regions: an internal region where the nuclear force dominates, and an external region, beyond the effects of the nuclear interaction, where only the Coulomb force comes into play. The point separating these regions is called the *channel radius*, and for a pair of particles 1 and 2, it is typically defined as

$$a_c = r_0 \left(A_1^{1/3} + A_2^{1/3} \right). \tag{3.4}$$

The parameter r_0 is around 1.35 fm. Since $r_0 A^{1/3}$ is the radius of a nucleus of mass A, equation 3.4 describes the case where the two nuclei in the channel are just ‘touching.’ The internal nuclear system is modelled as a number of states labelled by i, with energies E_i, total angular momentum and parity $J_i^{\pi_i}$. These states couple to the channel c by a *reduced width amplitude* γ_{ic}.

The levels are considered to be the exact solutions to the internal Hamiltonian for the compound system $\widehat{H}\phi_i = E_i\phi_i$. In this case, the total wave function of the system is $\Psi = \sum_i C_i\phi_i$. The reduced width amplitude is a measure of the probability of preforming the two particles in channel c, separated by the channel radius as

$$\gamma_{ic}^2 = \frac{\hbar^2}{2\mu_c a_c}|\phi_i(a_c)|^2, \tag{3.5}$$

where μ_c is the reduced mass of the two-fragment system. A theoretical maximum value for the reduced width γ_{ic}^2 is equal to $3\hbar^2/2\mu_c a_c$, which is called the Wigner limit [42]. This is derived by assuming an internal wave function, which is constant up to the channel radius, and is zero outside. If an excited state has a reduced width for α decay that is a substantial fraction of the Wigner limit, it indicates a possible α-cluster structure. In other words, the internal wave function is similar to the 'fragment' + α channel wave function.

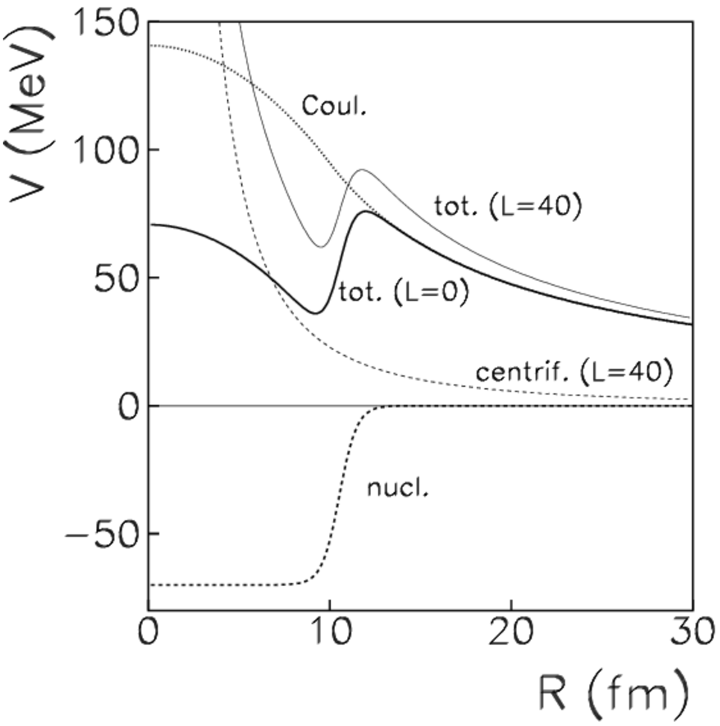

Figure 3.3: The functional form of the potential for varying centrifugal barriers in the ^{16}O + ^{208}Pb system. Image from reference [43].

The coupling between an internal level and a channel c is not just determined by the internal properties of the system; the Coulomb and angular momentum barriers suppress the ability of the nucleus to emit the appropriate pair of particles from the channel radius. The Coulomb and centrifugal barriers for a two-body system are shown in figure 3.3. The coupling is affected by the penetrability through the barrier $P_c(E_i)$, meaning that a *partial width* Γ_{ic} must be defined as

$$\Gamma_{ic} = 2P_c(E_i)\gamma_{ic}^2, \tag{3.6}$$

and the total width of a state is given by the sum of all of the partial widths of the open channels. Using R-Matrix theory, it is possible to derive the reaction cross section. In order to ignore interference effects between different states, the following discussion focusses on an isolated resonance. For a *narrow* resonance, where the decay penetrability for the channel does not increase significantly over the total width of the resonance, the simple Breit-Wigner form of equation 3.12 is obtained

$$\sigma_{c'c} \propto \frac{\Gamma_{ic'}\Gamma_{ic}}{(E-E_r)^2 + (\Gamma_i/2)^2}. \tag{3.7}$$

The measured resonance energy differs from the level energy by an amount equal to the *level shift* so $E_r = E_i + \Delta_i(E_r)$. This may be calculated from the *shift function*, $S_c(E)$ [44]. Similarly, the observed level widths also vary by an amount dictated by the shift function.

$$\begin{aligned} \Delta_{ic}(E) &= -(S_c(E) - B_c)\gamma_{ic}^2 & (3.8)\\ \gamma_{ic}(\text{obs.}) &= \frac{\gamma_{ic}^2}{1 + \sum_c \gamma_{ic}^2 \frac{dS}{dE}|_{E_r}}. & (3.9) \end{aligned}$$

Typically B_c is set to equal $S_c(E_r)$ when working with isolated resonances. The shift function and the penetrability are calculated in terms of regular and irregular Coulomb wave functions evaluated at the channel radius $F_\ell(Ka_c)$ and $G_\ell(Ka_c)$ as

$$S_{\ell i}(E) = P_{\ell i}(E)\left[F_\ell(Ka_c)F'_\ell(Ka_c) + G_\ell(Ka_c)G'_\ell(Ka_c)\right] \quad \text{and} \tag{3.10}$$

$$P_{\ell i}(E) = \frac{Ka_c}{F_\ell(Ka_c)^2 + G_\ell(Ka_c)^2} \tag{3.11}$$

respectively, where $F'_\ell(Ka_c)$ and $G'_\ell(Ka_c)$ indicate derivatives of these functions with respect to Ka_c $(K = \sqrt{2\mu_c E}/\hbar)$ and ℓ is the orbital angular momentum of the channel.

The cross section for an isolated broad resonance is parameterised similar to a simple Breit-Wigner profile but with an energy-dependent resonance energy and width

$$\sigma_{c'c} \propto \frac{\Gamma_{ic'}(E)\Gamma_{ic}(E)}{(E - E_i - \Delta_{ic}(E))^2 + (\Gamma_i(E)/2)^2}. \tag{3.12}$$

Therefore, rather than the symmetric Breit-Wigner line shape, more complicated asymmetric resonance profiles are expected for broader states. In a very extreme case, the multiplication of the increasing penetrability factor in the numerator of equation 3.12, via equation 3.6, with the decreasing Breit-Wigner tail of the resonance may result in the appearance of a *ghost state* [45, 46]. Both the 0^+ Hoyle state in ^{12}C and the ^{8}Be ground state have accompanying ghost states [47–50].

To derive these results, the R-matrix for an incoming and outgoing channel must be constructed

$$\mathbf{R}_{c'c} = \sum_{i=1}^{N} \frac{\gamma_{ic}\gamma_{ic'}}{E_r^i - E} \quad , \tag{3.13}$$

which has N resonances at energies $E = E_r^i$. As can be seen, the R-matrix is a function of energy, E, the resonance energies, E_r^i, and the reduced channel widths, γ_{ic} and $\gamma_{ic'}$. Another object called the S-matrix is defined as

$$\mathbf{S} = \frac{1 - \mathbf{R}(S - iP - a_c\beta)}{1 - \mathbf{R}(S + iP - a_c\beta)} e^{2i\phi}, \tag{3.14}$$

where ϕ is called the *hard-sphere phase shift* given as $\phi = -atan(^{F}/_{G})$ and β is a free parameter. The cross section is calculated from this S-matrix [44].

In reality, an experimentalist can measure an excitation spectrum/ reaction cross section over many scattering angles and through a variety of different incoming and outgoing channels. Such cross sections may include numerous resonances that are populated during the experiment. The challenge is then to extract the properties of these resonances using an R-matrix fit to the data. As has been mentioned, the properties of resonances, in particular the reduced channel widths, can lead to an understanding of the degree of clustering of the nuclear states. One program that can perform an R-matrix fit is called AZURE2 [51]. During a fit to experimental data, the resonance energies and reduced widths are varied such that the cross section, calculated from the S-matrix, best fits the experimental data. This is evaluated through a χ^2 minimisation procedure.

Chapter 4

Molecular structures in the mirror nuclei, beryllium-9 and boron-9

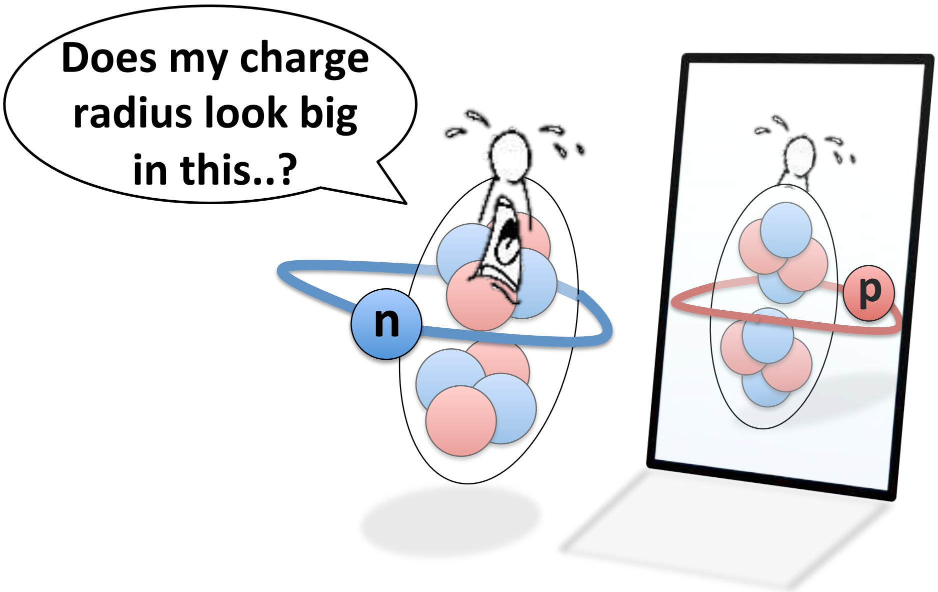

Chapter abstract

Beryllium-9 is thought to be the simplest example of a nuclear molecule. Whereas ^{8}Be is unstable to α decay, ^{9}Be is not; the extra valence neutron is though to exist in either σ- or π-type orbitals about two α-particle cores, increasing the binding energy. In this sense, the neutronic motion is analogous to electron orbits in atomic molecules. Three rotational bands in ^{9}Be have been identified in the past, corresponding to the collective rotations of various molecular configurations. A fourth rotational band, corresponding to the π-antibinding configuration, is predicted but has not yet been experimentally identified. To investigate the ^{9}Be excitation spectrum, the inelastic scattering and break-up reaction ^{9}Be(^{4}He,3α)n was measured using an array of double-sided silicon strip detectors at beam energies of 22 and 26 MeV. Excited states in ^{9}Be up to 8 MeV were populated and reconstructed through measurements of the final state reaction products. Evidence is provided for a state in ^{9}Be at $3.82^{+0.08}_{-0.09}$ MeV with a width $\Gamma = 1240^{+270}_{-90}$ keV. These parameters are consistent with two recent measurements of a new state in the mirror nucleus, ^{9}B. Analysing the reduced width of the state ($^{8}\mathrm{Be}_{\mathrm{g.s.}}$ channel), along with that of the proposed mirror state in ^{9}B, has led to a firm limit on the angular momentum $J \leq 7/2$ and a tentative assignment of $J^{\pi} = 1/2^{-}$ or $3/2^{-}$. This leaves the possibility that the newly-measured state is the hitherto unseen π-antibinding molecular band head.

This work has been published in the following articles. Some figures and text blocks from these publications are used in the following chapter.

R. Smith, M. Freer, C. Wheldon, N. Curtis, Tz. Kokalova, et al. *Disentangling unclear nuclear breakup channels of beryllium-9 using the three-axis Dalitz plot.* Journal of Physics: Conf. Series **863** (2017).

R. Smith, C. Wheldon, M. Freer, N. Curtis, Tz. Kokalova, et al. *Evidence for a 3.8 MeV state in ^{9}Be.* Physical Review C **94** (2016).

R. Smith, C. Wheldon, M. Freer, N. Curtis, Tz. Kokalova, et al. *Breakup branches of Borromean beryllium-9.* Proceedings of Nuclear Structure and Dynamics 15. Vol. **1681**. AIP Publishing, (2015).

4.1 Review of the beryllium-9 nucleus

Whereas the highly clustered ^{8}Be nucleus is unstable to α-decay by around 92 keV, the isotope ^{9}Be in its ground state is bound by around 1.6 MeV [52]. The addition of the extra valence neutron acts to increase the binding energy of the system, leading to the idea that it is shared between the two α-particles of ^{8}Be, in much the same way as electrons are shared in atomic molecules [53]. Hence, ^{9}Be is thought to be the simplest example of a *nuclear molecule* with its closest atomic analogy being the H_2^+ molecule. The following section begins with a theoretical discussion of the dynamics of a valence neutron when added to the deformed $\alpha - \alpha$ system of ^{8}Be. Then, the current experimental status of this nucleus is covered along with how the observed data support the theoretical models.

4.1.1 Two-centre shell model

Rather than utilising a spherically-symmetric Woods-Saxon potential [15], in the two-centre shell model the Schrödinger equation is solved for two overlapping spherical shell-model potentials as a function of their separation. The single-particle levels for the more complicated system may then be obtained. To approximate the true system, the case of two harmonic oscillator potentials are considered initially. The potential has the following form, where the two harmonic oscillator centres are located along the z-axis at positions $\pm z_0$,

$$V(x,y,z) = \frac{1}{2}m\left[\omega_x^2 x^2 + \omega_y^2 y^2 + \omega_z^2 (z - z_0)\right]. \tag{4.1}$$

Freer solved this potential [6] and identified that for two infinitely separated HO centres the level degeneracies are twice that of a single system, as expected. In the limit of zero separation, where the two oscillators totally overlap, the n_z quantum number possesses the values $2n_z$ and $2n_z + 1$. These two possibilities correspond to the two linear combinations of the wave functions of each separate oscillator.

$$\psi = \frac{1}{\sqrt{2}}\left(\varphi_1 \pm \varphi_2\right). \tag{4.2}$$

The energy levels and n_z quantum numbers of the system separate as the two centres get farther apart. Having solved the system, it is possible to place nucleons into the resulting single-particle levels in the two separate potentials. The energy levels of the full two-centre shell-model calculation are shown as a function of the centre separation r in figure 4.1. The systematic behaviour is similar to that of the two-centre harmonic oscillator.

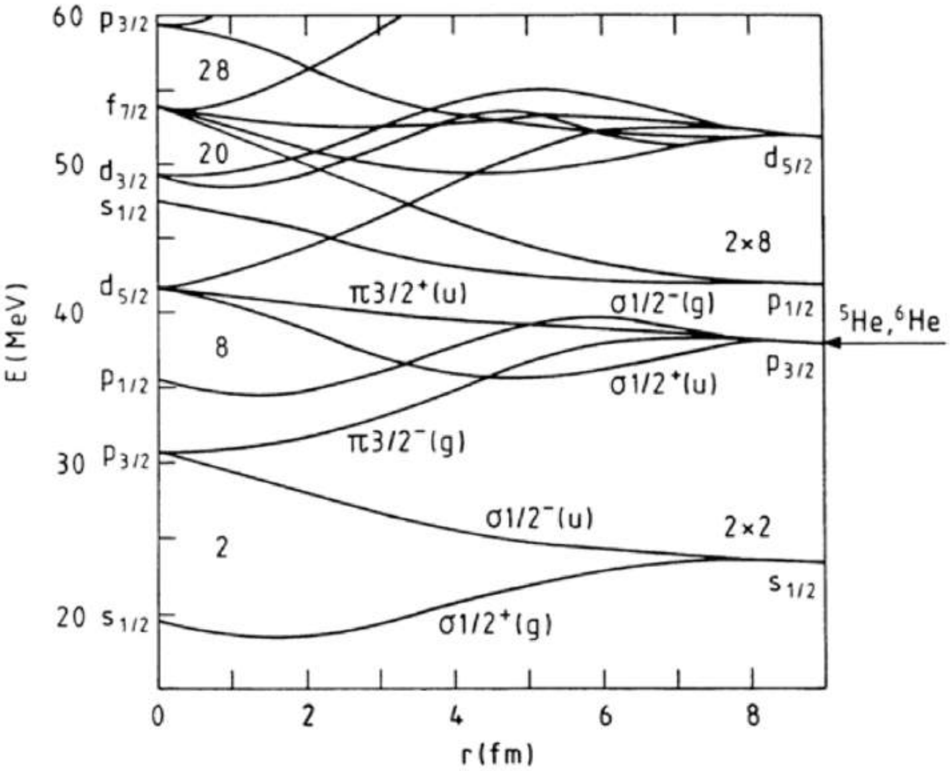

Figure 4.1: The energy levels of the two-centre shell model as a function of the α-cluster separation distance r. Figure from references [54] and [55].

In the case of ^{9}Be, the lowest two energy levels in this figure are full. The valence neutron may occupy the $3/2^-$, $1/2^-$, $3/2^+$ and $1/2^+$ levels. Similarly to the Nilsson model presented in section 2.3, since the deformed ^{9}Be system may collectively rotate, rotational bands with these K^π values can be generated. The energy ordering of the band heads depends on the deformation of each level.

4.1.2 Molecular model

To understand the potential $\alpha + \alpha + n$ structure of ^{9}Be from a molecular perspective, it is important to consider what happens when a valence neutron is added to a single α-particle. In the shell-model picture presented in section 2.2, the neutron resides in the lowest $p_{3/2}$ orbital. The $3/2^-$ ground state of ^{5}He supports this picture, and spectroscopic factors indicate that this is a fairly pure single-particle configuration [56]. The valence neutron in ^{9}Be should, therefore, occupy covalent orbitals, corresponding to a superposition of $p_{3/2}$ configurations in each of the α-particle cores. The neutron delocalisation acts to increase the overall binding energy of the nucleus. The two α-particle cores are separated along the z-axis.

Given the $L = 1$, $p_{3/2}$ orbitals occupied by the valence neutron, the wave function possesses a double-lobed, dumbbell-like shape. In the following discussion, rather than the full shell-model wave function, the neutron wave function is approximated as the solution to the simple harmonic oscillator potential, which, recalling from section 2.5, is parameterised by two quantum numbers [$n_\perp$,n$_z$]. The quantum numbers [1,0] and [0,1] correspond to p-orbitals either anti-aligned or aligned with the z-axis. Given these solutions, their possible linear combinations corresponding to σ- or π-type binding are shown in figure 4.2. The resulting superposition wave functions are shown in the right panel of figure 4.3.

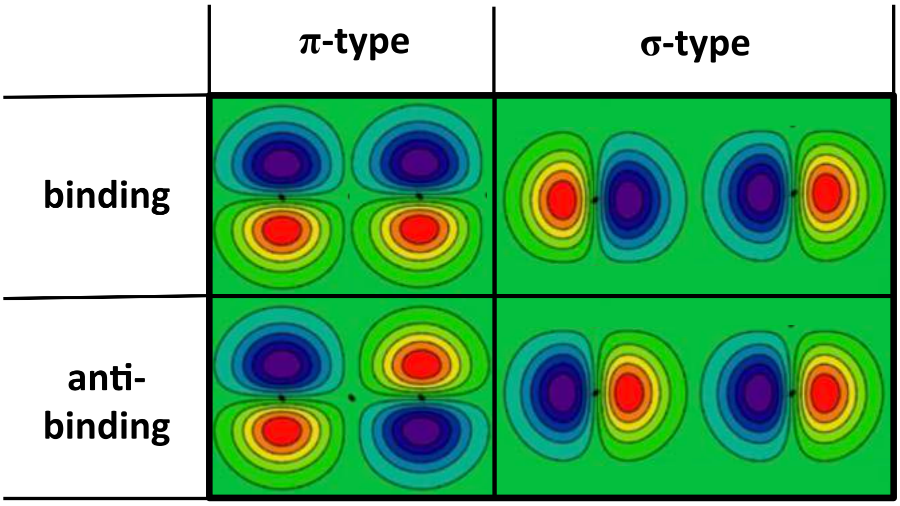

Figure 4.2: The relative alignments of the two $p_{3/2}$ orbitals with respect to the ^{9}Be deformation axis for the σ- and π-type bonding. Images from reference [6].

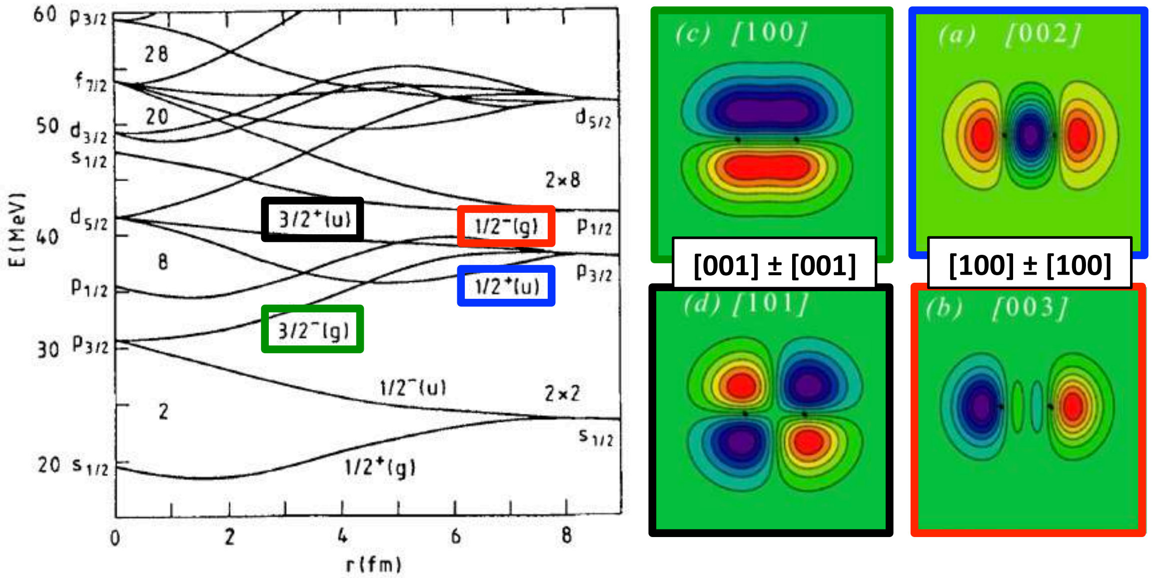

Figure 4.3: Left: energy levels of the two centre shell model. Right: the σ- and π-type molecular orbital wave functions associated with the valence neutron in ^{9}Be. These correspond to superpositions of [1,0,0] and [0,0,1] ($[n_x,\ n_y,\ n_z]$) harmonic oscillator wave functions. Images from references [55] and [6].

The two-centre shell model and molecular-orbit model are complementary descriptions of the ^{9}Be system. For example, the $3/2^-$ π-binding orbital in the right of figure 4.3 is the most compact arrangement so has a smaller deformation and moment of inertia. The $1/2^+$ σ-binding configuration on the other hand has a larger moment of inertia, and the neutron density in the centre acts to separate out the α-particle cores. These correspond to the ground state and first excited state of ^{9}Be. In the two-centre shell-model diagram on the left of figure 4.3, the only way that this energy level ordering may occur is if the $1/2^+$ level has a much larger $\alpha - \alpha$ separation r, which is entirely consistent with the molecular picture. The same systematics are observed in the experimental data (section 4.1.4).

The calculations of references [57, 58], using the generator coordinate method, calculated energy curves for the states in ^{9}Be as a function of the $\alpha - \alpha$ separation. The levels reach their respective minima at different separations, supporting the picture presented in figure 4.3. In this model there was found to be close to 100% overlap between the obtained ground state wave function and that of the pure $K = 3/2^-$ π-binding configuration. For the $1/2^+$ level, a

70% overlap was found with the σ-binding configuration. The valence neutron densities were also calculated and are shown for the $K = 3/2^-$ and $K = 1/2^+$ band heads in figure 4.4. The similarities with the densities of the simple harmonic oscillator wave functions in the right panel of figure 4.3 are clear.

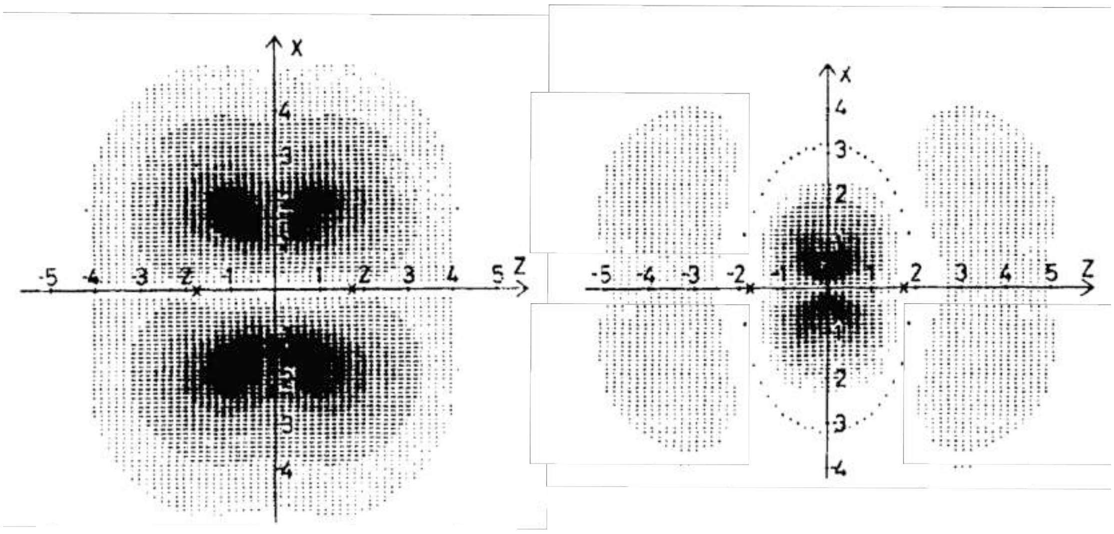

3/2⁻
≈ 100% [001] + [001]

1/2⁺
≈ 70% [100] + [100]

Figure 4.4: The valence neutron density calculated from generator coordinate method $\alpha + \alpha + n$ molecular calculations. Images from references [57, 58].

4.1.3 Shell model and no-core shell model calculations

Perhaps unsurprisingly, the spherical shell model has limited success in describing the properties of ^{9}Be. Although the natural parity states are satisfactorily reproduced using mean-field calculations [59], the very low excitation of the $1/2^+$ first unnatural parity state is problematic. To generate this state in the shell model involves the promotion of a nucleon into a higher oscillator shell so the state should have a high excitation energy. The deformed Nilsson model has more success and well-reproduces the ground state charge form factor for electron scattering [60]. However, in order to properly describe the excited $5/2^-$ level at 2.43 MeV, higher order deformation terms of the Nilsson potential (beyond r^2Y_{20}) were required. This fourth order hexadecapole deformed shape has been shown to be consistent with the dumbbell structure of two α-particles [57].

Shell-model calculations, restricted to interactions between valence nucleons in the $p_{3/2}$ orbital are unlikely to capture the highly collective behaviour that ^{9}Be seems to possess. On the other hand, no-core shell model calculations, where even core nucleons can contribute, have reproduced the molecular properties and rotational behaviour of ^{9}Be *ab initio*, provided the basis space in the calculations were sufficiently large [61, 62]. In one study, the intrinsic proton and neutron densities for the ^{9}Be ground state were calculated, and the density of the valence neutron was captured by taking the difference between the two [63, 64]. This process is shown in figure 4.5 and is excellent evidence that the molecular π-type bonding is correct for this state.

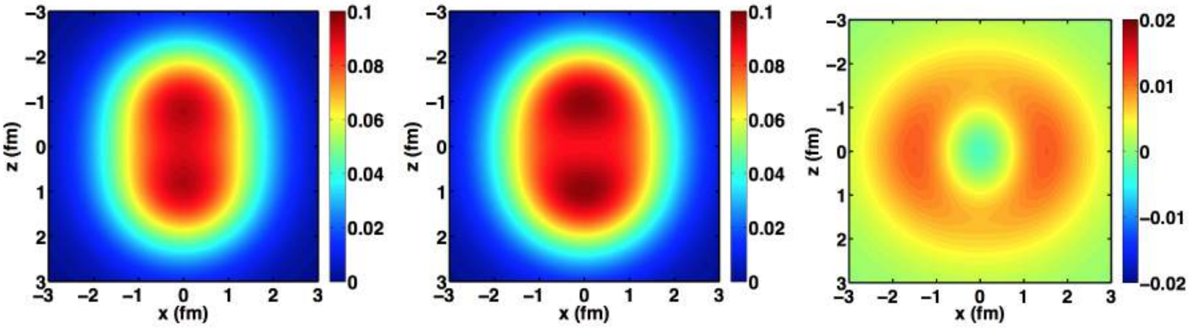

Figure 4.5: Nucleon densities (left: proton, centre: neutron, right: neutron − proton) for the ^{9}Be ground state in the intrinsic frame, from large-basis, no-core shell-model calculations. Images from references [63] and [64].

4.1.4 Experimental review of ^{9}Be

The latest experimental compilation of levels in ^{9}Be is given in reference [52]. Although this compilation is now quite old, there has not been much experimental attention given to ^{9}Be in recent years. Given that the levels of ^{9}Be are very broad (often > 1 MeV), and hence strongly overlap, the nucleus is difficult to study experimentally and a number of questions remain. There are many levels below 10 MeV that do not have firm J^π assignments or accurately measured widths. The current experimental status of the ^{9}Be and ^{9}B mirror pair is given in table 4.1.

^{9}B			^{9}Be		
J^π	E_x (MeV)	Γ (keV)	J^π	E_x (MeV)	Γ (keV)
$3/2^-$	0	0.54(21)	$3/2^-$	0	stable
$(1/2^+)$	≈1.6	–	$1/2^+$	1.684(7)	217(10)
$5/2^-$	2.361(5)	81(5)	$5/2^-$	2.429(1)	0.78(13)
$1/2^-$	2.75(30)	3130(200)	$1/2^-$	2.78(12)	1080(110)
$5/2^+$	2.788(30)	550(40)	$5/2^+$	3.049(9)	282(11)
$(\pi = -)$[1]	$3.91^{+0.09}_{-0.09}$ [2]	1520^{+230}_{-210} [2]	–	–	–
–	4.3(2)	1600(200)	$(3/2^+)$	4.704(25)	743(55)
–	–	–	$(3/2^-)$	5.59(10)	1330(360)
$7/2^-$	6.97(60)	2000(200)	$7/2^-$	6.38(6)	1210(230)
–	–	–	$9/2^+$	6.76(6)	1330(90)
–	–	–	$(5/2^-)$	7.94(8)	≈1000
$(7/2^-)$	11.65(60)	800(50)	$(7/2^-)$	11.283(24)	575(50)
$5/2^-$	12.19(40)	450(20)	$5/2^-$	11.81(20)	400(30)

Table 4.1: Comparison of ^{9}B and ^{9}Be experimental levels [52]. The horizontal lines highlight a newly-measured state in ^{9}B, which could correspond to the π-antibinding molecular configuration.

[1] Tentative assignment from reference [65].

[2] Weighted average of references [65, 66].

Given the excitation energies and J^π assignments of the ^{9}Be states, the known spectrum < 12 MeV has been grouped into three rotational bands with $K^\pi = 3/2^-$, $1/2^+$ and $1/2^-$, which are shown in figure 4.6. The $1/2^+$ and $1/2^-$ bands show the effects of Coriolis decoupling discussed in section 2.4. The $1/2^+$ band has a shallower gradient than the $3/2^-$ ground state band, indicating a larger moment of inertia, which is predicted by the molecular model in figure 4.3. Notably, the predicted $3/2^+$ rotational band has not been confirmed experimentally. The two-centre shell model indicates that a π-antibinding state with a relatively small moment of inertia should appear at an excitation energy higher than the other band heads. Furthermore, the *ab initio* no-core shell model calculations of reference [67] predict a $3/2^+$ level between 3.5−4 MeV. An experimental search for this potential molecular band head was the aim of the present study.

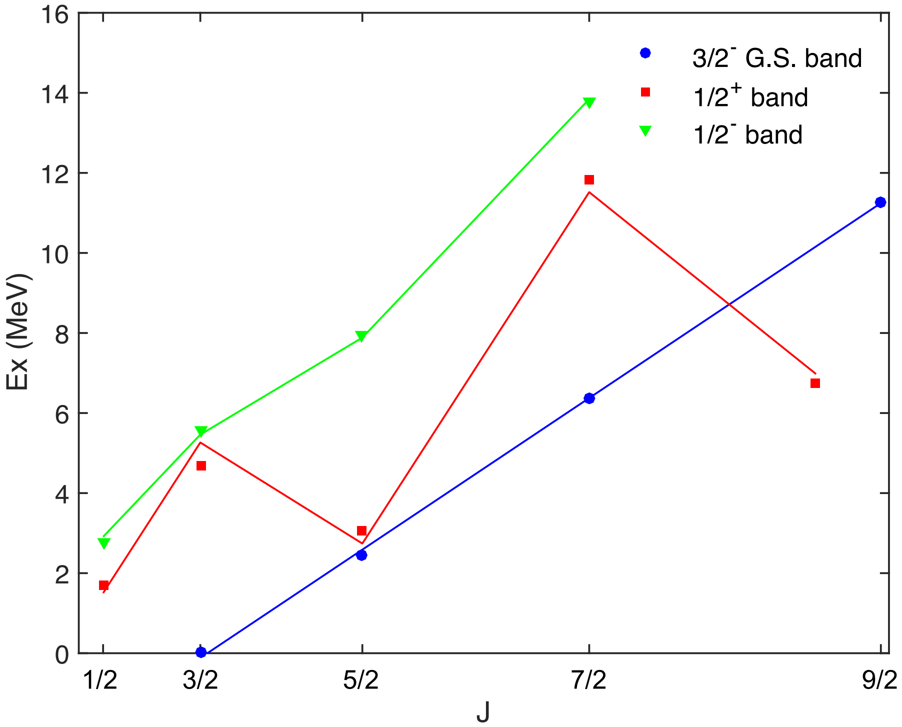

Figure 4.6: The known rotational bands of ^{9}Be based on the level compilation in reference [52]. Some angular momentum assignments are tentative and have been changed on this plot in order for the levels to exhibit the correct rotational trends. Please refer to table 4.1 for the J^π assignments of the most recent ^{9}Be level compilation.

4.1.5 Mirror nuclei

Much can be learned about a nucleus by examining its mirror partner. Mirror pairs of nuclei are the same, except the number of protons and neutrons are switched. States of the same isospin, T, in a set of nuclei with the same mass number, A, but with differing numbers of protons and neutrons, Z and N, are more generally named isobaric analogue states (IAS). It is known that the nuclear two-body interaction is approximately charge-independent, meaning that the nuclear potential between two neutrons, V_{nn}, is the same as that between two protons, V_{pp} [68]. Due to this property of the nuclear force, the many-body Hamiltonians for two mirror systems are the same, except for the different Coulomb interactions. The two nuclei should exhibit similar properties, aside from the fact that their levels will be shifted by a calculable amount due to the difference in the Coulomb energy [69, 70]. For cross section measurements in nuclear astrophysics, the properties of mirror nuclei are important. The symmetry between mirror nuclei sometimes means that astrophysically relevant proton capture reaction rates can be inferred from information obtained from transfer reactions with stable beams [71].

When considering Coulomb energy differences between mirror analogue states, it is useful to normalise the energies of excited states to those of the corresponding ground states. The majority of the Coulomb energy difference, which arises due to the difference in bulk Coulomb energy for the whole nucleus, will then cancel out. Therefore, the important considerations are how the Coulomb energy varies as a function of excitation energy and angular momentum for mirror analogue states. As illustrated by figure 4.7, the analogue levels in the ^{9}Be/^{9}B mirror pair show similar excitation energy-spin systematics/rotational bands. Only states with definite angular momentum and parity assignments can be confidently grouped in this way. Lines joining states with tentative J^{π} assignments are speculative, since the energy shift between such mirror analogue levels is non-trivial to calculate. It is therefore not guaranteed that the energy ordering is consistent between a pair of mirror nuclei. As previously mentioned, the energy differences between IAS are due to isospin non-conserving forces, such as the Coulomb interaction. In these systems, the evolution of the Coulomb energy difference with angular momentum is quite sensitive to differences in nuclear structure [72, 73].

On a very basic level, clustered and shell-model configurations possess very different physical sizes; a clustered state is larger than a compact shell-model system. Since the Coulomb energy is very sensitive to the volume occupied by the valence particle, the difference in the excitation energies of mirror analogue states should provide an insight into the structure [72, 74]. Shell-model-like states should differ in energy more than clustered states. This is an overly simplified picture, however, and other sources of such energy differences must be accounted for before making structural conclusions [73]. Notably, the influence of angular momentum must be considered. Nucleons in orbitals with different angular momenta and spins will interact differently with the nuclear volume, meaning that their energies will vary under the exchange of protons and neutrons in different ways.

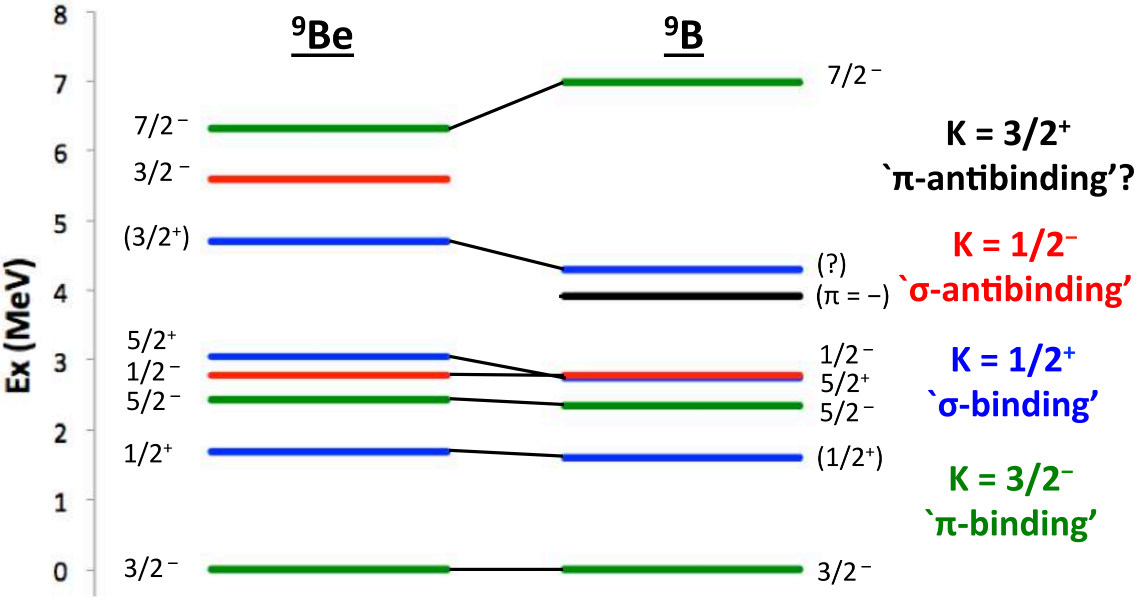

Figure 4.7: The level schemes of the ^{9}Be/^{9}B mirror pair [52]. The different colours highlight proposed rotational bands.

Some mirror nuclei exhibit much larger energy shifts than would be expected [75] and it is possible to explore whether the measured energy shifts are due to the influence of the Coulomb interaction alone. Such large energy differences are referred to as Thomas-Ehrman shifts [76, 77]. Since the nuclear interaction is fundamentally short-range, it will become weaker if the single-particle wave functions are distributed over a larger volume. An example of this situation could be a loosely bound proton occupying an s-orbital. Due to the lack of a centrifugal barrier, this orbital can have very large radius. The resulting difference in the single-particle energy leads to a difference in the wave functions between protons and neutrons. This affects the matrix elements of the residual nuclear interaction, even though the original nucleon-nucleon force is charge-symmetric.

The channel widths of mirror analogue states can provide an insight into their angular momentum and parity. In the ^{9}B nucleus, a broad level close to 4 MeV was recently measured [65, 66]. Aside from one other state, the levels in this energy region have firm J^{π} assignments, meaning that this new level could correspond to the missing π-antibinding molecular configuration band head. By measuring the properties of a mirror analogue state in ^{9}Be, it could be possible to infer its angular momentum and parity. Due to the similar ^{9}Be/^{9}B wave functions, their couplings to the respective ^{8}Be + n and ^{8}Be + p decay channels, defined by the reduced channel width (section 3.2), should be the same [78]. Therefore, their measured channel widths (i.e. the partial widths of the mirror states) should differ only due to the extra Coulomb barrier penetrability required for the proton decay. The aim of this experiment was to measure the properties of the hitherto-unmeasured mirror analogue state in ^{9}Be and to use its properties in conjunction with that of the ^{9}B state to analyse the nuclear structure.

4.2 Experimental details and apparatus

The experimental measurements were performed using the 10 MV FN Tandem Van de Graaff accelerator housed at the Nuclear Science Laboratory at the University of Notre Dame. A ^{4}He beam was incident on a thick 1000 μg cm^{-2} ^{9}Be target foil and data were acquired for a cumulative time of around 30 hours at an average beam current of 2 enA. Two beam energies of 22 and 26 MeV were used to acquire the data presented in this chapter. The experimental work was a collaborative effort between researchers from the Universities of Birmingham, Notre Dame, Wisconsin and the Weizmann Institute.

4.2.1 Notre Dame tandem Van De Graaff accelerator

This section describes the principles of operation of the FN Tandem Van de Graaff accelerator [79]. Often the subject of high school demonstrations, a Van de Graaff generator is a simple machine which produces a very high electric potential by collecting electrostatic charge from a source and gradually transferring it to a large, isolated metal anode through a rotating conveyor belt. This principle is illustrated schematically in figure 4.8a.

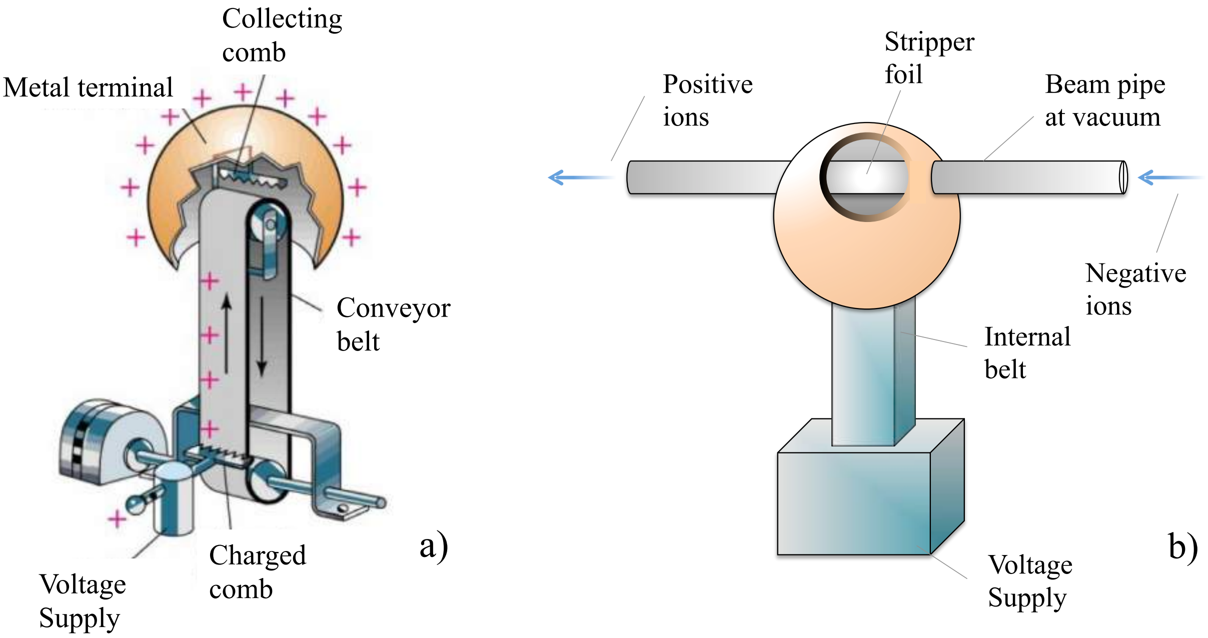

Figure 4.8: a) Expanded view of a generic Van de Graaff generator with the main components labelled. b) Schematic diagram illustrating the 'tandem' acceleration principle and how ions are accelerated practically using a Van de Graaff generator. Image in a) from reference [80].

The Van de Graaff generator principle was developed as a means to accelerate ions as early as the 1930's. Negative ions external to the Van de Graaff generator move in the strong $1/r^2$ electric field produced by the device which accelerates them towards the positively charged anode. A schematic diagram illustrating the tandem Van de Graaff acceleration principle is shown in figure 4.8b. As with a standard generator, the heart of the accelerator consists of a metal electrode called the 'terminal.' A very large positive charge is applied to this terminal via a high voltage supply and charge-transferring belt.

Without modification, any negative particle accelerated towards the terminal will collide into it, limiting the usefulness of the device. To overcome this, an evacuated beam pipe made from insulating glass cylinders passes through the terminal sphere, through the zero electric field region inside, and then out of the other side where the beam can be extracted to perform experiments. However, since the ion is negatively charged as it emerges from the other side of the terminal, it immediately experiences a restoring force back towards the centre of the system. Left to its own devices, the negative ion would oscillate about the centre of the terminal and could never be extracted. To overcome this issue, the negative ions pass through a thin (3 μg cm^{-2}) carbon 'stripper' foil in the centre of the accelerator. This ionises the beam and leaves it in a variety of positive charge states. The name 'tandem' accelerator owes itself to the fact that the now-positive beam is accelerated a second time away from the electrode, towards the experimental chamber and target.

For the system described so far, each acceleration stage is non-linear and varies as $1/r^2$ due to the geometry of the electric field. This is problematic for a number of reasons. Firstly, the weak field at large distances from the terminal means that the negative ions propagate notable distances at low velocities, meaning that their path through the system is susceptible to deflections from stray electric fields. Secondly, the high electric field close to the terminal can cause uncontrollable electric discharges. The issue of non-linearity is solved by constructing the vacuum tube in segments, consisting of glass cylinders glued to metal electrodes. Equal value resistors are connected between these electrodes which creates a potential divider circuit. The voltage difference across each gap is therefore uniform, leading to a uniform acceleration. This system is shown schematically in figure 4.9a and as a photograph in figure 4.9b. As shown in figure 4.9a, in this process, charge continually flows from the terminal to ground meaning that the charge on the terminal must constantly be replenished by the internal belt. The beam pipe of the FN Tandem at Notre Dame consists of around 200 electrodes connected by 600 MΩ resistors. To maintain a terminal voltage of 10 MV with this total 120 GΩ resistance between the terminal and ground, requires an 83 μA current supply to the terminal.

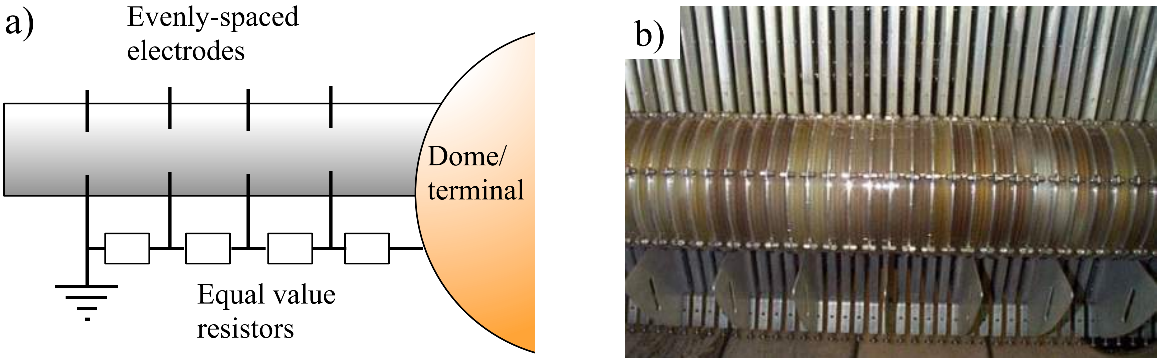

Figure 4.9: Controlling the electric field gradient of the Van de Graaff accelerator using metal electrodes and resistors along the length of the beam pipe. a) Schematic diagram illustrating the principle. b) Photograph of the set-up at the FN tandem accelerator at Notre Dame from reference [81].

The charging system for the Notre Dame FN Tandem is called a pelletron. Rather than a traditional charging belt as has been discussed so far, the pelletron uses a chain of charged metal pellets connected by nylon links. Each pellet in the chain carries a small charge, and as the chain rotates from the HV supply at the end of the accelerator to the terminal, charge is incrementally carried to the terminal. A detailed discussion of the pelletron charging system is given in reference [81].

This experiment used helium ions in a 2^+ charge state. The beam begins life in the helium ion source (HIS). This is depicted in figure 4.10. Within the source, a thin diameter tungsten wire, contained in a helium gas-filled cavity, is resistively heated by passing a high current through it. Electrons emitted from the hot filament wire ionise the helium gas that surrounds it. The electrons are confined within the cavity through the application of a magnetic field. This section of the source is known as a duoplasmatron [82]. The resulting helium ions (Q=1^+) are extracted through a small aperture by a −20 kV extraction electrode. This beam is then transported via a focusing electrostatic Einzel lens [83] to a region filled with lithium vapour. As the positive helium ions traverse this region, some pick up two or more electrons from the lithium to form a small number of negatively charged Q=1^{-} ions that can be injected into the accelerator.

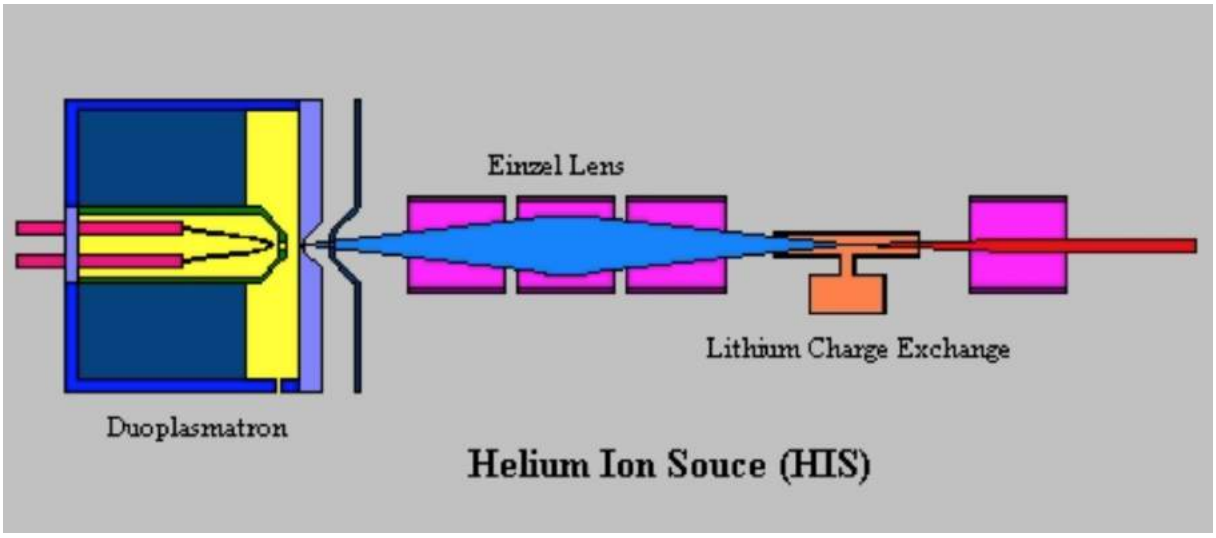

Figure 4.10: Overview of the helium ion source and its various component stages. Image from reference [81].

When the accelerated negative ions pass through the stripper foil, ions in a variety of positive charge states are produced. Therefore, a discrete spectrum of energies are present as the ions exit the accelerator. The terminal voltage is tuned such that just one of these charge states results in the desired beam energy for a given experiment. The contributions from all other charge states and resulting beam energies are removed through the use of a dipole ‘analysing’ magnet in place before the target chamber. This creates a homogeneous magnetic field perpendicular to the direction of the beam. In this field, the ions follow a circular trajectory with a radius depending on their momentum to charge ratio (P/Q). By tuning the magnetic field, the desired beam energy can be selected to exit the magnet and all other contributions can be removed.

It is easy to maintain a relatively constant terminal voltage on a Van de Graaff accelerator using a stabilising and feedback system; precision beam energies with resolutions of a few tens of keV are possible. Furthermore, it is quick to change the terminal voltage, meaning that the accelerator is well suited to resonance measurements where multiple beam energies are required over a short space of time.

4.2.2 Basic reaction dynamics

During the experiment, a beam of helium ions struck the fixed 1 mg cm^{-2} ^{9}Be target. As shown in figure 4.11, a fraction of the centre-of-mass (COM) energy was imparted to the recoiling ^{9}Be, populating an excited state in the nucleus. Since all of the ^{9}Be excited states are unbound and Borromean, the nucleus proceeded to decay via one of the break-up modes (^{8}Be + n) or (^{5}He + α) $\rightarrow \alpha + \alpha + n$ (direct break-up is also possible). The detection of the final-state particles resulting from the break-up allowed a full kinematic reconstruction of the reaction, since the particle detectors are sensitive to both the energy and position of the detected particles (see section 4.2.3). The neutron resulting from the break-up was not detected. However, its missing energy and momentum were calculated through the application of the conservation of linear momentum.

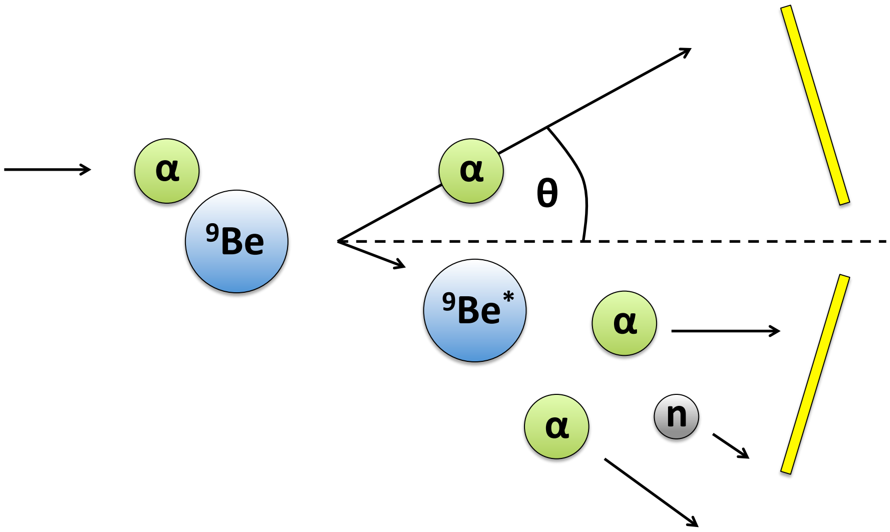

Figure 4.11: Microscopic, pictorial representation of the inelastic scattering and break-up of ^{9}Be. The α particle beam strikes a stationary ^{9}Be nucleus in the target, raising it into an excited state. This then breaks apart into its cluster constituents. The energies and angles of the charged particles in the final state were measured by an array of silicon detectors.

4.2.3 Detector set-up

The products of the ^{9}Be break-up were detected by an array of four in-plane 500 μm-thick *Micron W1* double-sided silicon strip detectors (DSSD) [Micron Semiconductor Ltd][84], which are contained in a vacuum chamber. Each detector was found to have a typical energy resolution of approximately 50-100 keV though this depends on the specific electronic components used. The arrangement of charged particle detectors inside the reaction chamber for the main study is shown schematically in figure 4.12a. Each DSSD has a total surface area of 5 × 5 cm^2 and all were aligned with their planes perpendicular to a line joining the target and detector centre. These were placed at distances 6.5, 10.7, 10.9, and 6.8 cm from the target position at centre angles $-69°$, $-30°$, $33°$ and $71°$, with respect to the beam direction, providing an overall angular coverage from 16° to 90°. A photograph of the detectors at their positions inside the experimental vacuum chamber is shown in figure 4.12b.

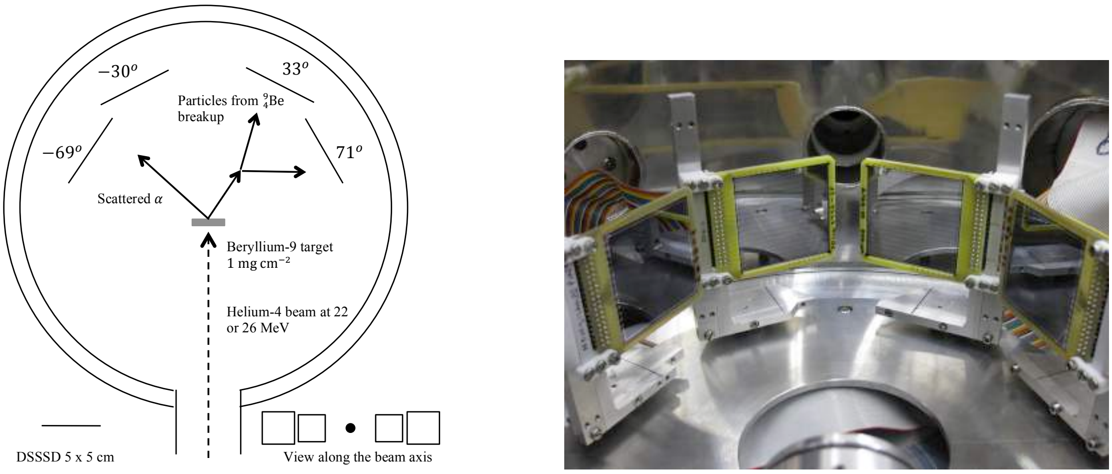

Figure 4.12: a) The positions of the detectors and target inside the vacuum chamber along with an illustration of the ^{9}Be break-up process. The bottom right image shows the detector array as viewed from the target position. b) A photograph of the detector array inside the experimental chamber.

Semiconductor detectors

The operation of all silicon particle detectors relies on the formation of a semiconductor junction [85, 86]. To describe the operation of a semiconductor detector, the simple case of a PN junction is considered, which can be produced by diffusing sufficient quantities of a p-type material into one face of a bulk n-type material. In this case, free electrons from the n-type material migrate

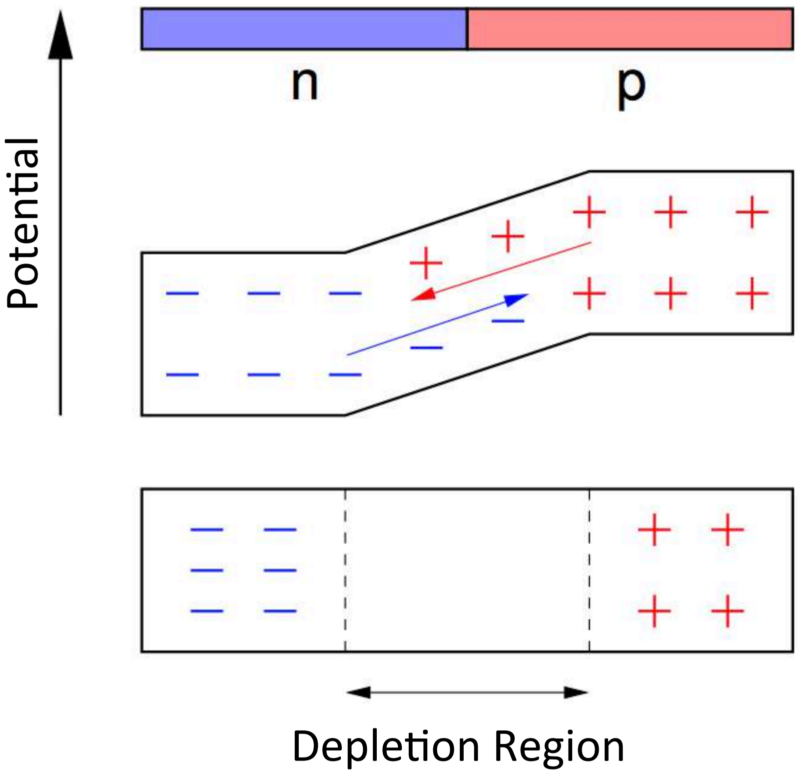

Figure 4.13: The formation of the depletion region at a P-N junction [82].

across the junction and recombine with the holes in the p-type material. Electrons entering the P-type material produce a negative charge and leave behind a positive charge in the n-type material. This sets up a small electric field, halting any further charge migration across the boundary. Near to the junction, a *depletion region*, absent from free charge carriers, is formed as shown in figure 4.13. This region forms the charge detection medium. Ionising radiation passing through on the depletion zone will excite electron-hole pairs; the amount depends on the stopping power of the medium, the initial energy of the impinging particle and the energy required to excite an electron-hole pair (typically $\approx$ eV). The electrons and holes produced are carried out of this region by the electric field. These are collected by electrical contacts on either side of the junction and produce a signal which can be detected.

As currently described, the PN junction will work as a particle detector. However, the situation can be improved by applying a reverse bias across the junction. This has the effect of further attracting electrons from the n-type side (making it more positive) to the p-type side (making it more negative). The heightened electric field increases the size of the depletion region thus increasing the physical size of the charge sensitive medium. Furthermore, application of a reverse bias improves the efficiency of charge collection by the electrodes [87]. At the correct operating voltage, the depletion region can occupy the majority of the detector volume. The maximum voltage is limited by the resistance of the material; exceeding this limit will cause a breakdown of the junction and the material will begin to conduct.

Although the reversed bias junction should be non-conducting, a small leakage current will flow when the reverse bias is applied. Firstly, despite the electric field impeding the diffusion of majority charge carriers, statistically, some will have a high enough velocity to still cross the junction. Once a majority carrier crosses the junction, it becomes a minority carrier. Holes in the n-type which are attracted by the negative voltage on the p-type and electrons in the p-type which are attracted by the positive voltage on the n-type will diffuse across the junction. Secondly, electron-hole pairs which can arise from impurities in the silicon, can be thermally excited and drift across the junction.

The leakage current will increase as the detector succumbs to radiation damage which causes the displacement of atoms in the silicon crystal lattice [88, 89]. The breakdown of the lattice inevitably signals a breakdown in the semiconductor band structure. This translates into increasing noise and a poorer energy resolution owing to a reduction in the amount of charge collected (due to the charge carrier trapping mechanism and decreases in the charge carriers mobility and lifetime).

Micron W1 double-sided silicon strip detectors

A schematic diagram of the Micron W1 DSSD is given in figure 4.14. The Micron DSSD being considered here consists of a semiconductor junction, obtained by using an ion implantation method. The cross section of the detector is visualised in the bottom panel of figure 4.14. The bulk of the detector is 500 μm-thick n-type silicon which is allowed to oxidise. Vertical strips of the oxide are etched away from the material, then bombarded with $\approx$10 keV boron ions. The exposed n-type material is converted to strips of p-type during this process. Aluminium contacts are added to the tops of each strip and are electrically isolated by a SiO_2 inter-strip

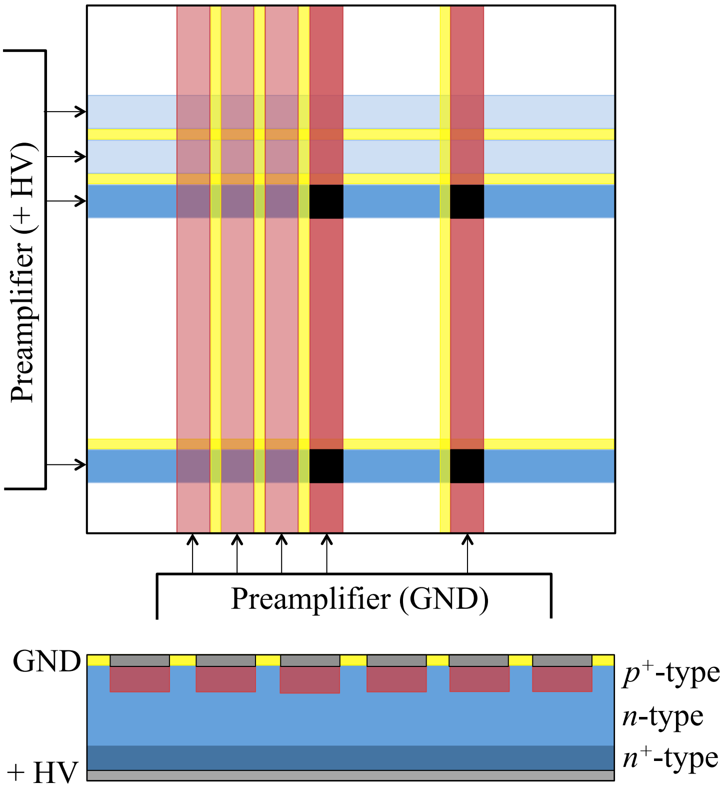

Figure 4.14: Schematic diagram of a double-sided silicon strip detector. The upper image shows the face of the detector and the lower image shows the cross section through the detector. When two particles hit the detector, four strips collect charge (two vertical on the front and two horizontal on the rear) which are highlighted in a darker shade. The crossing points in black mark the possible hit points.

region. Similarly, the rear of the detector consists of strips of arsenic-doped n-type silicon which are also covered by aluminium strips. The strips on the rear of the detector are perpendicular to the strips on the front face, which were orientated horizontally in the experimental chamber, as can be seen in figure 4.12b. The detectors were operated with the rear detector strips subject to a positive 100 V DC supply, with the front face strips kept at 0 V ground.

The detection of a charged particle causes a measured signal in a single front and rear strip and their crossing point provides the position of the detection. Multiple hits on the same detector result in several possible crossing points (hit positions) as shown in figure 4.14. By energy ordering the channels and matching the charges collected by the front and rear strips, it is possible to identify the two correct hit points, provided the detected particles are sufficiently different in energy. With these hit points known, the angles of the hits with respect to the beam direction and the target can be calculated using simple trigonometry as shown in figure 4.15. This is discussed in more detail in appendix B. Each strip has a width of 3mm, which, when combined with the distances of the detectors from the target, leads to a θ_x and θ_y angular resolution which ranges between 1.6° and 2.6°. The detected energy and these angles can be used to determine the linear momentum vectors of each detected particle, assuming each to be an α-particle.

The detectors were calibrated in energy using ^{148}Gd and ^{241}Am α sources (energies of 3.2 and 5.5 MeV, respectively). The α-particle energies were not corrected for energy losses in the dead layers of the detector since this was found to be very small compared with the intrinsic resolution.

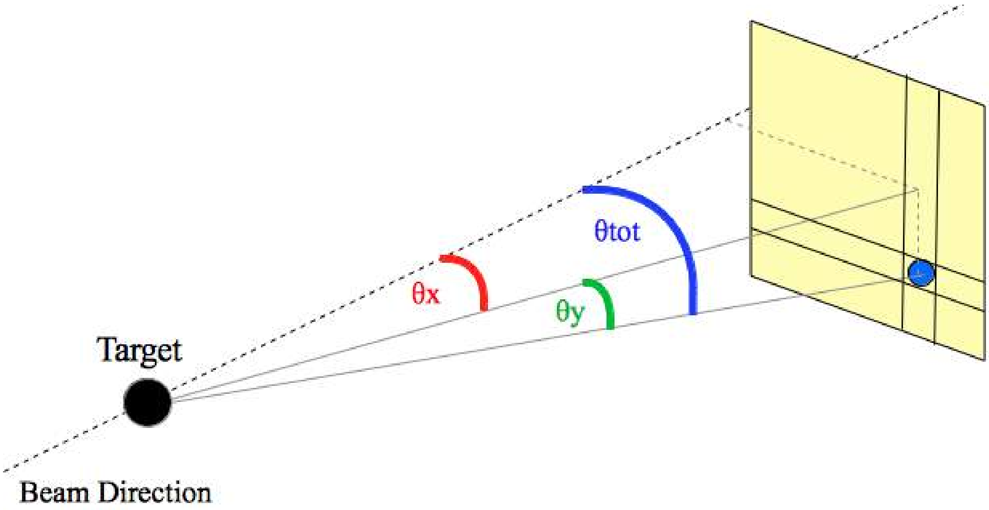

Figure 4.15: Notation for assigning the angle of the particle detection with respect to the initial beam direction and the target. Image from reference [90].

4.2.4 Electronics and data acquisition

Electronics

The aim of the chain of processing electronics was to convert the raw detection pulses that exit the detector array into a set of digital signals that are proportional to the energy of the detected quanta. The electronics are also used to check if signals are energetic enough to be considered for analysis. Furthermore, triggering and multiplicity conditions are applied, and detections are grouped into *events* where each detection across the array is identified as originating from the same nuclear reaction. The following section provides a simplified account of the processing electronics in order to provide an overview of the data acquisition system and to explain the basic functions of the various electronics modules. The processing electronics required a total of 128 data channels to accommodate the readout of all four 32-channel detectors.

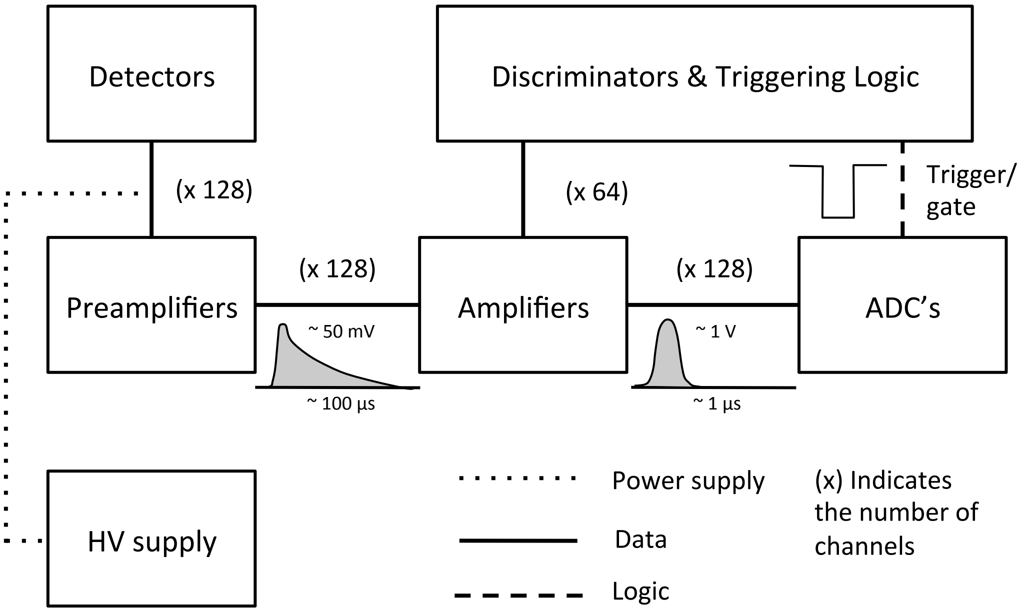

Figure 4.16: Simplified block diagram showing the ordering of the pulse processing electronics and data acquisition system.

A schematic block diagram showing the ordering of the electronic units is shown in figure 4.16 and is typical for such an experiment. A power supply applied a reverse bias to each detector through adapter boards, which contained load resistors and were placed between the Paisley charge-sensitive preamplifiers and the detectors. The adaptor boards were designed to split the bias across all 16 rear strips and provide a path to earth (via ground resistors) for the front strips.

The charge pulses exiting the detector channels due to an impinging charged particle were integrated by the preamplifiers. The output voltage is proportional to the integrated charge of the pulse provided to the input terminals. A simplified diagram of a charge-sensitive preamplifier configuration is shown in figure 4.17. The system works effectively if the input pulse duration is considerably shorter than the time constant of the system $R_f C_f$. The preamplifier noise characteristics are strongly dependent on the preamplifier input capacitance. This capacitance comes from the inherent capacitance of the detector but mainly from the connecting cables between the detectors and preamplifiers. Therefore, efforts were made to ensure that these cables were as short as possible given the vacuum chamber geometry.

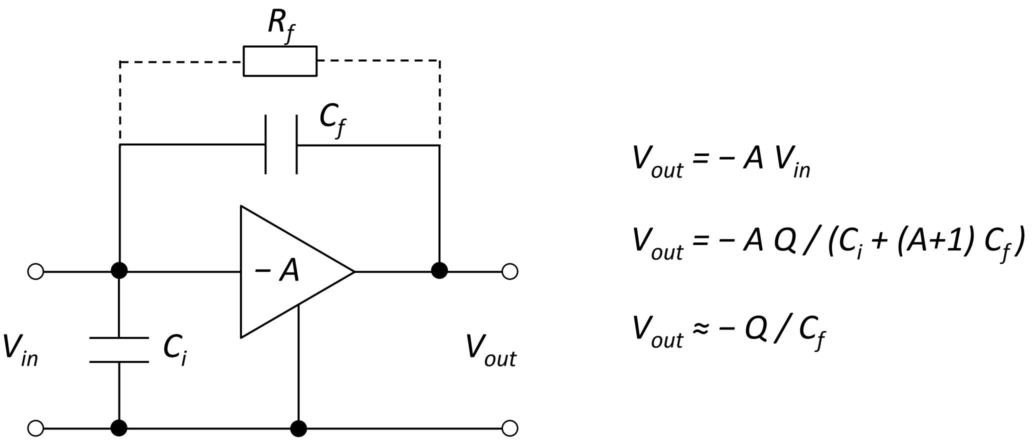

Figure 4.17: Diagram of a basic charge-sensitive preamplifier.

The pulses were then amplified by a set of 16-channel NIM Caen N568B linear amplifiers. The objectives of the amplifier were two-fold: amplitude gain and pulse shaping. The Caen N568B units accept pulses of either polarity and produce shaped output pulses, conforming to the NIM standard of 0−10 V amplitude. The shaping time can be selected between 0.2 μs to 6 μs and the gain ranges from a factor of 0.15 to 480. The gain is adjusted by coarse and fine controls. These amplifiers use a specific form of CR-RC shaping known as Gaussian or CR-$(RC)^n$ shaping. When a CR differentiation stage is followed by several RC integrations, the resulting output pulse has a Gaussian shape. In the simplest case, where the $\tau = RC$ shaping time is constant in both the differentiating and integrating circuits, the output pulse shape is described by the equation [4]

$$E_{out} = \left(\frac{t}{\tau}\right)^n e^{-t/\tau} \tag{4.3}$$

where n is the number of integration stages and t is the elapsed time. The output channels of the amplifiers are split. The × 10 outputs were sent directly to the Silena S9418 analogue-to-digital converters (ADCs) and the 1 × outputs were sent to the discriminators and triggering logic.

As explained, the set-up was subject to baseline electronic noise that primarily originates from the circuit prior to the preamplifiers. To overcome this, and only consider signals which correspond to particle detections, a system of four VME Caen V895 16-channel leading-edge discriminators were employed. If an input exceeds a discriminator channel's preset threshold level, a 50 mV square-wave logic pulse is outputted. Since the channels on the front and the back face of a detector originate from the same detection, the circuit was designed to only trigger from the channels from the front faces of each detector.

The outputs from the discriminators were used in the triggering logic circuit shown in figure 4.18. The discriminators each have an *or* and a *sum* output. These can be used to trigger the data acquisition in different ways. Connecting the sum outputs of the discriminators in a daisy chain allows the total number of detections across the detector array to be evaluated. A multiplicity condition was set for 3 or more coincident detections. If this is the case, a signal is sent to a logic fan in / fan out (FI/FO) NIM unit. This outputs a logic pulse if any of its input channels fire. At the same time, the *or* signal from the discriminators can be sent to another FI/FO. This FI/FO outputs a logic pulse if any detector in the array is found to fire. This singles trigger rate is scaled-down by a factor of 1000 using a rate divider unit (only 1/1000 inputs lead to an output from this unit). The scaled-down signal along with the multiplicity 3 signal are then sent to another FI/FO which produces the trigger for the ADCs.

The trigger signal has the purpose of notifying the ADCs of the forthcoming arrival of the energy signals from the amplifiers. Following the receipt of the trigger, the ADC modules are alert for 5 μs. All signals arriving within this time window are processed by the ADC modules which entails determining the pulse heights (proportional to the energy deposited in the detector). The Silena S9418 ADC modules use the Successive Approximations method to convert the raw analogue pulses from the amplifiers into binary signals [91]. The ADC control unit is connected to the chain of ADCs to allow control via a network connection. The overall result is that the system triggers mainly on events with a multiplicity of 3 or more (corresponding to ^{9}Be break-up events). The singles trigger and scaled-down signal result in the collection of some events corresponding to single detections for troubleshooting and diagnosing problems with the set-up. The multiplicity 1, 3 and busy signal were also sent to a scalar module which counts events and allows the dead time of the system to be quantified.

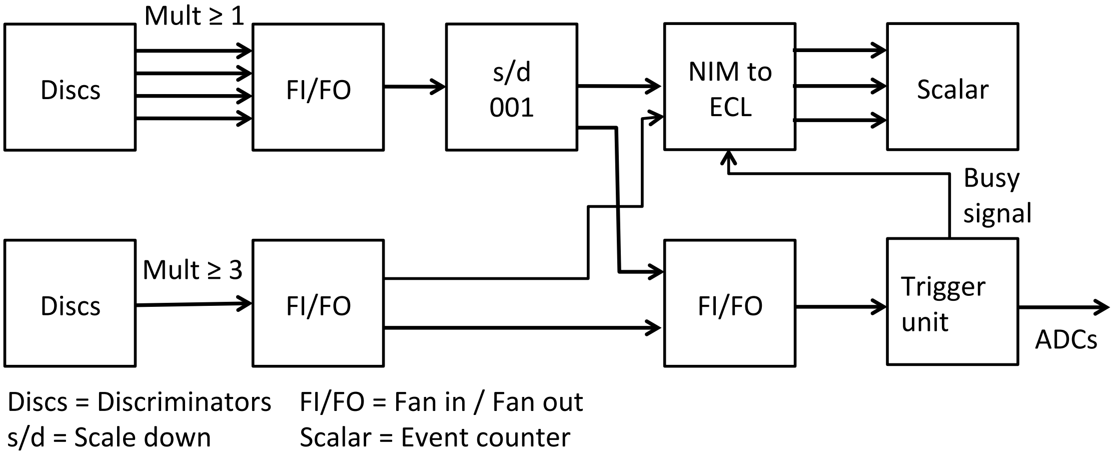

Figure 4.18: Triggering logic block diagram.

The important point from this description of the electronics and data acquisition system is that all of the particles striking the detectors within the 5 μs window are recorded as the same event in the data storage, and that it is possible to change the type of events considered by adjustments to the triggering logic. Due to the window's finite size, it is possible that signals which originate from distinct nuclear reactions are recorded as part of the same event by the data acquisition. These will form a background to the desired process being measured. The extent of this problem depends on the exact reaction being measured along with the beam current (reaction rate).

Data acquisition and analysis software

The data acquisition software used was called MIDAS (***M**ulti **I**nstance **D**ata **A**cquisition **S**ystem*) [92]. The software system includes a Graphical User Interface and hardware control servers.

Although MIDAS has a built-in data analysis and sorting capability, this was performed externally using SUNSORT [93]. The Sunsort documentation states: *"At the heart of the Sunsort package is a library of C functions which provides the user with facilities to access data ... and to decode this data into a simple array of ADC values. A user provided FORTRAN or C subroutine is linked to this library to form the core sort process. During sorting, the user's subroutine is called once per event and is passed the array containing the ADC values. The user can call upon various Sunsort library utility routines in order to, amongst other things, increment spectra, perform windowing operations and filter selected events back to a storage medium."*

A Fortran sort code was written to perform the primary data analysis, detailed in section 4.3. The sorting process involves determining if events correspond to the desired reaction and where this is the case, constructing a ^{9}Be excitation spectrum for these events.

4.3 Primary analysis

The data recorded during the experiment were analysed using a Fortran sort code. The aim of the primary analysis performed by this sort code was to convert the raw ADC values recorded from the detectors during the experiment into clean ^{9}Be excitation spectra. The process is described in detail throughout the following sections.

4.3.1 Determining the direction and momenta of the detected particles

The design of the double-sided silicon strip detectors, DSSDs, as described in section 4.2.3 means that when detecting an incident charged particle, the front strips of the detector collect the same number of holes as the rear strips collect electrons. Since, therefore, the energy detected on a front horizontal strip should be equal to that detected in a vertical rear strip, their crossing point allows the x-y position of the detection to be inferred. The energy of the particle is taken as the energy detected by the front face, since this has a slightly better resolution. If more than one particle is detected on a single DSSD, the signals collected by the front and rear strips are ordered in energy. By matching the energies on the front and rear strips, the hit positions of the different particles can be uniquely determined, provided that the particles have an energy difference greater than the detector resolution.

Once the x-y position of the hit on the detector has been determined, the diagram in figure 4.15 was used to calculate the horizontal and vertical angles, θ_x and θ_y, of each detection with respect to the target and the beam direction. The method of calculating these angles is explained in more detail in Appendix B. These values, along with the energies of the particles, are sufficient in order to calculate the momenta of the particles. Since the detected particles are assumed to be α-particles with mass, m_α, their momenta are defined non-relativistically as

$$\begin{aligned} P_\alpha &= \sqrt{2m_\alpha E_\alpha}, && (4.4)\\ P_{\alpha x} &= P_\alpha sin(\theta_x)cos(\theta_y), && (4.5)\\ P_{\alpha y} &= P_\alpha sin(\theta_y) \text{ and} && (4.6)\\ P_{\alpha z} &= P_\alpha cos(\theta_x)cos(\theta_y). && (4.7) \end{aligned}$$

4.3.2 Detector front and rear face energy matching

The energy-matching of the signals collected by the front and rear detector faces is best visualised using the plot in figure 4.19. For cases where the number of front strips that fired matched the number of rear strips that fired, the calibrated energy collected by the front strips are plotted against the corresponding energies from the rear strips. Genuine events correspond to where the front strip energy equals the rear strip energy (within the detector resolution) so they appear on a diagonal line $y = x$. Figure 4.19 shows data for a single detector and similar plots were constructed for the others. Software gates were placed over the diagonal bands for each detector to reduce background.

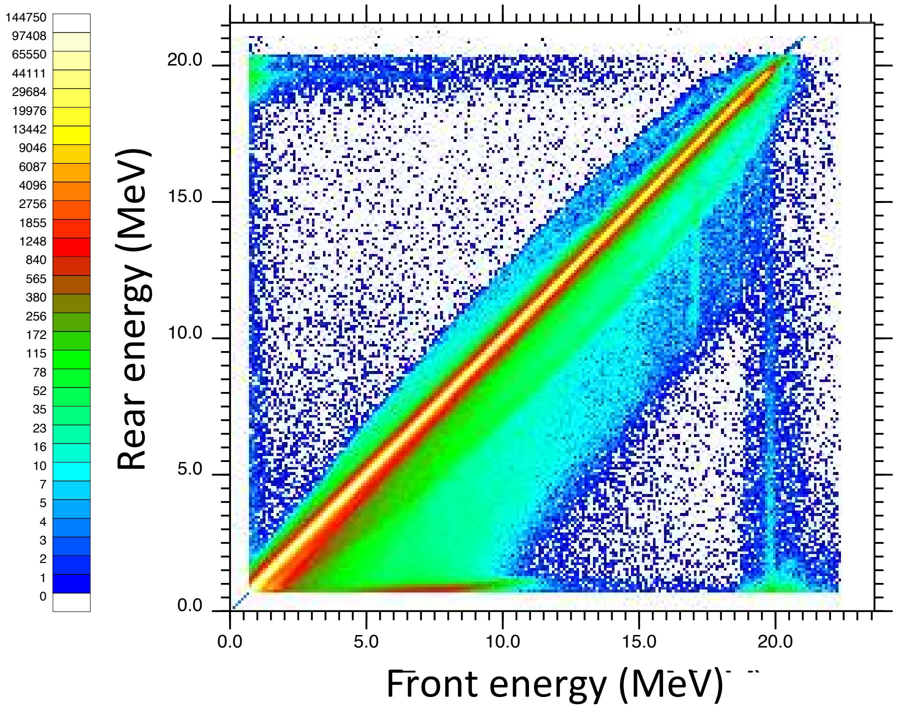

Figure 4.19: Plot of the energies collected by the front detector strips *vs.* the energies collected by the rear detector strips, on a single DSSD. ‘Good’ events lie on the diagonal line.

4.3.3 Kinematic lines

To confirm that the detectors were aligned correctly and to determine the composition of the target, the energies of the detected particles were plotted against their total scattering angle with respect to the target. The results for the 26 MeV data are shown in figure 4.20. A similar plot is obtained for the 22 MeV data. The lines corresponding to the theoretically-predicted energy values are overlaid on the data. Lines corresponding to the ^{9}Be ground state and 2.43 MeV $5/2^{-}$ level are clearly seen. The scattering of ^{4}He from ^{12}C and ^{16}O can be seen far more faintly at higher energies.

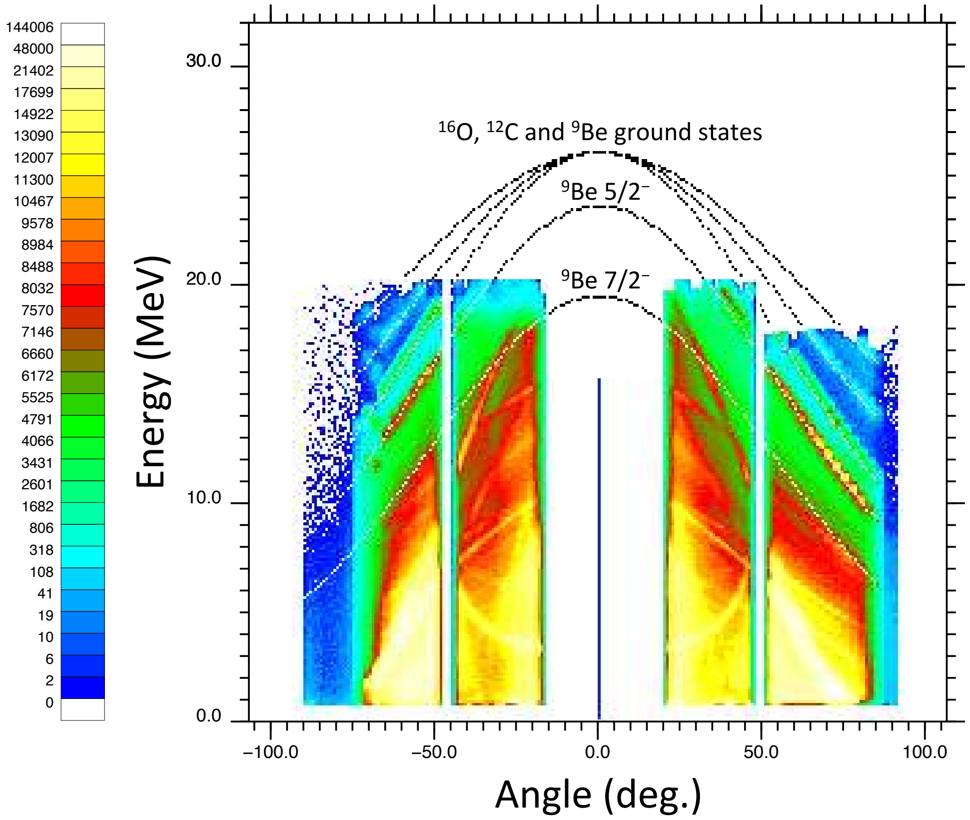

Figure 4.20: Plot of the energies of the detected particles as a function of the scattering angle (θ_{tot} in figure 4.15) for the 26 MeV beam energy data. The theoretical kinematic lines are overlaid.

4.3.4 Q-value spectra

A multiplicity condition of three hits across the detector array was demanded for a measured event to be considered for analysis. This would correspond to the scattered ^{4}He ion and the two α-particles resulting from the ^{9}Be break-up. The neutron, which is also emitted during the break-up, is undetected. However, since the beam momentum, along with the momenta of the charged final-state particles were known, the momentum of the neutron could be reconstructed from momentum conservation as

$$\mathbf{P}_{\mathrm{n}} = \mathbf{P}_{\mathrm{beam}} - \sum_{i=1}^{3} \mathbf{P}_{\alpha_{\mathrm{i}}}. \tag{4.8}$$

This allowed the Q-value of each reaction to be calculated by subtracting the energy before the reaction (beam energy) from the energy after (sum of all particle energies),

$$Q = E_{\mathrm{n}} + \sum_{i=1}^{3} E_{\alpha_{\mathrm{i}}} - E_{\mathrm{beam}}. \tag{4.9}$$

The resulting Q-value spectra are shown in figure 4.24 in section 4.3.5 later. However, a clear peak at the correct -1.57 MeV Q-value was observed in both the 22 and 26 MeV data sets, and a $\pm 2\sigma$ software cut about this peak was placed in order to predominantly select ^{9}Be break-up events. A substantial background remained beneath this spectrum, meaning that unwanted events made it through the software gate. Initially, software cuts placed either side of the ^{9}Be Q-value peak were used to gauge an approximate background profile for the excitation spectra. However, further gates later in the analysis meant that this background was negligible in the final ^{9}Be excitation spectra.

Impurities of ^{12}C and ^{16}O on the surface of the target can result in the reactions ^{12}C(^{4}He,3α)α and ^{16}O(^{4}He,4α)α, which will lead to the measured 3α final state. The elastic scattering lines in figure 4.20 in section 4.3.3 were examined in order to determine the composition of the target. The relative strengths of each kinematic line corresponding to ^{9}Be, ^{12}C and ^{16}O were normalised by the detection efficiency of the system using Monte-Carlo simulations (see section 4.4.1) and by the expected yield calculated from the Rutherford cross section. This leads to a composition of

$$^{9}\text{Be: } 92\%,\ ^{12}\text{C: } 6\%,\ ^{16}\text{O: } 2\%.$$

The ^{12}C contribution was removed from the data by assuming that the ^{12}C(^{4}He,3α)α reaction took place for each event. The potential fourth missing α-particle in the final state was reconstructed through momentum conservation and the Q-value of the reaction was calculated. This was plotted against the Q-value calculated assuming a ^{9}Be break-up. The results are shown in figure 4.21 for the 26 MeV beam data and a similar plot was obtained for the 22 MeV data set. The sharp, vertical line at -7.27 MeV corresponds to the break-up of ^{12}C and these events were removed by a software gate. The more complicated 5α final state resulting from the ^{16}O break-up could not be removed analytically (the two missing α-particles cannot be reconstructed simultaneously) and was assumed to contribute a small amount of background to the final excitation spectra.

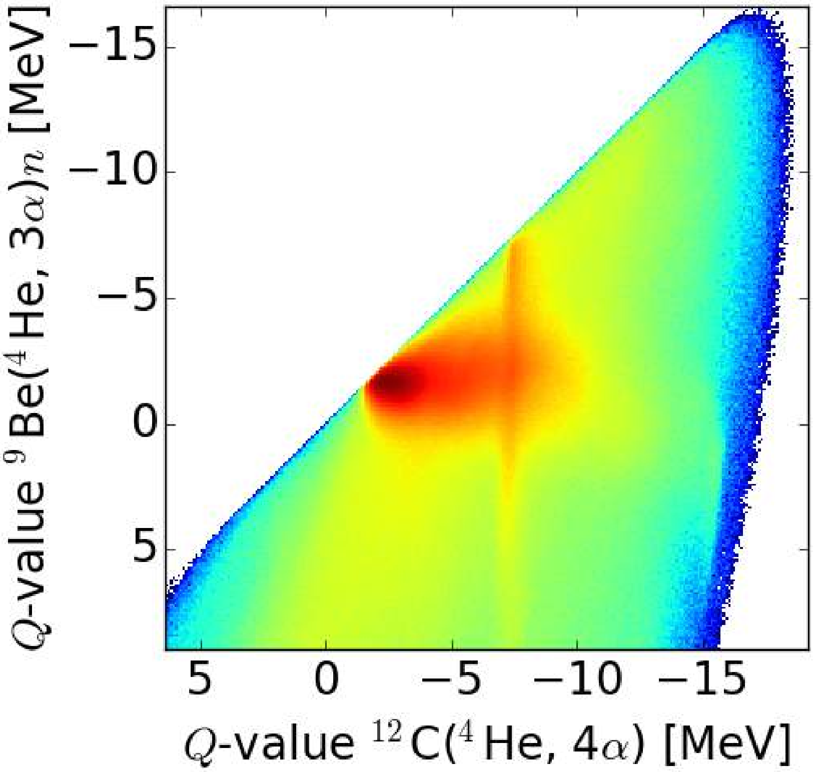

Figure 4.21: The calculated Q-value for ^{9}Be break-up plotted against the calculated Q-value for ^{12}C break-up. Plot from reference [94].

4.3.5 Target energy losses correction

Typical experiments use 100−200 μg/cm^2 thickness targets. The thick 1000 μg/cm^2 target used in this experiment is good because more reactions are measured since the probability of a interaction of the beam in the target is increased. However, the energy losses of the beam and the reaction products in the target must be carefully accounted for in order to extract any meaningful information from the experimental data. The 22 MeV beam can lose up to 230 keV in the target, if the interaction happens near to the target's rear face. The higher 26 MeV beam loses slightly less energy here. The break-up α-particles, because they are lower in energy than the beam, lose considerably more energy in the target. This is calculated as being up to a maximum of around 2 MeV. It is therefore very important that the effects of the particles travelling through the target are accounted for in the experimental analysis. The difference in the reaction happening in the front and rear faces of the ^{9}Be target are shown in figure 4.22. An interaction on the front face of the target results in minimal energy losses for the beam, but maximal for the reaction products. Similarly, an interaction on the rear face results in maximal energy loss for the beam, but minimal for the reaction products.

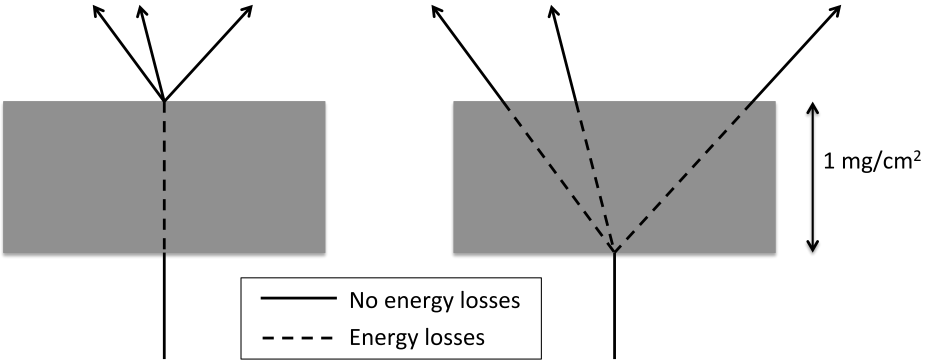

Figure 4.22: The energy losses of the beam and the reaction products in the cases where the reaction happens on the rear (left panel) or front (right panel) face of the target.

The picture presented by figure 4.23 was used to aid the calculations of the energy losses of the particles in the target. As was seen in section 4.3.4, using the momenta of the beam and charged reaction products, the momentum of the undetected neutron may be calculated. The resulting sum of the energies of all of the final state particles including the neutron energy, minus the energy of the beam should equal the reaction Q-value of −1.57 MeV. To correct for the energy losses of the particles, an iterative technique was developed. In the calculations, the value of D in figure 4.23 was incremented between the front and rear faces of the target (10 iterations were included). For each value of D, the energy loss of the beam was calculated and the energy at the interaction point E_b' was evaluated. How the energy losses were actually calculated is discussed shortly.

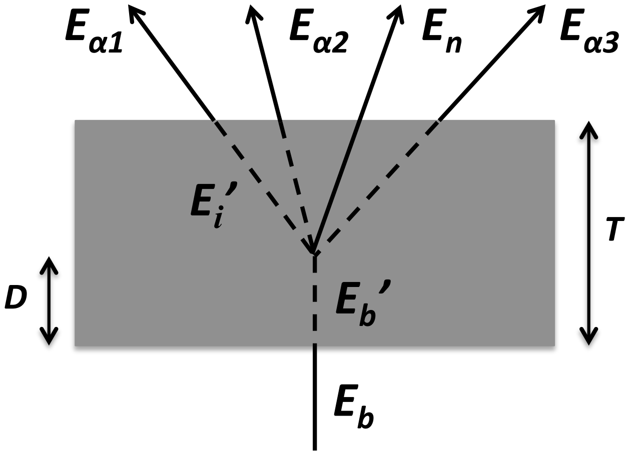

Figure 4.23: Diagram used to numerically calculate the energy losses of the particles in the target.

Based on the measured angles θ of all of the charged reaction products, the total distance through the target they travelled, based on the interaction point, D, were calculated as $d = (T - D)/cos(\theta)$. Given their measured energies and the distances they travelled through the target, their initial energies at the interaction point were calculated. The reduced beam energy and the corrected α-particle energies were used to calculate the energy of the undetected neutron. The total energy of the final state particles was then evaluated and the reaction Q-value added. This should result in the calculation of the reduced beam energy at the interaction point. This quantity was calculated for all iterations of the interaction distance D, and the point that most closely reproduced the correct beam energy was chosen as the interaction point.

To illustrate the improvement that this process provides, figure 4.24 shows the measured Q-value spectra for the reactions, before and after the energy-loss routine was implemented. A substantial improvement in the resolution of the Q-value was seen for both the 22 MeV and 26 MeV data sets. Figure 4.25 demonstrates the effect of the energy-loss corrections on the calculated excitation energies of ^{9}Be.

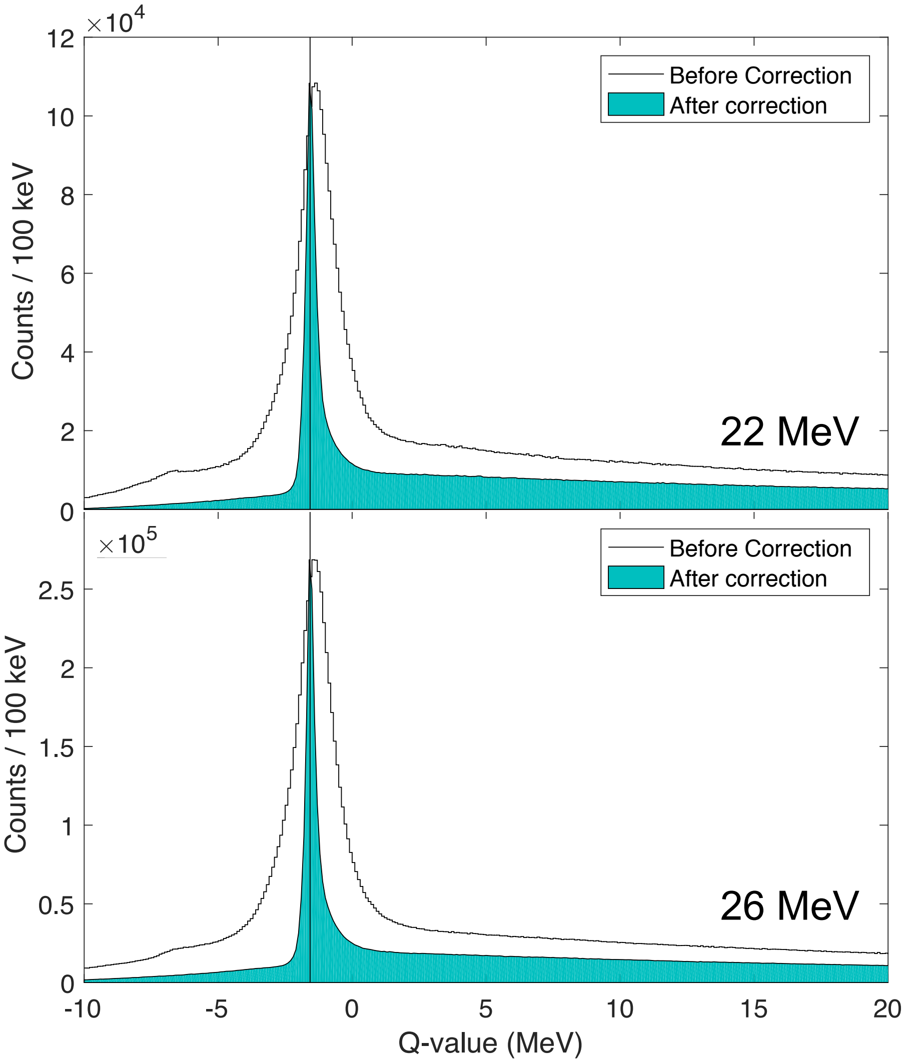

Figure 4.24: Q-value spectra before (line) and after (filled) the energy-loss correction routine was applied. 22 MeV and 26 MeV data occupy the upper and lower panels, respectively.

Monte-Carlo simulations, detailed in section 4.4.1, were performed to generate the excitation and decay of a 6 MeV state in ^{9}Be. With no experimental effects, a delta function at 6 MeV excitation should be reproduced. Due to experimental effects this is smeared out. Before the energy-loss corrections, the peak appears 300 keV above the true excitation energy and has a highly asymmetric shape. After the correction the peak appears at the correct energy, is narrower and is also symmetric. Evaluating the excitation energy resolution is important for extracting information from the measured excitation spectra as will be discussed in section 4.4. Typical energy-loss routines assume that the interaction happened in the centre of the target. Due to the substantial thickness of this target, that method was not sufficient. Although it removed the peak asymmetry, it gave a poorer excitation energy resolution by up to 50 keV.

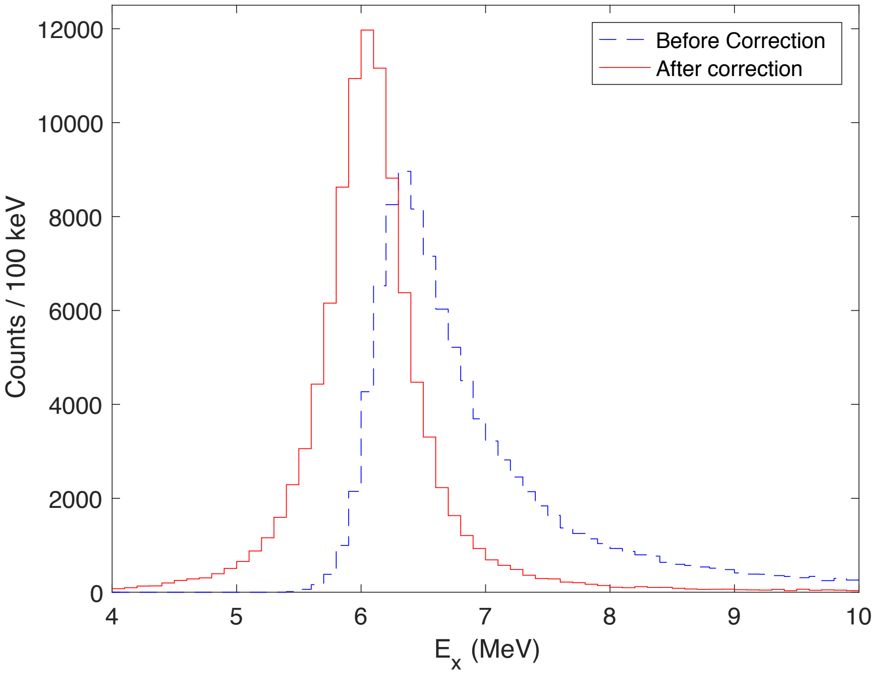

Figure 4.25: Simulated ^{9}Be excitation spectrum for a narrow state at 6 MeV, with and without target energy-loss correction.

The energy losses were calculated by using the `dedx.f` code [95]. This calculates stopping powers and ranges of particles travelling through a user-defined material and is based on the Oak Ridge `SPAR` code [96]. At high energies, where the interacting particles are completely ionised, Bethe's equation [97] is used with corrections for shell- and density-effects. At intermediate energies, where energy losses due to elastic Coulomb scattering can be ignored, an expression for the charge reduction of the ion, in conjunction with Bethe's equation is used. At low energies where charge reduction and nuclear Coulomb stopping effects are both important, the theory of reference [98] is used.

The code was used to calculate the range of α-particles in the ^{9}Be target for various suitable α-particle energies in 50 keV steps between 0.5 MeV and 32 MeV. These were then tabulated and used as a look-up table in the data analysis code. The energies of the measured α-particles were rounded to the nearest 50 keV and used to look up the corresponding ranges. This range was added to the proposed distance that each particle passed through the target. This was added to the calculated range, to give a total range. The range was then used to look up the α-particle energy corresponding to that total range. This was taken as the true energy.

4.3.6 Decay channel selection

Further selection can be achieved by placing constraints on the decay channel of the ^{9}Be states populated in the reaction. This is done for several reasons. Firstly, the decay channel of choice may be exclusive to ^{9}Be. Selection of this channel would then act to remove the contributions from contaminant reaction channels. Secondly, as discussed in section 4.3.7, in order to calculate the excitation energies of the states populated in ^{9}Be it is imperative to identify which of the final state α-particles is the scattered beam ion, and which two result from the break-up of ^{9}Be. Thirdly, the propensity for a state to decay through each channel can be an indicator of its angular momentum and parity and provide insight into the structure.

For the ^{9}Be excitation range populated in this experiment, four decay channels are open:

$$\begin{aligned} ^{9}\mathrm{Be}^{*} &\rightarrow {}^{8}\mathrm{Be}_{\mathrm{g.s.}} + n \rightarrow \alpha + \alpha + n && (4.10)\\ &\rightarrow {}^{8}\mathrm{Be}_{2+} + n \rightarrow \alpha + \alpha + n && (4.11)\\ &\rightarrow {}^{5}\mathrm{He}_{\mathrm{g.s.}} + \alpha \rightarrow \alpha + \alpha + n && (4.12)\\ &\rightarrow \alpha + \alpha + n && (4.13) \end{aligned}$$

The $^{8}\mathrm{Be}_{\mathrm{g.s.}} + n$ channel is the easiest channel to identify and will be the focus of the analysis. In order to identify this channel, the relative energies of pairs of α-particles in the final state E_{rel} were calculated as

$$E_{\mathrm{rel}} = \frac{1}{2}\mu v_{\mathrm{rel}}^{2}. \tag{4.14}$$

If the decay proceeded through a ^{8}Be intermediate state, the relative energies of two α-particles in the final state will form a known level in ^{8}Be. The final state α-particles were ordered by their angle of detection, meaning that $\theta_1(\alpha_1) > \theta_2(\alpha_2) > \theta_3(\alpha_3)$, and the relative energies E_{12}, E_{23} and E_{13} were calculated. A histogram of E_{12} is given in figure 4.26. In addition to the sharp peak corresponding to the narrow ground state of ^{8}Be at 92 keV, other features can be seen.

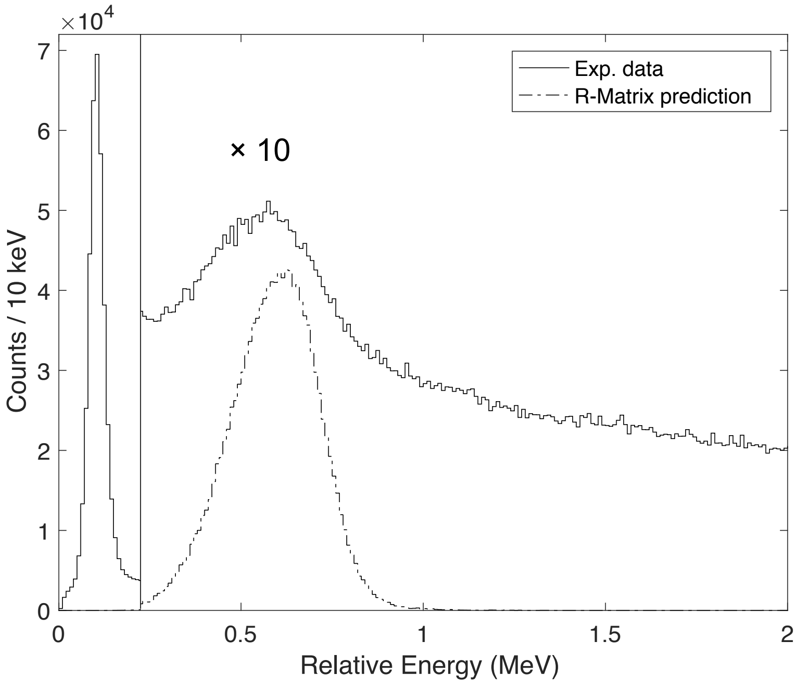

Figure 4.26: Relative energy spectrum between final state α-particles. The narrow peak at 92 keV corresponds the ^{8}Be ground state. The bump at ≈ 0.6 MeV corresponds to decays from the 2.43 MeV $5/2^-$ state in ^{9}Be to the tail of the $^8\mathrm{Be}_{2+}$ level. The dashed line shows the simulated decay of the $5/2^-$ state in ^{9}Be and the solid line shows experimental data.

Firstly, there is a large background, because only E_{12}, E_{23} or E_{13} can correspond to a state in ^{8}Be in any one reaction. The background to the E_{12} spectrum is when particles *2 and 3* or *1 and 3* come from a state in ^{8}Be. The bump at $E_{\mathrm{rel}} \approx 0.6$ MeV has previously been shown to correspond the 2.43 MeV $5/2^-$ state in ^{9}Be decaying to the tail of the broad $^8\mathrm{Be}_{2+}$ level [99]. The R-matrix theory described in section 3.2 is required to correctly describe the line shape of this feature. An R-matrix prediction for the $\ell = 1$ decay of the 2.43 MeV $5/2^-$ state in ^{9}Be decaying to the $^8\mathrm{Be}_{2+}$ resonance is shown by the additional dot-dashed line in figure 4.26. Experimental resolution effects were incorporated into this simulation.

It turns out that α decays of the 2.43 MeV level in ^{9}Be, through the broad $^5\mathrm{He}_{\mathrm{g.s.}}$, also produce a small bump around 0.6 MeV in the $\alpha - \alpha$ relative energy spectrum. Herein lies the difficulty in disentangling multiple break-up modes of low energy ^{9}Be states; the signatures for the $^8\mathrm{Be}_{2+}$ and $^5\mathrm{He}_{\mathrm{g.s.}}$ channels overlap in energy quite significantly. Hence, a complicated angular correlation analysis was required in order to differentiate between the two [99]. As the excitation of the nucleus increases, the two channels overlap less and can be distinguished, as demonstrated by reference [100].

The possible α-particle pairings to form states in ^{8}Be were disentangled by the two-dimensional relative energy spectrum shown in figure 4.27. The 2D plot allows much more structure to be seen. Along with the narrow ground state and bump at ≈ 0.6 MeV, the main peak of the $^{8}\mathrm{Be}_{2+}$ level can be faintly seen on both axes close to 3 MeV relative energy.

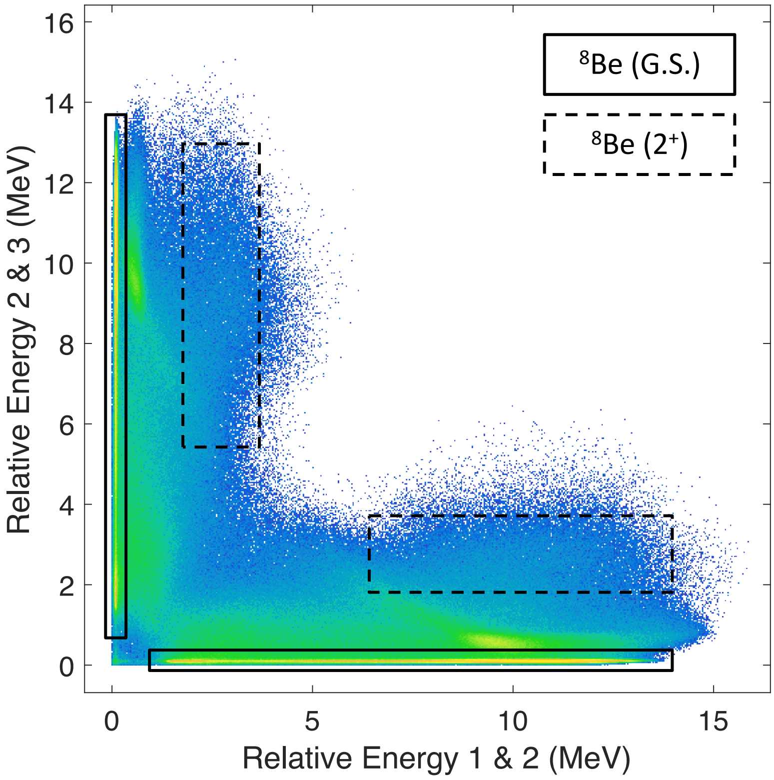

Figure 4.27: Two dimensional plot of α-particle relative energies from the 26 MeV data set. The 22 MeV data set produced an almost identical plot.

It transpired that only α_1 and α_2 *or* α_2 and α_3 in the final state, resulted from the decay of ^{9}Be. It was verified using the Monte-Carlo simulations that due to the kinematics of the break-up, whatever decay channel of ^{9}Be took place, the α-particles from the break-up were always detected with neighbouring angles, *i.e.* they never overlap in angle with the scattered beam. The reaction is, therefore, true to the simple picture presented by figures 4.12a. To select decays from the $^{8}\mathrm{Be}_{\mathrm{g.s.}}$, software gates were placed on the narrow horizontal and vertical bands at 92 keV relative energy in figure 4.27. This allowed the identification of the scattered beam ion as the third particle, allowing the excitation of ^{9}Be to be calculated.

4.3.7 Excitation energy calculation

Once the scattered beam particle was identified in the final state of three α-particles, the excitation of the ^{9}Be nucleus populated in the experiment could be calculated. Using the momentum of the detected scattered beam, the momentum of a proposed recoiling ^{9}Be was calculated as

$$\begin{aligned} \mathbf{P}_{\text{recoil}} &= \mathbf{P}_{\text{beam}} - \mathbf{P}_{\alpha_{\text{scatt}}} && (4.15) \\ E_{\text{recoil}} &= \frac{|\mathbf{P}_{\text{recoil}}|^2}{2m(^9\text{Be})}. && (4.16) \end{aligned}$$

Then, using energy conservation between the system before and after the scattering reaction, the ^{9}Be excitation energy is calculated as

$$\begin{aligned} E_{\text{beam}} &= E_{\text{x}}(^9\text{Be}) + E_{\text{scatt}} + E_{\text{recoil}} && (4.17) \\ E_{\text{x}}(^9\text{Be}) &= E_{\text{beam}} - E_{\text{scatt}} - E_{\text{recoil}}. && (4.18) \end{aligned}$$

The resulting ^{9}Be excitation spectra for the 22 MeV and 26 beam energy runs are shown in figure 4.28. Key states in ^{9}Be at 2.43, 6.43 and 11.28 MeV, belonging to the ground state rotational band, are marked on the plot. However, other features are not clear and there appears to be a high level of background, which is discussed next. The levels in ^{9}Be are often very broad $\approx$ 1 MeV, meaning that features are sometimes not clear due to the fact that they overlap. It is important to reduce the amount of background in order to best resolve the different ^{9}Be levels. This spectrum is modified by the detection efficiency of the set-up, which varies with excitation energy. Correcting for this is discussed in section 4.4.1.

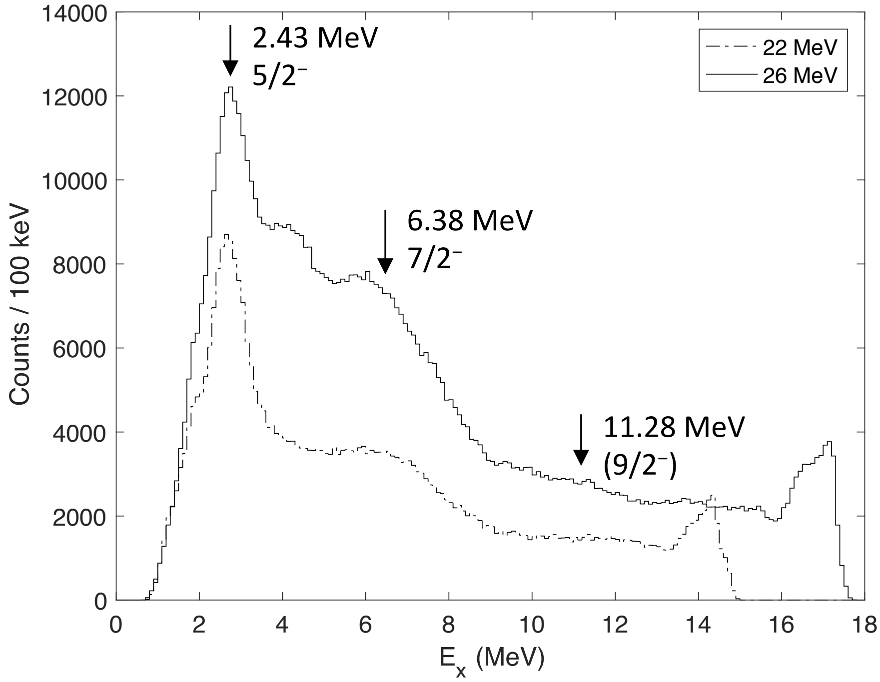

Figure 4.28: Excitation spectra for ^{9}Be, subject to the condition of a ^{8}Be$_{\mathrm{g.s.}}$ intermediate state. The 22 MeV beam data are shown by the dot-dashed line and the 26 MeV data are shown by the solid line. Some key levels in ^{9}Be are marked by the vertical arrows.

4.3.8 Further contaminant reaction channels

The discussion in section 4.3.4 described how interactions with ^{12}C contaminants in the target were removed from the analysis. However, even when just considering the ^{4}He + ^{9}Be interaction, there are reaction channels other than inelastic scattering that have to be accounted for. These include the ^{9}Be(^{4}He,^{12}C*)n reaction, populating states in ^{12}C, and the ^{9}Be(^{4}He,^{5}He$_{\text{g.s.}}$)^{8}Be$_{\text{g.s.}}$ neutron transfer reaction. To remove these contributions from the ^{9}Be spectrum, the Dalitz plot in figure 4.29 was constructed. This is shown for the 26 MeV data set, but the same analysis was performed for the 22 MeV beam data.

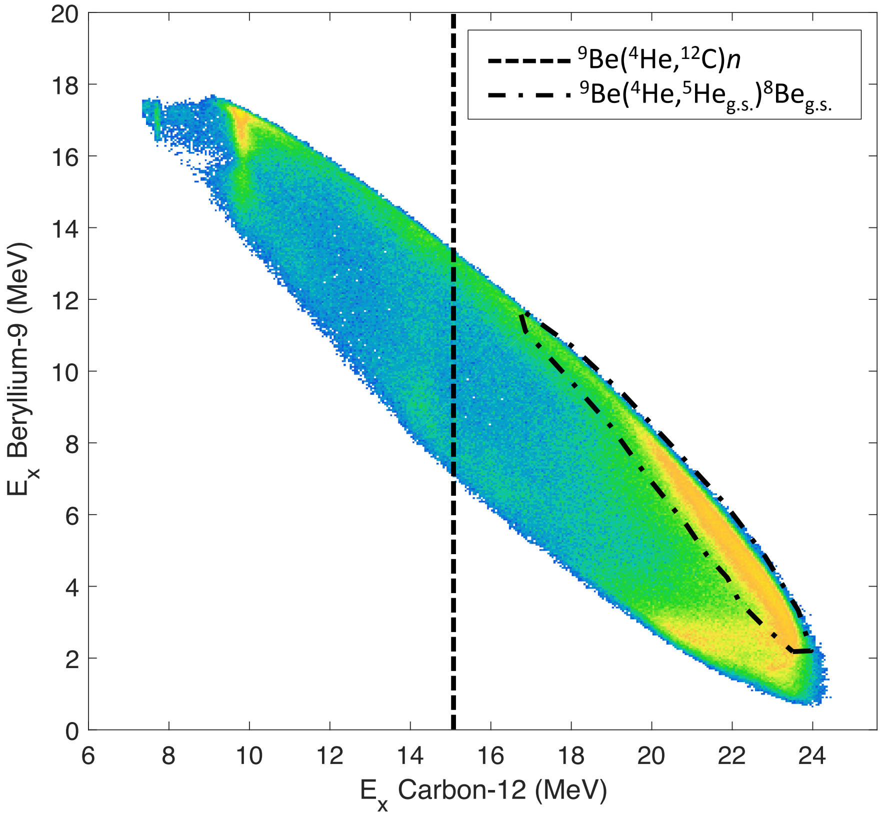

Figure 4.29: Excitation energy of a proposed ^{9}Be $(\alpha + \alpha + n)$ *vs.* the excitation energy of a proposed ^{12}C $(\alpha + \alpha + \alpha)$ (26 MeV beam data only). Broad horizontal lines correspond to states in ^{9}Be and the vertical lines correspond to the known natural parity states in ^{12}C. The diagonal band corresponds to the neutron transfer reaction and break-up of ^{5}He. The dashed and dot-dashed lines mark the regions occupied by contaminant reactions. See text for details.

Here, the excitation energy in ^{9}Be, calculated in section 4.3.7 is plotted against an excitation energy in ^{12}C calculated from the three final state α-particles. The momentum and energy of the proposed ^{12}C were calculated as

$$
\begin{aligned}
\mathbf{P}(^{12}C) &= \mathbf{P}_{\alpha_1} + \mathbf{P}_{\alpha_2} + \mathbf{P}_{\alpha_3} && (4.19)\\
T(^{12}C) &= \frac{|\mathbf{P}(^{12}C)|^2}{2m(^{12}C)}, && (4.20)
\end{aligned}
$$

and the excitation energy of ^{12}C was calculated as

$$
E_x = \sum_{i=1}^{3} E(\alpha_i) - T(^{12}C) - Q \;\; (\text{where } Q = -\,7.27 \text{ MeV}). \qquad (4.21)
$$

The plot shows some vertical lines, corresponding to known states in ^{12}C. Since events involving the 0^+ $^{8}\mathrm{Be}_{\mathrm{g.s.}}$ were exclusively considered, only natural parity states in ^{12}C are seen. The low-energy ^{12}C levels (up to the 14 MeV 4^+ level) were removed from further analysis by ignoring data that lay to the left of the dashed line in the Dalitz plot. The broader levels at higher energy in ^{12}C could not be clearly removed without distorting the low energy levels in ^{9}Be, so these contributions were modelled as a slowly varying background contribution to the ^{9}Be spectra.

Events residing in the diagonal dot-dashed region in figure 4.29 were also removed from the analysis. Monte-Carlo simulations indicated that the intense diagonal band is a signature for the $^{9}\mathrm{Be}(^{4}\mathrm{He},^{5}\mathrm{He}_{\mathrm{g.s.}})^{8}\mathrm{Be}_{\mathrm{g.s.}}$ neutron transfer reaction. By properly simulating the broad $^{5}\mathrm{He}_{\mathrm{g.s.}}$ level and including the effects of experimental resolution, simulated data were seen to reside exclusively in the dot-dashed region. Contributions from this channel were totally removed from the rest of the analysis.

To produce clean excitation spectra for ^{9}Be, the Dalitz plots corresponding to the 22 MeV and 26 MeV beam energies were projected onto the vertical axis, after these software cuts had been placed. These spectra are shown in figure 4.30.

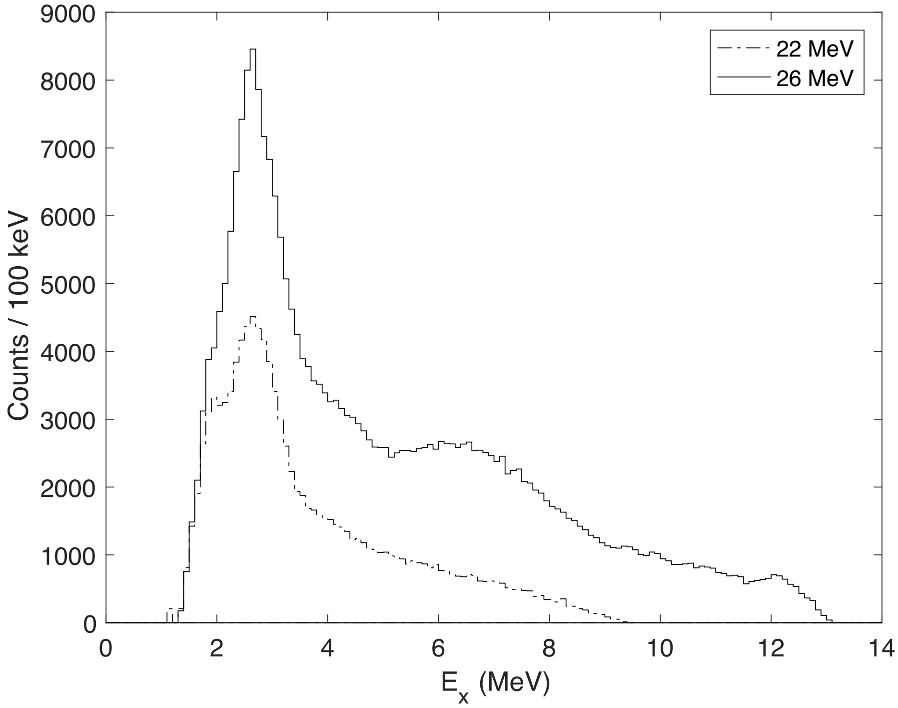

Figure 4.30: Excitation spectra for ^{9}Be, subject to the condition of a ^{8}Be$_{\text{g.s.}}$ intermediate state, and after all software cuts were placed. The 22 MeV beam data are shown by the dot-dashed line and the 26 MeV data are shown by the solid line.

4.4 Secondary analysis

The secondary analysis consisted of three main stages. Firstly, the effects of the experimental resolution and efficiency were investigated, through the use of Monte-Carlo simulations. These effects were then incorporated into the excitation spectra so that meaningful information could be extracted from the data. Secondly, the experimental spectra were fit with resonance line shapes to determine what states were populated in ^{9}Be. Thirdly, the measured energies and widths of the resonances were used to determine information such as their angular momentum and parity, which may provide an insight into the nuclear structure.

4.4.1 Monte-Carlo simulations

Simulations were performed using the Resolution8 (`RES8`) Fortran 77 code, which is designed for non-relativistic, thin-target experiments and can simulate various different types of reactions, such as scattering, transfer and resonance. The code is unpublished but further details can be found in references [101–103]. In its basic form, `RES8` is a two-body kinematics code, so models a break-up reaction as a chain of two-body decays, as shown in figure 4.31. The program allows the user to define a beam nucleus, target nucleus, the break-up pathways, the excitation energy of the particles produced in the reaction, the Q-values of each stage and the angular distribution of the emitted particles.

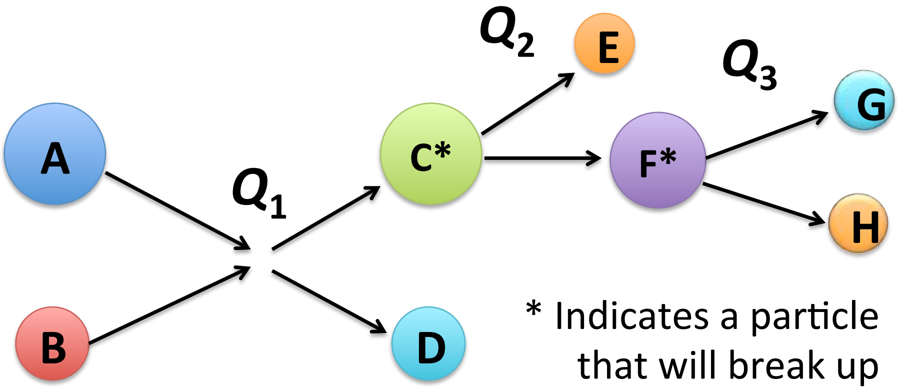

Figure 4.31: A sequential break-up reaction generated in `RES8`. $A + B \rightarrow C^{*} + D$ then $C^{*} \rightarrow E + F*$ etc.

In figure 4.31, where A is the target and B is the beam, the two-body kinematics for the first reaction stage Q_1 are generated for a scattering angle randomly sampled from a specified angular distribution. The product C* is populated in an excited energy state defined by the user. A state width can also be defined here, so that the populated excitation energy is sampled from a distribution. Given the chosen scattering angle and excitation energy, the kinetic energies and momenta of the C* and D particles are calculated. Break-up stages of either reaction product can then be specified. Here C* breaks up into E and F*. In the centre-of-mass frame of C*, given its excitation, and the Q-value, Q_2, the energies of the fragments E and F* are then calculated. Their angles with respect to the direction of the parent C* are sampled randomly from a given probability distribution. These particles can then be boosted into the laboratory frame using the momentum of C*. This process can be repeated for however many break-up stages are required. The intermediate result is that the energies and directions of all final-state reaction products in the laboratory frame are then known. Further effects are included before this stage: the beam energy can be smeared by a chosen distribution, and the beam systematically loses some energy as it traverses a randomly-chosen depth into the target.

After this stage, the final state particles (here we have D, E, G and H) lose energy as they exit the target from the beam depth. Their angular and energy straggle inside the target is also calculated. Then, the positions and intrinsic energy resolution of each of the detectors are defined. This then allows the detector pixel that each final state particle would hit to be identified and the detector response to be calculated. The centre θ_x and θ_y angles of the strips that are hit by each particle are chosen as the hit positions, and the particle energies are smeared by a specified Gaussian energy resolution. The result is that the program outputs a set of energies and angles of the final-state particles which include the effects of the experimental set-up. These data produced by `RES8` are then analysed in the same way as the experimental data, in order to account for any software cuts placed in the experimental data analysis.

The simulated data are used for three main reasons. Firstly, the various kinematical software cuts used to focus cleanly on measuring ^{9}Be break-ups rely on analysing the manifestation of contaminant reaction channels on each of the experimental plots (see section 4.3.8). Using the Monte-Carlo code allows the signature for each separate process to be identified, and to be removed from the analysis of the ^{9}Be scattering reaction. Secondly and thirdly, the experimental efficiency and excitation energy resolution must be quantified. These are discussed next.

Experimental efficiency

The two ^{9}Be excitation spectra shown in figure 4.30 are modified by an energy-dependent efficiency profile. This efficiency comes from two sources. Firstly, the four detectors used in the experiment do not provide a 4π solid angle coverage, so there will be a geometric efficiency in measuring the final state reaction products. The directions of the final state particles are inextricably linked to the excitation energies of the reaction products, meaning that the efficiency will vary with this parameter. Secondly, the kinematical software cuts applied during the data reduction and analysis will modify the profile of the excitation energy spectrum. For example, the removal of ^{5}He break-ups from figure 4.29 will cause a drop in the ^{9}Be yield between 2 and 12 MeV.

Given the 22 and 26 MeV ^{4}He beam energies, and the desired ^{9}Be break-up reaction, excitation energies in ^{9}Be up to 20.43 and 24.43 MeV are permitted. Therefore, a flat distribution of excitation energies between 1.57 MeV (^{9}Be n decay threshold) and these upper limits were generated in the simulations. After generating a large number of events (10^{6} for the final result), and passing these events through the experimental analysis code, the resulting ^{9}Be excitation spectra provide a value for the efficiency at each excitation energy. The efficiency in each excitation bin is given as the number of events in the bin, divided by the total number of events simulated in that bin. The efficiency profile used in the analysis for the 26 MeV data set is given as the black line in figure 4.32.

The final analysis assumed an isotropic initial scattering and an isotropic break-up of particles during the various decay stages of the reaction. In reality, this will not be the case. Due to the angular momenta of the various states populated in the experiment, the scattering will possess a non-uniform angular distribution. To test the validity of this assumption, efficiency profiles were generated for a number of different angular distributions of the inelastic scattering in the simulations. The different lines in figure 4.32 give the normalised efficiency profiles corresponding to the various angular distributions shown in figure 4.33.

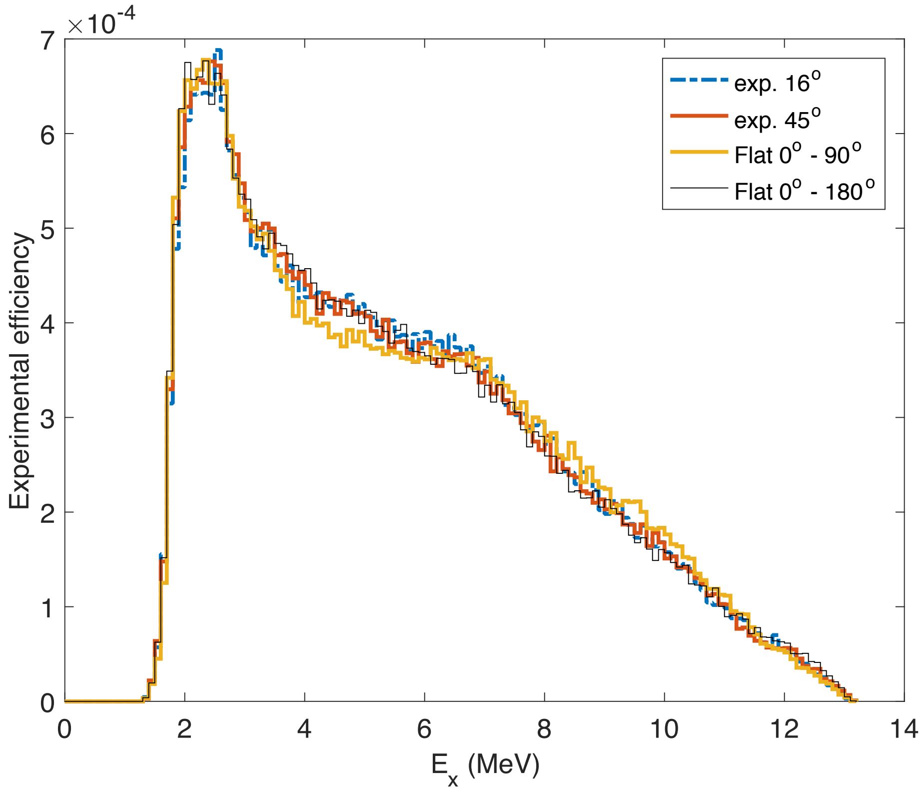

Figure 4.32: Efficiencies, as a function of ^{9}Be excitation energy, for the various angular distributions used in the simulations. A beam energy of 26 MeV was used in these simulations.

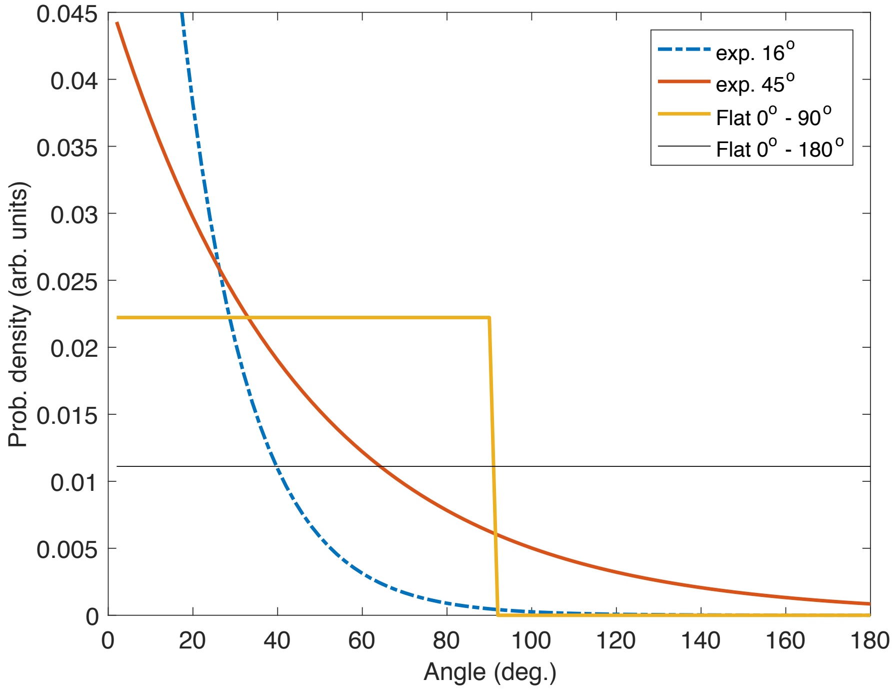

Figure 4.33: Angular distributions of the simulated inelastic scattering. A uniform angular distribution between $0^\circ - 180^\circ$ was used in the final analysis.

The absolute values of the efficiency were seen to vary quite considerably depending on the nature of the chosen angular distribution. Therefore, it is not possible to extract exact cross sections from these data. However, the relative values of the efficiencies, evaluated at each excitation energy, were seen to follow very similar profiles. To quantify this, over all of the trialled angular distributions, and at each point in excitation, the maximum difference between the efficiency profiles was calculated. This maximum percentage difference is given as a function of excitation energy in figure 4.34. The average difference across the whole of the 26 MeV beam energy spectrum is shown by the horizontal red line at 11%. The average over the region $<$ 10 MeV is given by the blue line at 8%. Similar results were found when considering the 22 MeV beam energy data. The assumption of a flat angular distribution of emitted particles was concluded to be accurate to around 10%.

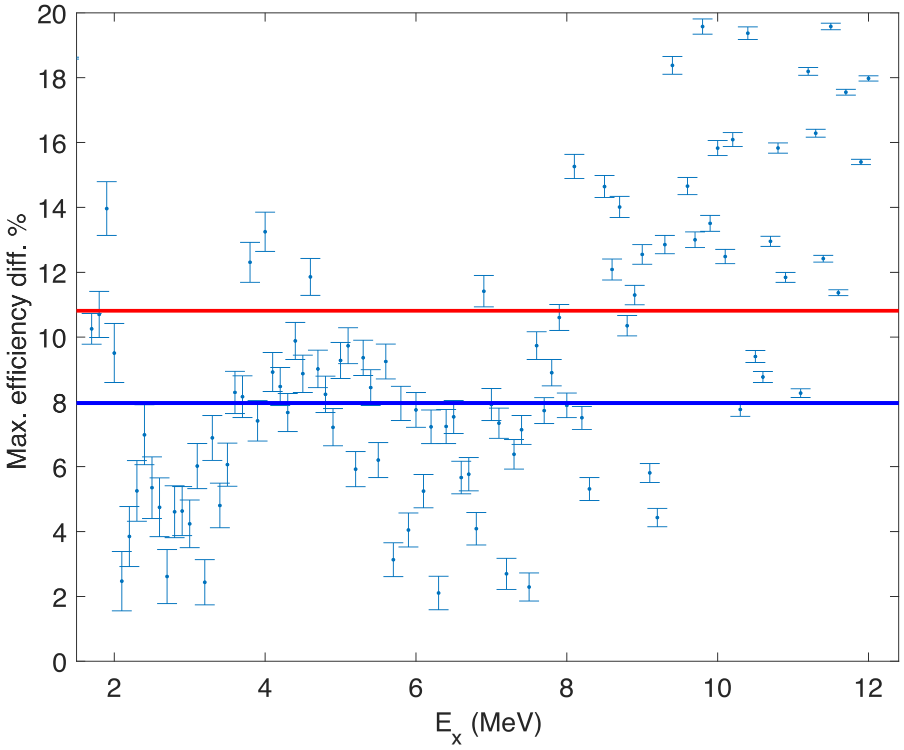

Figure 4.34: The maximum percentage difference between the efficiencies at each value of the excitation energy, calculated over all possible angular distributions used in the simulations. The red and blue lines show the average difference over the entire excitation range and the $0-8$ MeV range, respectively. Shown for 26 MeV beam data, though similar differences were seen for the 22 MeV data set.

The counts in each excitation bin in the experimental excitation spectra were divided by the efficiency in that bin, in order to correct for the experimental efficiency. The resulting excitation spectra are given by figure 4.35.

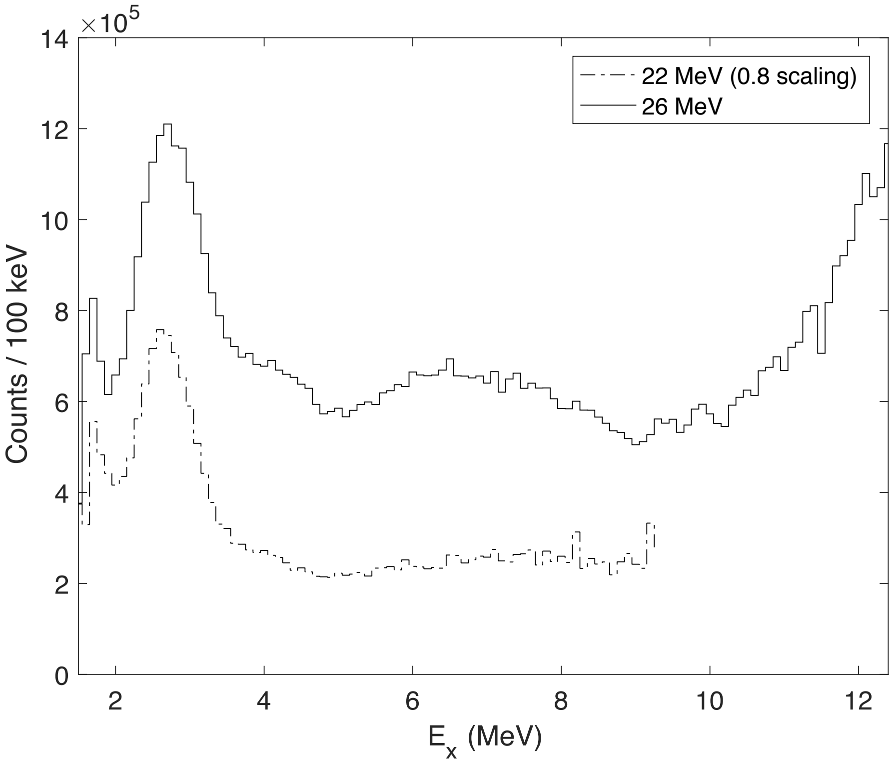

Figure 4.35: The calculated ^{9}Be excitation spectra, normalised by the efficiency at each energy. The 22 MeV beam data (scaled by a factor of 0.8) are shown by the dot-dashed line and the 26 MeV data are shown by the solid line.

Experimental resolution

Determining the experimental resolution as a function of excitation energy was important to properly interpret the measured excitation spectra. An infinitely narrow state populated in the experiment will not be reconstructed as such, and will be blurred due to the experimental resolution. Although a narrow isolated nuclear resonance with no scattering interference is modelled as a Breit-Wigner distribution, the states appearing in the experimental spectra were smeared by the experimental resolution. For the reaction $a+b \rightarrow c+d$, a resonance in the cross section at an energy E_R is described by the functional form [37]

$$\sigma(E) = \frac{\pi}{k^2} \frac{2J+1}{(2s_a+1)(2s_b+1)} \frac{\Gamma_{ab}\Gamma_{cd}}{(E-E_R)^2+\Gamma^2/4}, \tag{4.22}$$

where Γ_{ab} and Γ_{cd} are the partial widths for the input and output reaction channels, J is the angular momentum of the resonance, and s_a and s_b are the spins of the input particles. The total width of the resonance is given by Γ, which is simply the sum of the partial widths. In this experiment, for the i^{th} break-up channel of ^{9}Be, the functional form of the peak can be simplified to the Lorentzian lineshape,

$$\mathcal{L}(E|E_R, \Gamma_i, A_i) = \frac{A_i}{(E-E_R)^2+(\Gamma_i/2)^2}. \tag{4.23}$$

The experimental resolution acts to broaden the peaks in comparison to those predicted by equation 4.23. The response of the system to a state generated at fixed energy is called its spectral response function. The functional form of the spectral response depends on the type of experimental smearing. The Monte-Carlo simulations indicated that for excitation energies < 3.25 MeV, if a state is generated at a fixed excitation, then the resulting excitation spectrum has a Gaussian shape. However, at higher energies, the simulated levels are observed to have a Lorentzian shape, such as that shown in figure 4.25. This is due to the thick target and energy-loss correction routine. Simulations involving thinner targets gave a Gaussian smearing across the whole spectrum.

In the case of a Lorentzian spectral response function, the convolution between two Lorentzians, with widths Γ_1 and Γ_2, is another Lorentzian with a width of $\Gamma_1 + \Gamma_2$. For Gaussian smearing, the peaks manifest as Voigt profiles, which is the convolution of a Gaussian and a Lorentzian

$$V_j(E|E_j, A_j, \Gamma_j, \sigma) = \frac{A_j \Gamma_j}{2\sigma}\sqrt{\frac{\pi}{2}}\,\mathrm{Re}\left[w\left(\frac{(E-E_j)+i\Gamma_j}{\sqrt{2}\sigma}\right)\right], \tag{4.24}$$

where Re$[w]$ is the real part of the complex complementary error function (Faddeeva function). The effect of increasing Gaussian smearing on a Lorentzian profile is shown in figure 4.36.

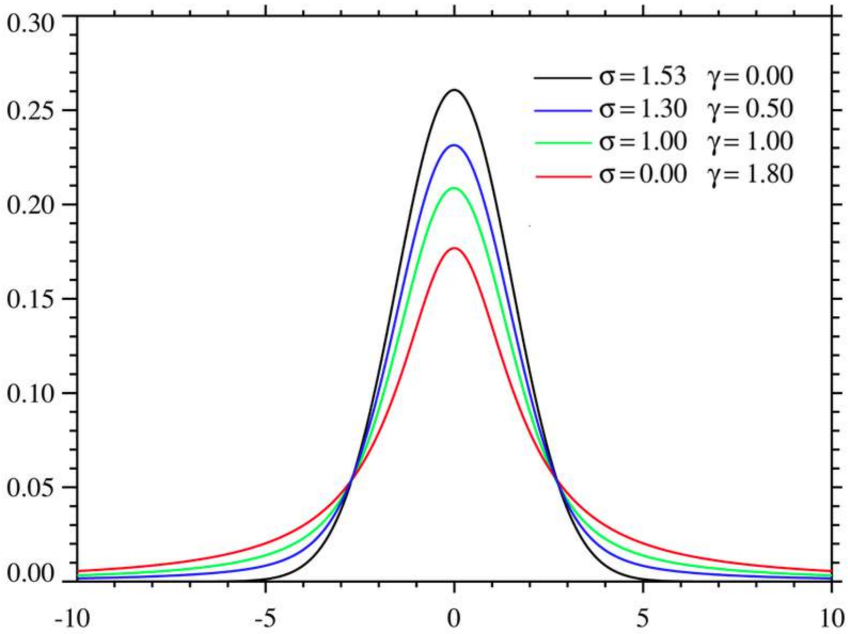

Figure 4.36: Plots showing the effect of increasing experimental Gaussian smearing, σ, on the appearance of a Lorentzian peak of intrinsic width γ, in the measured excitation spectrum

The simulations were used to evaluate the experimental resolution as a function of the excitation energy. In the simulations, states were generated at fixed excitation energies. The resulting peaks in the excitation spectra were fit with either a Gaussian ($<$ 3.25 MeV) or Lorentzian profile ($>$ 3.25 MeV). The results are shown in figures 4.37 and 4.38. In order to use this information during the peak fitting, it was necessary to interpolate between these data points. Therefore, the trend was phenomenologically modelled at a 7^{th} order polynomial which permitted the resolution to be calculated, with extrapolation errors, at any value of the excitation energy.

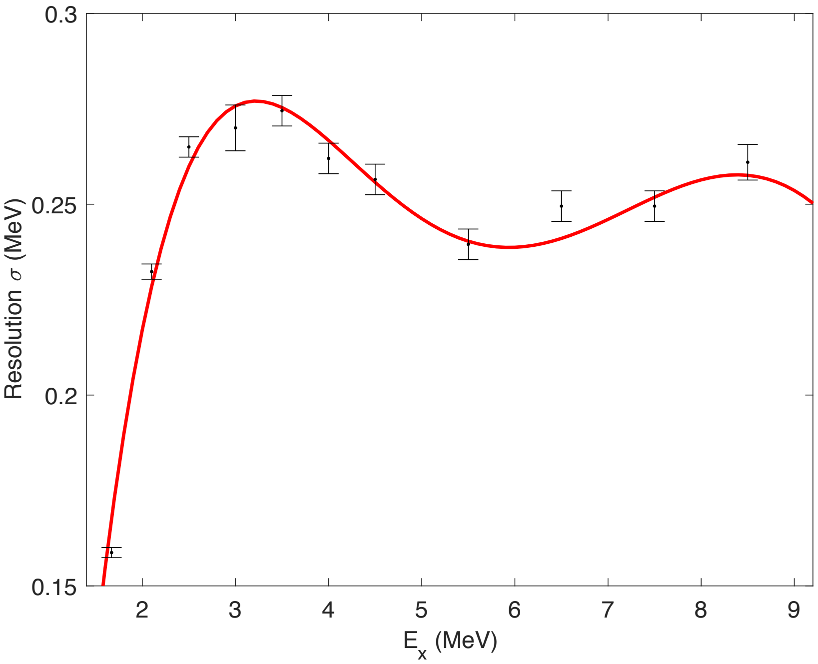

Figure 4.37: Plot of the excitation energy resolution ($\sigma \approx$ FWHM/2.35 for Gaussian peaks and Γ for Lorentzian peaks) for the 22 MeV beam energy, as a function of the ^{9}Be excitation energy. These results were derived from Monte-Carlo simulations.

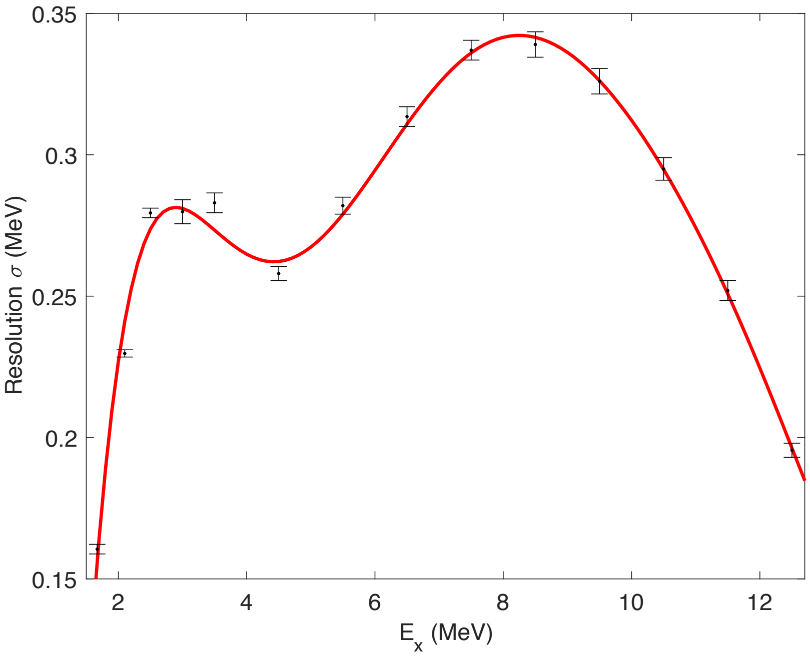

Figure 4.38: Plot of the excitation energy resolution ($\sigma \approx$ FWHM/2.35 for Gaussian peaks and Γ for Lorentzian peaks) for the 26 MeV beam energy, as a function of the ^{9}Be excitation energy. These results were derived from Monte-Carlo simulations.

The credibility of the Monte-Carlo simulations was tested by examining a single, narrow resonance in the ^{9}Be excitation spectrum. It was shown in figure 4.26 that the small peak in the $\alpha - \alpha$ relative energy spectrum, around 0.6 MeV, was due to decays of the 2.43 MeV $5/2^-$ state in ^{9}Be. This state has a negligible width < 1 keV, so its broadening in the spectrum is due to the experimental resolution alone. By placing a software gate on this region it was possible to focus on this one state in ^{9}Be. The resulting excitation spectra are shown in figures 4.39 and 4.40 for the 22 MeV and 26 MeV beam data, respectively. Gaussian fits to these peaks with an approximate linear background profile provided FWHM ($\approx 2.35\sigma$) of 22 MeV data: 626(8) keV, and 26 MeV data: 676(9) keV. These are consistent with the results of the Monte-Carlo simulations shown in figures 4.37 and 4.38.

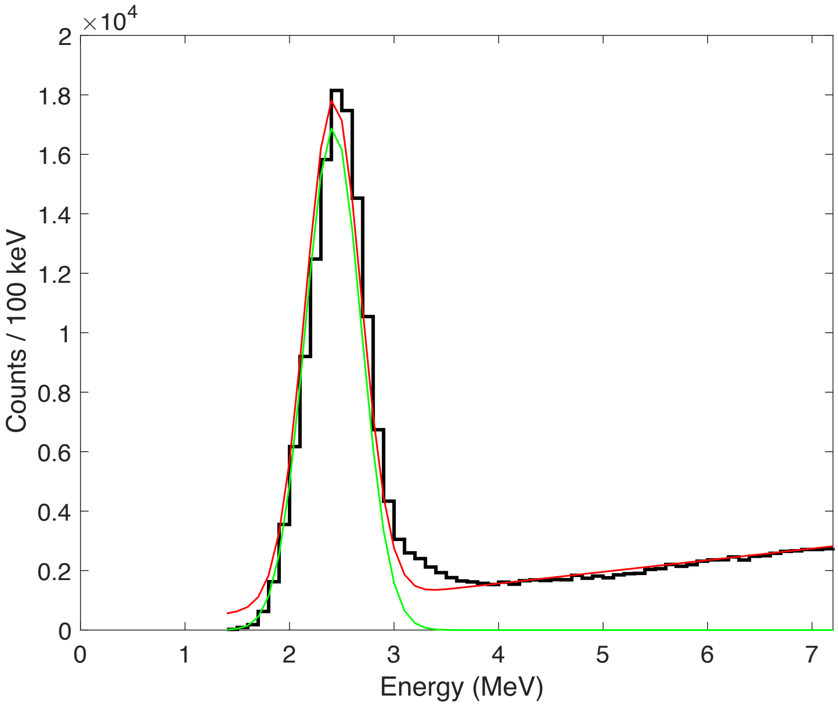

Figure 4.39: Fit to the 2.43 MeV $5/2^-$ state in ^{9}Be for the 22 MeV beam energy data. The red and green lines show the fit with and without a linear background, respectively.

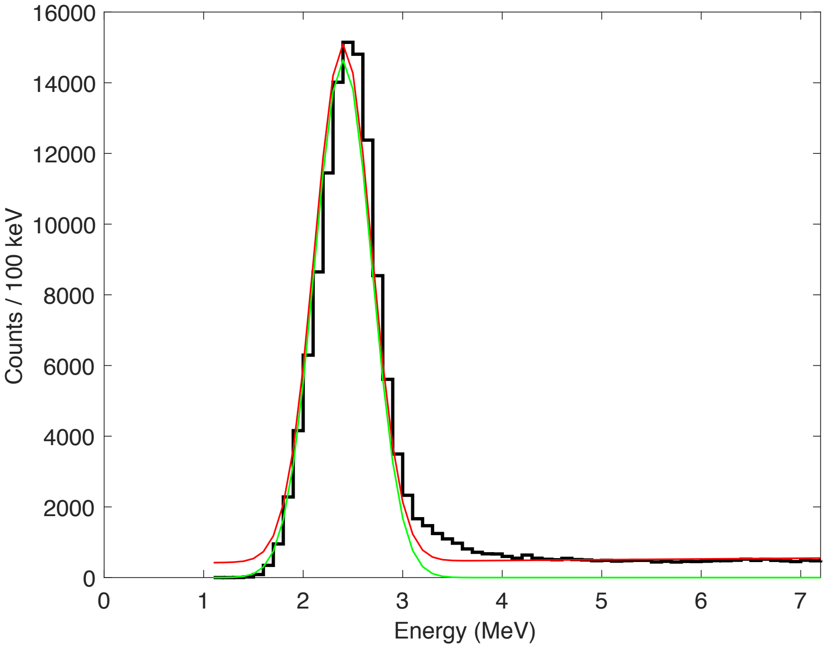

Figure 4.40: Fit to the 2.43 MeV $5/2^-$ state in ^{9}Be for the 26 MeV beam energy data. The red and green lines show the fit with and without a linear background, respectively.

4.4.2 Peak fitting

Before experimental smearing, the states in ^{9}Be are modelled as Breit-Wigner line shapes. Hence, after experimental smearing, the states in the excitation spectra below 3.25 MeV were approximated as Voigt profiles. States above this energy were modelled with Lorentzian profiles, with widths given as the sum of the natural width of the state, Γ_k, and the width of the Lorentzian experimental spectral response function, Γ_{R_k}. Figures 4.37 and 4.38 demonstrated that the experimental resolution varied relatively slowly with excitation energy. Therefore, the experimental resolution was approximated to be constant over each of the individual resonances.

The approximation was made that the spectrum can be simply described as a sum of peaks and that each of the states interfere constructively with one another other. The function fit to the experimental spectra for N_G Voigt profiles and N_L Lorentzian profiles is, therefore,

$$\begin{aligned} F(E|E_k, A_k, \Gamma_k, \sigma) &= \sum_k^{N_G} V_k(E|E_k, A_k, \Gamma_k, \sigma_k) + \sum_k^{N_L} \mathcal{L}_k(E|E_k, \Gamma_k, A_k, \Gamma_{R_k}) && (4.25) \\ &= \sum_k^{N_G} \frac{A_k \Gamma_k}{2\sigma} \sqrt{\frac{\pi}{2}} \mathrm{Re}\left[w \left(\frac{(E - E_k) + i\Gamma_k}{\sqrt{2}\sigma} \right) \right] && (4.26) \\ &+ \sum_k^{N_L} \frac{A_k}{(E - E_k)^2 + [(\Gamma_k + \Gamma_{R_k})/2]^2}. \end{aligned}$$

As was mentioned in section 3.2, the resonances that appear in the excitation spectra do not follow the simple Breit-Wigner form assumed by equation 4.25. Due to the changing decay penetrability of the ^{8}Be + n system with excitation energy, the width and energy will vary with excitation energy across the resonances. This means that for near-threshold states, the resulting excitation function may be highly asymmetric [40, 104]. This effect was calculated using R-Matrix theory for the known states in the spectrum, in order to determine if equation 4.25 was a good approximation. The resonance at 1.684 MeV, just 20 keV above the n threshold, is shown by the dark histogram in figure 4.41. The calculated excitation function is highly asymmetric, however, this asymmetry is very small compared to the Gaussian experimental resolution. The approximation of the state as a Voigt profile is reasonable, though an extended tail at higher energy is expected.

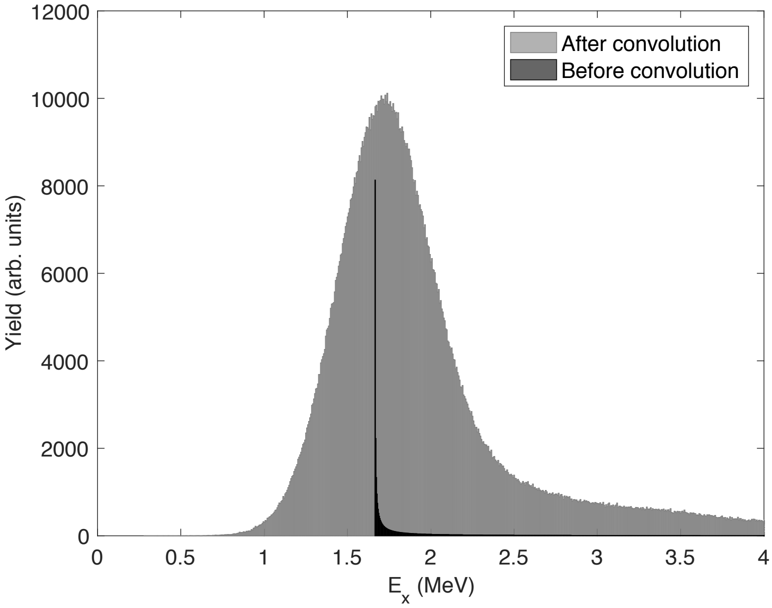

Figure 4.41: Predicted excitation function for the $1/2^+$ state at 1.684 MeV in ^{9}Be using *R*-Matrix theory ($\ell = 0$). The lighter histogram shows the peak shape after the data were blurred by a Gaussian spectral response function (FWHM 630 keV).

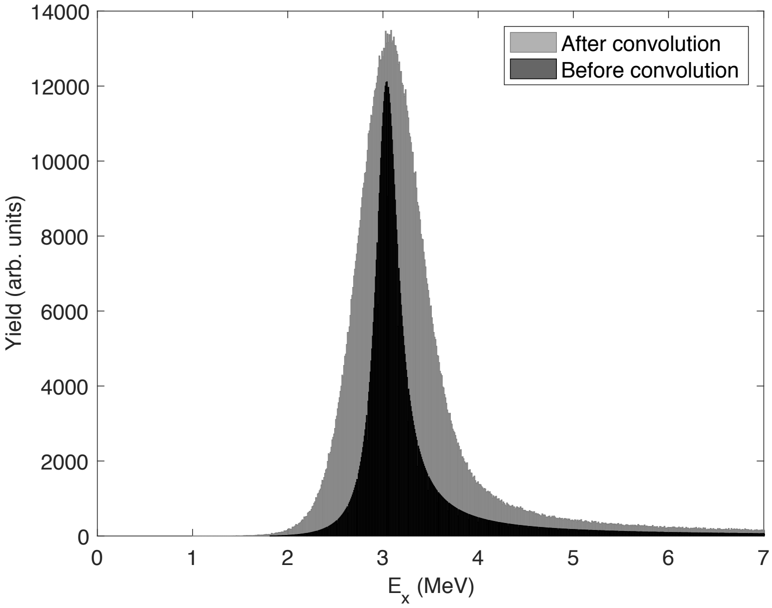

Figure 4.42: Predicted excitation function for the $5/2^+$ state at 3.05 MeV in ^{9}Be using *R*-Matrix theory ($\ell = 2$). The lighter histogram shows the peak shape after the data were blurred by a Gaussian spectral response function (FWHM 630 keV).

The $5/2^+$ state at 3.05 MeV was also generated using R-matrix theory and was seen to be slightly asymmetric in figure 4.42. Again, the Gaussian experimental smearing dominates the asymmetry. The R-Matrix calculations were performed using an unpublished code, and verified using the AZURE2 code [51, 105]. It was concluded that, given the experimental resolution, the form of equation 4.25 was a reasonable function to fit to the experimental data.

The data were fit using the *Tracey Peaker v 1.0* χ^2 minimisation program (`MATLAB 2012a`) [106]. Initially, the *known* states in ^{9}Be [52] were fit to the excitation spectra and the results are shown by figures 4.43 and 4.44.

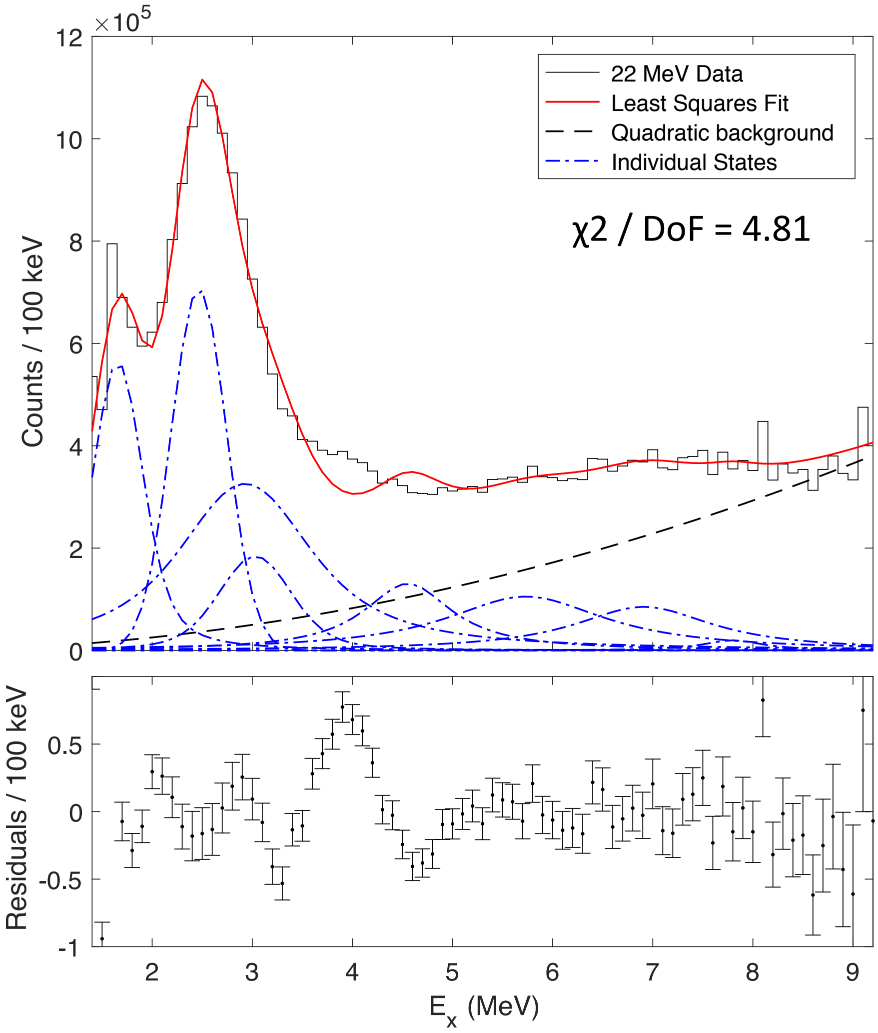

Figure 4.43: Fit of the known levels in ^{9}Be to the 22 MeV beam energy excitation spectrum. The lower panel shows the fit residuals, indicating an extra feature in the 4 MeV region.

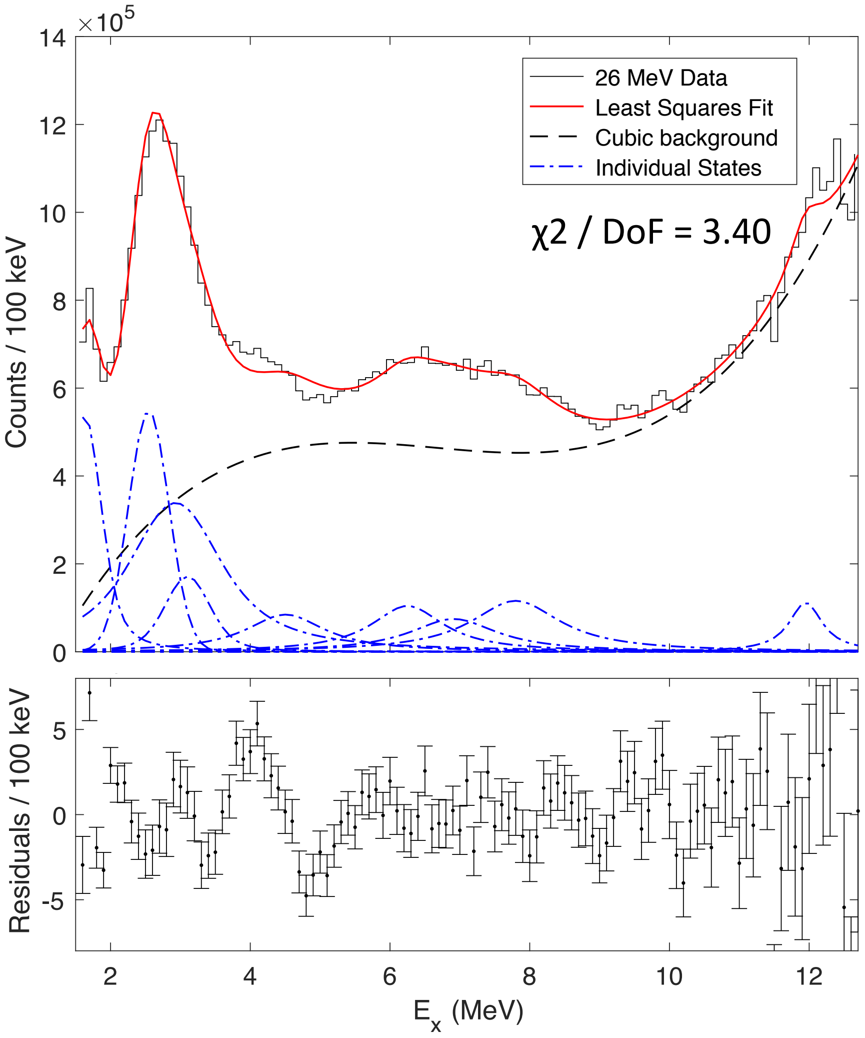

Figure 4.44: Fit of the known levels in ^{9}Be to the 26 MeV beam energy excitation spectrum. The lower panel shows the fit residuals, indicating an extra feature in the 4 MeV region.

The centroids and natural widths of each state were varied near to the tabulated experimental values [52]. The centroids were varied by ≈100 keV about the tabulated values. The widths, which were often poorly constrained by previous experiments, were permitted to vary within their previous experimental uncertainties [52]. The amplitudes of each peak were varied as free fitting parameters along with the width of the broad resonance at 7.9 MeV (tentative width assignment ≈1 MeV). The experimental resolution for each state was determined through figures 4.37 and 4.38, and was allowed to vary within the fit uncertainty.

The 26 MeV beam energy data required a cubic background to minimise χ^2 and the 22 MeV data were fit with a quadratic background. These backgrounds account for contributions from the contaminant ^{9}Be(^{4}He,^{12}C)n reaction that were not removed by the software cut to the Dalitz plot in figure 4.29. The differing background profiles are justified by considering the states in ^{12}C which are energetically accessible through the contaminant reaction at each beam energy. States in ^{12}C up to ≈25 MeV may be populated with the 26 MeV beam energy. Similarly, the lower beam energy may populate states up to ≈21 MeV. According to the Dalitz plot in figure 4.29, the highest energetically accessible levels in ^{12}C manifest at low ^{9}Be excitations. Between 20 and 25 MeV there is a particularly high density of 1^{-} and 3^{-} natural parity levels [107]. Since these levels are more accessible at the 26 MeV beam energy, they are more likely to contribute to the background of this excitation spectrum. Therefore, a background profile with a higher yield at lower ^{9}Be energies is required here. The cubic background provides this.

The fitted excitation spectra with the background profiles subtracted, are shown in figures 4.45 to 4.46.

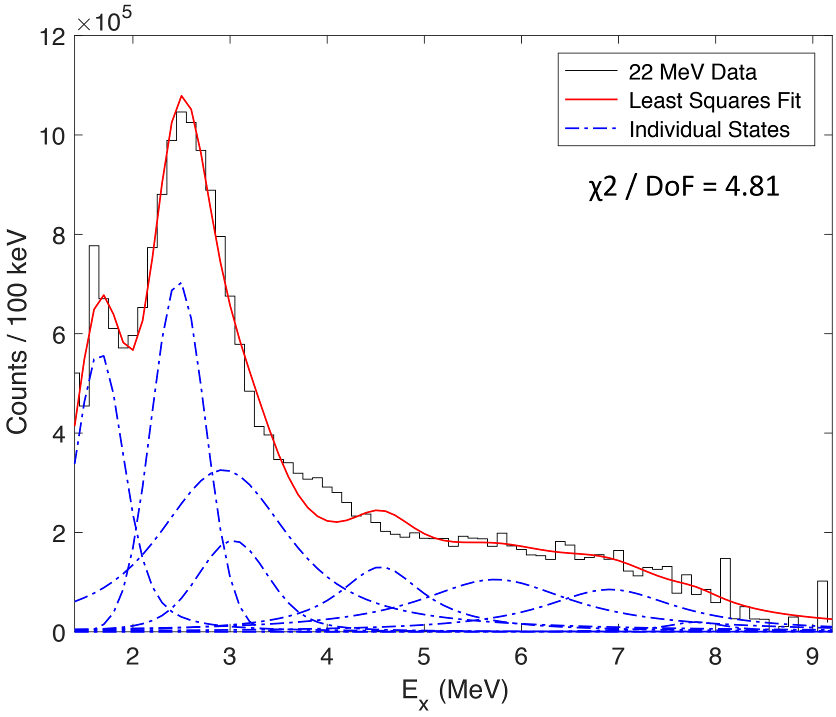

Figure 4.45: Fit of the known levels in ^{9}Be to the 22 MeV beam energy excitation spectrum, with the modelled quadratic background profile subtracted.

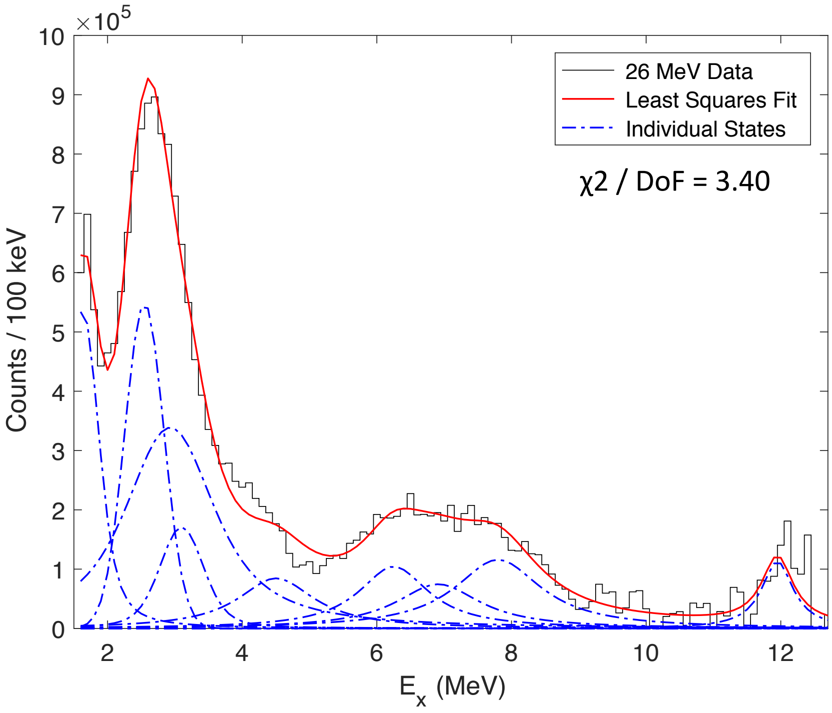

Figure 4.46: Fit of the known levels in ^{9}Be to the 26 MeV beam energy excitation spectrum, with the modelled cubic background profile subtracted.

For both spectra, the fit is particularly poor in the region of 4 MeV, which is reflected in the high values of χ^2 shown on figures 4.43 and 4.44. The residual plots in figures 4.43 and 4.44 both indicate the possibility of an extra feature around this energy. The position and width of the feature in the residual plots is approximately consistent between the two fits. This is not the first time an unknown feature has been noticed in this excitation region of ^{9}Be. High-energy neutron removal from ^{10}Be provided an increased yield around 4 MeV in the resulting ^{9}Be excitation spectrum, though this had too few counts to make any conclusions about its origin [108]. In addition, inelastic scattering of ^{6}Li from ^{9}Be populated a 4 MeV feature in the resulting excitation spectrum, which could not be reproduced by the known ^{9}Be states [100]. The present experiment has the possibility to explore the origin of this feature.

It was proposed that the feature may be adequately explained by a new, undocumented resonance in the ^{9}Be spectrum. This assertion was partly due to the consistent systematics shown in each of the residual plots, and partly due to two recent measurements of a state at similar excitation in the ^{9}B nucleus [65, 66]; the mirror to ^{9}Be. This state in ^{9}B was populated through the ^{9}Be(^{3}He,t)^{9}B reaction. This possibility was explored by introducing an additional broad resonance to the fitting routine and refitting the present data. The additional state was initially chosen to be at 4 MeV with a total width $\Gamma = 1.5$ MeV. These initial parameters were based on the behaviour of the fit residuals in figures 4.43 and 4.44, and the properties of the possible mirror analogue state in ^{9}B. The energy, width and amplitude of the resonance were allowed to vary freely during the χ^2 minimisation. The resulting fits with the inclusion of a new resonance are shown in figures 4.47 and 4.48.

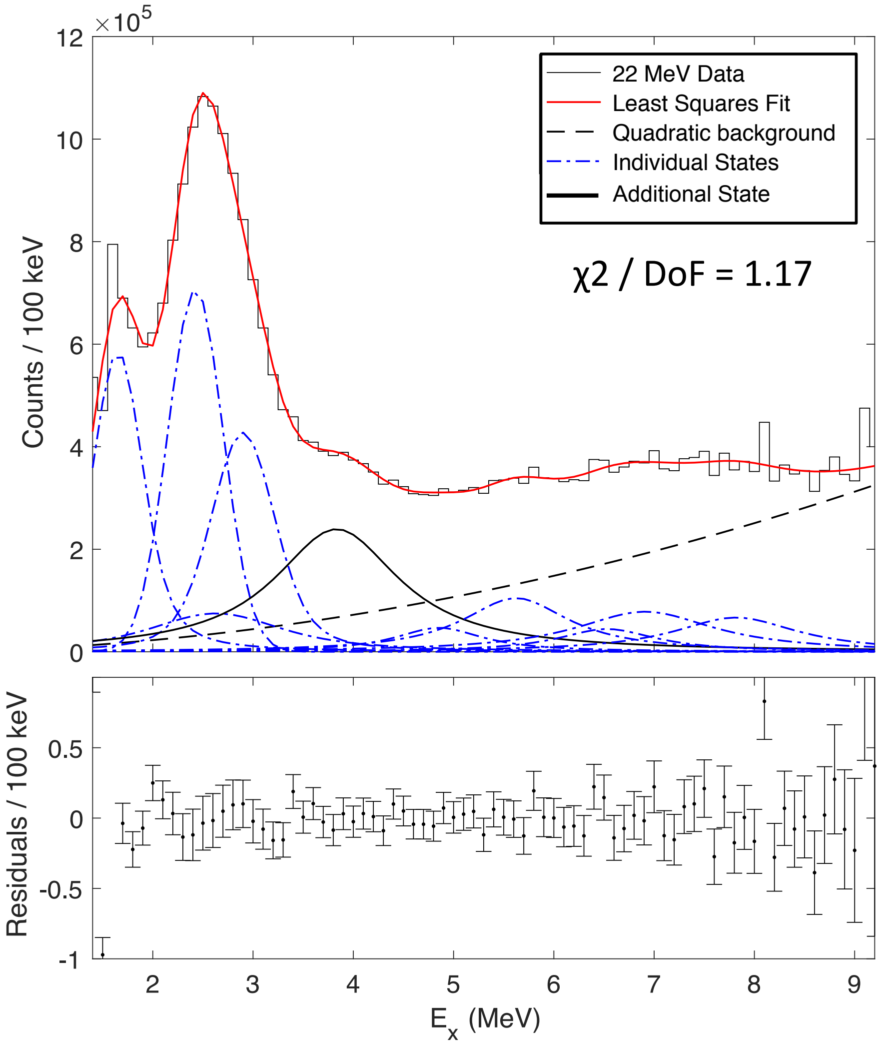

Figure 4.47: Fit of the known levels in ^{9}Be, and a new level at 3.8 MeV, to the 22 MeV beam energy excitation spectrum. The lower panel shows the fit residuals. See text for details.

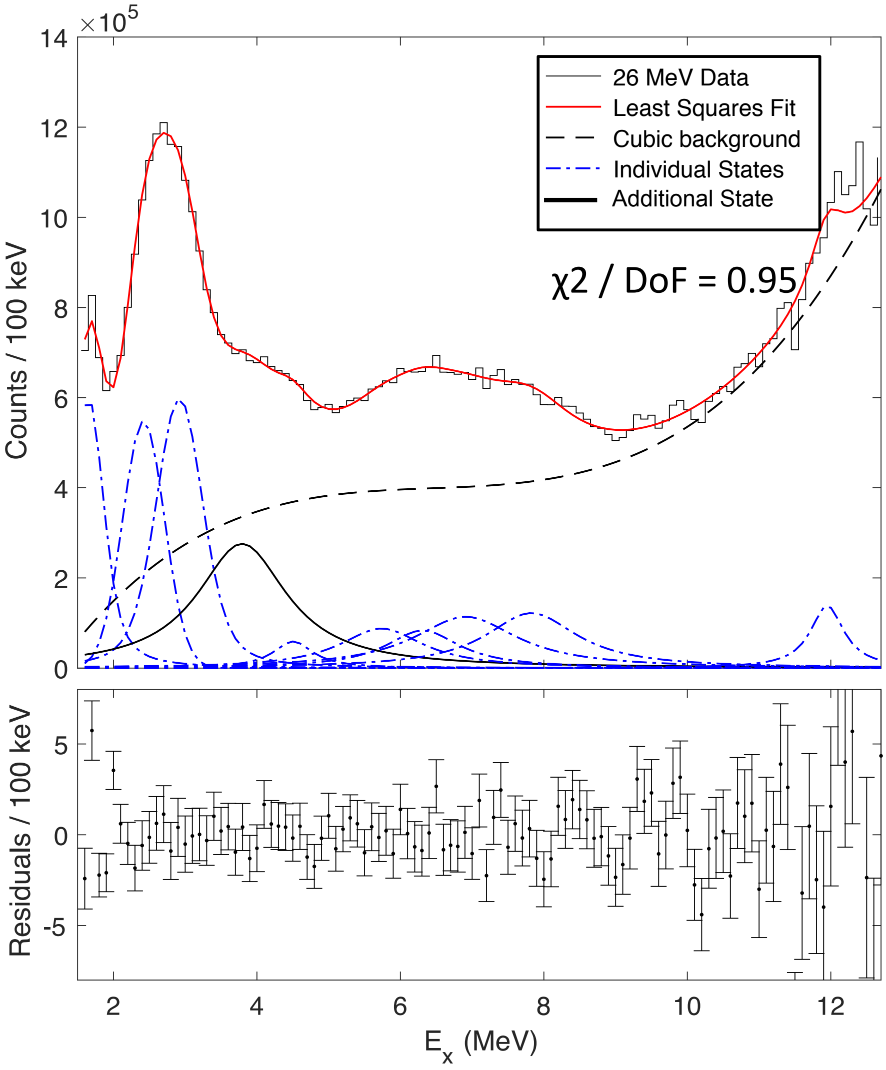

Figure 4.48: Fit of the known levels in ^{9}Be, and a new level at 3.8 MeV, to the 26 MeV beam energy excitation spectrum. The lower panel shows the fit residuals. See text for details

When including the additional state, χ^2 per degree of freedom for the fits were reduced (from 4.81 to 1.17 for the 22 MeV data and from 3.40 to 0.95 for the 26 MeV data). Consistent populations of each state are seen across both data sets, indicating that the background profiles are realistic. The parameters of the additional resonance are also consistent within uncertainties. For the 22 MeV data: $E_x = 3.83^{+0.09}_{-0.10}$ MeV and $\Gamma = 1240^{+366}_{-100}$ keV. For the 26 MeV data: $E_x = 3.79^{+0.14}_{-0.21}$ MeV and $\Gamma = 1250^{+390}_{-190}$ keV. If the feature was due to a contaminant reaction channel, like those discussed in section 4.3.8, simulations demonstrated that it would move in excitation between the two beam energies. This is strong evidence that the feature is really a part of the ^{9}Be spectrum. Figures 4.49 and 4.50 show the fits with the background profiles subtracted.

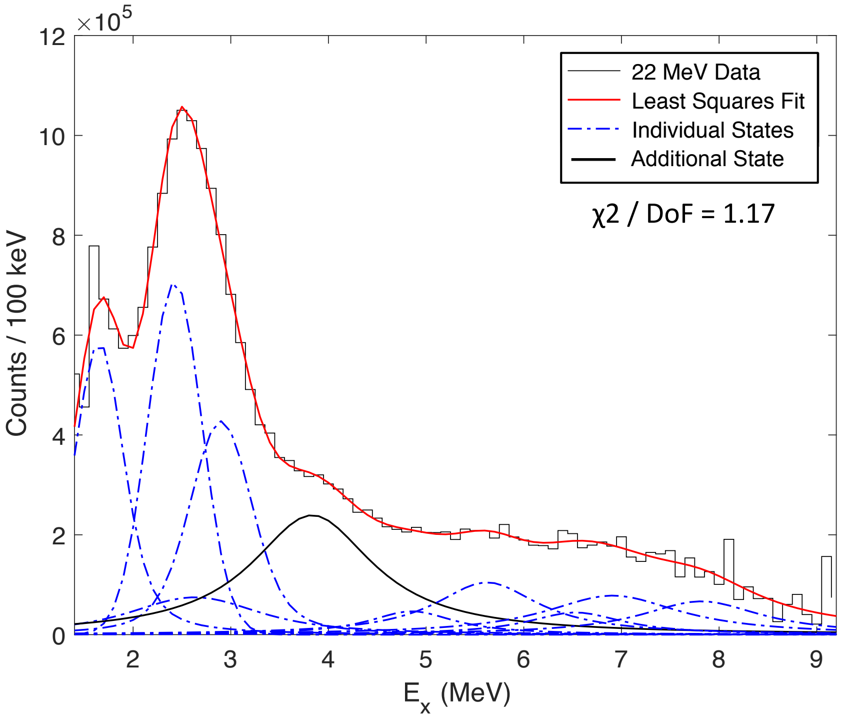

Figure 4.49: Fit of the known levels in ^{9}Be, and a new level at 3.8 MeV, to the 22 MeV beam energy excitation spectrum, with the modelled quadratic background profile subtracted.

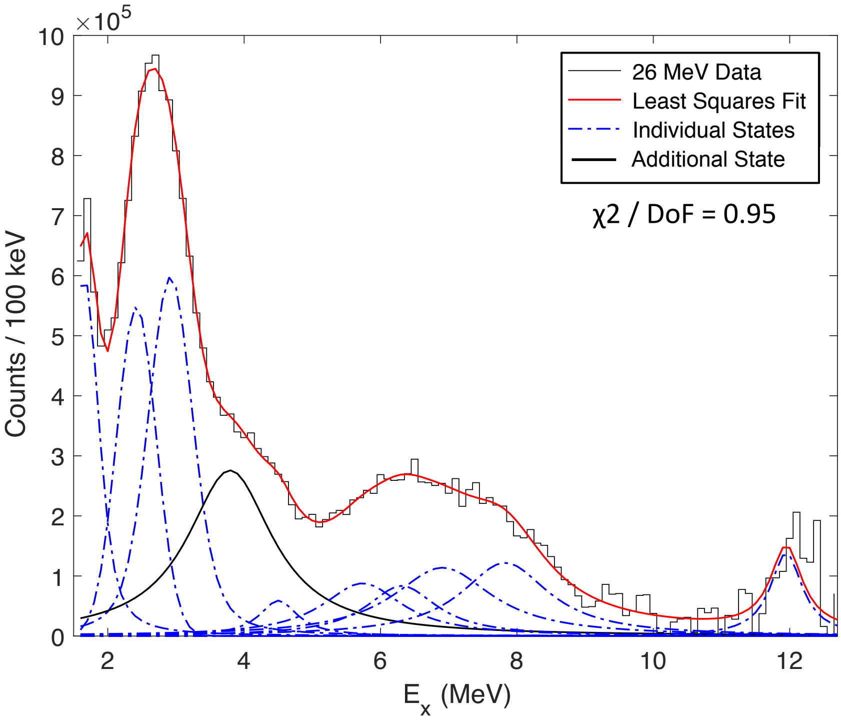

Figure 4.50: Fit of the known levels in ^{9}Be, and a new level at 3.8 MeV, to the 26 MeV beam energy excitation spectrum, with the modelled cubic background profile subtracted.

The quoted uncertainties on the fit parameters were evaluated numerically. The parameter of choice was fixed to values close to the optimal value, and the data were refit. The value of χ^2 was then tracked as a function of the value of the parameter. The upper and lower errors were defined by the value of the parameter, which resulted in a change in the χ^2 value of 1 [109]. The variation of χ^2 as a function of the energy and width of the extra level are shown in figure 4.51 for each beam run.

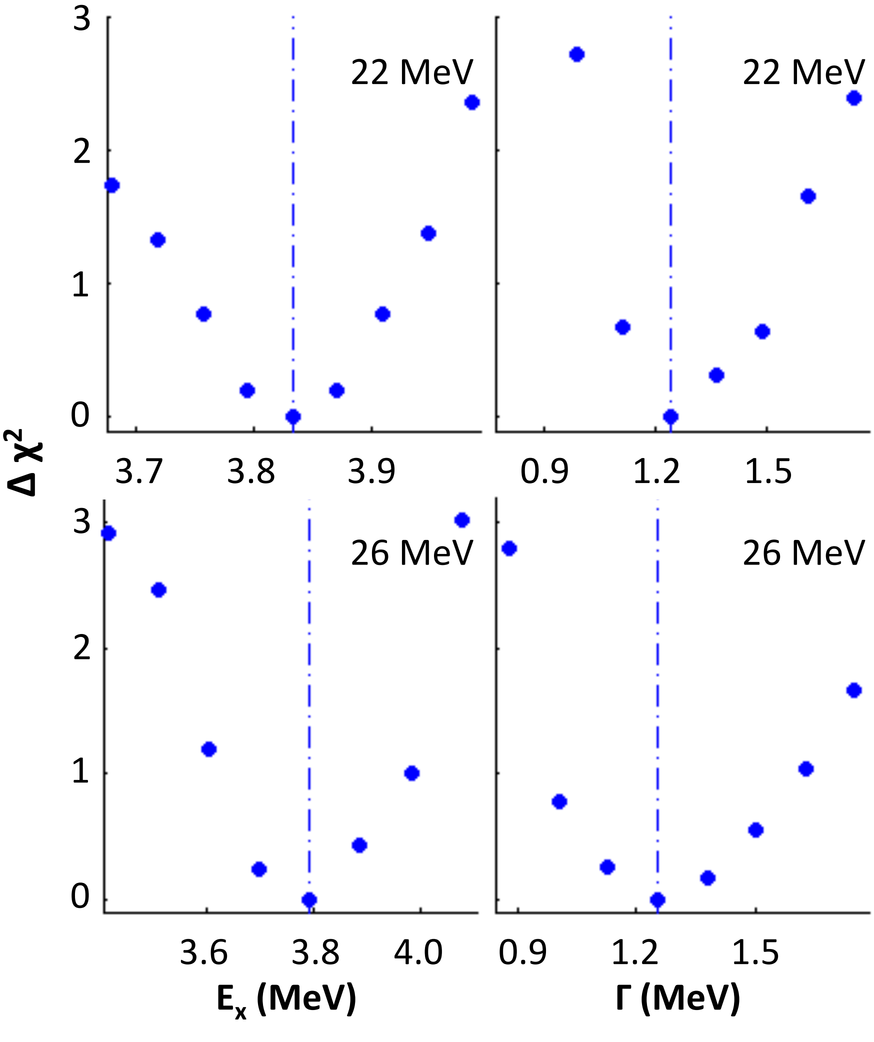

Figure 4.51: The change in the value of χ^2 for the fits, as the value of the energy and width of the state are varied close to their optimal values.

4.4.3 Reduced width calculations

The following section is adapted from the analysis in reference [74]. As discussed in section 4.1.5, it is insightful to compare the measured excitation spectrum of ^{9}Be with that of the mirror nucleus, ^{9}B. The potential mirror analogue states in these nuclei were shown in table 4.1. Up to around 3 MeV, J^{π} assignments allow a clear comparison between these nuclei. Below 12 MeV, the only other state in ^{9}B with a firm J^{π} assignment is the 6.97 MeV $7/2^{-}$ level. Between 3 and 7 MeV, a 4.3 MeV level in ^{9}B may possibly be the mirror analogue for the 4.7 MeV level in ^{9}Be. Additionally, the newly-measured ^{9}B level at 3.9 MeV [65, 66] could be the mirror analogue of the 3.82 MeV state measured by the current experiment. Due to the complexities in calculating the Coulomb energy differences between mirror analogue states, detailed in section 4.1.5, it is difficult to make confident comparisons without firm J^{π} assignments for the states.

Due to the experimental set-up and reaction, it was not straight-forward to perform an angular distribution analysis for the newly-measured state. However, some information about the J^{π} of the state can be obtained if it is assumed that it is the mirror analogue of the 3.9 MeV level in ^{9}B. The reduced width, γ_c^2, of a decay channel, c, is related to the channel partial width, Γ_c, and the decay penetrability, $P_{\ell c}$, by

$$\gamma_c^2 = \frac{\Gamma_c}{2P_{\ell c}}. \tag{4.27}$$

The reduced width of a state is often compared with the Wigner single-particle limit, γ_{w}^2, which is theoretically the largest allowed reduced width [42]. This corresponds to total preformation of the ejectile in the decaying nucleus. Therefore, a ratio of the reduced widths to the Wigner limit ($\theta^2 = \gamma^2/\gamma_{\mathrm{w}}^2$) should not exceed a value of 1.

The partial widths of states in mirror nuclei have been successfully calculated in the past by assuming that the ratio of the reduced widths to the Wigner limit ($\theta^2 = \gamma^2/\gamma_{\mathrm{w}}^2$) are equal between mirror analogue states [78]. This comparison was used in the present study to determine if the measured widths of the 3.8/3.9 MeV states in ^{9}Be/^{9}B are consistent with a decay of a particular orbital angular momentum ℓ. The methodology is pictured in figure 4.52. This allowed limits to be placed on the J^π of these levels, assuming that they are mirror analogues.

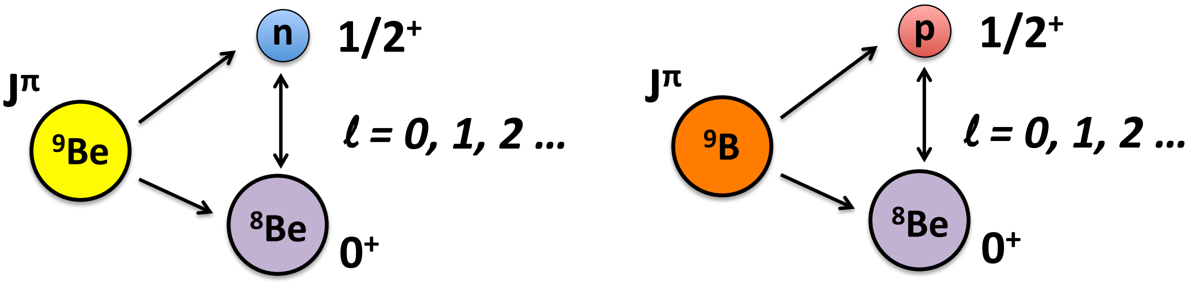

Figure 4.52: Reduced-width-to-Wigner-limit ratios (θ^2) were calculated for the two decay scenarios shown, for various values of orbital angular momentum ℓ. Each ℓ would correspond to the decay of a state in ^{9}Be/^{9}B of a particular J^π. If consistent θ^2 values are calculated for both nuclei, for a particular ℓ, limits on J^π can be inferred.

Testing on a known mirror analogue pair

To test this method, it was applied to the $^8\mathrm{Be}_{\mathrm{g.s.}} + n/p$ decay of the known $5/2^-_1$ ^{9}Be/^{9}B mirror analogue pair. Most states in these nuclei decay most strongly through the $^8\mathrm{Be}_{\mathrm{g.s.}}$ channel, however, this level has been shown to have a large α width in ^{9}B [72, 110]. In contrast, the state in ^{9}Be decays predominantly through the low-energy tail of the $^8\mathrm{Be}_{2^+}$ first excited state [99, 100]. Both states have a relatively small width for decays through the $^8\mathrm{Be}_{\mathrm{g.s.}}$. In these previous studies it was found that $\Gamma_{^8\mathrm{Be}_{\mathrm{g.s.}}}/\Gamma_{\mathrm{tot}} = 1.8(2)\%$ or $1.6(8)\%$ for ^{9}B and $6(1)\%$ or $11(2)\%$ for ^{9}Be [72, 99, 100, 110].

The decay penetrabilities and reduced widths were evaluated using the `ckin` code [111]. Using the energies and total widths of the $5/2^-_1$ states along with their branching ratios, the $^8\mathrm{Be}_{\mathrm{g.s.}}$ partial widths were calculated. The decay penetrability was then calculated for a number of values of the decay angular momentum, ℓ, using equation 3.11 in section 3.2. The `ckin` code utilises the Cern Libraries WCLBES code [112, 113] to calculate the regular and irregular Coulomb wave functions needed to evaluate equation 3.11. The reduced widths were calculated for various values of ℓ using equation 4.27 and the results are given in table 4.2.

ℓ	θ^2 (^{9}B)	θ^2 (^{9}Be)
0	$1.7^{+3.3}_{-1.0}\ \times10^{-4}$	$9.1^{+1.1}_{-3.7}\ \times10^{-6}$
1	$3.0^{+0.6}_{-1.8}\ \times10^{-4}$	$2.5^{+2.9}_{-1.0}\ \times10^{-5}$
2	$1.3^{+0.2}_{-0.7}\ \times10^{-3}$	$3.0^{+3.5}_{-1.2}\ \times10^{-4}$
3	$1.5^{+0.3}_{-0.9}\ \times10^{-2}$	$1.2^{+1.4}_{-0.5}\ \times10^{-2}$
4	$0.36^{+0.07}_{-0.21}$	$0.97^{+1.14}_{-0.40}$

Table 4.2: Calculation of $\theta^2 = \gamma^2/\gamma^2_{\rm w}$ for the ^{8}Be$_{\rm g.s.}$ + n/p decay channel of the $5/2^-_1$ state.

Cases of $\ell > 4$ are not given in the table, since the reduced widths exceed the Wigner limit ($\theta^2 > 1$). For an $\ell = 3$ decay, which is expected for this decay channel, the θ^2 values are consistent between the two mirror analogue states. For ^{9}B $\theta^2 = 1.46^{+0.29}_{-0.85}\ \times10^{-2}$ and for ^{9}Be θ^2 $= 1.18^{+1.39}_{-0.48}\ \times10^{-2}$. These are consistent with the known values, within uncertainties. For other values of ℓ, which are incorrect for this decay channel, the θ^2 values differ significantly between the two states. Hence, this demonstrates that the reduced widths for mirror analogue states are consistent.

Application to the new levels

The results when this method was applied to the 3.8/3.9 MeV pair in ^{9}Be/^{9}B are shown in table 4.3. The total widths of these states were measured experimentally, but the branching ratios were not. In order to calculate the partial widths of the ^{8}Be$_{\rm g.s.}$ + n/p channel, the two states were assumed to have the same branching ratio. The few measured branching ratios for known states in the two nuclei suggest that this is a reasonable assumption. Branching ratio measurements are scarce but key states that have received experimental attention show good agreement. As discussed in section 4.4.3, the $5/2^-_1$ states both show a small branching ratio for decays through the ^{8}Be$_{\rm g.s.}$ + n/p channel. Likewise, the mirror analogue $T = 3/2$ states around 15 MeV show similar decay systematics (table 9.4 of Ref. [52]).

The reduced widths were calculated for values of $\Gamma_{^8{\rm Be}_{\rm g.s.}}/\Gamma_{\rm tot}$ = 100%, 50% and 10%. The absolute values of the reduced widths depend on the chosen value of the branching ratio. However, the comparison between the possible mirror analogue states only depends on the assumption that they have the same branching ratio. Under this condition of similar branching ratios between the mirror analogue states, the reduced widths were calculated for various values of the orbital angular momentum, ℓ. When $\theta^2 > 1$, the results are omitted from the table ($\ell > 2$ for BR = 100% and 50% and $\ell > 3$ for BR = 10%).

	ℓ	θ^2 (^{9}B)	θ^2 (^{9}Be)
$\Gamma_{^8\mathrm{Be}_{\mathrm{g.s.}}}/\Gamma_{\mathrm{tot}} = 1$	0	$0.129^{+0.022}_{-0.020}$	$0.122^{+0.030}_{-0.011}$
	1	$0.182^{+0.032}_{-0.029}$	$0.197^{+0.052}_{-0.020}$
	2	$0.467^{+0.094}_{-0.081}$	$0.762^{+0.244}_{-0.101}$
$\Gamma_{^8\mathrm{Be}_{\mathrm{g.s.}}}/\Gamma_{\mathrm{tot}} = 0.5$	0	$0.065^{+0.011}_{-0.010}$	$0.061^{+0.015}_{-0.006}$
	1	$0.091^{+0.016}_{-0.014}$	$0.099^{+0.026}_{-0.010}$
	2	$0.233^{+0.047}_{-0.041}$	$0.381^{+0.122}_{-0.051}$
$\Gamma_{^8\mathrm{Be}_{\mathrm{g.s.}}}/\Gamma_{\mathrm{tot}} = 0.1$	0	$0.013^{+0.002}_{-0.002}$	$0.012^{+0.003}_{-0.001}$
	1	$0.018^{+0.003}_{-0.003}$	$0.020^{+0.005}_{-0.002}$
	2	$0.047^{+0.009}_{-0.008}$	$0.076^{+0.024}_{-0.010}$
	3	$0.291^{+0.069}_{-0.057}$	$0.898^{+0.352}_{-0.155}$

Table 4.3: The reduced-width-to-Wigner-limit ratios ($^8\mathrm{Be}_{\mathrm{g.s.}} + n/p$ channel) for the 3.9 MeV state in ^{9}B and the 3.8 MeV state in ^{9}Be for various values of the branching ratio.

The values of θ^2 are consistent between the two nuclei within the uncertainties, for $\ell = 0$ and $\ell = 1$ decays. If the assumption of similar branching ratios is correct for these two states, then decays through the $^8\mathrm{Be}_{\mathrm{g.s.}} + n/p$ channel are $\ell = 0$ or $\ell = 1$. This restricts the decaying ^{9}Be/^{9}B level to have $J = 1/2$ or $3/2$. Reference [65] also tentatively assigns the parity of the level in ^{9}Be as negative. If correct, this further restricts the value to $\ell = 1$, and corresponds to the decay of a $1/2^-$ or $3/2^-$ state. This conclusion relies heavily on the assumption of similar branching ratios for the possible mirror analogue states and further experimental work is required to determine these quantities. These branching ratios are also required in order to calculate the absolute values of the reduced widths which can be compared with theoretical calculations. Over the whole range of tested branching ratios (from $100\% \geq \Gamma_{^8\mathrm{Be}_{\mathrm{g.s.}}}/\Gamma_{\mathrm{tot}} > 0.5\%$) the decay is restricted to $\ell < 4$ for the reduced width to not exceed the Wigner limit. Therefore, there is strong evidence that these states have $J \leq 7/2$.

4.5 Interpretation of results

As discussed in section 4.1.4, the measured spectrum of ^{9}Be is described by three rotational bands, possibly corresponding to different molecular configurations of the valence neutron. Figure 4.53 shows that similar band structures appear in the ^{9}B mirror. Theoretical models also predict the existence of a missing $J = 3/2^{+}$ level [67]. No-core shell model calculations predict the state to lie somewhere between 3.4−4 MeV. Its exact energy depends on the type of nucleon-nucleon interaction used in the calculations. In the framework of α-clustering, this state would corresponding to a π-antibinding molecular band head [54, 55]. The molecular models predict the state to lie higher in energy than the other band heads.

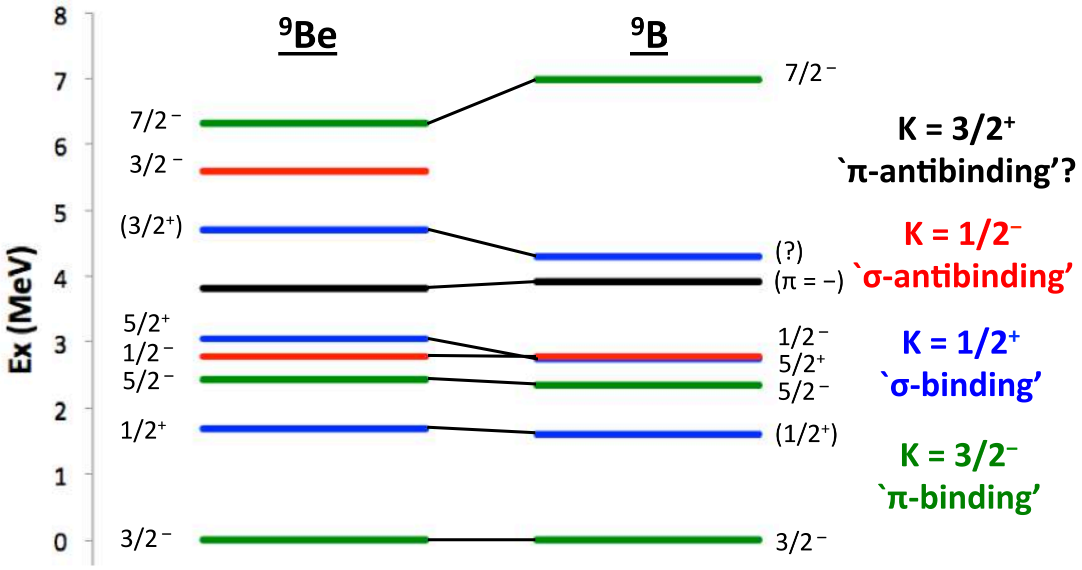

Figure 4.53: The possible rotational bands in the ^{9}Be/^{9}B mirror pair, with the inclusion of the newly measured states near to 4 MeV. Image from reference [114].

The newly-measured state is marked in black on the left hand side of figure 4.53. Indeed, it appears in excitation above the other band heads and at an energy consistent with the no-core shell model calculations of reference [67]. The reduced width comparison in the preceding section suggested that the decay of the new level through $^{8}\mathrm{Be}_{\mathrm{g.s.}} + n/p$ is characterised by $\ell = 0$ or 1, which is consistent with $J = 3/2$. A firm limit of $J < 7/2$ was placed on the state to ensure that its reduced width did not exceed the theoretical Wigner limit. Therefore, it is possible that the newly-measured level corresponds to the $J = 3/2^{+}$ molecular band head. However, the proposed mirror analogue state in ^{9}B has a tentative negative parity assignment, which does not support this claim.

The reduced width analysis made the clear assumption that the levels in ^{9}Be and ^{9}B were mirror analogue states. This assumption was based on their close proximity in energy alone, since no reliable J^{π} assignments exist for these levels. This assumption is not unreasonable given the low density of unassigned levels in this region and due to the fact that Coulomb energy differences are typically around 100 keV [73]. However, the origins of mirror energy differences are quite complicated, and it is possible that this pairing is incorrect. Assuming that the newly-measured 3.8 MeV level in ^{9}Be and the 3.9 MeV level in ^{9}B are mirror analogue states, insights into their structure could be learned from the difference in their excitation energies with respect to each of the ground states. However, to make a quantitative comparison with the precise magnitude of this shift and the structure described by the underlying wave functions, more theoretical input is needed.

4.6 Outlook

Given the previous discussion, it is clear that measurements of the branching ratios for the proposed 3.8/3.9 MeV mirror pair are required to add credence to the proposal that they correspond to the π-antibinding molecular band heads. The analysis currently relies on the assumption of similar branching ratios between the two states, which may not be true. The ambiguity surrounding the origin of the three final state α-particles in this experiment meant that only the $^{8}\mathrm{Be}_{\mathrm{g.s.}} + n/p$ channel could be examined. Selecting events where a pair of α-particles originated from the decay of ^{8}Be cleanly tagged the third α-particle as the scattered beam. Using a different beam such as ^{3}He in conjunction with particle identification capabilities would in principle make it clear which final-state charged particle is the scattered beam, and which result from the ^{9}Be break-up. The $\Gamma_{^{8}\mathrm{Be}_{\mathrm{g.s.}}}/\Gamma_{\mathrm{tot}}$ branching ratio could then be evaluated. Measuring the branching ratios for other decay channels would also be insightful. However, as references [100] and [99] note, the $^{8}\mathrm{Be}_{2^{+}}$ and $^{5}\mathrm{He}_{\mathrm{g.s.}}$ channels have strongly overlapping signatures for low energy states in ^{9}Be, which hinders such an evaluation.

Another promising avenue would be to examine the excited states of ^{9}Be populated through a reaction other than direct inelastic scattering. Reference [115] examined states in ^{16}O through the $^{13}\mathrm{C}(^{4}\mathrm{He},^{16}\mathrm{O})n$ reaction. As part of this experiment, there is evidence for the $^{13}\mathrm{C}(^{4}\mathrm{He},^{9}\mathrm{Be})2\alpha$ reaction as demonstrated by the ^{9}Be excitation spectrum shown by figure 4.54. This can correspond to inelastic scattering from ^{13}C, populating excited states in this nucleus. These then α-decay, populating states in ^{9}Be. By examining the excitation spectrum of ^{9}Be resulting from decays of states of particular J^{π} in ^{13}C, and noting the relative intensities of the ^{9}Be states populated, the angular momenta of the states may be inferred due to the different centrifugal barriers. For example, a $5/2^{-}$ state in ^{13}C will more readily decay to a $5/2^{-}$ state in ^{9}Be since there is no centrifugal barrier. Decays to a $1/2^{+}$ state in ^{9}Be would be suppressed due to the additional angular momentum barrier. If the 3.8 MeV state in ^{9}Be was recorded during this experiment, more strict limits on its J^{π} may be obtained. The data from reference [115] have been obtained and the analysis is ongoing.

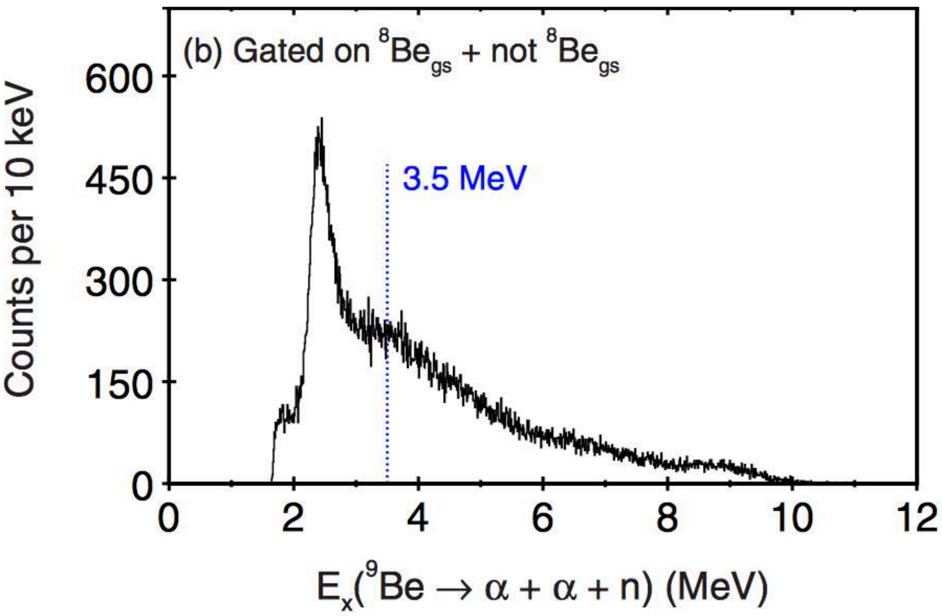

Figure 4.54: Excitation spectrum of ^{9}Be reconstructed from the decay of ^{13}C. Image adapted from reference [115].

Chapter 5

Investigating the 3α break-up modes of the ^{12}C Hoyle state

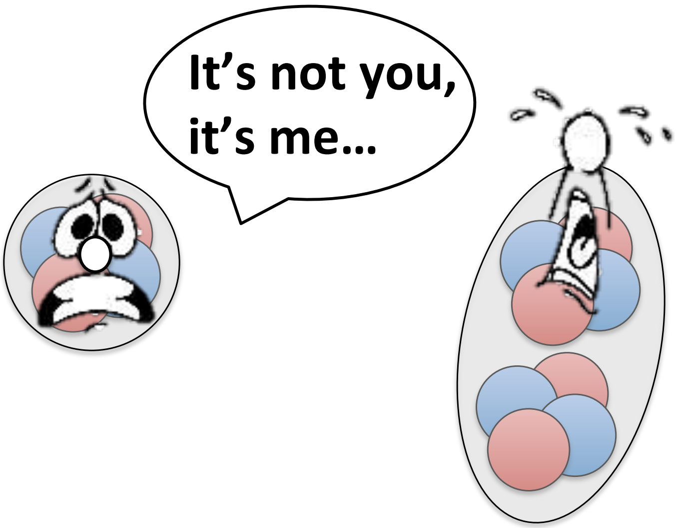

Chapter Abstract

The Hoyle state in ^{12}C is a crucial resonance in nuclear astrophysics since it enhances stellar helium burning through the triple-α process by over seven orders of magnitude. It is also interesting from a nuclear structure perspective, since the dominant degrees of freedom of this nucleus are those of α-particle clusters rather than individual nucleons. With this in mind, the Hoyle state may possess a number of interesting intrinsic structures, corresponding to different geometric configurations of its constituent α-particles. Indeed, theoretical calculations predict a myriad of possibilities, which are often in disagreement with one another. Due to challenges in experimentally confirming the structures of unbound nuclear states, insights into the structure of the Hoyle state have been based on indirect evidence. Recently there have been a number of experiments dedicated to measuring the rare direct decay of the Hoyle state into three α-particles, since this observable could be a direct and sensitive probe of its 3α structure. However, previous experiments have not been sensitive enough to measure this decay channel, which is severely hindered by the available phase space. This chapter presents a high-precision measurement of the 3α decay of the Hoyle state using the ^{12}C(α,α)3α inelastic scattering reaction at 40 MeV beam energy. The reaction products were measured using a bespoke array of double-sided silicon strip detectors and the experimental data were compared to Monte-Carlo simulations of sequential and direct decay mechanisms. No direct decays were observed, but an upper limit for the direct decay branch of 0.047% was obtained − almost one order of magnitude lower than previous experimental efforts. This value is lower than a number of theoretical estimates and opens new intriguing questions about the structure of this state.

This work has been published in the following article. Some figures and text blocks from this publication are used in the following chapter.

R. Smith, Tz. Kokalova, et al. *New Measurement of the Direct 3α Decay from the* ^{12}*C Hoyle State*, Phys. Rev. Lett. **119** (2017).

5.1 Introduction

Few nuclei have received as much attention throughout the history of nuclear physics as carbon-12. Carbon, (named from Latin: *carbo* “coal”) is the principal component of organic molecules, meaning that it is key to life as we know it, and in coal has driven our society through the industrial revolution and beyond.

In these contexts, carbon is important due to its unique *chemical* structure. Each carbon atom can form stable bonds with up to four other atoms at a time [116] (usually oxygen, hydrogen, nitrogen, sulphur and phosphorus). Similar to other non-metals, carbon needs eight electrons to fill its valence shell. Therefore, each of its four valence electrons participate in bonding, meaning that a carbon atom’s bonds will be distributed evenly over its surface. These bonds form a tetrahedron as illustrated in figure 5.1. A huge variety of *organic* molecules can be built from carbon atoms; no other element comes remotely close. Some examples of organic molecules are shown in figure 5.1. Importantly, carbon can also bond with other carbon atoms to form chains, which are almost unlimited in length. This property allows the production of carbon nanotubes and graphene [117, 118], which both possess unusual properties and have a great many applications.

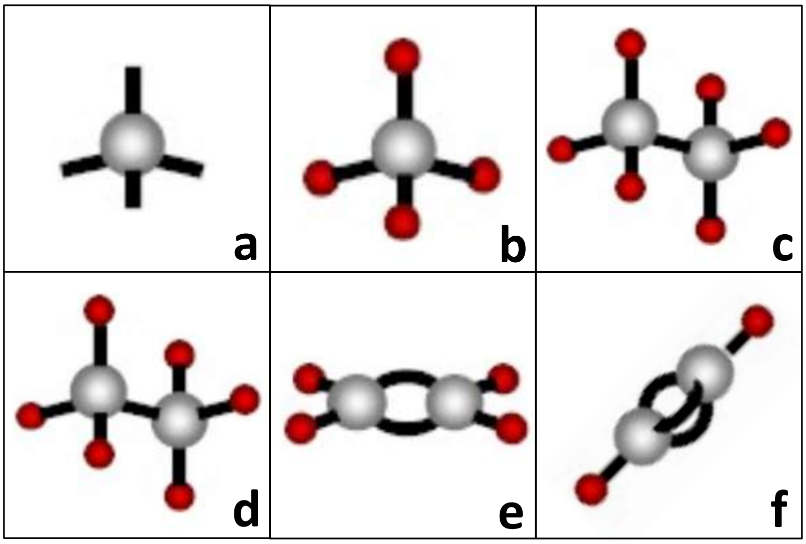

Figure 5.1: Organic molecules: a) carbon tetrahedral bonds b) methane c) ethane. Various carbon-carbon bonds: d) single bonding e) double bonding f) triple bonding. Images adapted from reference [119].

Given its key role in our lives, and its abundance on Earth, one might expect that carbon is readily produced in the universe, through a fairly robust process. In fact, the opposite is the case; carbon would not exist in such vast quantities without an unusual feature of its *nuclear*, rather than chemical, structure, the former of which is not yet fully understood [120].

After the big bang, the table of nuclear isotopes was sparse. The theory of Big Bang Nucleosynthesis predicts that the mass of the universe is mainly hydrogen, followed by roughly 25% helium, around 0.01% deuterium, and even smaller quantities of lithium and beryllium [121]. Figure 5.2 shows the main nuclear reaction chain for Big Bang Nucleosynthesis. To consider how heavier elements are produced, we must focus our attention to stellar nucleosynthesis.

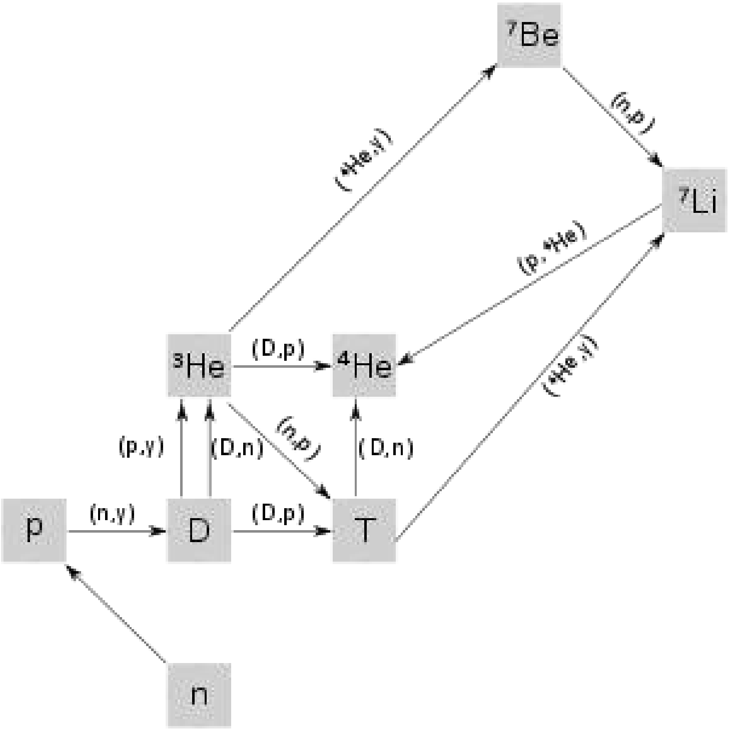

Figure 5.2: The proposed nuclear reaction chain for Big Bang Nucleosynthesis. Image from reference [122].

The majority of stars in our galaxy are *main sequence* stars, which are defined by the fact that they fuse the abundant hydrogen into helium, to produce thermal energy through a variety of different cycles. The most common, corresponding to stars below around 1.5 solar masses and temperatures below 1.8×10^7 K, is the proton-proton cycle. After the hydrogen fuel has been consumed, the star undergoes a structural change and evolves away from the main sequence.

Depending on its mass, the star may evolve into a red giant stage. Here, the temperature in the core increases to around 10^8 K, meaning that the thermal energies of the helium nuclei are high enough to begin fusing to form heavier elements. However, a bottleneck, which suppresses the production of heavier nuclei is quickly met due to the fact that there are no stable A = 5 or 8 nuclei. The predominant ^{4}He + ^{4}He and ^{1}H + ^{4}He fusion reactions are therefore ineffective. The $^2\text{H} + ^4\text{He} \rightarrow ^6\text{Li} + \gamma$ and $^3\text{H} + ^4\text{He} \rightarrow ^7\text{Li} + \gamma$ reactions do contribute, but the low densities of deuterium and tritium mean that these are not significant.

In order to overcome this bottleneck, ^{12}C is produced through the triple-α process [123, 124], which is depicted pictorially in figure 5.3. In this process, two ^{4}He nuclei fuse to form ^{8}Be. With a lifetime of 10^{-16} s, ^{8}Be is unstable to α-decay. The continuous production and decay of ^{8}Be leads to an equilibrium concentration of this nucleus in the core of the star. With a small probability, the ^{8}Be may then scatter from a third ^{4}He, populating the continuum of the compound nucleus ^{12}C, just above the 3α threshold (7.27 MeV). This is then followed by an electromagnetic decay to the ^{12}C ground state [125]. Sir Fred Hoyle recognised the need for a resonance near the threshold energy in ^{12}C in order to boost this process by a factor of 10^{7-8} [126, 127]. This was needed to explain the excess abundance of ^{12}C in the universe and the observed ratio of the ^{12}C to ^{16}O. An s-wave capture of the third ^{4}He results in the lowest potential barrier, so it was proposed that this state had $J^\pi = 0^+$.

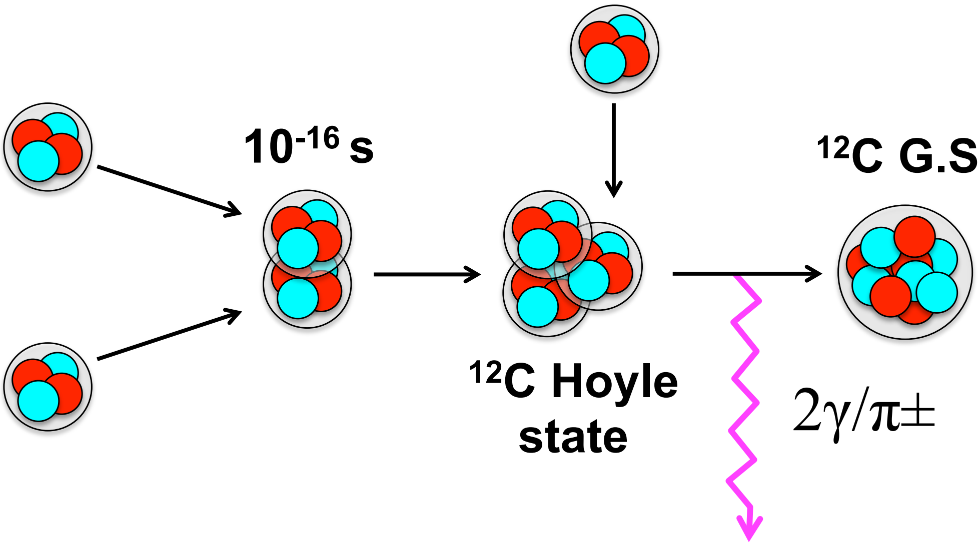

Figure 5.3: Triple-α process: The sequential capture of three α-particles to form ^{12}C in its ground state.

The energy of the Hoyle state was measured around the same time as Hoyle's assertion [128], partly due to his insistence when working as a visiting academic at Caltech. Its angular momentum and parity were confirmed shortly later [129]. However, a state around the correct energy in ^{12}C was measured several years earlier [130]. It has been suggested that Hoyle's prediction of the existence of a 7.65 MeV resonance was an excellent example of the anthropic principle [131]. This principle states that since intelligent life exists, certain properties of the universe must also exist. In other words, the 7.65 MeV resonance in ^{12}C must exist for humans to be comprehending it. Whether Sir Fred Hoyle utilised the anthropic principle to solve the carbon production problem has been the subject of some debate [132]. Nevertheless, the existence of the Hoyle state resonance in ^{12}C just above the 3α threshold is crucial for the development of carbon-based life in the universe.

Despite the success of the Hoyle state in resolving the carbon production problem, a new puzzle emerged. It turns out that it is very difficult to describe the Hoyle state using common models of atomic nuclei, such as the famous, and rather successful, shell model. Owing to its role in nucleosynthesis, it was soon proposed that this state could be described as a system of interacting α-particles, where the degrees of freedom of individual nucleons are not important [133].

Despite 60 years of theoretical and experimental study, the nature of the Hoyle State in ^{12}C has not been well elucidated. Even if the state is α-clustered, what geometric configuration do the α-particles take? Does it exist as a superposition of shell-model-like and α-cluster-like states? Or could the underlying fermionic degrees of freedom of individual nucleons be ignored, opening the possibility that the Hoyle state is the nuclear analogue of a Bose-Einstein condensate? The following pages begin by discussing the role of the Hoyle state in stellar helium burning in more detail. Some theoretical models that are used to describe the structure of the Hoyle state are then discussed, along with their sometimes conflicting conclusions. Ways to experimentally examine the structure of this state are also described, along with the insight that measuring its direct decay could provide. The experiment that was performed to measure the direct decay branch using the ^{12}C(α,α)3α reaction in complete kinematics, is described in detail. The results and implications for the structure of the Hoyle state are then discussed.

5.2 The Hoyle state in stellar nucleosynthesis

The properties of the Hoyle state resonance are crucial for determining the helium burning rates in red giant stars, due to the role it plays in the triple-α process. Salpeter suggested in 1952 that the sequential, rather than simultaneous, capture of three α-particles dominates the reaction rate [134]. This is because the resonance energy of the $^{8}\mathrm{Be}_{\mathrm{g.s.}}$ at 92 keV lies very close to the maximum of the Gamow window for stellar environments with temperatures like in the cores of Red giant stars. The Gamow peak is a convolution of the energy distribution of the particles in the stellar medium, given by the Maxwell Boltzmann distribution, and the quantum mechanical Coulomb barrier transmission probability for the $^{4}\mathrm{He}$ + $^{4}\mathrm{He}$ system. This description of the Gamow window is depicted in figure 5.4. The peak in the Gamow window gives the highest probability for a reaction to take place.

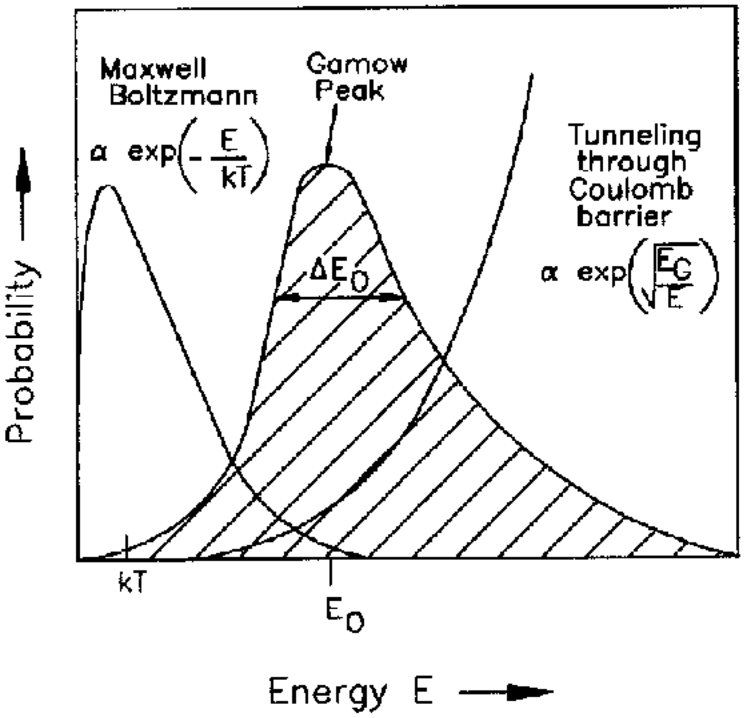

Figure 5.4: Schematic plot of a Gamow peak from reference [135] showing the contributions from the Maxwell Boltzmann distribution of particle energies and the Coulomb barrier tunnelling probability.

The resulting equilibrium abundance of $^{8}\mathrm{Be}$ allows the occasional capture of a third α-particle. Rather than a further decay back to three α-particles, due to the properties of the Hoyle state, a radiative decay to the ground state is enhanced. The rate is calculated as [44]

$$R \propto T^{-3/2} \frac{\Gamma_\alpha \Gamma_{\mathrm{rad.}}}{\Gamma_{\mathrm{tot.}}} \exp^{-E_R/k_B T}. \tag{5.1}$$

The parameters Γ_α and $\Gamma_{\mathrm{rad.}}$ represent the Hoyle state α and combined radiative widths, respectively. The temperature is given by T and the energy of the resonance above the 3α threshold is E_R. The total width of the state, $\Gamma_{\mathrm{tot.}}$, is the sum of all of the partial widths. The above equation assumes that the only contribution to the α width is the $^8\mathrm{Be}_{\mathrm{g.s.}} + \alpha$ channel. However, the width for the direct 3α reaction, $\Gamma_{3\alpha}$, must also be considered. Since the probability of the convergence of three α-particles simultaneously is incredibly small, this channel is unlikely to contribute to the formation of ^{12}C at these temperatures. However, since this direct width contributes to the denominator of the term

$$\frac{\Gamma_\alpha \Gamma_{\mathrm{rad.}}}{\Gamma_{\mathrm{tot.}}} = \frac{\Gamma_{\alpha+{}^8\mathrm{Be}} \Gamma_{\mathrm{rad.}}}{\Gamma_{\alpha+{}^8\mathrm{Be}} + \Gamma_{\mathrm{rad.}} + \Gamma_{3\alpha}}, \tag{5.2}$$

the inclusion of a non-zero direct 3α contribution will decrease the reaction rate. Therefore, a precision measurement of the $\Gamma_{3\alpha}/\Gamma_{\mathrm{tot.}}$ quantity is needed. The triple-α reaction rate is still much debated. A continuum-discretised coupled channel reaction calculation (CDCC) predicted a significantly higher 3α reaction rate below 10^8 K [136]. This calculated that the s-wave resonances in the sequential α capture reactions do not dominate at low T, and that the direct 3α reaction becomes more important. As shall be seen in section 5.5.1, the Coulomb barrier tunnelling probability can be much lower for the simultaneous confluence of three α-particles compared with the sequential capture, and therefore becomes more significant at lower temperatures. Direct reactions at lower temperatures will depend on the value of $\Gamma_{3\alpha}$.

A number of recent experimental studies have measured the direct 3α decay width of the Hoyle state. Raduta *et al.* calculated a 17% direct decay branch [137], which would affect the calculated triple-α reaction rate by several orders of magnitude. Several other studies have placed limits on the direct decay branch at much lower levels, the lowest being 0.2% [138–140]. The experiment presented in this chapter builds on these latter studies.

5.3 Theoretical models of ^{12}C and the Hoyle state

A wide variety of theoretical models have been used to try to understand the structure of ^{12}C. Many of these have been covered in the general introduction to nuclear structure models in section 2. Therefore, rather than providing in-depth explanations of the calculations, this section will review their successes and failures when applied to the ^{12}C nucleus.

5.3.1 Mean field models of ^{12}C

At one end of the spectrum lies the description of the atomic nucleus in terms of a mean field interaction, set up by the presence of all of the nucleons. In typical shell-model calculations, the valence nucleons, which lie above a closed shell, are allowed to interact with one another and dominate the dynamics of the nucleus. The nucleons lying below the shell closure are said to form part of the inert core. As illustrated in figure 5.5 [141], these type of calculations well-reproduce the binding energy of the ground state, and the excitations of the 4.4 MeV 2^+ and 9.6 MeV 3^- levels, suggesting that these states have a similar structure, which is well described by the single-particle picture. On the other hand, the second 0^+ state in these calculations (Hoyle state) is systematically under-bound by several MeV, suggesting that it has a different structure.

The various columns in figure 5.5 compare the experimental levels (leftmost column) with shell-model calculations, which utilise different two nucleon (NN) interactions. They only permit valence nucleons to contribute to the excitation spectrum. Importantly, these calculations are linked by their rather limited shell-model basis. The rightmost column used the Cohen and Kurath (CK) interaction (0*p*-shell) to calculate the positive parity states and the Millener and Curath (MK) interaction (*p*-*s*-*d*-shell) was used for the negative parity states [142]. The calculations of reference [141] use their own derived MK3W interaction using a slightly larger $2\hbar\omega$ and $3\hbar\omega$ model space for the positive and negative parity solutions respectively.

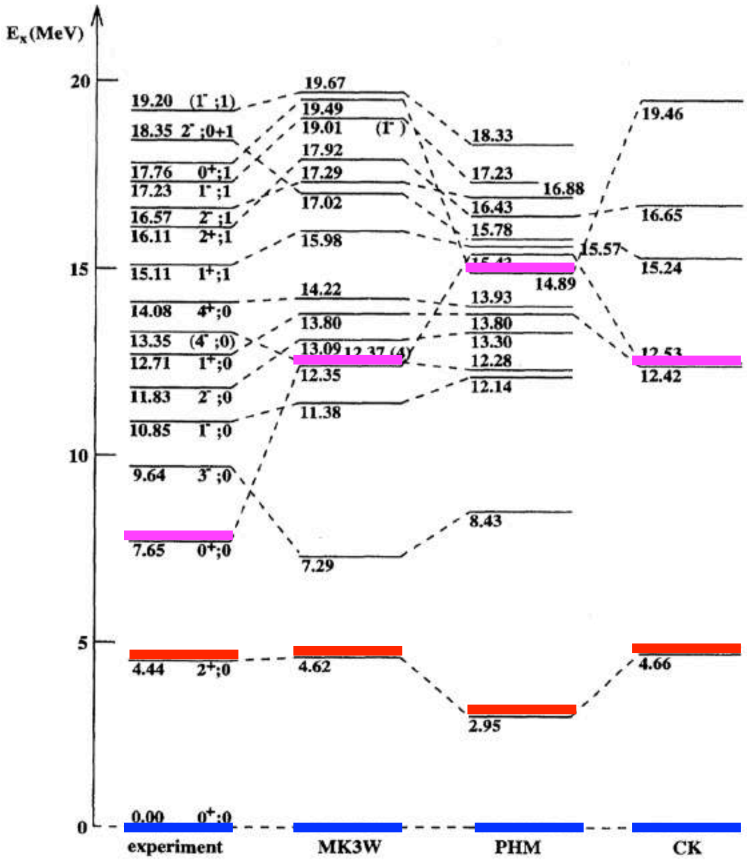

Figure 5.5: The results of mean field calculations of ^{12}C from reference [141]. The experimental levels are given in the leftmost column, and shell-model calculations using the various NN interactions are shown in the remaining three columns. Blue lines show the ground-state energies and the red lines show the energies of the first excited 2^+ state. The magenta lines give the energies of the Hoyle state, which differ significantly between calculations and experiment.

5.3.2 *Ab initio* approaches to ^{12}C

No-Core shell-model

It is unsurprising that normal shell-model calculations do not reproduce the Hoyle state properties. In order to describe the α-cluster picture of the Hoyle state, introduced in section 5.1, a high degree of collectivity in the nucleus must be permitted. If the Hoyle state consists of three α-particles, and its excitations correspond to rotations or vibrations of this deformed object, clearly a *core + valence nucleons* treatment is not sufficient. Computing power has advanced significantly since 1995, when reference [141] was published. It is now possible to solve for the excitation spectra of a nucleus in a fully *ab initio* way, using a shell-model basis where even core nucleons can contribute. These are called *no-core shell-model* calculations. A large number of oscillator shells can be included in the basis space – the best calculations reach N_{max} = 16. Furthermore, realistic nucleon-nucleon and three-nucleon interactions, derived from chiral effective field theory, are now used [3]. By utilising a symmetry-guided shell-model framework, reference [143] successfully reproduce the excitation energy and electromagnetic decay properties of the Hoyle state. Their results are shown in figure 5.6.

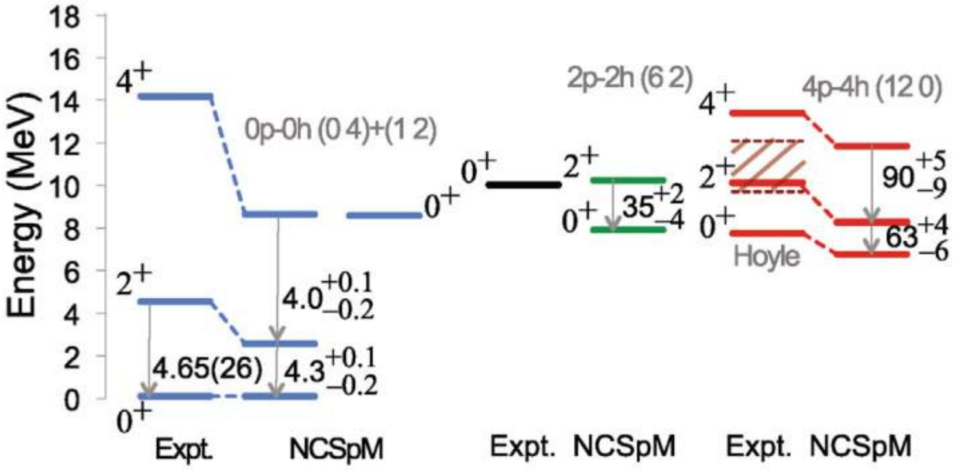

Figure 5.6: The results of no-core symplectic model (NCSpM) calculations utilising a symmetry-guided basis [143].

Lattice Monte-Carlo simulations

A famous calculation of the properties of the Hoyle state was performed using lattice effective field theory [144]. Lattice effective field theory integrates the theoretical framework of chiral effective field theory (EFT) with computationally-intensive lattice simulations. In the calculations, the problem is formulated on a four-dimensional lattice. Space is discretised as a periodic cubic lattice with lattice spacing a and periodic length L (typically 10 fm) and time constitutes the fourth dimension. Nucleons are treated as point-like particles that can only exist on lattice sites, and are permitted to interact due to pion exchange, generated by auxiliary fields (a field whose equations of motion admit a single solution).

The calculation is considered as fully *ab initio* since the inter-nucleon interactions are derived from QCD. As shown in figure 5.7 a), the alpha particles forming the ground state of ^{12}C are arranged in a compact triangle. In figure 5.7 b), for the Hoyle state, they exist in a more spatially-extended 'bent arm' configuration.

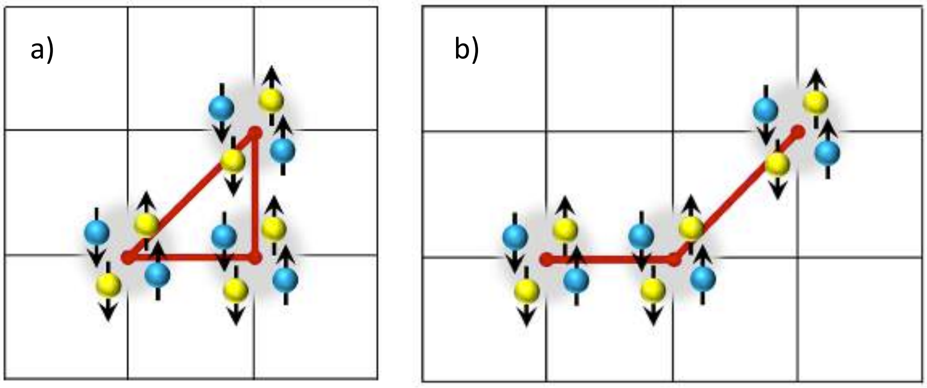

Figure 5.7: The arrangement of the three α-particles in ^{12}C from calculations in reference [144].

5.3.3 Antisymmetrised molecular dynamics (AMD) and fermionic molecular dynamics (FMD)

The approaches of the AMD and FMD calculations make no assumptions about the preformation of α-clusters in nuclei, and in this sense are *ab initio*. However, they use effective NN interactions. The AMD method is reviewed in reference [145]. In the AMD, the individual nucleonic degrees of freedom are explicitly included in the A-nucleon wave function and there are no constraints that α-clusters are formed. The wave functions of individual nucleons are treated as spatially-varying Gaussian wave packets, but with spin and isospin components. The energy of the system is computed using variational methods and an effective NN interaction. This method permits the concurrent calculation of shell-model-like and α-clustered states, allowing the whole spectrum of ^{12}C to be calculated. The AMD model provides a good description of the ^{12}C spectrum as shown in figure 5.8, where the energies of the shell-model-like ground state, first 2^+ state and 3^- state are reproduced equally as well as the clustered Hoyle state.

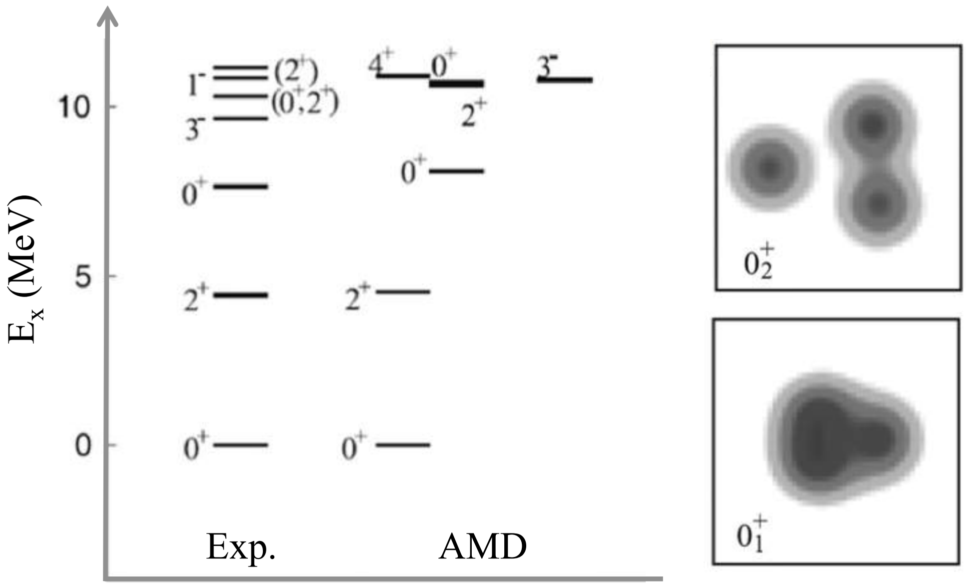

Figure 5.8: The energy levels and intrinsic nucleon densities of ^{12}C predicted by AMD calculations [146].

With the exact wave function of the A-nucleon system being known, it is possible to examine the structure of the calculated nucleus in its *intrinsic* frame. The wave functions resulting from an AMD calculation carry good quantum numbers, in particular, the total angular momentum and parity. It must be considered that the calculated states in the *laboratory* frame are described as an average over all possible orientations of the intrinsic frame. It is possible to break the symmetry and examine the nuclear densities of the calculated states in their intrinsic frames. These are shown for the ground state and 0_2^+ Hoyle state in the right panel of figure 5.8. The ground state is observed to have a compact structure, and the Hoyle state can be seen to possess a more diffuse ^{8}Be + α structure. Indeed, the Hoyle state has been measured to possess a large radius compared with the ^{12}C ground state [147–152].

The formulation of FMD calculations is essentially the same as for the AMD, except for the fact that the width of the Gaussian wave packets, which represent the wave functions of each of the nucleons, are also treated as a variational parameter. Schematically, the results of the AMD and FMD calculations are very similar – the dominant nucleon densities of the Hoyle state indicate a more diffuse structure than the compact ground state [153]. FMD does significantly under-bind the Hoyle state but successfully reproduces the form factor for electron inelastic scattering from the ground state to the Hoyle state [153].

5.3.4 Cluster models and dynamical symmetries

The preceding subsections have described the ^{12}C nucleus on the level of individual nucleons. However, if the Hoyle state is α-clustered, it begs the question as to whether this type of structure may persist throughout the rest of the spectrum. It is also possible that cluster degrees of freedom are important even in the ground state. Therefore, nuclear models that treat ^{12}C as a system of interacting α-particles may form a way to extract some simplicity from this complicated twelve-nucleon system.

The α-cluster model was developed by Brink [154, 155] after having first been put forward by Margenau [156]. Here, α-clusters are assumed to have formed in the nucleus as quartets of protons and neutrons in the $0s$ state. Each cluster is then treated as a Gaussian wave packet with a scalable width, which determines the size of the cluster. The degrees of freedom of the constituent nucleons are ignored, aside from the fact that the whole wave function is antisymmetrised using a Slater determinant, to reflect the underlying fermionic structure. For small separations of the clusters, the antisymmetrisation means that they lose their identities as individual clusters. At large cluster separations, the α-clusters may retain their identity as bosons. Using this basis, the Hamiltonian for the 3α system can be written, by utilising an effective $\alpha - \alpha$ interaction. The optimal arrangement of α-clusters is then found by varying the relative coordinates and the sizes of the clusters to minimise the energy of the system. Using this approach, two energy minima are found; an *equilateral triangle* and a *linear chain* of α-particles.

A more sophisticated approach is to describe the cluster states of ^{12}C in terms of representations of unitary algebras $U(\nu + 1)$, with ν being the number of space degrees of freedom. [157]. In the specific case of a three cluster system, the number of space degrees of freedom, after removing of the centre of mass motion, is 6. The space degrees of freedom can be taken as the Jacobi coordinates of the three α-particles, $\overrightarrow{\rho}$ and $\overrightarrow{\lambda}$, which are defined in reference [157]. This *Algebraic Cluster Model* (ACM) treats the α-particles as bosons, and describes their relative motion using the $U(7)$ spectrum generating algebra, with the condition of $\mathcal{D}_{3h}$ triangular symmetry. This theoretical treatment then allows a Hamiltonian to be constructed, which reflects $U(7)$ dynamical symmetries and can be solved analytically.

The rotation-vibration eigenstates of the 3α system are written as

$$\left|N,(\nu_1,\nu_2^{\ell_2}),K,L^P\right\rangle, \tag{5.3}$$

where N denotes the number of bosons, ν_1 and $\nu_2^{\ell_2}$ denote the type of excitation (*breathing* or *bending* vibration) and ℓ_2 is the angular momentum of the bending vibration. The angular momentum is given by L, its projection onto the symmetry axis by K, and the parity by P. The energy eigenvalues depend on these quantum numbers and are given by the equation in reference [158]. To provide a simple understanding, the picture shown in figure 5.9 demonstrates how the states belonging to the ground state rotational band of ^{12}C can be generated in terms of rigid rotations about the various symmetry axes of an equilateral triangle configuration. The sequence 0^+, 2^+, 4^+ can be generated by rotating the system as shown in the left panel of figure 5.9, giving rise to the $K^\pi = 0^+$ rotational band. The centre panel of figure 5.9 shows that by giving each α-particle one unit of orbital angular momentum, about an axis perpendicular to the plane of the triangle, a 3^- state is generated. As illustrated by the rightmost panel of figure 5.9, the 4^- and 5^- states are a result of superimposing the two types of rotation.

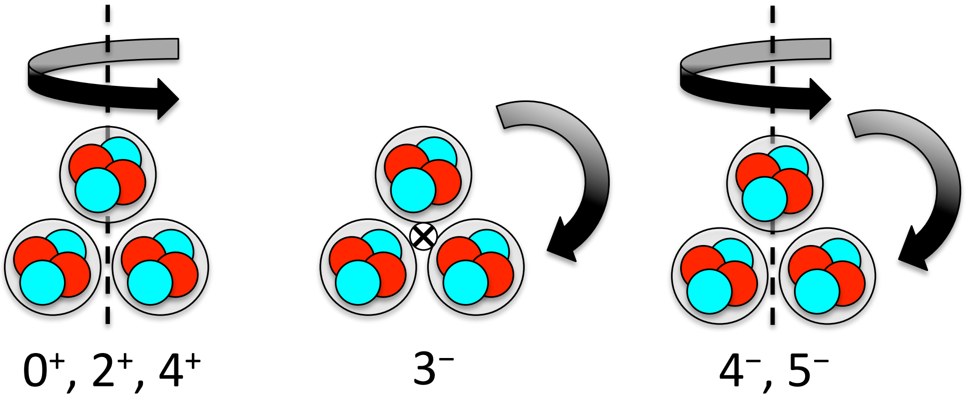

Figure 5.9: Explaining the angular momenta and parities of the ground state rotational band based on an equilateral triangle configuration of α-particles.

The Hoyle state and its rotational excitations are characterised by a 'breathing mode' vibration of the α-particles, illustrated in figure 5.10 a). The 1^- state at higher energy is generated through a 'bending mode' vibration shown in figure 5.10 b).

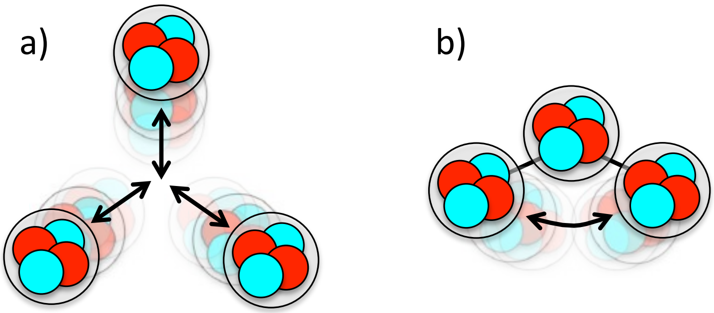

Figure 5.10: The a) *breathing* and b) *bending* mode vibrations that give rise to the 0^+ Hoyle state and the 1^- state in ^{12}C, respectively.

Once again, by rotating these structures in addition to their quantised modes of vibration, more rotational bands can be generated. These are depicted in figure 5.11. The ACM does not predict absolute excitation energies. Instead, the calculated energies were scaled to the experimental data, and are shown by the lines in figure 5.11.

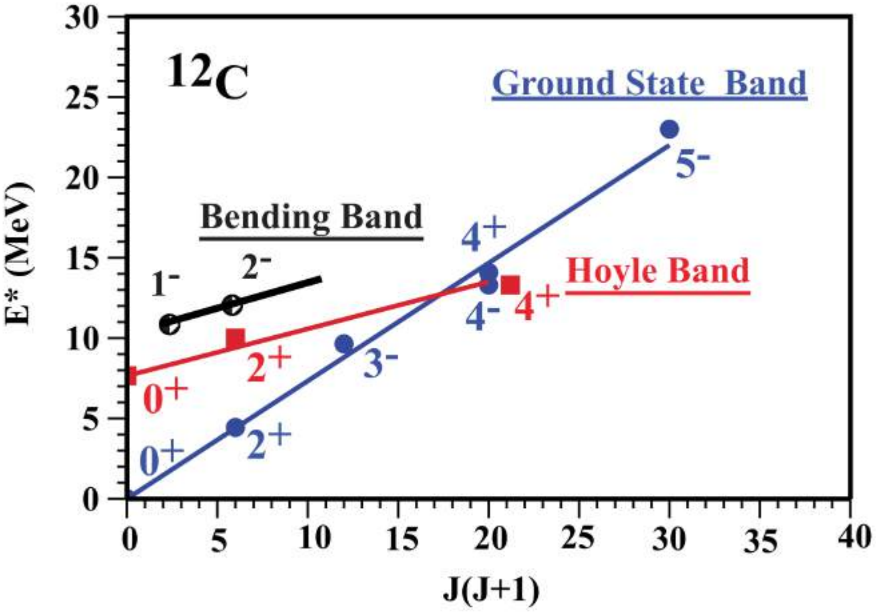

Figure 5.11: The rotational bands of ^{12}C. The points depict experimental measurements and the lines show the predictions from the ACM. Image from reference [158].

5.3.5 Bose-Einstein Condensates

Driven by developments in the field of cold atom physics [159] it has been hypothesised that the Hoyle state corresponds to a dilute gas of α-particles [160]. The 0^+ α-particle has the properties of a boson and the large physical size of the Hoyle state could allow the internal fermionic degrees of freedom of the α-particles to be neglected. If this assumption were correct, then all three α-particles would be able to occupy the lowest $0s$ state of their mean interaction potential. In this sense, the state would be like a Bose-Einstein condensate (BEC). Nuclear α-condensates would differ from their atomic BEC counterparts in many ways, and it is not yet fully clear how the theory can be adapted to the context of a nucleus.

At around the time of the millennium, a number of theoretical studies investigated the possibility of an α-condensate state [161, 162]. They concluded that α-condensation would only occur at a nuclear density around one fifth of the normal saturation density, and that at higher densities nucleon-nucleon pairing would dominate. For a near-threshold state in an α-conjugate nucleus, with an unusually large radius, the possibility of an α-condensation exists. Experiments indicate that the Hoyle state may possess a nuclear volume up to four times larger than the ^{12}C ground state [147–152], meaning that this state may be a good candidate for α-particle condensation.

To theoretically describe such a structure, Tohsaki, Horiuchi, Schuck and Röpke adapted the Brink wave function to reflect to possible condensate nature of this state [160, 163, 164]. On a basic level, the wave function of an $N\alpha$ system is given as

$$|\Phi_{N\alpha}\rangle = \left(C_\alpha^\dagger\right)^N |\text{vac.}\rangle\,. \tag{5.4}$$

The creation operator, $C_\alpha^\dagger$, is such that for a system of 12 nucleons

$$\langle \mathbf{r_1}, \mathbf{r_2}..., \mathbf{r_{12}}|\Phi_{N\alpha}\rangle = \mathcal{A}\left[\phi_\alpha(\mathbf{r_1}..., \mathbf{r_4})\phi_\alpha(\mathbf{r_5}..., \mathbf{r_8})\phi_\alpha(\mathbf{r_9}..., \mathbf{r_{12}})\right]. \tag{5.5}$$

The total wave function for ^{12}C is given by $\Phi_{N\alpha}$ and $\mathcal{A}$ is the antisymmetrising operator. The twelve nucleons are grouped into $0s$ quartets, denoted by $\phi_\alpha(\mathbf{r_1}..., \mathbf{r_4})$, with these equal to

$$\phi_\alpha(\mathbf{r_1}..., \mathbf{r_4}) = e^{-2\mathbf{R}^2/B^2}\varphi_{0s}(\mathbf{r_1} - \mathbf{R})\chi(\mathbf{r_1})\tau(\mathbf{r_1}) \;\; ... \;\; \varphi_{0s}(\mathbf{r_4} - \mathbf{R})\chi(\mathbf{r_4})\tau(\mathbf{r_4}). \tag{5.6}$$

The χ and τ denote the spin and isospin character of the created nucleon and B is a parameter which describes the size of the Gaussian distribution of the three α-particles. $B = (b^2 + 2R_0^2)^{1/2}$, where R_0 is the radius of the whole nucleus. Finally, $\varphi_{0s}(\mathbf{r_i} - \mathbf{R})$ is a Gaussian wave packet given by

$$\varphi_{0s}(\mathbf{r_i} - \mathbf{R}) = \left(\frac{1}{\pi b^2}\right)^{3/4} e^{-(\mathbf{r_i}-\mathbf{R})^2/(2b^2)}. \tag{5.7}$$

The symbol b is the size parameter of the α-particle and $\mathbf{r_i} - \mathbf{R}$ is the relative coordinate of nucleon i.

The overall wave function is antisymmetrised by the operator $\mathcal{A}$ in equation 5.5 and expresses the case where the three α-particles occupy the lowest $0s$ orbital of a harmonic oscillator potential ($e^{-2\mathbf{R}^2/B^2}$) where B adjusts the physical size of the potential. The overall picture of the system is then nicely summarised pictorially by figure 5.12. The scaling parameter b gives the size of the α-particles and B gives the size of the whole nucleus. In the one limiting case of $b = B$, the wave function simplifies to a slater determinant of a product of single-particle harmonic oscillator wave functions. In the other extreme, where $B \gg b$, or as $B \to \infty$, the antisymmetrisation becomes less important and the wave function becomes the product of three Gaussians, describing a free α-particle gas. In this sense, the single particle and α-particle characters of the nucleus are both captured by this powerful wave function.

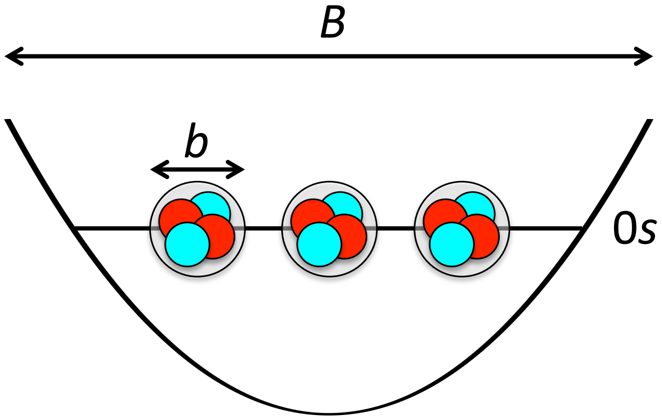

Figure 5.12: Pictorial representation of the THSR wave function of reference [160].

From here, energy surfaces in the two parameter space defined by R_0 (B) and b, $E(R_0, b) = \langle \Phi_{N\alpha}(R_0, b)|\widehat{H}|\Phi_{N\alpha}(R_0, b)\rangle$, are calculated. The Hamiltonian contains the kinetic energy, the Coulomb energy, and the effective NN interaction detailed in reference [165]. The calculated energy surface contains some interesting features and is shown in figure 5.13. It shows a minimum at $b \approx R_\alpha = 1.44$ fm, $R_0 \approx 2$ fm, with a binding energy of -85.5 MeV (more weakly bound than the experimental ground state). A saddle point also appears again at $b \approx R_\alpha = 1.44$ fm, but at a much larger $R_0 \approx 10$ fm, and with a binding energy of -81.1 MeV. This saddle point lies close to the threshold energy for 3α emission and helps to stabilise the possible α-condensed state.

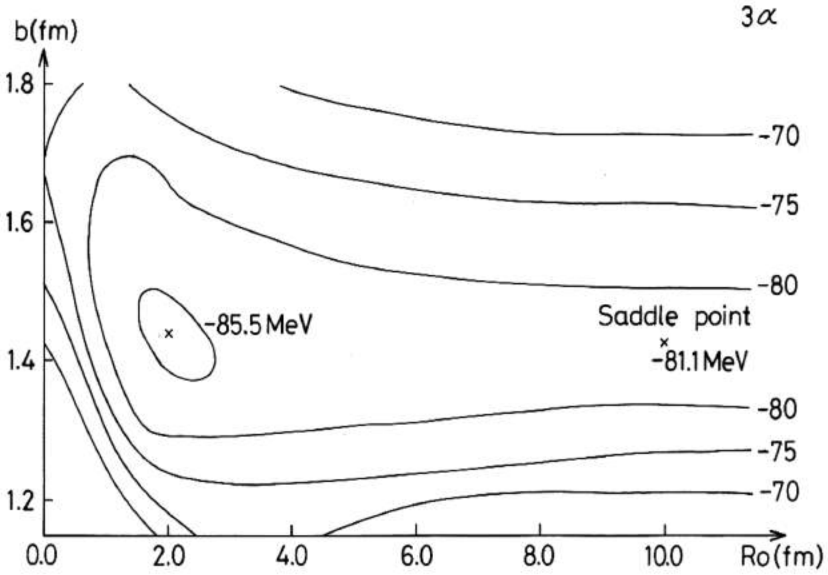

Figure 5.13: Contour plot for ^{12}C of the calculated $E(R_0, b)$ energy surface from reference [160].

A full quantum mechanical treatment of the 3α system was then performed, using $b = 1.44$ fm, and treating R_0 as a discretised variable in the generator coordinate method [166]. This allows the estimation of the values of the variational parameter R_0 for the different states of the system. The lowest 0_1^+ state corresponds to the ^{12}C ground state. It is more unbound than the experimentally-measured ground-state energy but has a similar RMS radius at 2.97 fm (exp. = 2.65 fm). The next 0_2^+ excited state lies at 7.65 MeV excitation but has a much larger calculated radius of 4.29 fm. This corresponds to a factor of three increase in the nuclear volume compared with the calculated ground state and a factor of five greater than the experimental ground state volume. Therefore, the second 0_2^+ Hoyle state corresponds to a very dilute system of low density, suggesting that an α-condensate may exist.

A major success of the THSR approach is that it reproduces the absolute values of the charge form factor for inelastic electron excitation from the ground state to the Hoyle state [167]. This excellent agreement with experimental data indicates that the Hoyle state is indeed a large, diffuse system and strongly influenced by the α-particle structure. The decomposition of the THSR 0_2^+ wave function into the α-particle orbitals reveals a 70% overlap with the wave function for three α-particles occupying the lowest $0s$-orbital, indicating that the picture presented by figure 5.12 is a reasonable approximation of the Hoyle state [168]. Conversely, the ^{12}C ground state shows a largely fragmented occupation of the α-particle orbitals, illustrating that the α-particles lose their identities in the more compact ground state, as would be expected from the antisymmetrisation.

5.4 The 3α decay of the Hoyle state

One way to examine the size of the Hoyle state is through electron inelastic scattering as was discussed in section 5.3.5. However, an alternative, powerful probe into the size and structure of the Hoyle state may be to consider the ways that it decays into three α-particles. This is also important for astrophysical calculations as discussed in section 5.2. Using intensity interferometry techniques [169], it has been proposed that the size of a decaying nucleus could be determined by quantum statistics and the final state Coulomb interactions of the emitted particles. The emission of α-particles from ^{12}C is, in principle, sensitive to the initial geometric arrangements of these α-particles in the nucleus, prior to decay. Considering the sequential decay of $^{12}\text{C} \rightarrow {}^{8}\text{Be}_{\text{g.s.}} + \alpha$, the Coulomb repulsion between the first emitted particle and the two from the subsequent decay of the ^{8}Be, should perturb their relative velocities as they separate.

Freer showed in 2007, that for this channel, the Coulomb imprint in the relative velocity spectrum is lost, since the lifetime of the $^{8}\text{Be}_{\text{g.s.}}$ is around 10^{-16} s [170]. When the two α-particles emerge from the decay of ^{8}Be, they are sufficiently far from the first emitted α-particle that the Coulomb field is weak, and the differences in their final-state interactions become negligible. For sequential decays of higher energy states in ^{12}C through the short-lived excited $^{8}\text{Be}_{2^+}$ (width $\approx$ 1.5 MeV), it has been shown that final-state Coulomb interactions are important in describing experimental data [171–173]. Here, the decay of the short-lived intermediate state happens close to the first emitted α-particle, meaning that the energies of the particles as they separate are more sensitive to the Coulomb interaction.

The situation most sensitive to the Coulomb influences of each of the α-particles is that of a direct decay, where all three particles are emitted simultaneously from the ^{12}C nucleus, and no intermediate resonances are formed. As discussed later in section 5.5.2, the direct decay is rare since its phase space is severely hindered compared with the sequential decay process. The preceding paragraphs have discussed that under a direct decay process, the relative energies of the three emitted α-particles are sensitive to the initial configuration of the α-particles in ^{12}C. Now, various potential Hoyle state structures are discussed along with what their corresponding α energy signatures could be under a direct decay process.

5.4.1 Structures and 3α decay signatures

Figure 5.14 schematically shows the types of direct decays that would be expected for the various 3α configurations of the Hoyle state. This section briefly describes and justifies each of these pictures.

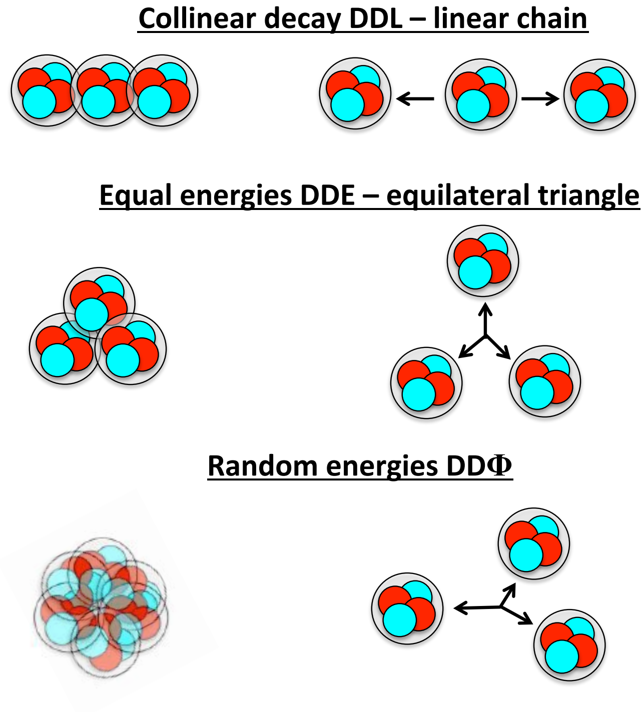

Figure 5.14: Schematic diagram of the types of α-particle emissions expected for various structures.

Linear 3α chain

A recent microscopic dynamical study of the triple-α reaction involving three ^{4}He nuclei using time-dependent Hartree-Fock (TDHF) calculations, concluded that for the linear chain state in ^{12}C to exist for any appreciable length of time, the ^{8}Be + α reaction must proceed collinearly [174]. In other words, a smaller impact parameter relative to the ^{8}Be deformation axis was preferred. Therefore, it is natural to assume that the reverse process is also true; when the linear chain breaks up into three α particles, it should do so in a collinear way, as shown for the 'DDL' model in the top panel of figure 5.14. An experimental observation of this type of decay could be evidence for the 3α linear chain nature of the Hoyle state, such as those predicted by basic α-cluster models [154, 155] and the Skyrme model [175].

Equilateral triangle

The equilateral triangle picture was shown to beautifully describe the spectrum of ^{12}C by Marín-Lámbarri *et al.* [158], through an algebraic cluster model with imposed $\mathcal{D}_{3h}$ point symmetry. This structure has the proposed 'DDE' direct decay signature shown by the middle panel of figure 5.14. In the $\mathcal{D}_{3h}$ model, the Hoyle state is interpreted as a 'breathing mode' excitation of the ground state where each of the α-clusters vibrate along the radial lines shown in figure 5.14. It may, therefore, be expected that this is the trajectory followed during the decay. Energy and momentum conservation states that they emerge at equal energies, and with relative angles of 120°. Previously, experiments have searched for this type of decay [139], however, since this is a quantum system, the particles cannot ever emerge with the same energy. Due to the fact that the particles are trapped in the Hoyle state (experimental radius ≈ 3.2 fm) then due to Heisenberg's position and momentum uncertainty principle, there must also be an uncertainty in their momenta. A simple calculation results in a spread in their relative energies of ≈ 30 keV. Therefore, when modelling this DDE decay (section 5.8.7), the α relative energies were sampled from a Gaussian distribution of $\sigma = 30$ keV. This is similar to the approach of Itoh *et al.* [140].

Bose-Einstein condensate

In the Bose-Einstein condensate model, the α-particles are assumed to sit in the same $0s$ orbital. Their common wave functions inside the nucleus leads to the idea that they too should be emitted from the nucleus with the same energy, smeared only by the Heisenberg position momentum uncertainty principle. In fact, the velocity distributions of rubidium atoms were used to measure the size of atomic Bose-Einstein condensates [159]. It has also been proposed that an α gas may decay randomly to the available phase space, evenly sampling each of the emission energies and angles that are allowed by conservation laws. This DDΦ decay model has provided the standard for recent direct decay measurements [139, 140].

5.4.2 Full three-body calculations

The preceding schematic models assume a one-to-one relationship between the final state distribution of α-particle energies and the structure of the initial ^{12}C state inside the Coulomb barrier. However, as already alluded to in the introduction to this section, it is necessary to understand how the Coulomb interactions between the particles may modify their final state configuration. Furthermore, the decay barriers are significantly altered by the inclusion of an attractive $\alpha - \alpha$ interaction. Therefore, some further theoretical input is required.

Several attempts have been made to understand the decay and structure of the Hoyle state by performing full three-body quantum mechanical calculations. In one study by Alvarez-Rodríguez *et al.*, the 3α decays of states in ^{12}C were calculated using the hyperspherical adiabatic expansion method of the Faddeev equations [176]. The Faddeev equations simultaneously describe all the possible interactions in a system of three particles in a fully quantum mechanical way and the three body interaction term was chosen to depend only on the *hyprerradius*, ρ. The hyperradius is introduced and defined in section 5.5.1 later.

The adiabatic hyperspherical expansion method involves firstly solving the angular part of the Schrödinger equation and then expanding the full wave function using these angular wave functions as a basis [177]. Fully solving the problem in this way allows the tracking of the components of the wave function with a varying hyperradius, *i.e.* as the system separates. As shown by figure 5.15, the 0_2^+ Hoyle state is described predominantly by the $n = 1$ angular basis function, f_1, over all values of the hyperradius, suggesting that its structure does not change much during the decay. In this sense, the final state distribution of α-particle energies may be a good reflection of the initial structure. For other states in ^{12}C, a strong dynamical evolution of the wave function is observed, and so the same conclusions cannot be made. The calculations also predict a direct decay branch of the Hoyle state at 1%, which is considerably larger than the experimental upper limit. This method also permits the energy distributions of the final state α-particles to be calculated, but their results for the Hoyle state are not discussed in reference [176].

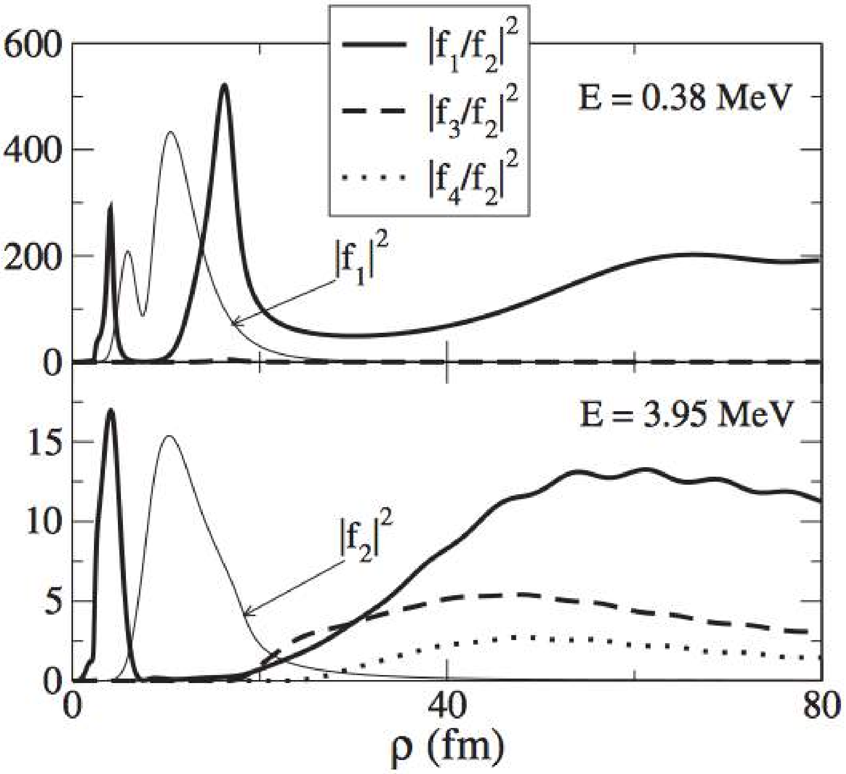

Figure 5.15: The ratios of the adiabatic components of the Hoyle state (upper panel) and 0_3^+ resonance (lower panel) in ^{12}C. The ratio of f_2 to f_3 varies during the decay of the Hoyle state, but the f_1 component remains dominant over all hyperradii. Here, E is the energy above the α-particle decay threshold. Image from reference [176].

Another theoretical study by Ishikawa gives a detailed prediction of the direct decay component of the decay of the Hoyle state [178]. A wave function for the reaction $\gamma + {}^{12}\mathrm{C} \rightarrow 3\alpha$ was defined and solved using the Faddeev three-body formalism [179]. In these calculations, the α-particles are treated as bosons and their four-nucleon structures are just considered to be incorporated into the $\alpha - \alpha$ interactions used. This work predicted that the direct decay contributed at the total level of $\approx 0.1\%$, with DDE and DDL contributions at the levels of 0.005% and 0.03% respectively. So far, no experiment has had the sensitivity required to test these predictions.

5.4.3 Decay signatures of an α-condensed state

In 2006 Kokalova *et al.* proposed an experimental method for testing Bose-Einstein condensation in nuclei [180]. Firstly they asserted that cluster emission from an α-condensed state of a nucleus is enhanced for decays into α-condensed subsystems due to a significant decrease in the barrier for the decay; a feature of the extended radius of an α-condensate. Secondly, they postulated that since the α-clusters exist in the same $0s$ orbital for a condensate, that any kind of partition of the system into α-condensed subsystems is equally probable. For example, a 5α condensate state in ^{20}Ne may decay through any of the following channels:

$$\begin{aligned} ^{20}\mathrm{Ne} &\rightarrow {}^{16}\mathrm{O}_{0^+} + \alpha && (5.8)\\ &\rightarrow {}^{12}\mathrm{C}_{0_2^+} + {}^{8}\mathrm{Be} && (5.9)\\ &\rightarrow {}^{12}\mathrm{C}_{0_2^+} + \alpha + \alpha && (5.10)\\ &\rightarrow {}^{8}\mathrm{Be} + {}^{8}\mathrm{Be} + \alpha && (5.11)\\ &\rightarrow {}^{8}\mathrm{Be} + \alpha + \alpha + \alpha && (5.12)\\ &\rightarrow \alpha + \alpha + \alpha + \alpha + \alpha. && (5.13) \end{aligned}$$

Provided that the subsystems are also α-condensates, the propensities for decays through each of these channels will depend on the corresponding barrier transmission probabilities only. In the case of the ^{12}C the decay is rather more limited to:

$$\begin{aligned} ^{12}\mathrm{C}_{0_2^+} &\rightarrow {}^{8}\mathrm{Be} + \alpha && (5.14)\\ &\rightarrow \alpha + \alpha + \alpha. && (5.15) \end{aligned}$$

It has been suggested that the ^{8}Be ground state is the simplest example of an α-condensate [181]. With this being the case, if the ^{12}C Hoyle state is an α-condensate, the direct 3α decay branching ratio should depend only on the phase space for the decay and barrier penetrabilities, which are calculated next. These calculations indicate that the direct 3α branching ratio should be around 0.06% – lower than the current experimental upper limit.

5.5 Sequential and direct decay calculations

Sequential three-body decays proceed through an intermediate resonance, leading to the idea that the energy of the first emitted particle is fixed by the masses of the two break-up fragments due to energy and momentum conservation. The energies of the secondary particles that are emitted depend on the energy of the intermediate state. Direct three-body decays on the other hand populate the three-body continuum with no intermediate step. These are more complicated to analyse in detail since a wide variety of relative particle motions are permitted as shown by figure 5.16.

In the simplest terms, the relative importance of sequential and direct decays can be split into two factors: the phase space available for the decay and the transmission probability through the Coulomb barrier. For example, when ^{12}C breaks up into three α-particles, a decay where the three daughters are emitted with equal energies and equal angles between them has a significantly lower Coulomb barrier than a collinear decay, where the particles lie on a straight line. This section describes a method of calculating the transmission probability through the Coulomb barrier for two-body and three-body decays. It also details how the relative phase spaces between two-body and three-body decays can be calculated. These are then brought together in order to estimate the branching ratios for direct and sequential decays of the ^{12}C Hoyle state.

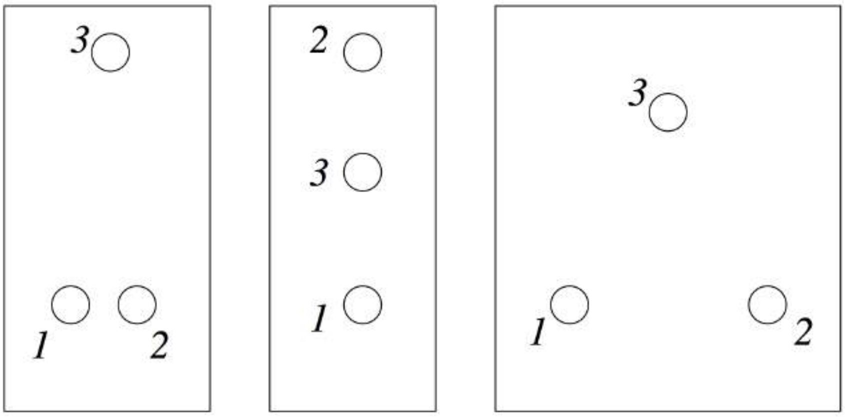

Figure 5.16: Various geometric configurations of a three-body decay. The situations are labelled from left to right as *other collinear*, *extreme collinear* and *equal energies*. Other collinear: particles 1 and 2 remain close during the decay (similar to a sequential decay). Extreme collinear: the decay is collinear and one particle remains stationary. Equal energies: the particles are emitted with equal energies and with equal angles between them. Image from reference [182].

5.5.1 Semi-classical approach to barrier transmission

The semi-classical approach presented in reference [182] was used to examine the nature of the sequential and direct decay mechanisms of the Hoyle state. This approach utilises the WKB approximation [183], which is a method for obtaining an approximate solution to the time-independent one-dimensional Schrödinger equation. Its application in this case is calculating tunnelling rates through Coulomb potential barriers.

In the simple two-body decay of ^{12}C where an α-particle is emitted leaving a ^{8}Be daughter, the Schrödinger equation can be solved for the relative motion of the two daughter nuclei. If the two daughters have charges Z_1 and Z_2 and a separation of r fm, the coulomb potential that they feel is given by the equation

$$V(r) = \frac{Z_1 Z_2 e^2}{r}, \tag{5.16}$$

where $e^2 = 1.44\ MeV$ fm. The variation of this potential for a ^{8}Be + α decay as a function of the separation r is shown in figure 5.17. At a separation r_0 the two daughters are touching and the attractive strong nuclear force takes over. Since the Hoyle state is unbound by 380 keV, it is possible for the ^{12}C nucleus to decay in this manner by tunnelling through the Coulomb barrier between r_0 and a second radius r_1 (around 40 fm). This 40 fm represents the classical turning point in the potential for a particle with 380 keV energy.

In the region beyond 40 fm the wave function is an oscillatory solution of the form $\psi(r) = Ae^{\pm i\kappa r}$ with $\kappa = \sqrt{2\mu\left(E - V(r)\right)}/\hbar$ and μ as the reduced mass of the two particles. For the classically forbidden region $r < 40$ fm, the wave function is an exponential solution of the form $\psi(r) = Be^{\pm\kappa r}$ with $\kappa = \sqrt{2\mu\left(V(r) - E\right)}/\hbar$. The WKB method matches the wave functions at the classical turning points in order to find a solution. The principal WKB approximations are that the potential is a slowly-varying linear function at the classical turning points and that the amplitude and phase of the exponential function vary slowly compared with the de Broglie wavelength, λ.

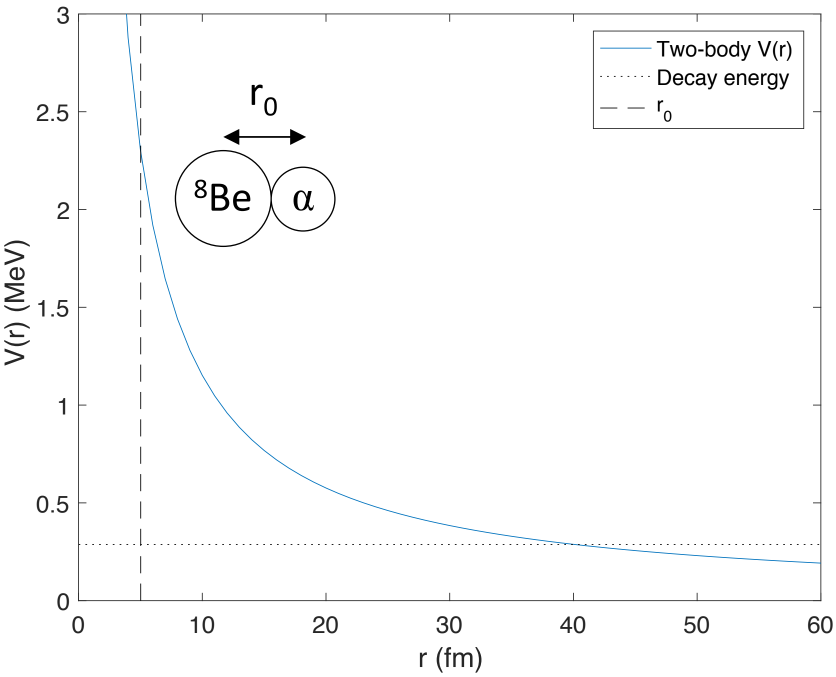

Figure 5.17: The ^{8}Be + α Coulomb barrier as a function of the separation of the two fragments.

Under these approximations it can be derived that the tunnelling probability is given by the equation

$$T = \frac{1}{1+e^{2S}} \approx e^{-2S}, \quad \text{where} \quad S = \frac{1}{\hbar}\int_{r_0}^{r_1} dr\sqrt{2\mu\left(V(r)-E\right)}. \tag{5.17}$$

Based on the derivation in reference [182], for a Coulomb potential, this can be simplified to

$$S = \frac{\pi}{2}\left(Z_1 Z_2 e^2\right)\sqrt{\frac{2\mu}{\hbar^2 E}}. \tag{5.18}$$

The equivalent calculation for a three-body decay is less simple due to the fact that each particle must tunnel through a Coulomb barrier set up by all three particles, according to equation 5.19. As the system moves apart during the decay, the potential changes in a more complicated way, which depends on the relative directions of the three particles. With reference to figure 5.18, the total Coulomb potential for a particular orientation of particles is given by equations

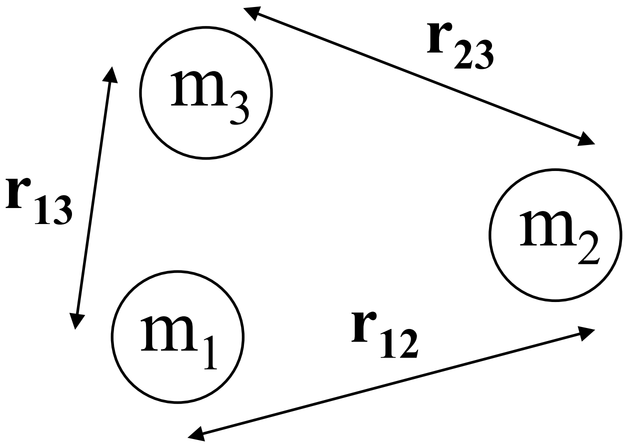

Figure 5.18: The relative coordinates between the three particles in a direct decay.

$$V(\mathbf{r_{12}}, \mathbf{r_{13}}, \mathbf{r_{23}}) = \frac{Z_1 Z_2 e^2}{r_{12}} + \frac{Z_1 Z_3 e^2}{r_{13}} + \frac{Z_2 Z_3 e^2}{r_{23}} \tag{5.19}$$

$$V(\mathbf{r_{12}}, \mathbf{r_{13}}, \mathbf{r_{23}}) = \sum_{i<k} \frac{Z_i Z_k e^2}{r_{ik}}, \tag{5.20}$$

where i, k are a permutation of 1, 2 and 3. Due to these complications it is useful to introduce a quantity called the *hyperradius*, ρ, which is defined as

$$\rho^2 \equiv \frac{1}{mM} \sum_{i<k} m_i m_k r_{ik}^2, \tag{5.21}$$

where $\mathrm{M} = \sum_j m_j$ and m is an arbitrary normalisation mass. It is easily shown that for whatever orientation the three particles have and however they share the decay energy, the hyperradius increases linearly with time during the decay. If a random decay orientation is chosen and the system is propagated in time steps, the relative coordinates, r_{ik}, increase. Calculating the hyperradius as time progresses shows that it increases linearly, whatever the chosen orientation. Writing the Coulomb potential in terms of the hyperradius makes it simpler to calculate the probability for transmission through the Coulomb barrier.

A given decay path is defined by specifying how the distance between the particles increases as function of ρ. The positive scaling constants s_{ik} can be defined by normalising the relative distances between the particles by the hyperradius as

$$s_{ik}^2 \equiv \frac{r_{ik}^2}{\rho^2}. \tag{5.22}$$

These scaling constants, s_{ik}, provide a way to parameterise the geometry of the decay. Making reference to figure 5.16, reading from left to right, if $s_{13} \approx s_{23}$ and $s_{12} \approx 0$ then particles 1 and 2 remain close until particle 3 has travelled far away. This is almost equivalent to a sequential decay. If $s_{13} \approx s_{23}$ and $s_{12} \approx s_{13} + s_{23}$, then we have a collinear decay where particle 3 remains stationary. If $s_{12} \approx s_{13} \approx s_{23}$ we have the case where the particles separate at equal angles to one another.

The Coulomb potential can be parameterised by the hyperradius and scaling constants as

$$V(\rho) = \sum_{i<k} \frac{Z_i Z_k e^2}{r_{ik}} = \frac{1}{\rho} \sum_{i<k} \frac{Z_i Z_k e^2}{s_{ik}}. \tag{5.23}$$

Therefore, for a general decay geometry, parameterised by the scaling constants, s_{ik}, the potential barrier can be calculated as a function of ρ. The Coulomb barriers corresponding to the three geometries shown in figure 5.16 are plotted in figure 5.19. This shows an interesting result. An ‘equal energies’ decay has the lowest Coulomb barrier. A totally collinear decay has the largest Coulomb barrier. The barrier for a decay where two of the particles remain close together (similar to a sequential decay) lies somewhere between the other two extremes.

The transmission probability is calculable using equation 5.23 as

$$T = \frac{1}{1 + e^{2S}} \approx e^{-2S} \quad \text{where} \quad S = \frac{1}{\hbar} \int_{\rho_0}^{\rho_1} d\rho \sqrt{2m\left(V(\rho) - E\right)}. \tag{5.24}$$

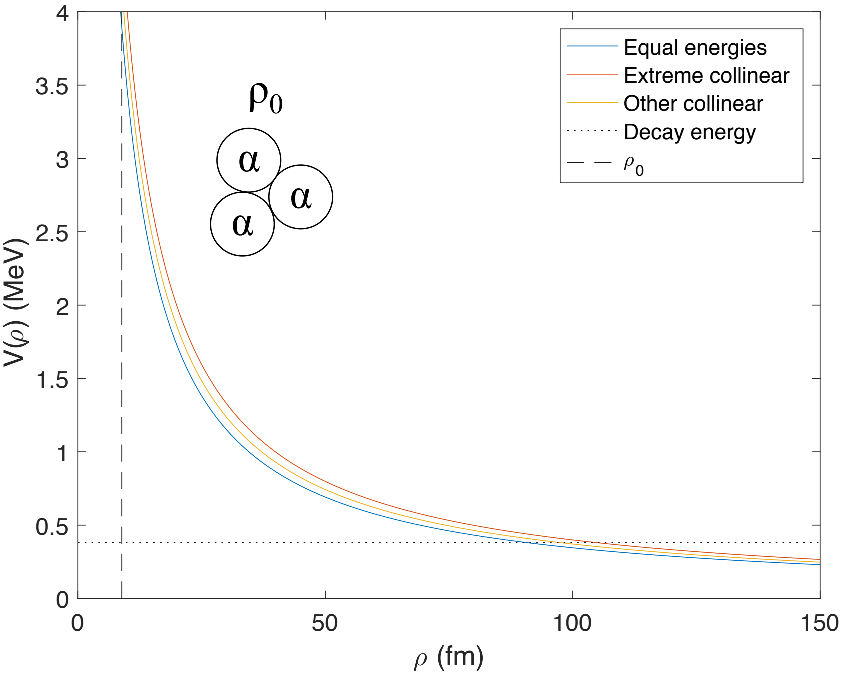

Figure 5.19: The three-body α + α + α Coulomb barrier as a function of the *hyperradius*, ρ. The lines depict three extreme situations: the three particles are emitted with the same energy and at equal angles to each other (blue line); a collinear decay where one particle is given the maximum 2/3 of the total decay energy and the others are emitted perpendicular to this particles direction (yellow line); a collinear decay where one α particle remains at rest (red line).

Equation 5.24 can either be numerically integrated or approximated [182] as

$$S = \frac{\pi}{2} \sum_{i<k} \frac{Z_i Z_k e^2}{s_{ik}} \sqrt{\frac{2m}{\hbar^2 E}}. \tag{5.25}$$

In order to calculate the relative probabilities for sequential and direct decays, the transmission probability for three-body decays must be calculated over all possible decay orientations and an average value taken, $T3_{\text{av}}$. This method assumes that decays to anywhere in the available phase space are equally probable. This would not be true if the Hoyle state had a strong ^{8}Be + α structure, as predicted by *fermionic molecular dynamics* and *antisymmetrised molecular dynamics* calculations [184, 185]. It is thought that this would be the case if the state was treated as a structure-less 'gas' of α-particles [180]. In this instance, the relative decay widths for various channels should depend only on the decay penetration factors.

The Matlab code, given in reference [186], was written, which generates a large number of random decay orientations for the three-body decay of ^{12}C into three α-particles. These are chosen to evenly sample the phase space while conserving energy and momentum. As is discussed in references [139] and [140], and later in section 5.8.6, this corresponds to randomly sampling the kinematically-allowed region of the symmetric Dalitz plot for the decay. The three-body decay transmission probability, $T3_{\mathrm{av}}$, was calculated over 10^6 random geometries and the average value was calculated. The two-body decay transmission probability, $T2$, for ^{8}Be + α was also calculated. The branching ratio for a direct decay was then calculated as

$$BR = \frac{T3_{\mathrm{av}}}{T3_{\mathrm{av}} + T2} \approx 1/3. \tag{5.26}$$

It has also been proposed that for an α-gas-like state, there is a propensity for the α-particles to be emitted with similar energies as a reflection of their underlying identical wave functions in the decaying nucleus [137]. In this case, three-body transmission probabilities should only be calculated for decay geometries parameterised as $s_{12} \approx s_{13} \approx s_{23}$. This results in a much higher branching ratio $BR \approx 6$. The value quoted in equation 5.26 is therefore a lower limit on the direct decay contribution.

However, caution should be taken when interpreting this value. As noted in reference [187], this method treats the system from outside the range of the strong interaction meaning that only Coulomb (and centrifugal) barriers remain. However, this assumes that the small distance many-body dynamics is unimportant in the decay process. More advanced three-body models include both the short range and the long range interactions in computing resonances [188, 189]. In the case of the Hoyle state, the width calculated using WKB methods was evaluated to be around 60 eV. This is three times larger than the full computation [188] and about eight times larger than the experimentally measured value of 8.5 eV [190].

Furthermore, to calculate the true value of the branching ratio, the magnitude of the relative phases spaces available for sequential and direct decays must be calculated, which is discussed in the next section.

5.5.2 Phase space calculations

To calculate the phase space for two-body and three-body decays, the Fermi break-up model was used [191]. The break-up probability of a nucleus decaying into n fragments, excluding the effects of the Coulomb barrier penetration, is given by

$$W(E,n) = \left(\frac{V}{\Omega}\right)^{n-1} \rho_n(E), \tag{5.27}$$

where, $\rho_n(E)$ is the density of final states, $\Omega = (2\pi\hbar)^3$ is the normalisation volume and V is the volume of the decaying nucleus. Here, V is defined as $4\pi R_0^3/3$. The nuclear radius, R_0, is defined in the standard way $R_0 = 1.4A^{1/3}$.

In the Fermi break-up model, the density of final states is defined as

$$\rho_n(E) = M_n(E) S_n G_n. \tag{5.28}$$

The S_n term counts the number of states with different spin orientations. For n break-up fragments, each of spin, s_b, the S_n term is given by

$$S_n = \prod_{b=1}^{n} (2s_b + 1)\,. \tag{5.29}$$

For the decay of the Hoyle state to ^{8}Be + α or to 3α, $S_2 = S_3 = 1$, since all of the fragments are $s = 0$. The G_n term is called the permutation factor, which accounts for the identities of the components in the final state to avoid double counting states. The number of particles of type j is given by n_j, and k is defined as the number of groups of identical particles. The G_n term is given as

$$G_n = \prod_{j=1}^{k} \frac{1}{n_j!}. \tag{5.30}$$

For example, in some decay configuration involving two identical particles, p_1 and p_2, there will be a configuration where $p_1 = k_1$ and $p_2 = k_2$. Since the particles are identical, we will also have the reverse case $p_1 = k_2$ and $p_2 = k_1$. The integral over all phase space will contain both cases separately. However, in quantum mechanics, the fact that these are identical particles means that these two situations are actually the same state and will have been double counted. This is corrected for by the G_n term. In the case of sequential decay, $k = 2$, $n_1 = 1$ and $n_2 = 1$, so $G_n = 1$, which is what is expected since the daughter particles in the sequential decay are not identical. For the direct decay, $k = 1$ and $n_1 = 3$, so $G_n = 1/6$.

The $M_n(E)$ factor in equation 5.28 is the phase space factor, which can be introduced by examining figure 5.20. Here, the question can be asked, "what is the net phase space for the particles to end up with these energies in the final state?" The answer must be zero if the energy and momentum are not conserved. In the relativistic case, the invariant mass of the system must also be conserved.

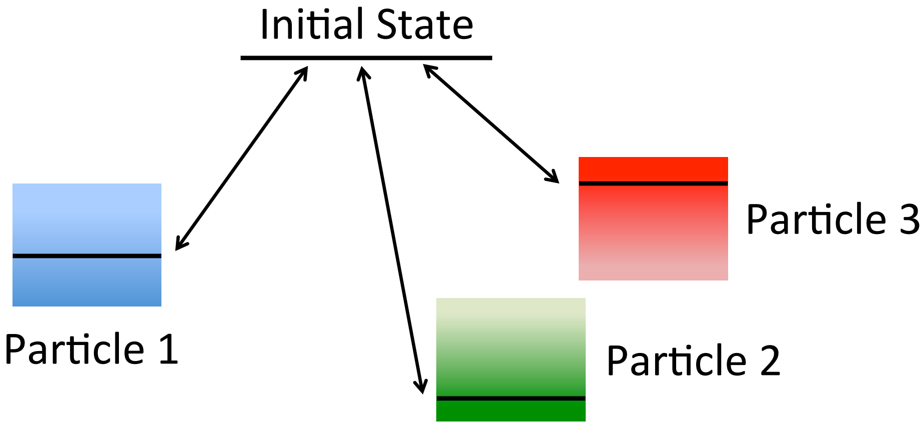

Figure 5.20: Decay from a single state into three particles.

If these constraints are satisfied, the total phase space is the product of the individual phase spaces

$$\rho = \rho_1(E_1, \mathbf{p_1}) \times \rho_2(E_2, \mathbf{p_2}) \times \rho_3(E_3, \mathbf{p_3}). \tag{5.31}$$

In the language of four-vectors, $p = (E, \mathbf{p}c)$, this reduces to

$$\rho = \rho_1(p_1) \times \rho_2(p_2) \times \rho_3(p_3). \tag{5.32}$$

To quantify the total phase space, all of the kinematically-allowed four-vectors must be integrated over as

$$\rho_{\text{tot}} = \frac{1}{(2\pi)^4} \int_{\text{allowed}} d^4p_1\ d^4p_2\ d^4p_3\ \rho_1(p_1)\ \rho_2(p_2)\ \rho_3(p_3). \tag{5.33}$$

To permit this, several Dirac delta δ and Heaviside-Lorenz Θ functions must be used in the integral to enforce the conservation laws. Therefore, in the case of an n-body decay, the integral will have the form

$$\rho_{\text{tot}} \propto \int \delta^4(\sum_i^n p_i - \sum_f^n p_f)\ \prod_{j=1}^n \delta(p_j^2 - m_j^2c^2)\ \Theta(p_j^0)\ d^4(p_j). \tag{5.34}$$

This complicated-looking equation simply states that the phase space is evenly distributed over all n final state particles, subject to energy, momentum and mass conservation. The first term, $\delta^4(\sum_i p_i - \sum_f p_f)$, ensures that energy and momentum are conserved between the initial and final states. The product is over all outgoing particles. The $\delta(p_j^2 - m_j^2c^2)$ ensures that the outgoing particles are on mass shell (real), and $\Theta(p_j^0)$ ensures that their energies are positive. In the non-relativistic case, the integral can be solved analytically for an n-body decay [192] to give

$$M_n(E, n) = \left(\frac{1}{\sum_{b=1}^n m_b} \prod_{b=1}^n m_b \right)^{3/2} \frac{(2\pi)^{3(n-1)/2}}{\Gamma(3(n-1)/2)} E^{3n/2-5/2}, \tag{5.35}$$

where Γ is the Gamma function, m_b are the masses of each fragment and E is the decay energy. Equation 5.27 was then evaluated and the ratio of the phase spaces for the two-body and three-body decay of the Hoyle state was found to be $W(E_3, 3)/W(E_2, 2) = 1.8 \times 10^{-3}$. Combining this with the relative transmission probabilities through the Coulomb barrier, detailed in section

5.5.1 (equation 5.26), gives a prediction for the direct decay branching ratio as 6×10^{-4} (0.06%). This value is particularly applicable to an α-condensate structure for the Hoyle state, since the decay of a condensate state into α-condensed subsystems should only depend on the phase space and barrier penetrabilities.

5.6 Experimental details and apparatus

5.6.1 Birmingham MC40 cyclotron accelerator

The experimental measurements were performed at the University of Birmingham MC40 cyclotron which produced a 40 MeV ^{4}He beam with an average current of 6 enA. The beam was formed by feeding ^{4}He gas into a hot-filament floating-cathode ion source [193] which formed the helium in a Q = 2^{+} charge state.

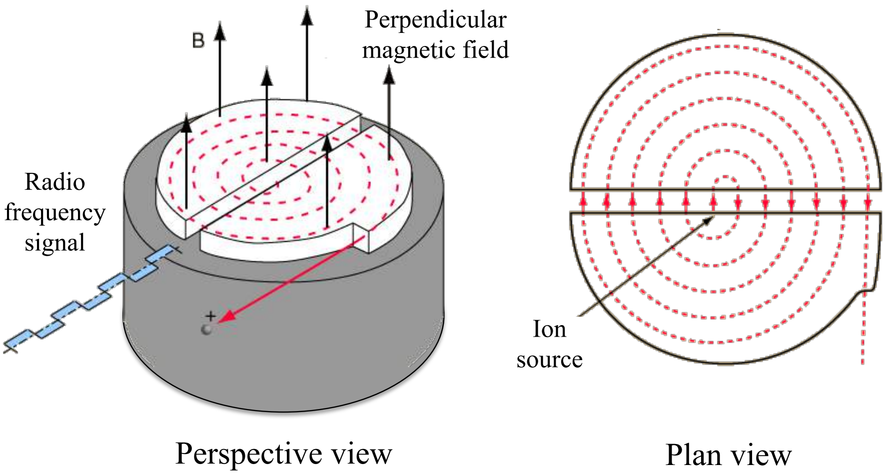

Figure 5.21: The basic operation of a cyclotron accelerator. The images are adapted from [194]. In reality, the RF signal has a sinusoidal form and the cyclotron orbits become closer together at larger radii.

The basic principles of operation of a cyclotron accelerator are depicted in figure 5.21. A cyclotron is circular in design and has an approximately constant magnetic field perpendicular to this plane (approximately 1.8 T at Birmingham). The Lorentz force, therefore, requires that the charged beam particles follow a circular trajectory when moving in this plane. The ions are inserted into the centre of the accelerator and are attracted to one of the D-shaped electrodes (a *dee*), which is held at a negative potential. When the particle enters the dee, it no longer feels the electrostatic force and is free to travel in a semi-circular path at a constant speed. During this motion, the two dees switch polarity, meaning that as the particle exits the first dee, it is attracted to the second one and repelled by the first one. It therefore gains energy and enters the second dee. Again, it travels in a semi-circular path but with a slightly larger radius. Driving the potential on the dees at the aptly named *cyclotron frequency*, given in equation 5.38, means that this acceleration process happens a number of times, accelerating the particle to higher and higher energies until its orbital radius reaches the edge of the accelerator, where it is extracted. The cyclotron frequency is derived by firstly equating the centripetal force experienced by an ion, with the Lorentz force, which is maintaining its circular trajectory.

$$\frac{mv^2}{r} = qv|\overrightarrow{\mathbf{B}}|, \tag{5.36}$$

$$=> \frac{v}{r} = \frac{q|\overrightarrow{\mathbf{B}}|}{m}. \tag{5.37}$$

The time period of a single cyclotron orbit can be identified as $2\pi r/v$, hence, the angular frequency is given as

$$\omega = \frac{q|\overrightarrow{\mathbf{B}}|}{2\pi m}. \tag{5.38}$$

Given a particular magnetic field strength $\overrightarrow{\mathbf{B}}$ and extraction radius R_0, the energy of an accelerated particle of mass m and charge q, in the non-relativistic limit, is given by

$$E_0 = \frac{q^2|\overrightarrow{\mathbf{B}}|^2 R_0^2}{2m}. \tag{5.39}$$

At relativistic energies, the mass of the ion increases, meaning that its motion moves out of phase with the driving frequency of the dees. This can be corrected for by utilising a more complicated magnetic field (Azimuthally Varying Field cyclotrons).

The Birmingham MC40 cyclotron is designed slightly differently to this simplistic picture [195]. The particle orbit is split into four quadrants. The alternating voltage is applied to two 90 degree 'half-dee' cavities which are mounted radially opposite each other, while the other two 'dummy dees' are held at ground potential. This means that ions are accelerated four times on each orbit, which in turn permits a wider range of ions and energies that can be accelerated using the limited range of frequencies available from the RF source. Further subtleties such as an azimuthally-varying field to aid beam focusing are also present. The beam energy depends on the radius of beam extraction. This can vary by 1-2 mm and leads to a typical 100-300 keV uncertainty [82].

The name, MC40, originates from the fact that this machine can accelerate protons up to 40 MeV. This is called the k-number and has a value of 40. Given equation 5.39, this fact may be used as a calibration to calculate the maximum energies achievable for a range of ions of mass m_i and charge state q_i, as

$$E_i = 40 \times \frac{q_i^2}{q_p^2}\frac{m_p}{m_i} \text{ MeV.} \tag{5.40}$$

Upon extraction from the accelerator, the beam was directed towards the target and measurement apparatus using the Vivitron 12-way switching magnet, from Strasbourg, installed in 2005.

5.6.2 Detector set-up

The ^{4}He beam bombarded a 100 μg cm^{-2} natural carbon target after entering the vacuum chamber. A collimator and anti-scatter system cleanly focus the ions into a $\approx$ 2mm beam spot on the target. The products of the ^{12}C(α,α)3α break-up reaction were measured by an array of six *Micron W1* double-sided silicon strip detectors (DSSDs) [Micron Semiconductor Ltd] [84]. The operation of these detectors was discussed in the previous chapter (section 4.2.3) so the details are omitted here. The arrangement of the detectors inside the reaction chamber is shown schematically in figure 5.22 a) and as a photograph in 5.22 b). Each DSSD has a total surface area of 5 × 5 cm^2 and allows both the energy and the direction of a particle to be determined. The momentum vector of each detected particle could then be calculated, assuming each to be an α-particle.

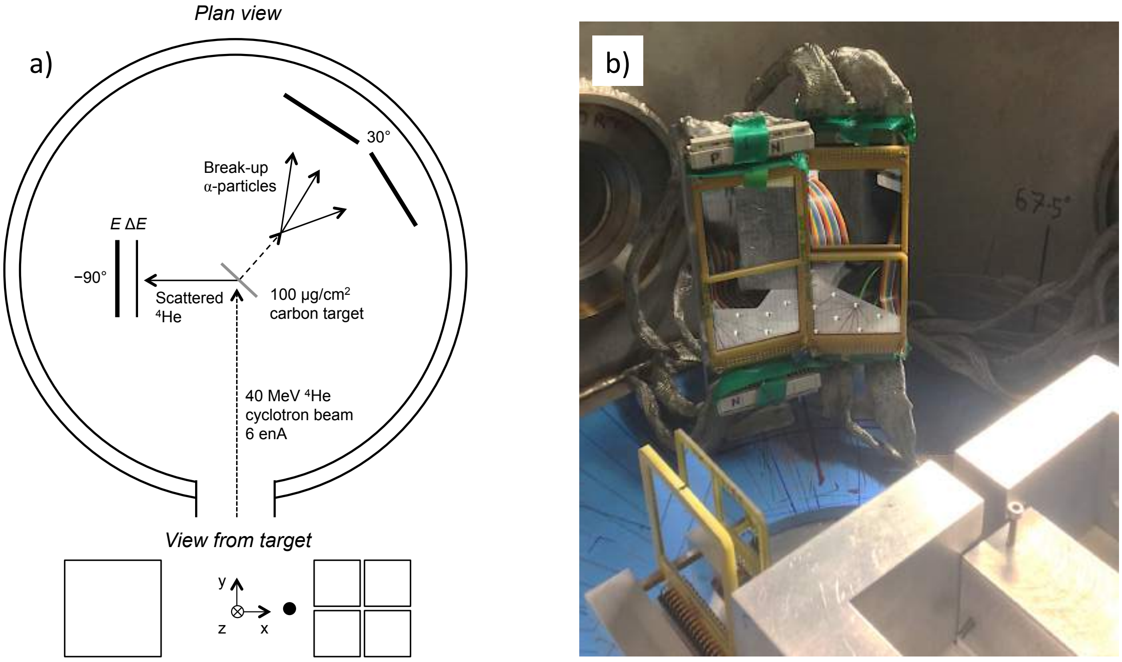

Figure 5.22: a) The positions of the detectors and target inside the vacuum chamber along with an illustration of the ^{12}C break-up process. b) A photograph of the full detector set-up inside the reaction vacuum chamber.

The detectors were arranged to maximise the efficiency for measuring the break-up of ^{12}C through its Hoyle state. The telescope set-up at 90° is set to measure the scattered ^{4}He beam. This arrangement consists of a thin 65 μm DSSD, followed by a thick 500 μm detector. As shown later in section 5.8.3, this allows the isotope being detected to be identified. The large scattering angle ensures that a substantial fraction of the beam momentum is imparted to the recoiling ^{12}C. In the centre-of-mass frame of the decaying ^{12}C, it breaks apart into three α-particles with very low energies, due to the proximity of the Hoyle state to the 3α threshold. As the ^{12}C has a large momentum, these α-particles are then boosted into the lab frame to have an average energy around 6 MeV. The ^{12}C target was rotated by 30° in order to minimise the energy losses of the break-up α-particles before hitting the detectors.

The Quad arrangement of 500 μm DSSDs was positioned to collect all three α-particles from the Hoyle state break-up (complete kinematics). An array of four detectors was chosen for two reasons. Firstly, four detectors, twice as far from the target provides a superior angular granularity compared with a single detector closer to the target, since the detector strips subtend a smaller angular range. Therefore, the momentum of the detected particles can be measured more accurately.

Secondly, two previous measurements of the direct decay of the Hoyle state noted that, when measuring multiple particles with similar energies, it was possible to accidentally miss-assign the hit positions of each particle [138, 140]. Section 4.3 details how, when multiple particles hit the same detector, the signals collected by the front and rear detector strips are energy ordered. The signals on the front and rear strips are then matched, and their crossing point provides the hit position. In cases where the particles have very similar energies, due to the finite energy resolution of the detectors, it is possible for the energy order of various particles to be switched. In this case, when the front and back strips are energy ordered and matched, the extracted strip crossing point is incorrect. This worsens the resolution and provides an experimental background. Using four separate DSSDs allows for the possibility that each break-up α-particle is detected in a separate DSSD, therefore eliminating this background. In this experiment, events where two particles strike the same DSSD and events where each particle strikes a different DSSD are considered separately. In events where two particles hit the same DSSD, since the resolutions of the detectors are known, the probability of angular mismatch is easy to calculate and was incorporated into Monte-Carlo simulations of the reaction.

5.6.3 Electronics and data acquisition

The electronics and data acquisition system is fundamentally similar to what was used for the ^{9}Be experiment in chapter 4 section 4.2.4. Therefore, this section will only give a brief overview of the electronics chain used to convert the raw current pulses that exit the detector array when measuring an event, into a set of digital signals which can be recorded and analysed on a computer. The details of how each electronic component works are covered in the previous chapter and is not repeated. The electronics chain is shown as a block diagram in figure 5.23.

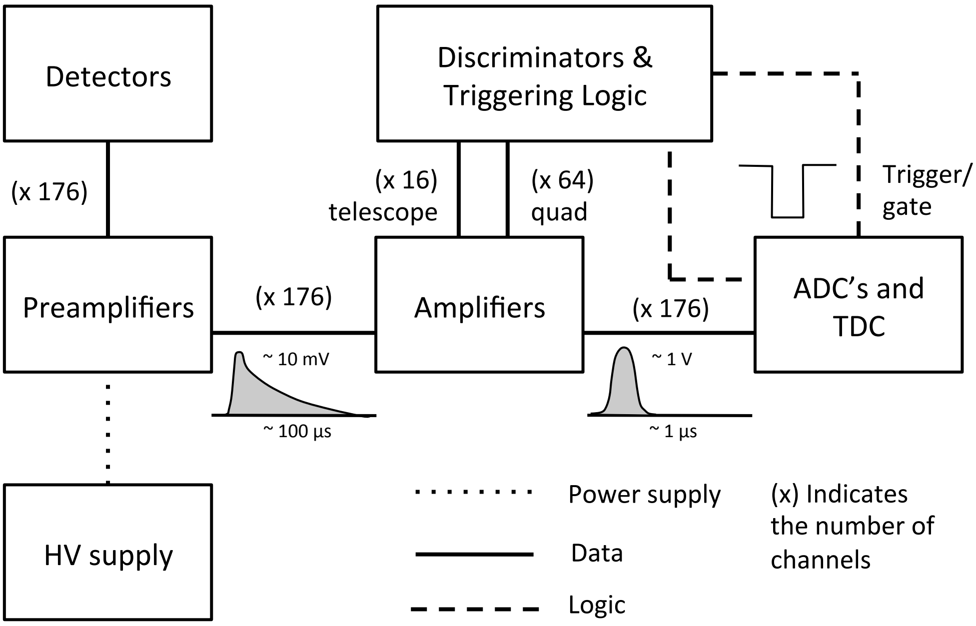

Figure 5.23: Chain of electronics used in the experiment. It is broadly the same as that used in the ^{9}Be experiment (figure 4.16). The main difference is the number of data channels, and that the signals from the telescope and Quad array of DSSDs are used separately in a more complicated trigger.

As an overview, the reverse biases for the DSSDs were applied via six Mesytec MPR 32-channel preamplifiers. The thick 500 μm detectors took a bias of 80 V and the thin 65 μm detector took 20 V. The signals from the detectors are integrated by the preamplifiers. These signals are then amplified by eleven 16-channel Caen N563B spectroscopy amplifiers. The signals from the front strips of each detector (apart from the thin ΔE) are passed to five 16-channel Caen V895 leading-edge discriminators, with thresholds around 350 keV. A *sum/majority* threshold of ≥ 3 hits across the Quad array was demanded in coincidence with an *or* trigger from the rear detector in the telescope, using the triggering logic shown in figure 5.24. This trigger produces a gate, which is sent to the six Silena VME 9418 ADCs. After this gate, the ADCs remain active for 5 μs and records the signals arriving from the amplifiers.

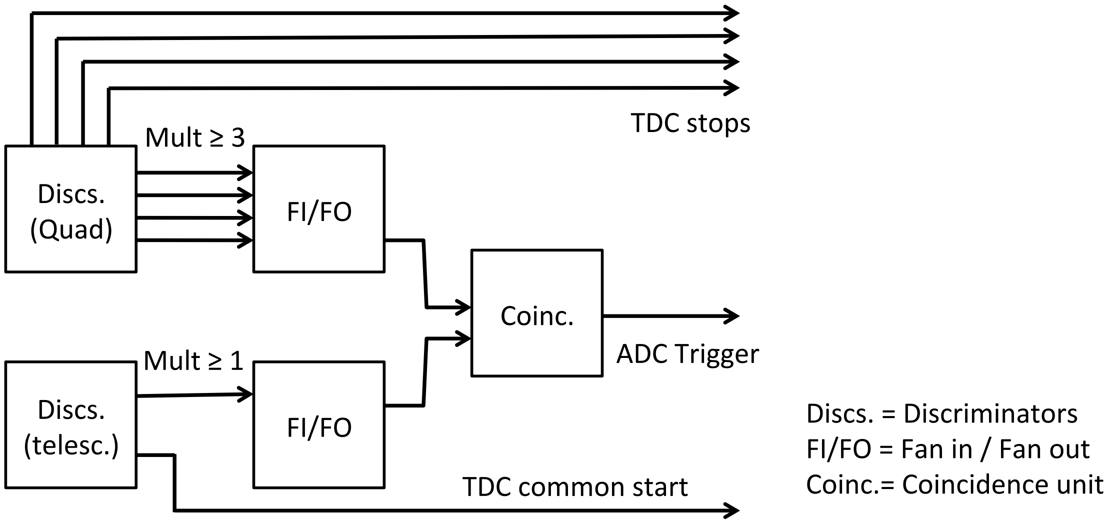

Figure 5.24: Triggering circuit for the experiment. The aim was to demand three hits in the quad arrangement of DSSDs, in coincidence with a single hit in the $\Delta E - E$ telescope. In addition to triggering, the *or* outputs from the discriminators were input to the TDC.

In addition, some timing information was recorded through the Caen V775 time-to-digital converter (TDC). The TDC range was set to 5μs. Here, the times of the *or* outputs from the discriminators for each detector in the Quad array were recorded with respect to a common TDC start signal coming from the *or* of the rear telescope detector. During the 5 μs ADC gate, signals corresponding to more than one reaction may enter the ADCs and be saved as part of the same event. However, these random coincidences will arrive at a different time to the genuine event in the ADC window. Having the trigger times of each detector could help to suppress these contributions. However, there were some synchronisation problems interfacing the Silena ADCs with the Caen TDC into the same data stream. In the end, the timing information was not utilised.

The timing information would have provided some level of selectivity, however, our ability to distinguish random and real coincidences is reduced in this set-up due to the leading-edge discriminators. These cause an effect known as *time walk* in the timing signal, which leads to a poor time resolution. In specialist timing circuits, superior resolution can be achieved by using constant-fraction discriminators.

5.7 Monte-Carlo simulations

As was seen in chapter 4, Monte-Carlo simulations are essential for a quantitative analysis of experimental results, and to compare with theoretical predictions. In the case of the ^{9}Be experiment, Monte-Carlo simulations were used to determine the experimental efficiency and resolution as a function of ^{9}Be excitation energy. In this study, the experimental data were compared to the results of Monte-Carlo simulations of the break-up reaction, in order to extract the direct 3α decay branching ratio. Therefore, it was important to ensure that the simulations are an accurate reflection of the experiment. Hence, at each stage of the data analysis, the experimental data are compared with the Monte-Carlo-generated events, in order to check for consistency. For these reasons, an initial discussion of the Monte-Carlo simulations is useful.

The simulations detailed in this chapter are structured into three parts as follows.

Firstly, the physical reaction process and reaction kinematics are generated. The Monte-Carlo events were generated using the same code as detailed in section 4.4.1 (references [101, 102]). This code calculates the reaction process as a sequential break-up: a lineage of independent two-body decays that lead from the initial to the final state. Therefore, extra subroutines were written to generate the various direct decay processes. Beam energy spread and beam divergence were included when generating ^{12}C(α,α)3α break-up reactions using this code. Isotropic angular distributions of the particles were chosen due to the angular momentum of the reaction of interest, but more complicated anisotropic distributions can be included at this stage.

Secondly, due to the unique detector geometry (incompatible with the general Monte-Carlo code), all generated events were output to a file and the other experimental effects (listed below) were enforced in a separate sort code. Thirdly, this code was used to analyse the simulated data in the same way as the experimental data. This way it is subject to the same data reduction cuts as the experimental data in order to permit a meaningful comparison.

Experimental effects

1. Energy loss of the beam in the target

2. Energy losses of the reaction products in the target
3. Angular and energy straggle in the target
4. Angular straggle in the front face of the DSSD telescope
5. Angular granularity of the detector strips
6. Energy resolution of the detectors (see section 5.8.2)
7. Pile-up of hits on the same strip
8. Background due to event mixing
9. Mis-assignment of hit positions when multiple particles hit the same detector

The majority of these effects were included in the simulations detailed in section 4.4.1. Effects 8 and 9 were not included in any previous simulations but are important when analysing this data set.

Effect 8

Effect 8 simulated the background due to event mixing. As mentioned in section 5.6.3, due to the relatively high 6 enA beam current, particles from two separate reactions may hit the detector array during the 5 μs window of the ADCs, registering as a single event. This produces an unavoidable background since it is a limitation of the measurement apparatus. This could have been reduced to an extent, using the timing of the detections, but this could not be implemented. It is, therefore, important to correctly include this event mixing effect in the Monte-Carlo simulations of the measurement process.

It was first necessary to confirm that the background was really due to event mixing. Since this effect should scale linearly with the beam current, several short experimental runs at varying beam currents were recorded. The excitation spectra for ^{12}C were measured (see section 5.8.4 later) and the total peak-to-background ratios were recorded as a function of the beam current. A plot of this is shown in figure 5.25. A clear correlation was observed, indicating that event mixing plays a significant part in this experimental background. However, extrapolating a linear fit back to zero beam current does not lead to a zero background. This indicates that an extra background is present. This was attributed to measuring decays from the tail of the known broad 0^+ state at 10.3 MeV. Since the shape of the background did not significantly change depending on the beam current, it was proposed that the extra background could be phenomenologically modelled as a higher level of event mixing.

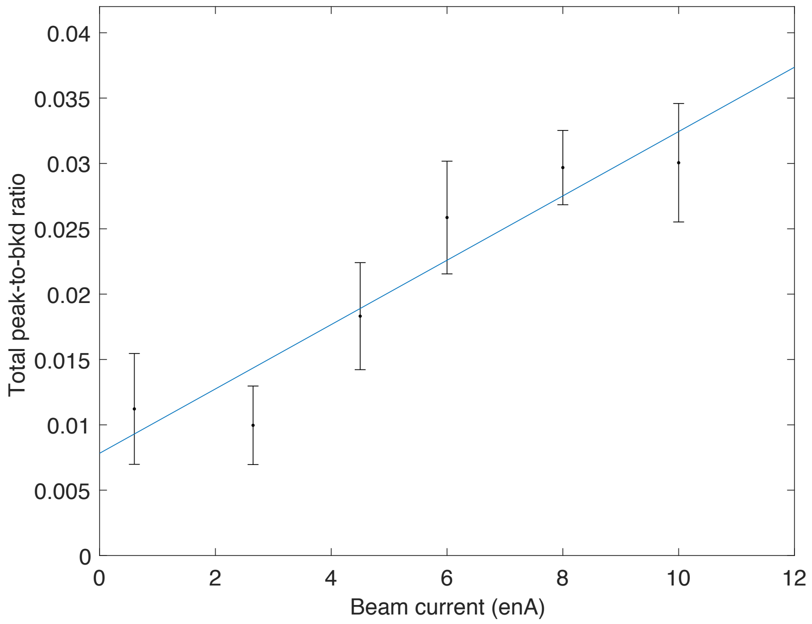

Figure 5.25: Plot of the total Hoyle state peak-to-background ratio for the ^{12}C excitation spectrum (see figure 5.36 later for a spectrum). Extrapolating to zero beam current does not give zero background. Therefore, a small background source, around 1/3 of the amount at 6 enA beam energy, remains.

Since multiple states in ^{12}C are populated in the experiment, not just the Hoyle state, and particles associated with these events may be measured in coincidence with a genuine Hoyle state break-up, simulations of the break-up of the 9.6 MeV 3^- state in ^{12}C were also included. The ratio of events corresponding to this reaction and the Hoyle state break-up were guided by the experimental data (peak areas in figure 5.36, seen later). The probability of event mixing in the simulations was adjusted so that the peak-to-background ratios in the simulations, matched those of the experimental spectra.

The event mixing was implemented in the Monte-Carlo sort code. When reading in simulated events one-by-one, the energies and directions of each particle in the event were saved. Then, when reading in the next event, a random number was generated. If this number was below the predefined event mixing probability, one of the saved particles from the previous event, chosen at random, was added to the current event. No further selectivity on the event mixing meant that this should most accurately reflect the true random process. Of course, it is possible that two random particles may be measured in coincidence with another event. This process is less probable and was not added to the simulation, since the single particle mixing well-reproduces the experimental background.

Effect 9

The process of mis-assigning the hit positions of particles on a detector is illustrated in table 5.1 and figure 5.26.

part.	E	σE_f	σE_b	ord. f	ord. b	E'_f	E'_b	ord. f	ord. b
α	6	0.4	0.5	1	1	5.9	5.8	1	1
β	5.5	0.4	0.5	2	2	5.6	5.7	2	2
α	6	0.4	0.5	1	2	5.9	5.7	1	2
β	5.5	0.4	0.5	1	2	5.6	5.8	2	1
α	6	0.4	0.5	1	2	5.7	5.9	2	1
β	5.5	0.4	0.5	1	2	5.8	5.7	1	2
α	6	0.4	0.5	1	2	5.8	5.9	2	2
β	5.5	0.4	0.5	1	2	5.6	5.7	1	1

Table 5.1: Illustration of the mis-assignment of hit positions of particles on the same DSSD. Particles α and β have simulated energies E. They each deposit a signal in a front and back strip. The energy orders of the two front, or two back strips that fire are given by ord. f and ord. b. The front and rear strip energies are smeared by σE_f and σE_b to give new energies E'_f and E'_b. These may have a new energy order (ord. f and ord. b). If this is the case, their hit positioned are switched horizontally, vertically, or both. Rows separated by horizontal lines from top to bottom are depicted in figure 5.26 panels a) $-$ d).

The Monte-Carlo simulations are powerful, because the parameters of each reaction product are known prior to applying any experimental resolution effects. Therefore, we know exactly which particle hits which strip, and what their energies are. This information can be saved before the experimental effects are applied. We know which strips the particles hit and what the energy resolution of each strip is (see section 5.8.1). The energy resolution can then be applied randomly to the simulated data. By ordering the energies collected by the front and rear strips *after*

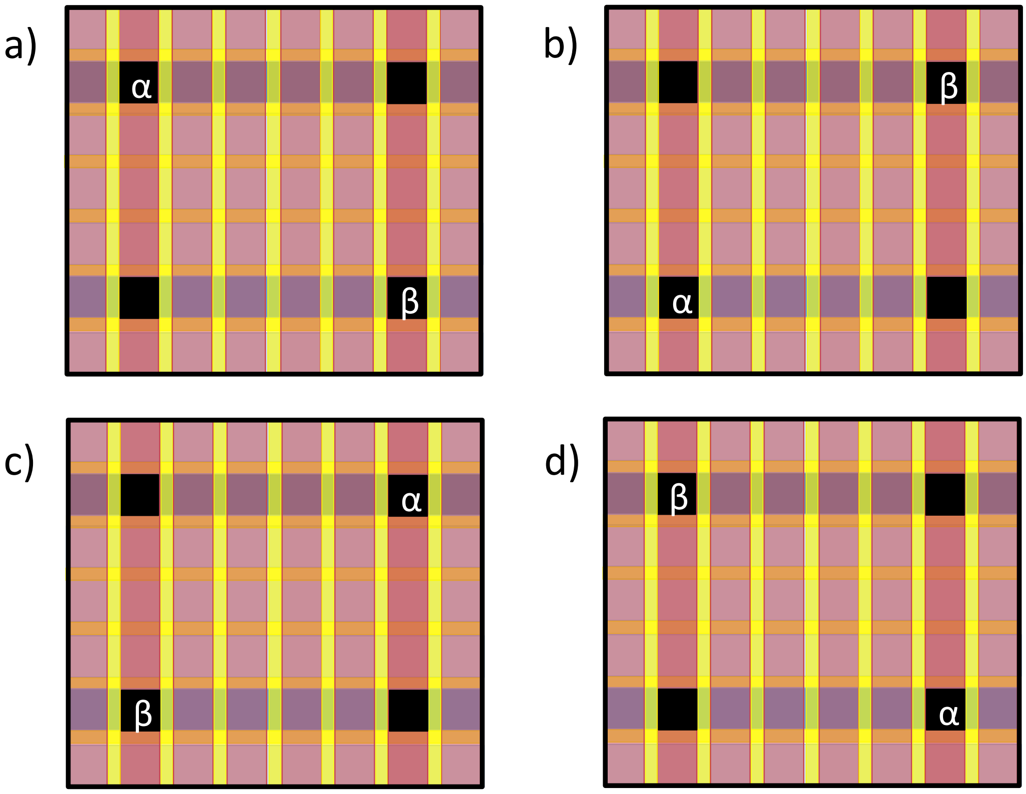

Figure 5.26: Figure relating to table 5.1. Illustrating how the deduced hit position of two particles changes if the energies detected by the front and rear strips change order between the two particles, α and β. Panels: a) The correct hit positions; b) If the rear energies become switched; c) if the front energies become switched; d) If front and rear energies become switched.

these effects have been applied, the front and rear strips can be matched in energy, providing two hit positions by the crossing points. However, if the energy order of two of the particles are swapped, for either the front or rear strips, or both, then the deduced hit positions are incorrect.

This effect has no impact on the cleanest subset of data, corresponding to the hit pattern where one particle strikes each DSSD. In this case, the hit position of a particle is ambiguously defined in both the experimental data and the simulations. It is important when considering the case where two α-particles hit the same detector. As shall be seen in section 5.8.6, the data for this second hit pattern has a higher background, which is well-reproduced by this position swapping effect.

5.8 Primary analysis and data reduction

The data recorded during the beam run were analysed within the SUNSORT framework [93] using Fortran sort codes. The aim of the primary data analysis stage is to convert the raw data recorded during the beam run into the various spectra for the ^{12}C nucleus, allowing as little experimental background through to these spectra as possible.

For this experiment the primary analysis can be separated into several stages. Firstly, a calibration of the detectors is required in order to convert the ADC values into energies and to verify the measured positions of the detectors. The experimental energy resolution of the detectors was then determined. The remainder of the primary analysis can be separated into several event filtering and calculation steps that shall be described in more detail throughout the following sections.

5.8.1 Detector energy and position calibration

The aim of detector energy calibration was to convert the amplitude of the raw voltage pulses recorded by the ADCs into units of energy. This was achieved by examining the responses of the detectors when measuring quanta of a known energy. The detectors were exposed to a mixed α-emitting source of ^{239}Pu, ^{241}Am and ^{244}Cu (α-particle decay energies of ^{239}Pu: 5.105 (11.9%), 5.143 (17.9%), 5.155 (70.8%) MeV, ^{241}Am: 5.388 (1.7%), 5.443 (13.1%), 5.486 (84.8%) MeV and ^{244}Cu: 5.763 (23.1%) and 5.805 (76.9%) MeV).

In each case, exposing the detectors to the source allowed an energy spectrum to be constructed for each individual detector channel. An example spectrum is shown in figure 5.27 a). Fitting a Gaussian line shape to each peak allowed their centroids to be extracted. The most intense peaks in the spectrum correspond to the strongest transitions for ^{239}Pu, ^{241}Am or ^{244}Cu. Less intense lines can also be seen as lower energy tails, which correspond to weaker transitions in each of the isotopes. For high-resolution detector channels, the various transitions can be resolved, leading to the situation shown in figure 5.27. For detector channels with poorer resolution, the weaker transitions in each isotope were phenomenologically modelled as a second peak. In these cases, a total of six peaks were fit, and only the most intense peaks were considered. The average resolution for individual strips was around 35 keV.

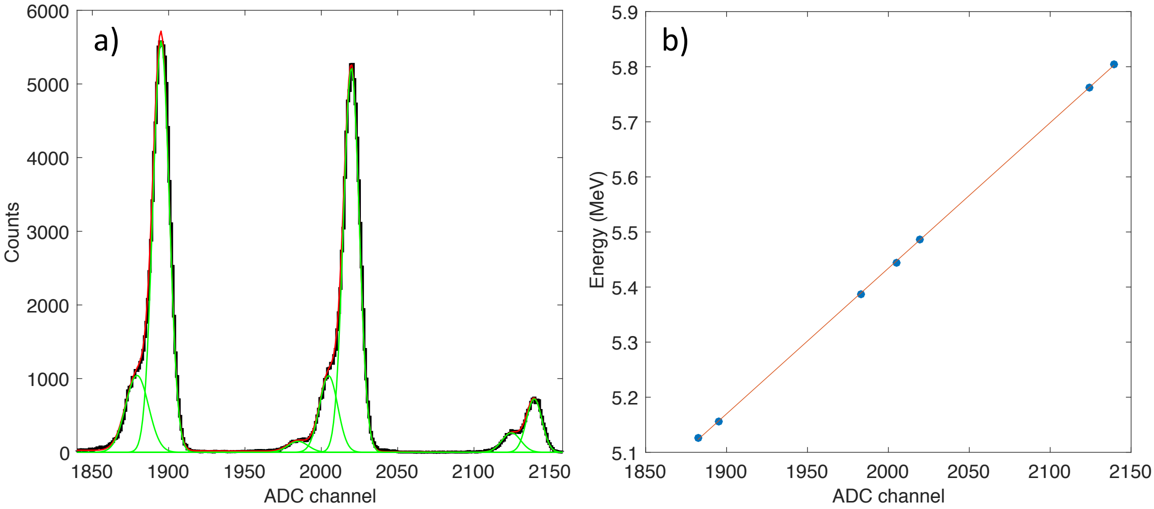

Figure 5.27: a) A total of seven Gaussian peaks fitted to a raw α-particle calibration spectrum from a single detector channel. b) A plot of peak centroid *vs* α-particle energy.

The centroids of the peaks were then plotted against the known α-particle energies and linear least squares fits were performed as shown in figure 5.27 b). For poor resolution channels, only the three strongest transitions were included in the fit. This allowed the relationship between signal amplitude and energy to be determined for each detector channel. A total of 176 detector channels were calibrated, corresponding to each strip in the detector array. Since the experimental measurements were performed intermittently over several weeks, recalibration was performed for each experimental run. A total of five such calibrations were performed over the course of the experiment.

The break-up α-particles striking the Quad array have energies close to those of the calibration source, which means that the above process works well for these detections. However, the scattered beam striking the 90° telescope has energies up to around 17.5 MeV. Given the uncertainty in the calibration gradients, this results in an extrapolation uncertainty of several tens of keV at these high energies. This effect is discussed further in section 5.8.2.

Several further considerations were made when calibrating the detector array, since an excellent energy calibration was required in order to achieve the highest experimental resolution. Firstly, a feature of the detectors that should to be highlighted here is the very thin silicon dead layer of 100 nm, which covers the majority of the detector surface. The energy loss in this dead layer varies significantly as a function of the energy of the ion and was calculated to be ≈ 25 keV for 1 MeV ^{4}He ions and ≈ 9 keV for 10 MeV ^{4}He ions. However, as previously noted, due to the arrangement of the quadrant detectors, the average lab frame energy of the break-up α-particles from ^{12}C, is very close to the 3α calibration energies. This means that any systematic energy shift due to the dead layer is approximately constant between calibration and experiment for measuring the break-up α-particles. Therefore, the energy loss through the dead layer is taken into account in the energy calibration. The DSSD telescope detects the scattered beam, which is much higher in energy than the calibration sources. Therefore, a small systematic error in this energy is expected.

A more significant systematic effect concerns the energy losses of the calibration α-particles in the source itself. The source consisted of a steel disk with one face thinly coated in a layer of radioactive material of unknown thickness. Particles emitted at various angles with respect to the normal of the disk will emerge with different energies, since they will, on average, traverse a greater or lesser thickness of the source material. A short experiment was performed in order to measure the energies of the α-particles as a function of their emission angle. A schematic diagram of the set-up is shown in figure 5.28 a) and the results are shown in figure 5.28 b). As expected, for greater emission angles, the energy of the calibration particles is lower. To minimise this systematic effect to < 2 keV, the calibration source was positioned such that the maximum angle subtended by the detectors, with respect to the normal of the source, was 10°.

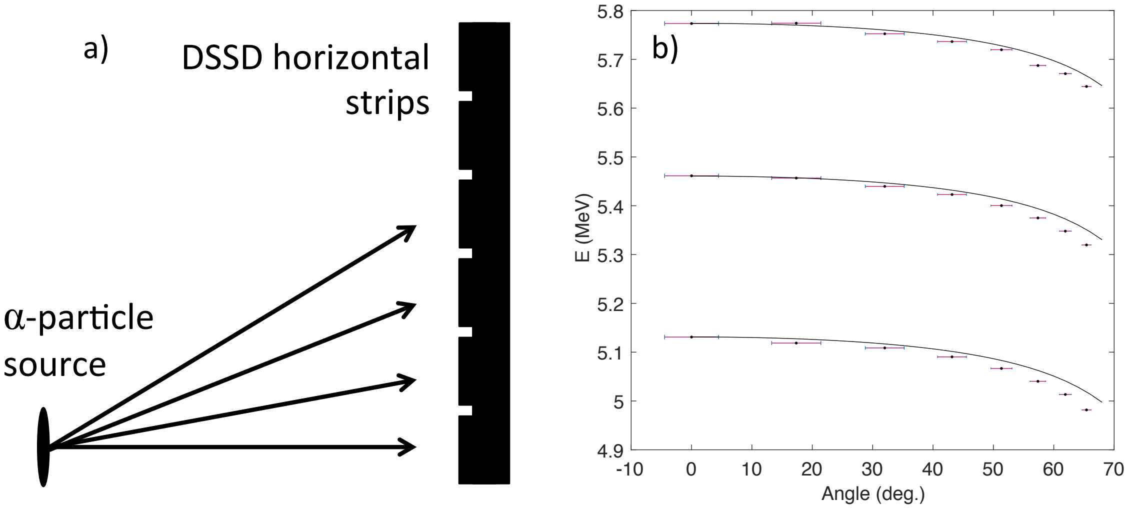

Figure 5.28: a) Schematic diagram of the set-up used to measure the energy losses of the calibration α-particles in the source. b) A plot of the average α energy *vs.* the angle of emission from the source. The points show experimental data and the line shows the Bethe formula prediction for ^{4}He ions travelling through a 0.55 μm-thick even mixture of ^{239}Pu, ^{241}Am and ^{244}Cu. To obtain plot b), the detector strips were calibrated in energy at zero degrees, since this is where the energy losses are minimal. The calculations assumed a linear energy loss through the source material, which causes the disagreement between the experimental data and the Bethe formula prediction at large angles.

The detectors were positioned in the chamber using a ruler, so their positions were only known to an accuracy of around 3-5 mm. The positions of the detectors were further calibrated by measuring scattering of the ^{4}He beam from a carbon target at 12.3 MeV and 40 MeV beam energies. Known two-body kinematic formulae (see appendix C) were used to determine what energy the α-particles should be when entering a particular detector strip after scattering. This was compared with the detected energy after the α calibration. Any discrepancies highlighted systematic errors such as slightly incorrect detector positions and angles and allowed for their correction in the analysis code. Only minor corrections were required. The energies of the detected α-particles as a function of their total scattering angle are shown in figure 5.29.

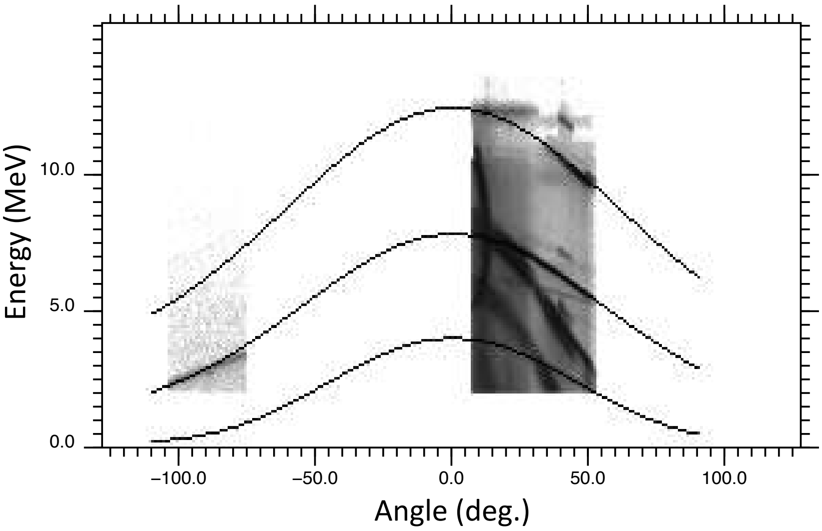

Figure 5.29: The energies the scattered α-particles as a function of their angles for a beam energy of 12.3 MeV. The position of the telescope was calibrated with a 40 MeV beam energy and the Quad array was calibrated with a 12.3 MeV beam energy. The positions of the detectors were slightly adjusted so that the kinematic predictions (black lines) best overlaid the experimental kinematic lines. The calculated kinematic lines correspond to populating the recoiling ^{12}C in its ground state, 4.4 MeV 2^+ state and 7.65 MeV 0^+ Hoyle state.

Summary

Using a mixed α-emitting source, each detector channel was calibrated in energy. The source was positioned a sufficient distance away from the detectors such that the energy losses of the α-particles in the source itself were minimised. The average resolution for individual strips was determined to be around 35 keV. When accurately calibrated in energy, the energies of a scattered beam of α-particles were analysed as a function of their scattering angle. This allowed any small discrepancies in the measured detector positions to be corrected.

5.8.2 Detector energy resolution

By measuring a source of α-particles, the energy resolution was seen to be around 30-40 keV, depending on the strip. However, it was noticed that the true experimental resolution is much poorer than this, when measuring nuclear reactions using the cyclotron beam. The resolution was observed to become poorer for higher beam currents. The reason for this will be explored later. It was important to quantify the true resolution so that the Monte-Carlo simulations are accurate.

A novel method was used to determine the detector energy resolution. Upon detecting a particle, the same number of electrons should be collected by the rear strip as the number of holes by the front strip. This would result in identical pulses (of opposite polarity) registering the same energy. However, due to the resolution of each strip, that is not the case; there will be a difference between the energies collected. If front and rear strips are assumed to have the same resolution, σE, then the difference in energy between the front and back strips $\Delta E = E_f - E_b$ will follow a distribution with $\sigma \Delta E = \sqrt{2}\sigma E$. By measuring this distribution, $\sigma \Delta E$ may be measured and the strip resolution, σE then inferred. The measured ΔE distributions for different beam currents are shown in figure 5.30.

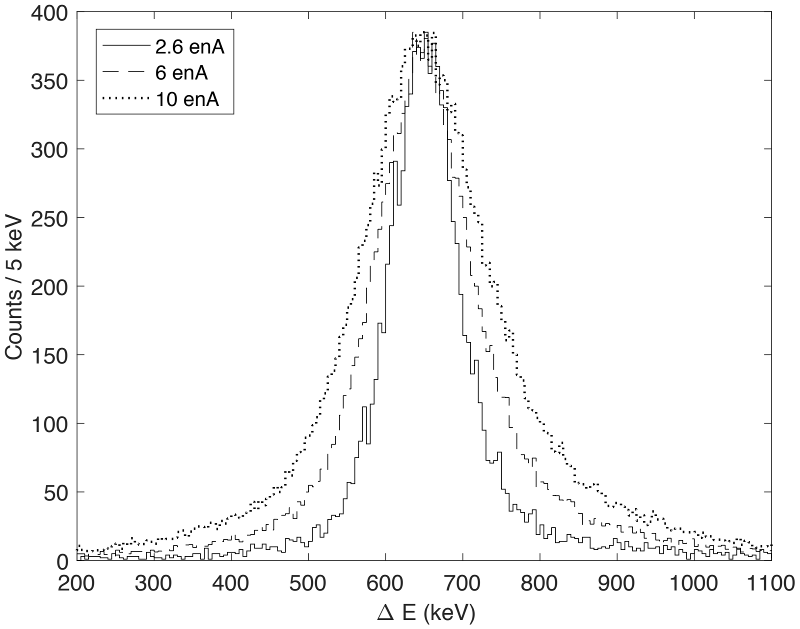

Figure 5.30: Normalised distributions of the ΔE quantity for various values of the beam current.

A plot of the average detector resolution σE as a function of the beam current, is shown in figure 5.31. The resolution is seen to be approximately linearly dependent on the beam current. Extrapolating the linear fit back to zero beam current reproduces a value close to the observed resolution when measuring the α-source.

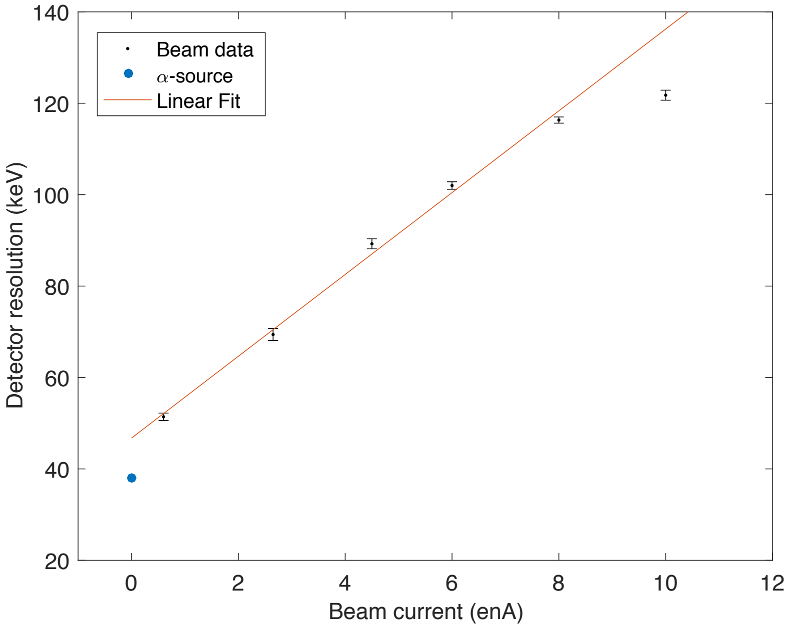

Figure 5.31: The average detector resolution as a function of the beam current. The points with error bars show the beam data, the circular point shows the resolution for the α-source, and the line shows a linear least squares fit to the first 4 points.

As the high-intensity beam passes through the target, atoms of the target material are ionised, providing low energy delta electrons and X-rays. When these strike the front of the detector they will increase the baseline electronic noise, leading to a worsening of the resolution. Since the flux of these particles will depend on the beam current, it makes sense to see a linear dependence of the resolution on the beam current. To minimise this effect, a magnetic field between the source and the detectors would readily draw the electrons away from the detectors, while leaving the paths of the heavier reaction products relatively unperturbed. It is worth noting that the E detector of the $\Delta E - E$ telescope, at 90° to the beam, showed a weak dependence on the beam current. This is expected since it is far away from the beam direction and has a thin ΔE detector to shield it from delta electrons.

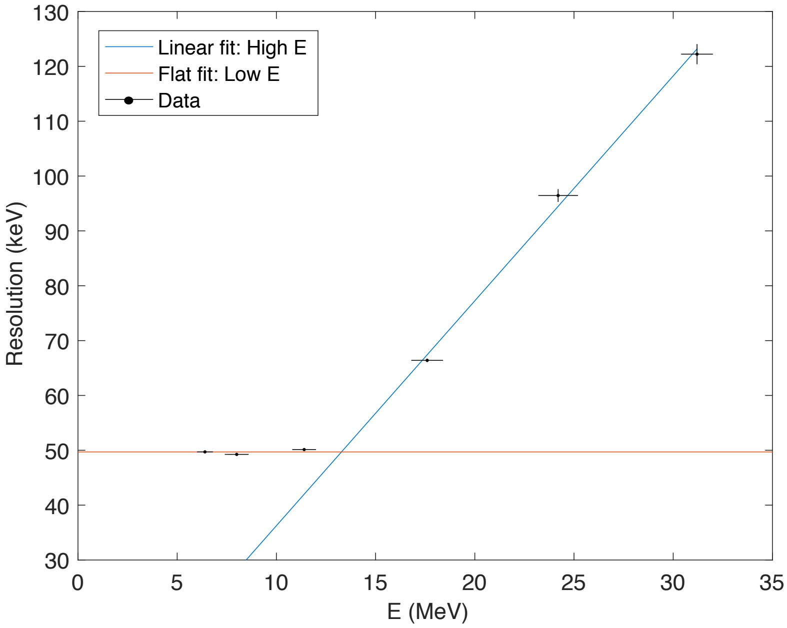

Figure 5.32: The measured resolution as a function of the particle energy, for the rear detector in the $\Delta E - E$ telescope.

As mentioned in section 5.8.1, the scattered beam into the $\Delta E - E$ telescope has energies ranging from 11.5 - 17.5 MeV, considerably higher than the ≈ 5.5 MeV calibration sources. When extrapolating to higher energies, any uncertainty in the measured energy, due to the calibration fit gradient, is linearly amplified. This means that the effective experimental resolution across the detector is worse at these higher energies. To quantify this effect the experimental data at 6 enA beam current were analysed. The width of the $\Delta E = E_f - E_b$ distribution was tracked as a function of incident particle energy. This allowed the resolution, σE, to be calculated as before. The results are given in figure 5.32. For low energies, the resolution is approximately constant, as signified by the horizontal fit line. At higher energies the resolution is seen to depend linearly on energy. At 17.5 MeV, the resolution is around 14 keV worse than at low energies. This effect needed to be included in the Monte-Carlo simulations.

Summary

The resolution of the detectors was found to be different when measuring reactions using a high intensity beam of particles, compared with when measuring radiation from the α-particle source. This was quantified by measuring the difference in the energy collected by the front and rear strips when a single particle was detected. The resolution was seen to have a linear dependence on beam current. This was attributed to the fact that when exposed to the beam, atoms of the target material are ionised, providing low energy delta electrons and X-rays, which strike the detectors. Furthermore, the detector energy resolution was seen to worsen linearly at energies higher than 12 MeV. This is due to the fact that the detectors were calibrated in energy with points around 5 MeV. Uncertainties in the fit gradient meant that extrapolations to higher energies may deviate away from their true values in a linear fashion. These effects were incorporated into the Monte-Carlo simulations of the reaction.

5.8.3 Particle identification telescope, hit multiplicities and hit patterns

Once the detector channels are calibrated in energy, the next step is to check for the required hit pattern of particles across the detector array. A single α-particle (scattered beam) detected in the DSSD telescope in coincidence with three break-up α-particles in the quad array were demanded for each valid event, since this is the expected distribution of hits for the desired reaction. Although this condition is imposed electronically in the trigger for the ADCs, inevitably some measured events do not meet these criteria, and further event selection in software is required.

The pair of DSSD detectors on one side of the beam axis are designed to collect the scattered α-particle which is expected to have an energy between 11.5 and 17.5 MeV if the 7.65 MeV Hoyle state is excited in the reaction. Their telescope configuration, where the thin 65 μm detector is followed by the thick 500 μm detector, permits the charge and mass of the detected particle to be determined. A particle of energy E will deposit a fraction of its energy ΔE in the thin detector. The remaining energy E' is picked up by the thick, rear detector. The energy lost in the thin detector is governed by the non-relativistic Bethe formula [97] (often known as the Bethe-Bloch formula) which approximates the mean stopping power of ions in different media as

$$-\frac{dE}{dx} = \frac{4\pi n z^2}{m_e v^2}\left(\frac{e^2}{4\pi\epsilon_0}\right)\left[\ln\left(\frac{2m_e v^2}{I}\right)\right], \tag{5.41}$$

where v is the velocity of the ion, z is its charge, m_e is the electron mass, ϵ_0 is the vacuum permitivity, I is the mean excitation potential of the medium. The electron number density of the material is denoted by n, which is calculated as

$$n = \frac{N_A Z \rho}{A M_u}. \tag{5.42}$$

Here, N_A is Avogadro's number, Z is the atomic number of the medium, A is the atomic mass and M_u is the molar mass constant. Under the assumption of a thin detector, where the energy of the ion does not change significantly as it passes through ($\Delta E \ll E$) then ΔE is proportional to equation 5.41. In other words, the energy loss of the ion in the medium is inversely proportional to its energy E and proportional to the square of its charge.

For each event where a signal is collected by both the front and rear detectors in the telescope, giving energies of ΔE and E' respectively, a plot of ΔE *vs.* $E' + \Delta E$ (E) can be constructed. Such a plot for the data acquired during the experiment is shown in figure 5.33. Different types of detected ions are signified by the loci of high intensity and follow a hyperbolic form. Due to the form of equation 5.41, particles with the same z are plotted in broadly similar regions on the plot. The different isotopes which have the same z but different mass provide the finer structure. The different ions are marked on figure 5.34 based on the predictions of equation 5.41.

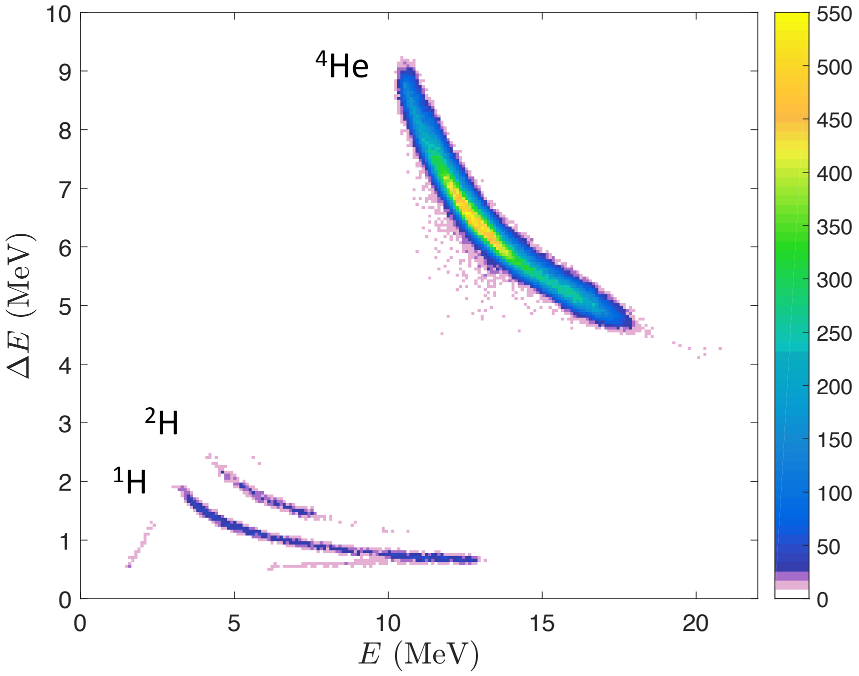

Figure 5.33: Plot of ΔE *vs.* E for the particles scattered into the telescope arrangement. Data are shown with a linear intensity colour scale. Since there was a high beam current of ^{4}He ions, the most intense band corresponds to these particles.

The difference between the prediction for ^{4}He ions and the data, is because when the incident ion has low energy, the approximation that the particle loses energy linearly in the thin ΔE detector is less valid, meaning that the energy deposited here is not proportional to equation 5.41. The deposited energy is actually higher than what is predicted. The energy cut-off on the

ΔE axis is due to the energy threshold of the thin DSSD. By placing a software gate around the α-particle region, the number of considered events drops by a factor of 33% (67% of original data are considered for further analysis).

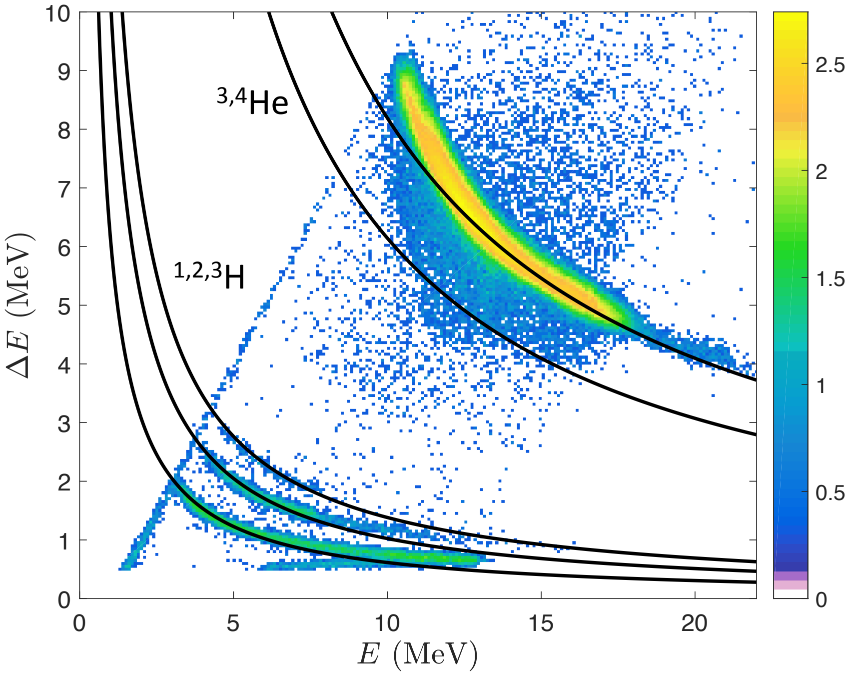

Figure 5.34: Plot of ΔE *vs* E for the particles scattered into the telescope arrangement, with a logarithmic (base 10) colour scale. The predictions of the Bethe formula (equation 5.41) are shown for various ions by the black lines.

Once this cut has been placed, the event multiplicity across the quad array of DSSDs was evaluated for each event. The event multiplicities are shown by the bar plot in figure 5.35. Since this array of detectors should collect the α-particles resulting from the break-up of ^{12}C, then the maximum number of particles detected should be three. A higher multiplicity is a sign of measuring contaminant reactions or event mixing due to the relatively high beam current. Indeed, the multiplicity sharply drops for numbers greater than three.

Only complete kinematics events were considered for this measurement, in order to achieve the cleanest, highest resolution data. Therefore, only multiplicity-3 events were considered for further analysis. This event selection stage had a 14% efficiency, meaning that this fraction of data were considered for further analysis. To more cleanly select the reaction of interest, particle detections had a threshold of 3 MeV set in the software, since the break-up α-particles resulting from the decay of the Hoyle state will have energies greater than this. Up to this point, it is known from the particle identification telescope that a ^{4}He ion has scattered into the telescope. It is also known that this was measured in coincidence with three hits across the quad detector array. The distribution of particles across the detector array is consistent with the inelastic scattering from ^{12}C and a subsequent break-up into three α-particles.

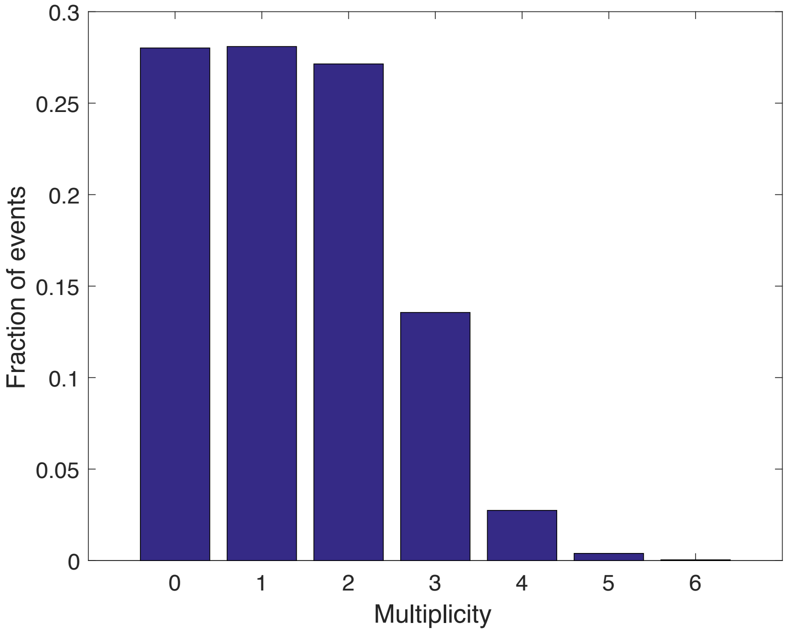

Figure 5.35: The relative frequencies of hit multiplicities measured across the quad array. Since the Hoyle state breaks up into three α particles, the frequency is expected to drop sharply beyond this multiplicity.

Section 5.6 described that the four DSSDs were chosen to operate within a quadrant geometry for two reasons. Firstly, four detectors further back from the target provide a superior angular resolution than a single detector which is closer to the target. Secondly, this geometry permits each α-particle from the ^{12}C break-up to strike a separate DSSD; when two particles with a similar energy hit the same detector their hit positions may be swapped, leading to an intractable background. From here in the analysis, the data were split into two categories. The first category corresponds to the case where each α-particle strikes a separate DSSD. The second category corresponds to where two particles do strike the same DSSD and the third strikes a separate detector. Of the multiplicity-3 data, 21% occupied category one, and 73% occupied category two. The remaining 6% of data occupy a third category, where all three α-particles hit the same DSSD. These relative values agree with the results of the Monte-Carlo simulations.

Summary

The ΔE-E telescope arrangement of detectors, designed to collect the scattered α-particle beam, was shown to allow the identification of particles with different charges, Z, and different masses, A. The data follow the relationship predicted by the Bethe-Bloch formula. A software cut was placed in order to focus on the detected α-particles, while ignoring the contributions of other ions. For these events, the number of particles detected by the quad array of DSSDs was evaluated. A histogram of the multiplicities showed a sharp drop after a multiplicity of three, indicating the break-up of ^{12}C into three α-particles.

5.8.4 Excitation, total energy, and total momentum spectra

Excitation spectra 1

Excitation energy spectra were calculated for the ^{12}C nuclei excited during the reaction. Firstly, the excitation energies were calculated by using the scattered ^{4}He beam, which was detected in the telescope configuration. As described in section 4.3.7 for the ^{9}Be experiment, using momentum conservation between the initial and final states, it was possible to calculate the momentum of a proposed recoiling nucleus (^{12}C in this case) as

$$\overrightarrow{\mathbf{P}}(^{12}\mathrm{C}) = \overrightarrow{\mathbf{P}}_{\mathrm{beam}} - \overrightarrow{\mathbf{P}}_{\alpha}. \tag{5.43}$$

This quantity is calculated from the momentum of the scattered ^{4}He, $\overrightarrow{\mathbf{P}}_{\alpha}$, and the beam only. Knowing the momentum of the recoiling ^{12}C allows its kinetic energy $T(^{12}\mathrm{C})$ to be calculated. Using energy conservation, the excitation energy of the proposed recoiling ^{12}C can be calculated as

$$E_x = T(^{12}\mathrm{C}) + E_{\alpha} - E_{\mathrm{beam}}. \tag{5.44}$$

The resulting ^{12}C excitation spectrum, corresponding to the subset of data where the break-up α-particles are detected in separate DSSD quadrants, is shown in figure 5.36. The ^{12}C excitation spectrum, corresponding to when two break-up α-particles are detected in the same DSSD quadrant, is shown in figure 5.37. In both cases, the 0^{+} Hoyle state at 7.65 MeV is strongly populated, as is the 3^{-} level at 9.64 MeV. An excitation energy resolution of 570 keV FWHM was achieved for the Hoyle state. Data within $\pm 2\sigma$ of the Hoyle state peak centroids were considered for further analysis. These cuts had an average efficiency of 56%.

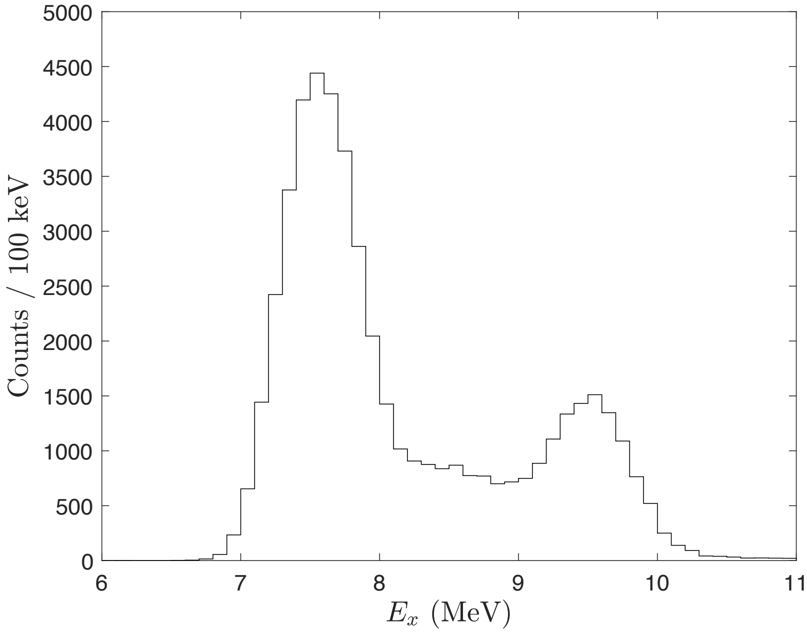

Figure 5.36: Histogram of the excitation energies of the recoiling ^{12}C, for the case that the three break-up α particles strike separate DSSDs. The Histogram shows 50,368 events.

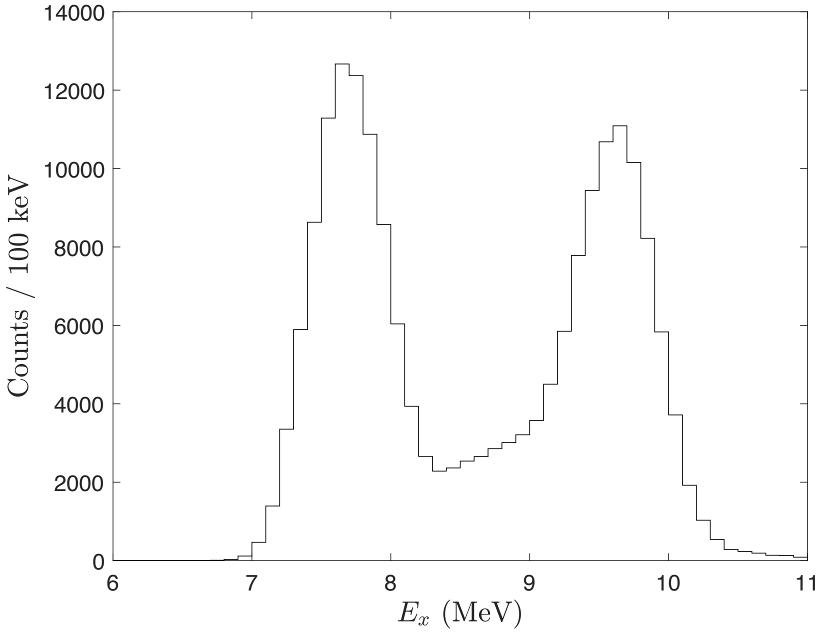

Figure 5.37: Histogram of the excitation energies of the recoiling ^{12}C, for the case that the two break-up α particles strike the same DSSD. The Histogram shows 194,095 events.

Total energy spectra

With a cut placed on the excitation energy of ^{12}C, the energies of the particles detected in the final state were summed. By subtracting the Q-value for the overall ^{12}C(α,α)3α reaction (-7.27 MeV) from the total 4α energy, the beam energy should be calculated.

Figures 5.38 and 5.39 show histograms of the calculated *total energies* for the experimental data. Figure 5.38 corresponds to the low-background situation where each α-particle from the ^{12}C break-up strikes a separate DSSD in the array. The data corresponding to when two break-up α-particles hit the same DSSD are shown in figure 5.39.

In each plot, the (red) line shows the results of Monte-Carlo simulations of the sequential decay reaction mechanism. The simulations include experimental resolution effects and event mixing for background. The peak widths ($\approx$300 and 350 keV) and the general background shapes are well-reproduced by the simulations. To minimise background events, only data within $\pm 2\sigma$ of the peak centroid were considered for further analysis. This cut had an 85% efficiency for the first hit pattern and an efficiency of 78% for the second hit pattern.

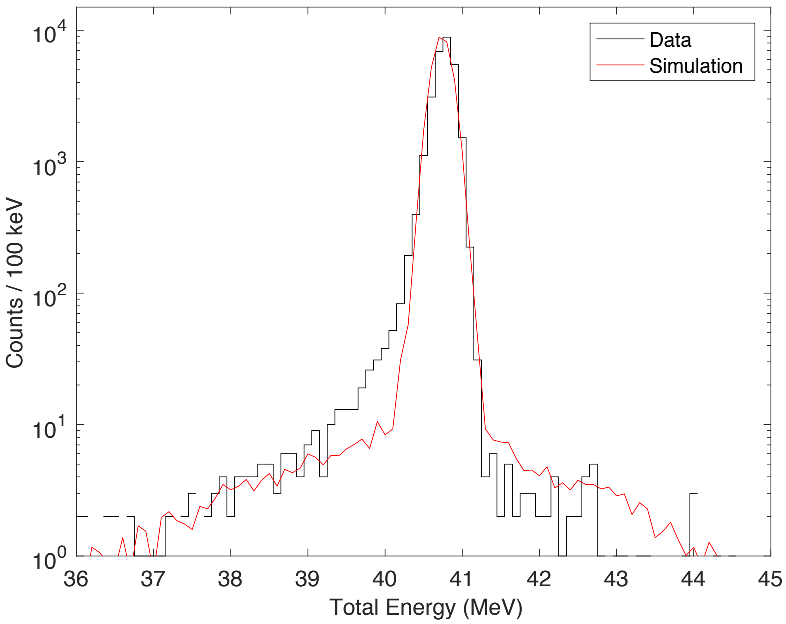

Figure 5.38: Histogram of the total energy of the particles measured in the final state, subject to the constraint that the three break-up α particles strike separate DSSDs. The histogram shows 28,252 experimental events and the (red) line shows 146,238 scaled Monte-Carlo events. Data are plotted on a logarithmic vertical scale.

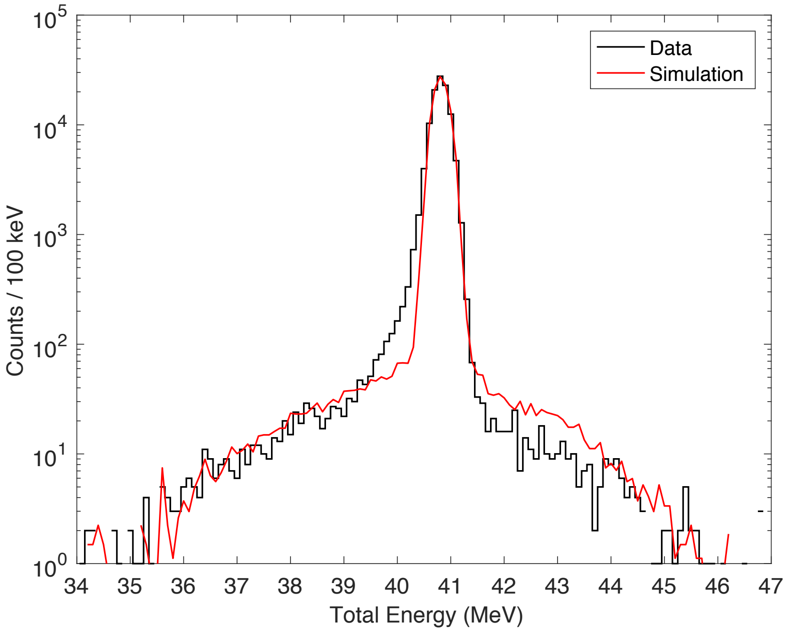

Figure 5.39: Histogram of the total energy of the particles measured in the final state, subject to the constraint that two break-up α particles strike the same DSSD. The histogram shows 109,004 experimental events and the (red) line shows scaled 161,583 Monte-Carlo events. Data are plotted on a logarithmic vertical scale.

Excitation spectra 2

With several software cuts in place, to ensure that decays from the Hoyle state are considered, and that the contributions from background processes are minimised, the excitation energy of ^{12}C was calculated again. This time it was calculated from the three α-particles resulting from the ^{12}C break-up. Since the excitation is now calculated without the beam energy (and its associated 200 keV energy spread) a superior excitation energy resolution is achieved. By using the measured momenta of the three α-particles, the momentum and kinetic energy of the decaying ^{12}C was calculated. Then the excitation energy of the decaying ^{12}C was calculated as

$$E_x = \sum_{i=1}^{3} E(\alpha_i) - T(^{12}C) - Q \text{ (where } Q = -\,7.27 \text{ MeV).} \tag{5.45}$$

The resulting ^{12}C excitation spectrum, corresponding to the subset of data where the break-up α-particles are detected in separate DSSD quadrants, is shown in figure 5.40. The histogram depicts the experimental data and the red line shows the results of the Monte-Carlo simulations. The 40 keV peak resolution and the general shape of the background are well-reproduced by the simulations. A software cut of $\pm 2\sigma$ about the Hoyle state peak was placed.

The ^{12}C excitation spectrum, corresponding to when two break-up α-particles are detected in the same DSSD quadrant, is shown in figure 5.41. The 42 keV peak resolution is well-reproduced but the background profile shows less agreement. The background levels between the experiment and simulation are around the same level in the region of the peak, but diverge in other parts of the spectrum. Once again, a software cut of $\pm 2\sigma$ about the Hoyle state peak was placed. The discrepancy between the experiment and simulation at higher excitations is likely due to the effects of higher energy resonances. The 0^+ level at 10.3 MeV has a 3 MeV width, meaning that the tail of this state is expected to manifest in the excitation regions near to the Hoyle state. For both hit patterns, the event mixing background used in the simulations well reproduce the measured spectrum in the region of the Hoyle state. This indicates that within the cut on the Hoyle state, the main contribution to the background is the event mixing, and that the contributions of higher energy resonances may be ignored.

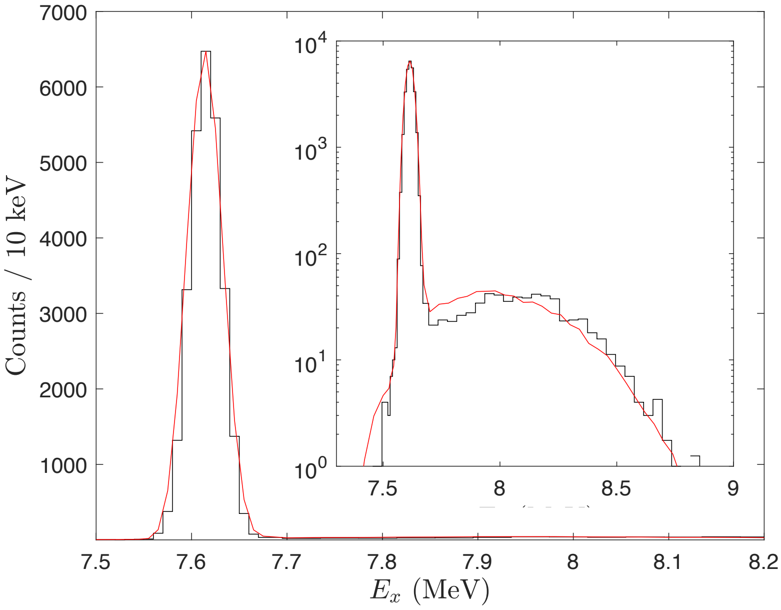

Figure 5.40: Excitation energy spectrum of ^{12}C calculated from the three break-up α-particles. Events are chosen where each α-particle is detected in a separate DSSD. A total of 2.4×10^4 events are plotted. The histogram depicts experimental data and the solid (red) line shows the results of Monte-Carlo simulations. The main panel shows the data on a linear scale and the inset uses a logarithmic scale for a closer examination of the background.

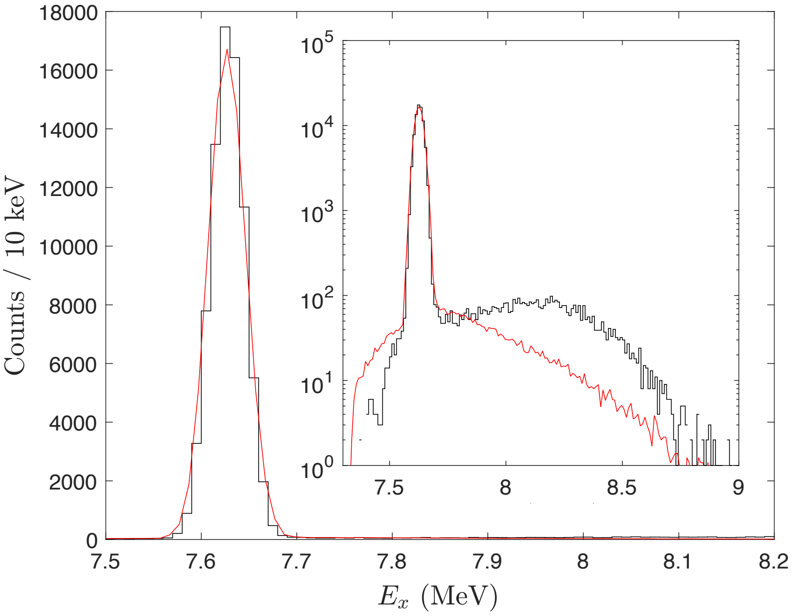

Figure 5.41: Excitation energy spectrum of ^{12}C calculated from the three break-up α-particles. Events are chosen where two α-particles are detected in the same DSSD. A total of 8.5×10^4 events are plotted. The histogram depicts experimental data and the solid (red) line shows the results of Monte-Carlo simulations. The main panel shows the data on a linear scale and the inset uses a logarithmic scale for a closer examination of the background.

Total momentum spectra

A final software cut was placed on the total momentum of each event in the x, y, z cartesian directions. The beam direction was chosen to be along the z-axis. This means that in the x and y directions, the total momenta of the final state particles must sum to zero. In the z direction, the total momentum, minus the beam momentum, should also be zero. For each event, the momenta in each of these directions were calculated and plotted as a histogram. The data, corresponding to the case where the three break-up α-particles were detected in separate DSSDs in the array, are plotted in figure 5.42. The data, corresponding to the case when two break-up α-particles hit the same DSSD are plotted in figure 5.43. The z-direction plot is shifted by the initial beam momentum for ease of comparing the three distributions. Only data that simultaneously lie within $\pm 2\sigma$ of each of these peak centroids were considered for further analysis. The peak centres are offset slightly from zero, which is where they expected to be found. This small systematic shift is a result of an imperfect measurement of the positions of the detectors.

Due to the number of software cuts in place, the data are very clean, and mostly consist of Hoyle state break-up events. However, despite this, a total of 20 counts can be seen outside of the main body of these peaks for hit pattern 1 in figure 5.42. Significantly more points can be seen beyond the tails of the peaks for hit pattern 2 in figure 5.43. This is due to the mis-assignment of the hit positions when two particles strike the same DSSD. Since the direct break-up process has such a small branching fraction, these counts are significant, and it is important that they are factored when calculating any branching ratio. Placing $\pm 2\sigma$ software cuts on the momentum peaks provides a way to minimise this background, however, some background exists beneath the peaks. Assuming that the background is uniform, with four counts in each bin (mean P_x background around the peak), around 50 background events are predicted to bypass this cut into the final spectra.

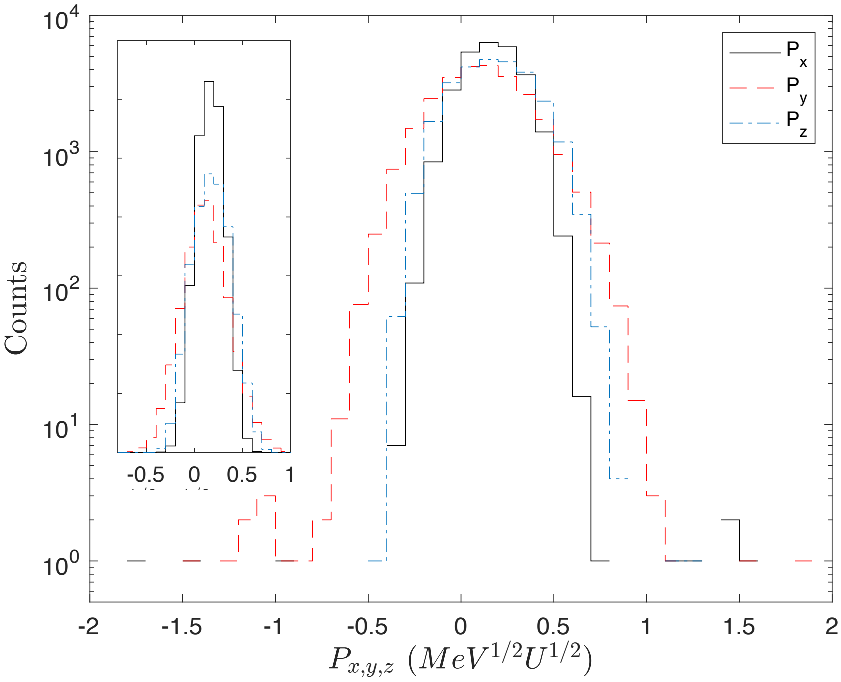

Figure 5.42: Distribution of the total momenta in the x, y and z directions. This plot shows data subject to the condition that the three break-up α-particles hit different DSSDs.

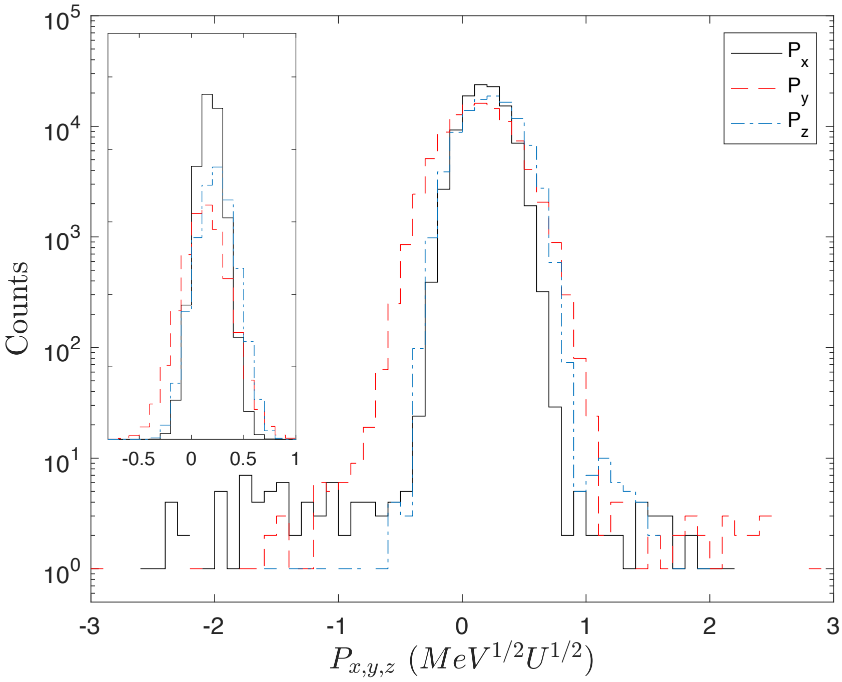

Figure 5.43: Distribution of the total momenta in the x, y and z directions. This plot shows data where two break-up α-particles hit the same DSSD.

Summary

The aim of this section of the analysis was to cleanly focus on events corresponding to the break-up of the ^{12}C Hoyle state into three α-particles. Data reduction was achieved in several ways. Firstly, for each hit pattern, the scattered α-particle detected in the ΔE-E telescope was used to reconstruct the excitation energy of the recoiling ^{12}C. The 0^+ Hoyle state at 7.65 MeV and 3^- state at 9.64 MeV were strongly populated. Software cuts were placed about $\pm 2\sigma$ of the Hoyle state peak centroids.

Then, the total energy of each event was calculated, and histograms were plotted. These total energy spectra, taking into account the break-up Q-value of ^{12}C, peaked at the correct beam energy. Again, software cuts were placed about $\pm 2\sigma$ of the total energy peak centroid. The peak widths and tails of the distribution were well reproduced by Monte-Carlo simulations. The backgrounds were due to event mixing and mis-match of the hit positions of the particles on the DSSDs.

Excitation energy spectra were calculated again, this time using the three break-up α-particles detected by the quad array of DSSDs. An excellent energy resolution of 40 keV was achieved and the small background profiles were well reproduced by the Monte-Carlo simulations. Software cuts were placed about $\pm 2\sigma$ of the Hoyle state peak centroids.

A final software cut was placed on the total momenta of the detected particles in each of the cartesian directions. A small amount of data were seen to lie beyond the total momentum peaks, which were excluded by placing software cuts about $\pm 2\sigma$ of the peaks.

Monte-Carlo simulations indicated that, after these software cuts were placed, only 0.03% of background events remained.

5.8.5 Break-up channel visualisation

The aim of the experiment was to determine if the Hoyle state in ^{12}C breaks up through an intermediate state in ^{8}Be (sequential decay) or through a direct process where the three break-up α-particles are emitted from the nucleus simultaneously. The sequential decay scheme is shown in figure 5.44 below. Here, the first decay stage has a decay energy denoted by Q_1. The first α-particle is emitted and shares the energy Q_1 with the ^{8}Be daughter. The energy sharing only depends on the masses of the two fragments, so the first α-particle receives an energy of 2/3 Q_1. This corresponds to around 1/2 of the total decay energy $Q_1 + Q_2$. In the second decay stage, with a decay energy of $Q_2 = 92$ keV, this energy along with the kinetic energy of the ^{8}Be fragment is shared between the two remaining α-particles.

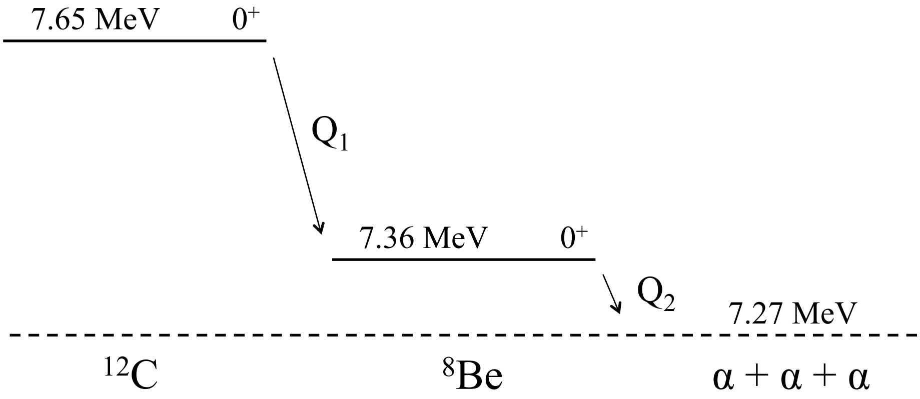

Figure 5.44: Level scheme for the sequential decay of ^{12}C into three α-particles, through the intermediate ^{8}Be ground state.

To provide a level of selectivity when examining the possible break-up channels of ^{12}C, it is instructive to analyse the energy distributions of the α-particles measured in the final state. Firstly, based on the measured momenta of these three break-up α-particles, the ^{12}C centre-of-mass velocity was calculated. Then this was used to transform the measured energies and momenta of the three break-up α-particles into this CoM frame. By examining the energies of the particles in the ^{12}C rest frame, a direct comparison can be made between these energies and the decay scheme of figure 5.44. In the final state the three α-particles were randomly labelled as α_1, α_2 and α_3. Then, their energies in the ^{12}C CoM were calculated as a fraction of the total decay energy ($Q_1 + Q_2 = 380$ keV). This yields three values ϵ_1, ϵ_2 and ϵ_3, which, based on the conservation of energy, should vary from 0 to 1.

The distributions of the fractional α-particle energies are shown in figure 5.45. The narrow peak at $\epsilon = 1/2$ corresponds to decays that proceed through the ^{8}Be ground state. Points outside of these peaks correspond to when either one of the other two α-particles are emitted from ^{12}C first, or that the decay proceeded through a direct decay where there are fewer restrictions on the relative energies of the α-particles.

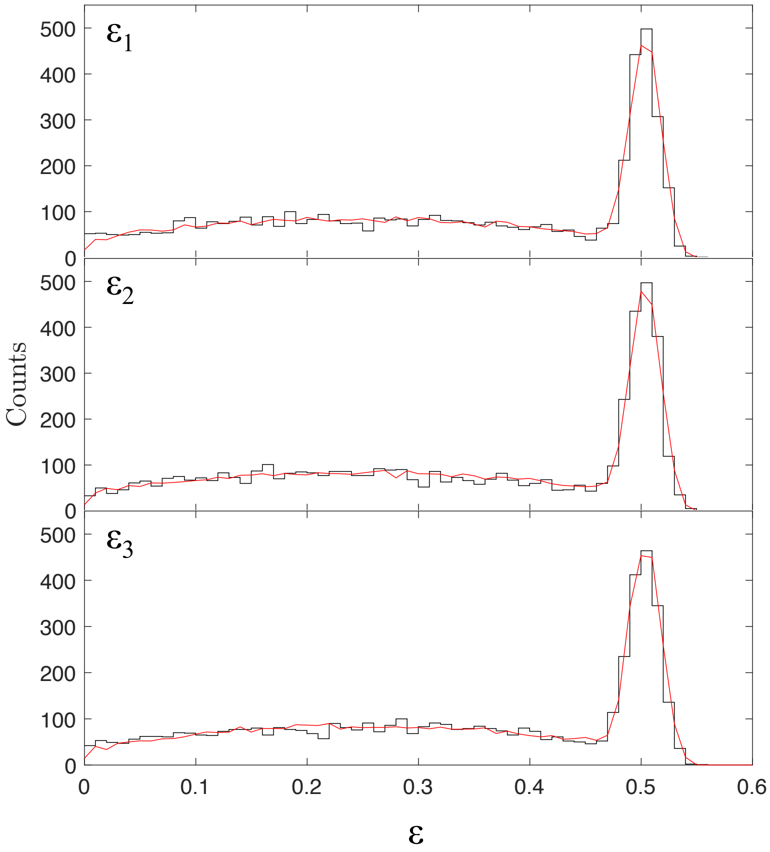

Figure 5.45: Histograms of the fractional energies of each α-particle in the CoM of the decaying ^{12}C. The histogram shows experimental data and the red line shows the Monte-Carlo simulations of the sequential decay process. A peak at $\epsilon = 1/2$ in these spectra corresponds to the case where that α-particle is emitted first, in a sequential decay through the ^{8}Be ground state.

Disentangling the different scenarios is difficult when using these one-dimensional plots. In order to achieve this it is instructive to plot the data shown by these histograms on a single two-dimensional diagram called a *Dalitz plot*.

5.8.6 Dalitz Plots

The Dalitz plot, first used by R. H. Dalitz to examine the τ-meson decay channels [196], is a specific type of *ternary plot* [197], which allows three quantities to be plotted on a single two-dimensional diagram, provided that they sum to a constant value. Consider figure 5.46 a). In the ^{12}C to 3α decay situation, the fractional energies of the three break-up α-particles, ϵ_i, must sum to a constant 1. Therefore, when points are plotted in three-dimensional space, they are constrained to lie on a plane with the equation $\epsilon_1 + \epsilon_2 + \epsilon_3 = 1$.

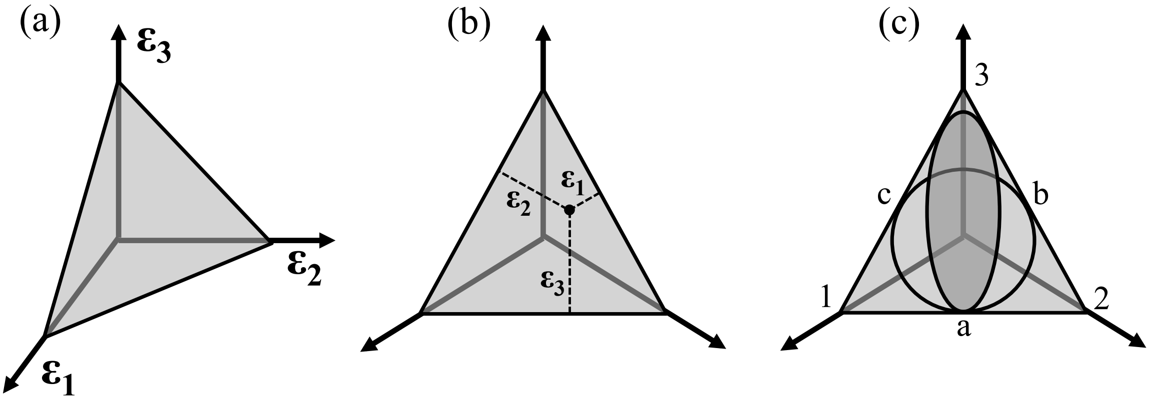

Figure 5.46: The construction of a symmetric Dalitz plot. Panel a) Illustrates that data must lie on a plane when plotted in 3-dimensional space if ϵ_1, ϵ_2 and ϵ_3 sum to a constant value. Panel b) depicts the projection of this diagram into 2-dimensional space. Panel c) shows the bounds of the Dalitz plot due to energy and momentum conservation. See text for details. Image from reference [198].

When observing this plot along a direction normal to the surface, the diagram condenses into a two-dimensional plane, shown in figure 5.46 b). The 2D coordinates on this plane, X and Y, can be written as a combination of ϵ_1, ϵ_2 and ϵ_3 as

$$X = \frac{1}{\sqrt{3}} \left(\epsilon_2 - \epsilon_1 \right) \quad \text{and} \quad Y = \frac{1}{3} \left(2\epsilon_3 - \epsilon_2 - \epsilon_1 \right). \tag{5.46}$$

These equations are derived in appendix D.1. This plot relies on Viviani's theorem. Named after Vincenzo Viviani, this theorem states that the sum of the distances from any interior point to the sides of an equilateral triangle equals the length of the triangle's altitude. Here, ϵ_1, ϵ_2 and ϵ_3 must sum to 1. The origin of the Dalitz plot is at the centre.

The conservation of energy ensures that no fractional energy ϵ can exceed 1, which only permits points to lie within the shaded triangle bounded by $\epsilon_i = 1$. Also shown in figure 5.46 c), momentum conservation requires data to lie in an inscribed circle if the break-up fragments have equal masses. This result is derived in appendix D.2. By extension, for unequal masses, the data are constrained to lie in an inscribed ellipse. The elliptical eccentricity, and hence the positions of points a, b and c in figure 5.46 c), depends on the ratio of the masses $m_1 : m_2 : m_3$.

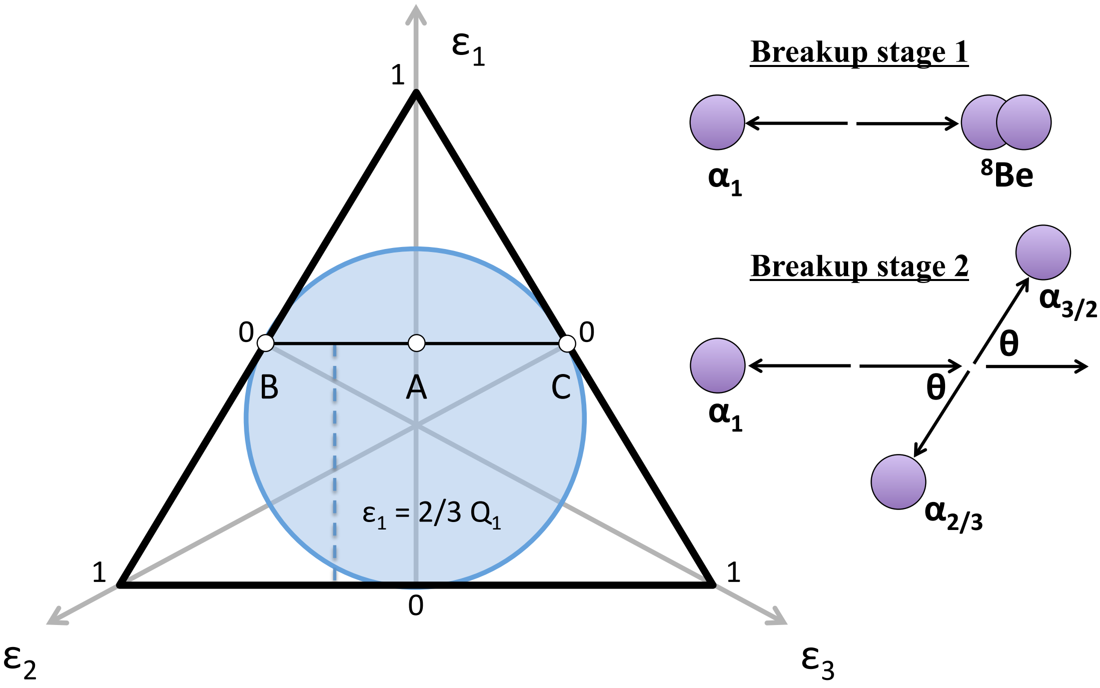

Figure 5.47: Depiction of the sequential break-up of ^{12}C along with where on the Dalitz plot these points will lie.

To link the Dalitz plot back to the physical process, consider the situation presented in figure 5.47. Here, α-particle 1 is emitted from ^{12}C first. It carries away 2/3 of the initial decay energy, which is around 1/2 of the total decay energy as illustrated by figure 5.44. This means that on the Dalitz plot, $\epsilon_1 \approx 1/2$. This region of the plot is depicted by the black line BAC in figure 5.47. From here, the second break-up stage defines where on this line the data point lies. If the break-up angle θ is 90° to the direction of the initial α-particle, then the data occupy point **A** on the plot. In the ^{12}C CoM, the final two α-particles carry away the same energy. The other extreme situation is that in the second break-up stage, α_2 and α_3 are emitted collinear to the first α-particle ($\theta = 0°$ or $180°$). In this case, one of these α-particles has a maximal energy and the other has zero energy. These correspond to points **B** and **C** in figure 5.47. Any collinear decay occupies the extremities of the Dalitz plot, lying on the edge of the circle. Break-up angles in the second stage between 0° and 180° occupy the space between **B** and **C**.

The width of the black line is due to the natural width of the intermediate state resonance and the experimental resolution. In cases where the initial state or intermediate resonance are particularly broad, the effects of varying penetrability through the Coulomb barrier must be considered when predicting the Dalitz plot distribution. This is achieved through applying R-matrix theory. Here, both the Hoyle state and intermediate $^{8}\mathrm{Be}_{\mathrm{g.s.}}$ are narrow, and so this effect is ignored. The ^{8}Be ground state ghost anomaly is expected to contribute, but only at the order of 10^{-6} compared with the narrow ground state peak [45, 46, 48, 49, 139]. In general, a variation in intensity along the line is expected due to the angular distributions for the two break-up stages. In this particular case of Hoyle state (0^{+}) to ^{8}Be (0^{+}) + α (0^{+}) to $\alpha + \alpha + \alpha$ (0^{+}), the angular momentum of the decay is zero meaning isotropic angular distributions are expected. Therefore, no variation of the intensity across the Dalitz plot is expected.

In the case of general direct break-ups, the three α particles can decay to anywhere in the available phase space, provided that energy and momentum are conserved. Therefore, points can lie anywhere inside the blue, shaded circular region of figure 5.47. The point at the very centre of the Dalitz plot corresponds to the case that each α-particle is emitted from the ^{12}C nucleus with the same energy ($\epsilon_1 = \epsilon_2 = \epsilon_3 = 1/3$) and at angles of 120° to one another. In the other extreme case, the particles may be emitted collinear to one another, and their energies may be shared in any way that permits this. These cases would correspond to points on the very edge of the shaded circle in figure 5.47.

In the experimental analysis, α-particles 1, 2 and 3 are assigned randomly, meaning that the line in figure 5.47 is repeated across the ϵ_2 and ϵ_3 axes. Therefore, in the experimental Dalitz plots, the data occupy triangular loci. As illustrated by figure 5.45, the fractional energies of each α-particle in the CoM of the decaying ^{12}C were calculated. Equations 5.46 were then used to calculate the Dalitz plot coordinates for each event and a 2D histogram was incremented. These Dalitz plots are shown in figures 5.48 to 5.50. The Dalitz plots are drawn upside-down for aesthetics.

Separate Dalitz plots are drawn for three situations. The case where each α-particle hits a separate DSSD provides the cleanest data with superior resolution. This is shown in figure 5.48. The case where two α-particles are permitted to hit the same detector is shown in figure 5.49. There are considerably more counts but with a poorer resolution and higher background. The third case, where one particle misses the detector array completely and is reconstructed from momentum conservation, is shown in figure 5.50. This has much poorer resolution.

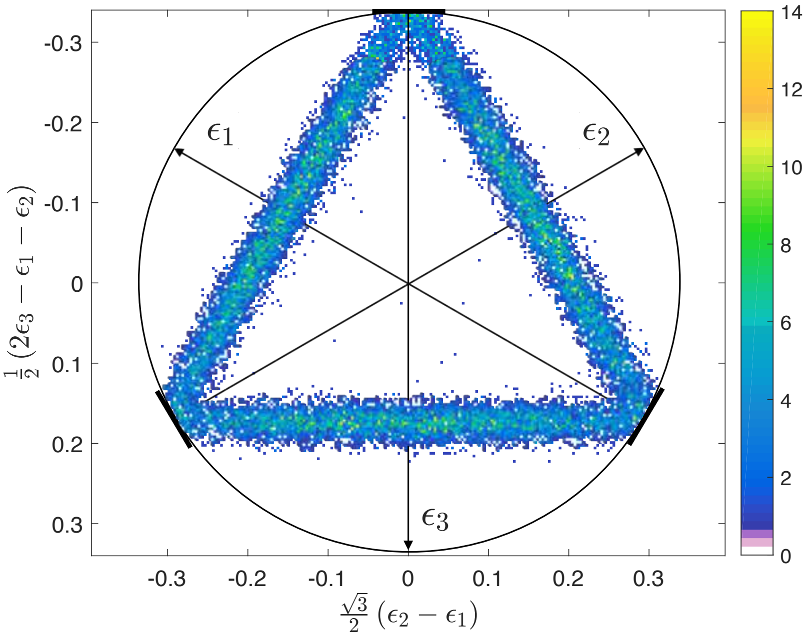

Figure 5.48: Symmetric Dalitz plot showing the fractional energies of the three break-up α-particles. This shows 2.4×10^4 Hoyle state break-up events, corresponding to the case where each α-particle was detected by a separate DSSD. Sequential decay events are forced to lie on the triangular locus.

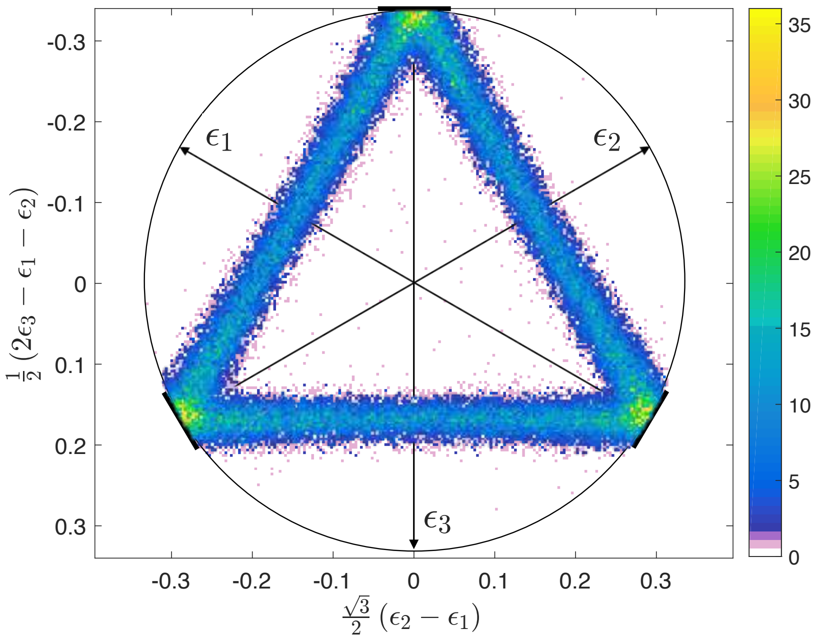

Figure 5.49: Symmetric Dalitz plot showing the fractional energies of the three break-up α-particles. This shows 6.9×10^4 Hoyle state break-up events, corresponding to the case where two α-particles were detected by the same DSSD.

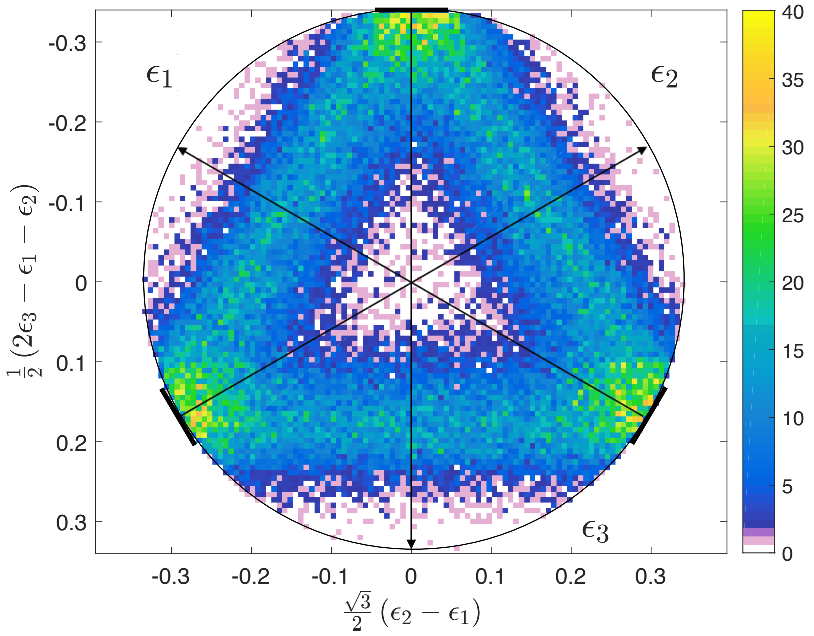

Figure 5.50: Symmetric Dalitz plot showing the fractional energies of the three break-up α-particles. This shows 6.0×10^4 Hoyle state break-up events, corresponding to the case where two α-particles were detected by the DSSD array, and the third was reconstructed.

Since all of the decay stages are isotropic, provided that the data lie on a triangle, uniform intensities of points are expected. However, due to the desired hit patterns across the detector array, differences in intensities are observed. Events where the particles emerge with similar energies are more likely to satisfy the requirement that each α-particle hits a separate DSSD. Therefore, a higher intensity of points are observed for regions which lie at smaller radii from the centre of the Dalitz plot in figure 5.48. Likewise, events which are more collinear are more likely to satisfy the condition that two α-particles hit the same DSSD. Therefore, a higher intensity of points are seen closer to the edge of the Dalitz plot in figure 5.49.

It is easy to see, most clearly in figures 5.48 and 5.49, that the sequential decay of the Hoyle state dominates, since most data lie on the triangular loci. Very few points lie in the areas outside and inside of the triangles, which are expected to be occupied by events originating from direct decay processes. Any direct decay contribution is small, and in order to quantify this, the experimental data were compared with Monte-Carlo simulations of sequential and direct decay processes. To permit a quantitative comparison, figures 5.48 and 5.49 were modified. Due to the 120° rotational symmetry of the Dalitz plot, it is possible to fold the experimental data such that a single sextant of the Dalitz plot is occupied. This was achieved through a series of inversions and rotations of the X and Y Dalitz plot coordinates of each event. The folded data are shown in figure 5.51.

At this point, it is constructive to compare these figures with those of two previous measurements of the Hoyle state decay, shown in figure 5.52 and from references [139, 140]. In the present study, a total of 9.3×10^4 events were measured. The previous two studies measured around 5×10^3 and 2×10^4 events respectively. By comparing figures 5.51 and 5.52, it is clear that the present measurements have significantly lower backgrounds than previous experiments. A similar experimental resolution was achieved by each of the experiments, denoted by the width of the triangle bands. However, references [139, 140] relied on the technique of kinematic fitting to achieve this resolution. The technique is described later in section 5.8.8 but was not used in the present analysis. It was found to considerably improve the resolution of the events where one α-particle was reconstructed (figure 5.50), but did not significantly improve the resolution when applied to complete kinematics events (figures 5.48 and 5.49).

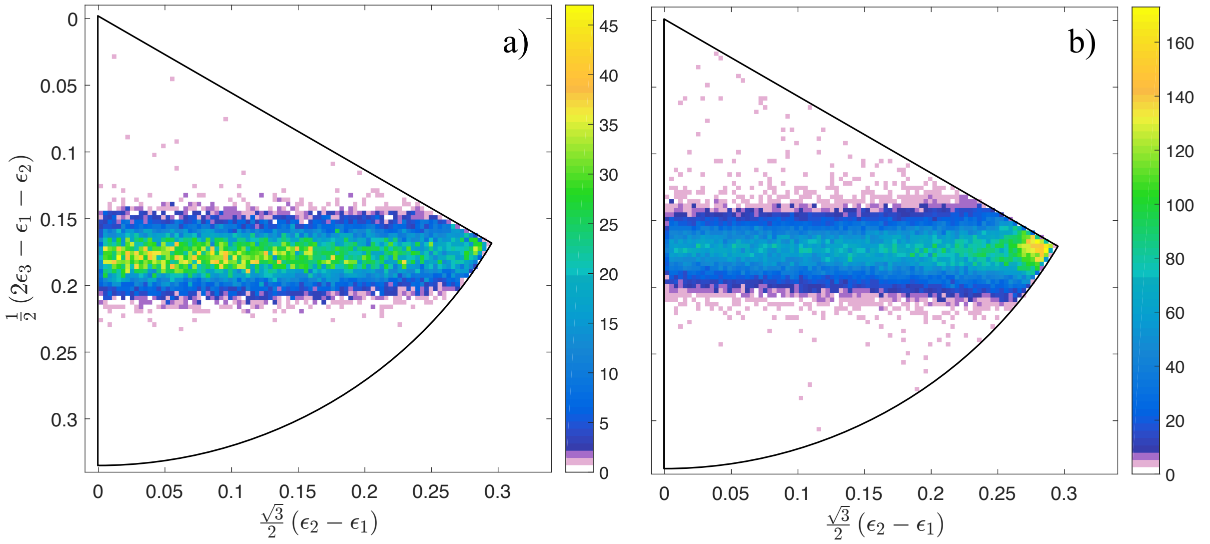

Figure 5.51: Dalitz plots folded so that the data occupy one sextant of the plot. Panel a) shows the case where each break-up α-particle is detected by a separate DSSD (2.4×10^4 events) and panel b) shows the case where two α-particles hit the same DSSD (6.9×10^4 events).

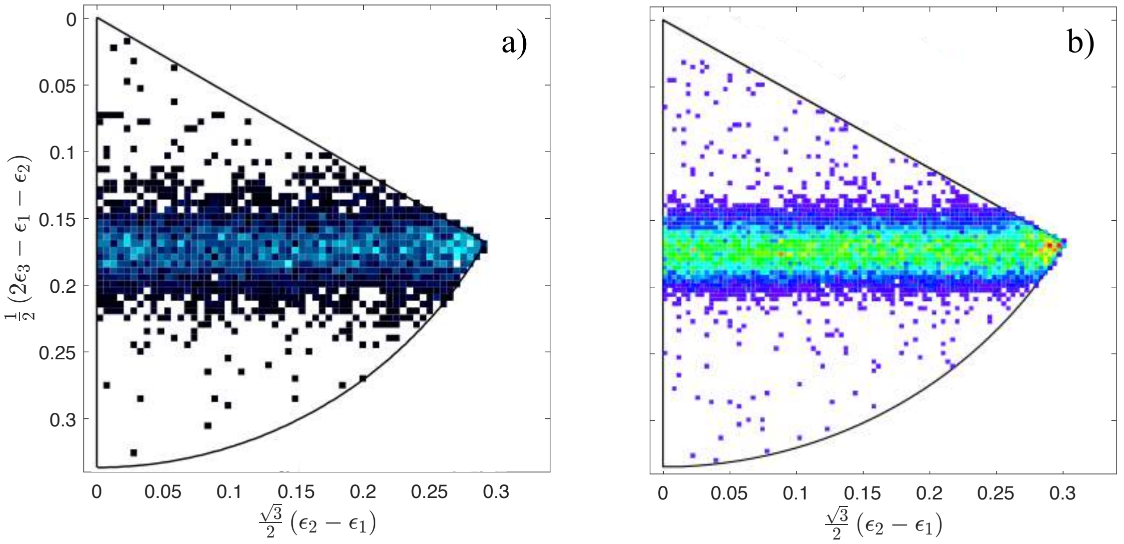

Figure 5.52: Folded Dalitz plots from two previous measurements of the Hoyle state break-up. Panel a) shows data from reference [139] and depicts around 5×10^3 events. Panel b) shows data from reference [140] and depicts around 2×10^4 events.

Summary

The sequential and direct decays of the Hoyle state can be disentangled by examining the relative energies of each of the three α-particles that are emitted during the break-up. This is because, during the sequential decay, the first emitted α-particle has a fixed energy, determined by the masses of the ^{8}Be and α-particle fragments (around 1/2 of the total decay energy). A convenient way to do this is to plot all three of the energies on a single two-dimensional Dalitz plot. On the Dalitz plot, sequential decays of the Hoyle state appear as a triangular locus. During a direct break-up, the decay energy can be shared between the three α-particle fragments in a more complicated way, which appears as a background to this triangle. Due to the 120° rotational symmetry of the Dalitz plot, it is possible to manipulate the data such that they occupy a single sextant of the plot. Comparing the resulting plots with those of previous publications indicates the present experiment has higher statistics and lower background.

5.8.7 Simulated Dalitz plots

Simulated sequential decay Dalitz plots

Firstly, let us examine the simulations of the sequential decay process in more detail. Separate Dalitz plots are drawn for the two complete kinematics situations. The case where each α-particle hits a separate DSSD is shown in figure 5.53. The case where two α-particles are permitted to hit the same detector is shown in figure 5.54. The same simulated data are analysed in each case. A total of 2.15×10^8 of random events were generated. Of these, any events which resulted in one or more particles striking the detector array were saved to a file. The energies, θ_x and θ_y values for each particle in the event were saved. This had an efficiency of 23%, resulting in 5×10^7 events. These events were then analysed by the sort code used for the experimental data in order to generate figures 5.53 and 5.54. The resolution and variation in intensity across the Dalitz plots are consistent with the experimental data shown in figures 5.48 and 5.49. These Dalitz plots were folded in the same way as the experimental data and the resulting plots are shown in figure 5.55.

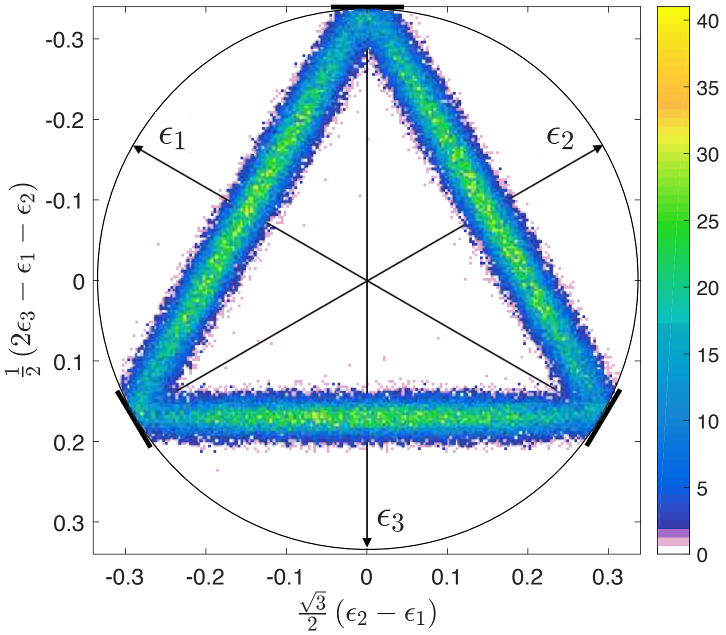

Figure 5.53: Symmetric Dalitz plot showing the fractional energies of the three break-up α-particles from the sequential decay Monte-Carlo simulations. This corresponds to the case where each α-particle strikes a separate DSSD, and shows 1.09×10^5 Hoyle state break-up events. Sequential decay events are forced to lie on the triangular locus. The analogous experimental data are shown in figure 5.48.

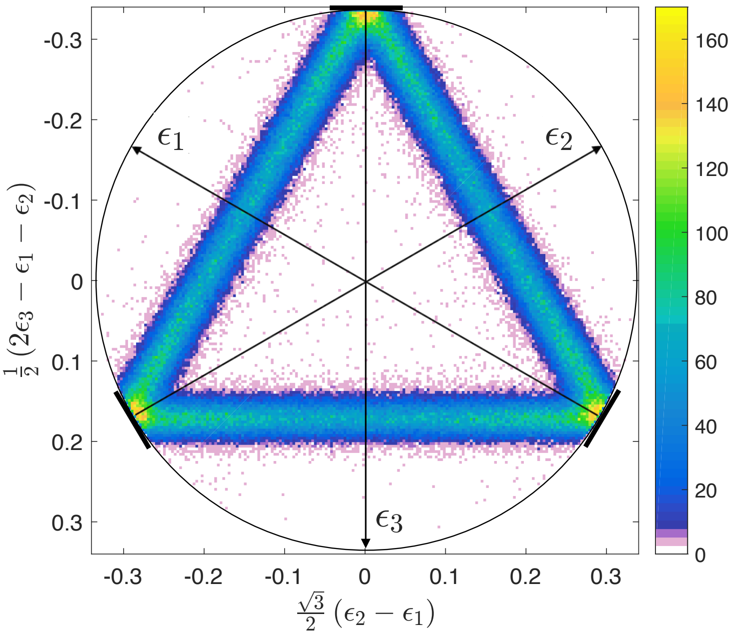

Figure 5.54: Symmetric Dalitz plot showing the fractional energies of the three break-up α-particles from the sequential decay Monte-Carlo simulations. This corresponds to the case where two α-particles hit the same DSSD, and shows 4.2×10^5 Hoyle state break-up events. Sequential decay events are forced to lie on the triangular locus. The analogous experimental data are shown in figure 5.49.

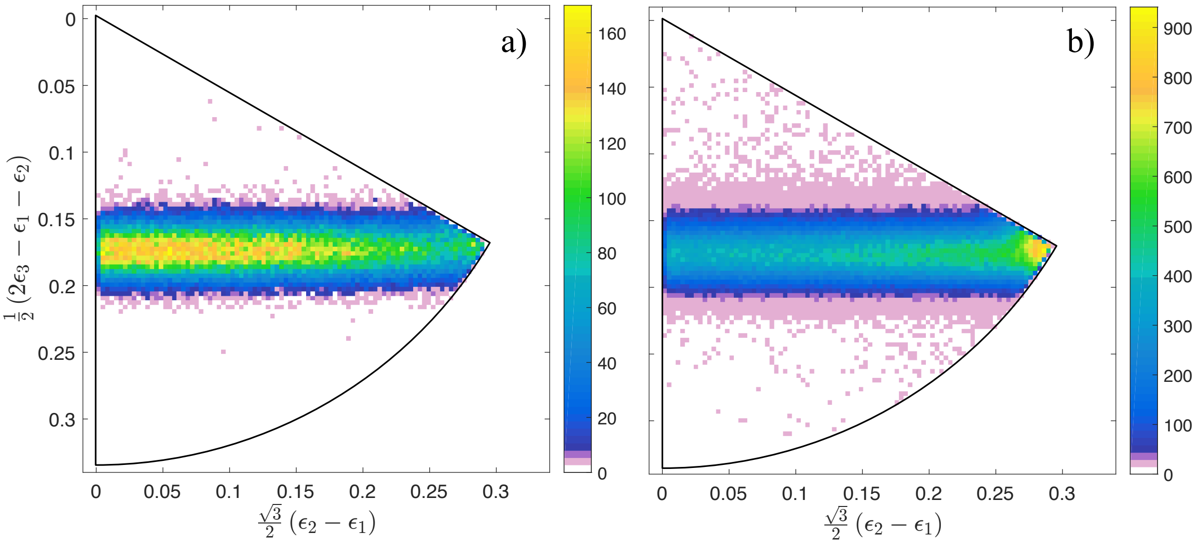

Figure 5.55: Simulated Dalitz plots folded so that the data occupy one sextant of the plot. Panel a) shows the case where each of the break-up α-particles hit a separate DSSD and panel b) shows the case where two α-particles hit the same DSSD. The analogous experimental data are shown in figure 5.51.

Simulated direct decay Dalitz plots

For the direct decay of the Hoyle state, four break-up models were considered, and were discussed in section 5.5. The so-called DDΦ model assumes that the three α-particles may decay to anywhere in the available phase space without preference, uniformly filling the Dalitz plot. The DDE model assumes that the three α-particles are emitted with approximately the same energy, only smeared due to Heisenberg's position-momentum uncertainty principle. This produces points close to the centre of the Dalitz plot. The DDL model assumes that the break-up is collinear, as a reflection of a possible linear chain structure of α-particles in the initial state. This leads to points on the edge of the Dalitz plot. Finally, a more complicated model was developed, DDP^2, which assumes that the three α-particles may decay to anywhere in the available phase space, but accounts for the varying penetrability through the Coulomb barrier. The folded Dalitz plots corresponding to the DDΦ, DDE and DDL decays are shown in figure 5.56.

Direct-decay Monte-Carlo simulations were generated and analysed in the same way as the sequential decay simulations and the experimental data. For each decay model, N random events were generated. Of these, n events resulted in one or more particles hitting the detector array. The n events were analysed by the sort code, resulting in i events making their way to the final Dalitz plot. The value of i is dependent on the required hit pattern and other software cuts in the analysis. The total efficiency ϵ is defined as i/N. The N, n, i and ϵ values are shown in table 5.2.

	N	n	i (patt. 1)	ϵ (patt. 1)	i (patt. 2)	ϵ (patt. 2)
Sequential	2.15×10^8	5×10^7	1.09×10^5	0.051%	4.20×10^5	0.20%
DDΦ	2.56×10^8	6×10^7	2.59×10^5	0.10%	1.10×10^6	0.43%
DDE / DDP^2	2.81×10^8	6×10^7	4.10×10^5	0.15%	8.59×10^5	0.31%
DDL	1.84×10^8	4×10^7	3.23×10^4	0.018%	1.02×10^6	0.55%

Table 5.2: Comparing the number of generated Monte-Carlo events N, with the number that reach the final Dalitz plots i. This provides a measure of the experimental efficiency ϵ. Separate results are shown for the cases where each α-particle hits a separate DSSD (hit pattern 1) and where two hit the same DSSD (hit pattern 2).

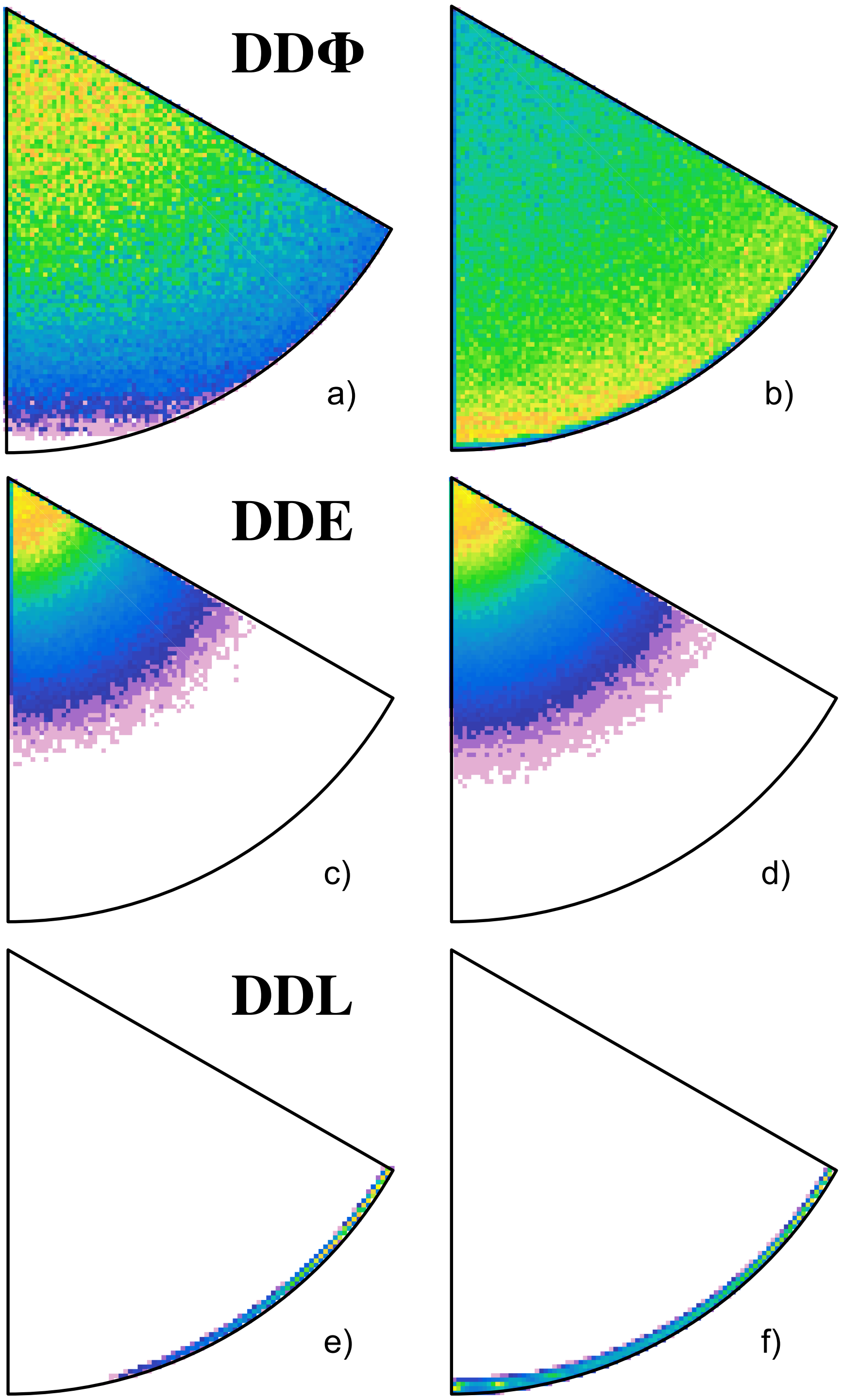

Figure 5.56: Simulated Dalitz plots for each of the direct decay models, folded so that the data occupy one sextant of the plot. The left panels show data that satisfy the strict hit pattern of one α-particle in each DSSD. The right panel shows data that correspond to the case where two break-up α-particles hit the same DSSD. The top, middle and bottom rows show the DDΦ, DDE and DDL break-up models, respectively.

Figures 5.57 a) and b) show the DDP^2 direct decay profile (phase space + penetrability). Unlike the plots in figure 5.56, this plot excludes the effects of the experimental resolution and geometry. As can be seen, due to the fact that the transmission probability is lowest for DDE-type decays, where the α-particles emerge with similar energies, there is a higher probability for decays with this configuration. The radial projection of this Dalitz plot is well approximated by a Gaussian with $\sigma \approx 29$ keV. In this sense the DDP^2 profile is very similar to the DDE decay profile, which also has a higher propensity for decays to the centre of the Dalitz plot. By coincidence, the α-particle energies in the DDE decay were modelled by a normal distribution with $\sigma = 30$ keV. Therefore, the DDE and DDP^2 type decays are considered the same for the remainder of the analysis. In reality, there is a radial asymmetry in the Dalitz plot of figure 5.57 a), so the DDE and DDP^2 profiles do differ by a small amount.

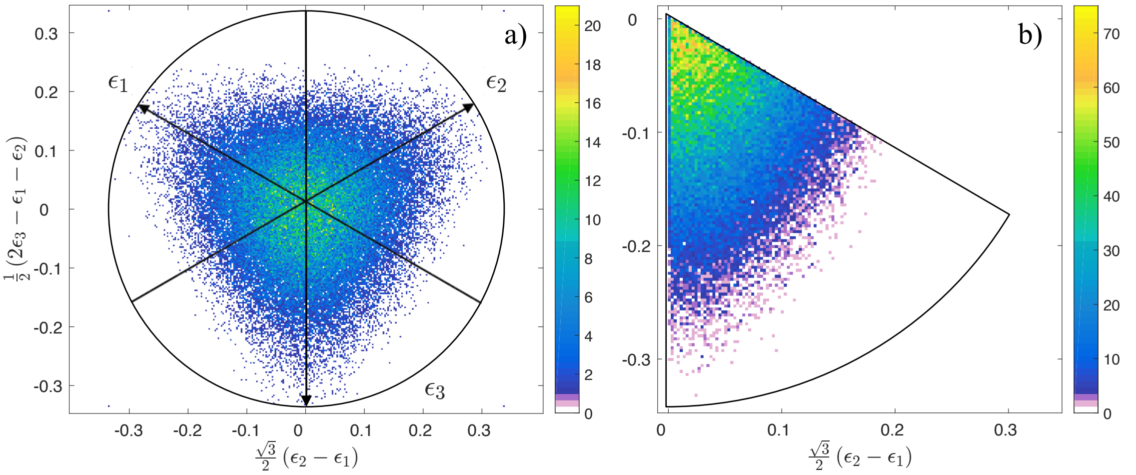

Figure 5.57: a) Simulated Dalitz plot for the DDP^2 direct decay. This is DDΦ uniform phase space decay but accounts for how the Coulomb barrier transmission probability depends on the emission angles of the three break-up α-particles. b) Folded DDP^2 Dalitz plot. The plots show 500,000 simulated events and do not include experimental effects.

Summary

In order to evaluate the relative contributions of sequential and direct decays to the experimental data, detailed Monte-Carlo simulations were performed, using the code discussed in section 5.7. The simulations of sequential decays appear to reproduce the experimental Dalitz plots very well. Simulations of several direct decay models were also performed. It is thought that these different decay types could reflect the internal structure of the Hoyle state. A new direct decay type, DDP^2, was developed. This corresponds to decays uniformly to the available phase space, but with the inclusion of the directional dependence of the Coulomb barrier transmission probability. This decay type was shown to manifest similarly to the DDE decay model on the Dalitz plot.

Along with the effects of the experimental resolution, that act to widen the triangular locus of the Dalitz plot, the various decay models are each subject to a different detection efficiency. Since the different decay kinematics determine the energies and directions of the particles, this will effect the probability of them striking the detector array with the desired hit pattern. The efficiencies are tabulated in table 5.2 and are important considerations when fitting the Monte-Carlo simulations to the experimental data.

5.8.8 Kinematic fitting

For the present experiment, an improvement in the resolution of the Dalitz plots may permit a clearer distinction between sequential and direct decay contributions to the experimental data. The experimental resolution arises from several sources, described in detail in section 5.7. Quantities such as the energy of the particles and their hit position on the detector array can only be known to a certain level of accuracy. The width of the DSSD strips provides an angular granularity and the detectors have a Gaussian energy resolution as discussed in section 4.2.3. Due to this experimental resolution, along with systematic effects, the momenta of the particles reconstructed in the final state cannot be known exactly. However, it is possible to improve the resolution of the measured quantities by applying a process called *kinematic fitting*, which is widely used in particle physics [199] but has rarely been used in nuclear spectroscopy [139].

An adequate, and commonly-adopted approach to charged-particle spectroscopy is to measure all but one of the final state particles, as was the case in the beryllium-9 experiment discussed in chapter 4. By using linear momentum conservation, between the initial and final states, the momentum vector of the undetected particle can be calculated, leading to a full description of the final state. In this experiment, however, all four of the final state particles are measured in *complete kinematics*, meaning that the system is over-constrained.

This being the case, if the total energy of the final-state particles is calculated, and the break-up Q-value is subtracted, then the initial beam energy should be obtained. Due to the experimental resolution, the exact beam energy is not calculated; a distribution, centred on the correct energy, is obtained (see figure 5.38). Likewise, if the Hoyle state was populated in the experiment, the excitation energy calculated from the three break-up α-particles should equal 7.65 MeV. In reality, the calculated excitation energies are smeared by the experimental resolution, leading to a distribution with a width of $\approx$ 40 keV (see figure 5.40). The idea of kinematic fitting is to identify and use these physical constraints of the system, and vary the experimental measurements (energies and angles of the particles) such that these constraints are matched *exactly*. In theory, this brings the experimentally measured quantities closer to their true values. The more constraints that a system has, the more accurately the measured parameters can be known. The amount that each parameter can move from its initial value is modulated by its measurement uncertainty. This means that poorly measured parameters can change more easily, and parameters with a small uncertainty do not change much from their initial values.

Mathematically, kinematic fitting is performed using the method of Lagrange multipliers, where the difference between the measured parameter values and their true values are minimised subject to a number of constraint equations. This process is described in detail in appendices E.1 and E.2. A program called ***F**ast **U**ni**versal** **K**i**n**ematic **Fit**ting* `FUNKI_FIT.F90` was written, which performs kinematic fitting on a generic physical system, with a number of user-defined constraint equations. The code is published in reference [200]. Kinematic fitting deals with quantities that carry statistical errors following a normal distribution. However, as shown in section E.1, kinematic fitting can also improve systematic uncertainties in certain circumstances.

Kinematic Fitting for the Hoyle State break-up

When considering the break-up of the Hoyle state, a number of constraint equations can be derived, and applied in the kinematic fitting. Firstly, the energy of the system must be conserved – the sum energy after the reaction must equal the beam energy plus the break-up Q-value (-7.27 MeV). Secondly, the vector momentum in the final state must equal the momentum of the ^{4}He beam. Thirdly, the excitation energy in ^{12}C calculated from the three break-up α-particles must equal 7.65 MeV. These can be written as the following equations:

$$\begin{aligned} E_1 + E_2 + E_3 + E_4 - Q - E_\mathrm{b} &= 0, && (5.47) \\ \overrightarrow{\mathbf{P_1}} + \overrightarrow{\mathbf{P_2}} + \overrightarrow{\mathbf{P_3}} + \overrightarrow{\mathbf{P_4}} - \overrightarrow{\mathbf{P_b}} &= 0 \quad \text{and} && (5.48) \\ E_1 + E_2 + E_3 - E_\mathrm{C} - Q - 7.65 &= 0, && (5.49) \end{aligned}$$

where E_C is the kinetic energy of the recoiling ^{12}C, which is calculated from the momenta of the three break-up α-particles, α_1, α_2 and α_3. Given the vector nature of equation 5.48, this leads to a total of five constraint equations.

The kinematic fitting procedure was applied to each subset of experimental data. These correspond to the cases where each final-state α-particle is required to hit a separate DSSD quadrant, the case where two α-particles hit the same DSSD, and the case where one α-particle is completely undetected.

For the cleanest subset of data, where each α-particle strikes a separate DSSD, the resolution of the Dalitz plot is improved by a small factor of 0.9. This improvement is not as significant as shown by previous studies [139], or as significant as the predicted improvement (see appendix E for details on how this is calculated). When applied to data from Monte-Carlo simulations, where the sources of uncertainty were known exactly, the resolution did improve by the predicted factor of $\approx 1/\sqrt{2}$. This meant that the experiment and simulation were not directly comparable after kinematic fitting. The discrepancy may be because of sources of experimental uncertainty that were not accounted for. The fitting process also does not improve the situation for the case where two α-particles are permitted to strike the same DSSD quadrant. As discussed in section 5.7, the ambiguity in the true hit positions of these particles on the detector leads to a worsening of the resolution of the Dalitz plot, along with an increased background. In the case where the hit position of the particle on the detector is mis-assigned, the kinematic fitting varies the position of the hit between the limits of the wrong detector strips. Although this leads to the constraint equation being satisfied, the overall effect is to further worsen the resolution of the Dalitz plot and to increase the background.

The clearest improvement in the resolution of the Dalitz plot was seen when considering the subset of data where only two break-up α-particles strike the detector array, along with the scattered beam. The third, unmeasured α-particle from the ^{12}C break-up was reconstructed through momentum conservation between the initial and final states. Hence, this particle carries a combination of the errors on the energies and angles of all other detected particles. The errors on the energy and directions of the reconstructed particle were approximated by propagating uncertainties through the equations that were used to reconstruct these quantities from the measured particles. The resulting Dalitz plot has a highly smeared triangular locus as shown in figure 5.50. However, as shown for the simple example in figure E.5, if one parameter has a poor resolution when compared with the others, kinematic fitting may significantly improve the situation. Indeed, this was found to be the case, and the Dalitz plot after kinematic fitting is shown in figure 5.58. The projection of the folded Dalitz plot onto the vertical axis (see section 5.9.1 for details) is shown in figure 5.59. The resolution is still significantly poorer than when the reaction was measured in complete kinematics. Hence, these data were not used when evaluating the direct break-up contribution.

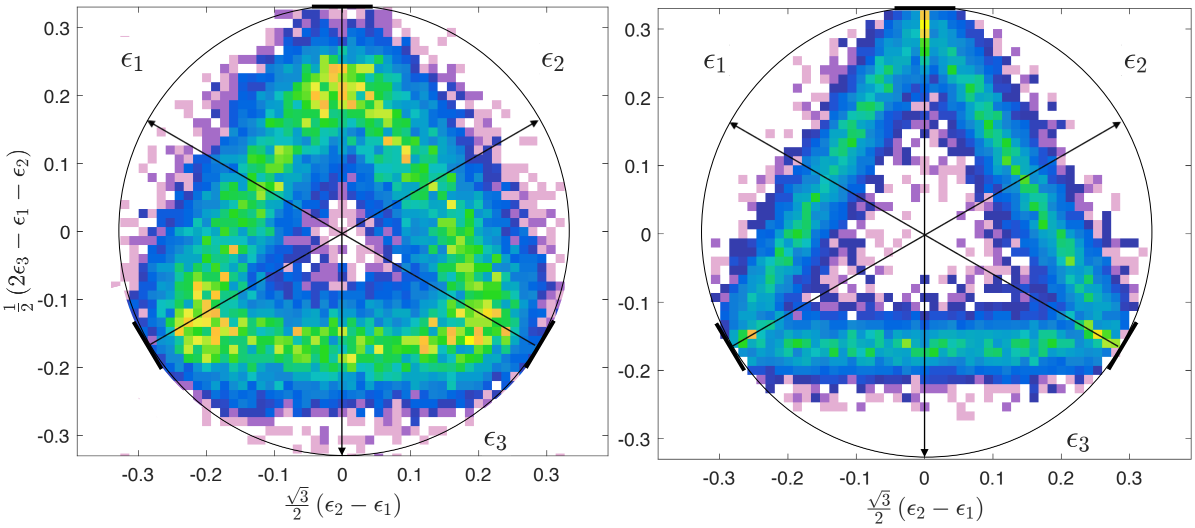

Figure 5.58: Dalitz plot showing the fractional energies of the three break-up α-particles. This shows 6.0×10^4 Hoyle state break-up events, corresponding to the case where two α-particles were detected by the DSSD array, and the third was reconstructed. The left panel shows the data before kinematic fitting, and the right shows data after kinematic fitting.

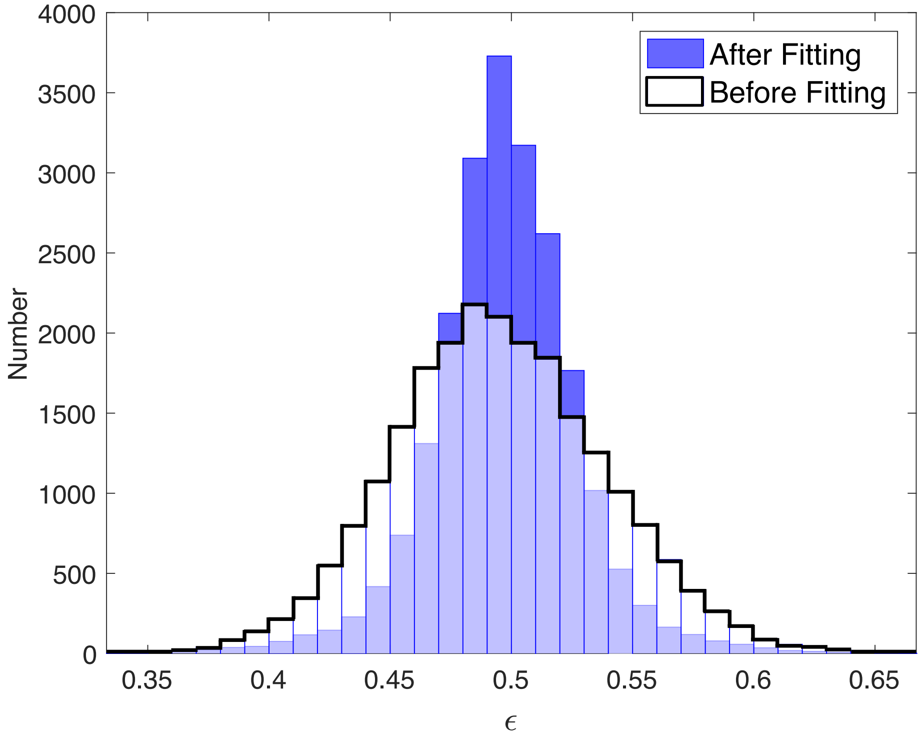

Figure 5.59: Histograms of the projected Dalitz plot, before and after kinematic fitting.

Summary

Kinematic fitting is commonly used in particle physics and can provide a way to improve the resolution of experimental data. By varying the energies and angles of each detected particle, along with the beam energy, by amounts dictated by their experimental uncertainties, some improvements to the resolution of the Dalitz plots were made. Its effect on the cleanest subset of data was minimal, so the technique was not used in the final analysis. However, a large improvement was seen when considering the subset of data where one break-up α-particle missed the detector array and was reconstructed. Nonetheless, this subset of data still possessed a far poorer resolution than for complete kinematics events and so was not used in further analysis.

5.9 Secondary analysis

In order to disentangle the sequential and direct break-up channels, the Dalitz plots for the experimental data and Monte-Carlo simulations were compared. This is done in order to determine if there is a direct decay component to the experimental data, or whether the measurements can be described exclusively by a sequential decay model.

5.9.1 Dalitz plot projections

In order to permit a quantitative comparison between the experimental data and the Monte-Carlo simulations, the 2D folded Dalitz plots shown in figure 5.51 for the experimental data were projected onto the vertical axis to produce two one-dimensional histograms, which are shown in figure 5.60. The Monte-Carlo simulations of the sequential break-up process are also plotted as lines on the same figure. The tails of figure 5.60 b) are well-reproduced by the Monte-Carlo simulations of the sequential decay process. They derive from the mis-assignment of the hit positions of the particles, which arises when multiple particles hit the same DSSD.

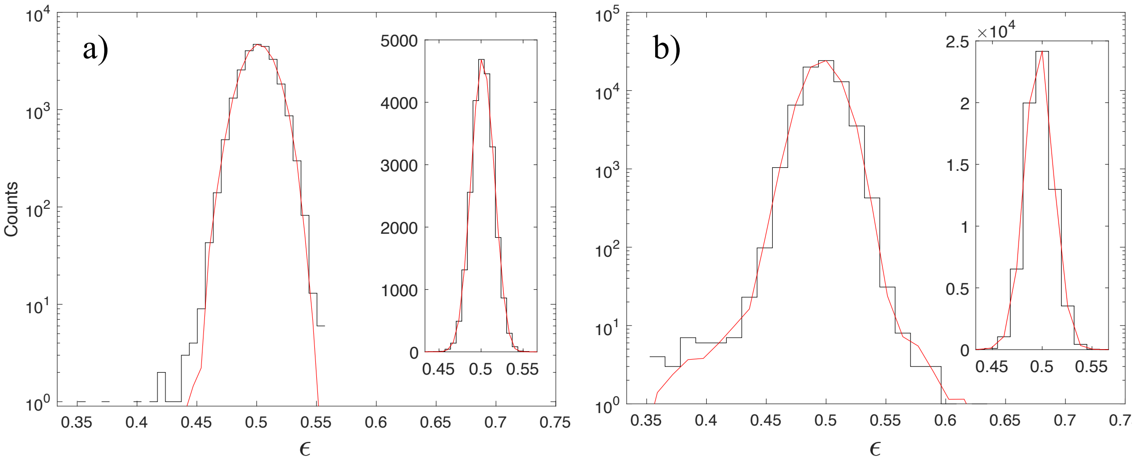

Figure 5.60: One-dimensional projections of the folded Dalitz plots onto the vertical axis. The black histogram depicts experimental data and the red lines show the Monte-Carlo simulations. Panel a) shows the case where each break-up α-particle is detected by a separate DSSD and panel b) shows the case where two α-particles hit the same DSSD. The main panel of each plot shows the data plotted on a logarithmic scale in order to examine the tails of the distributions. The insets show the same data plotted with linear scales.

The Monte-Carlo simulations of the sequential decay were fit to the experimental data subject to the condition of equal counts in the experimental and simulated distributions. The fit for the case where each α-particle hits a different DSSD results in a χ^2 per degree of freedom of 1.16. The fit where two α-particles hit the same DSSD results in a χ^2 per degree of freedom of 0.96. In both cases the fits lie close to the 50% confidence level in the χ^2 distributions. The goodness of fit, without the inclusion of any direct decay component, indicates that the decay of the Hoyle state is predominantly sequential. However, in order to determine if there are direct decay contributions to the data, and decide which of the three-body break-up models are most likely, these 1D histograms were compared with further Monte-Carlo simulations of the direct decay processes discussed in section 5.8.7.

To illustrate the manifestation of each direct decay type on the one-dimensional projection of the Dalitz plot, figures 5.61 and 5.62 were generated. The distribution of points for DDΦ, DDE/DDP^2 and DDL decay models, generated by the Monte-Carlo simulations, at the level of 0.1%, are shown overlaid on the experimental data. The efficiencies for detecting each type of decay are included in these plots, which is why some direct decay modes seem more prevalent than others.

As described in section 5.1, reference [137] declared a 7.5% DDE decay contribution and a 9.5% DDL decay contribution. The 0.1% DDΦ, DDE/DDP^2 and DDL distributions superimposed over the experimental data show that the claimed direct branching ratios are inconsistent with the current data. The plots indicate that any direct decay contributions are much smaller than these sources claim. Therefore, the present experimental data are more in line with references [139] and [140], which measured no significant direct decay contributions.

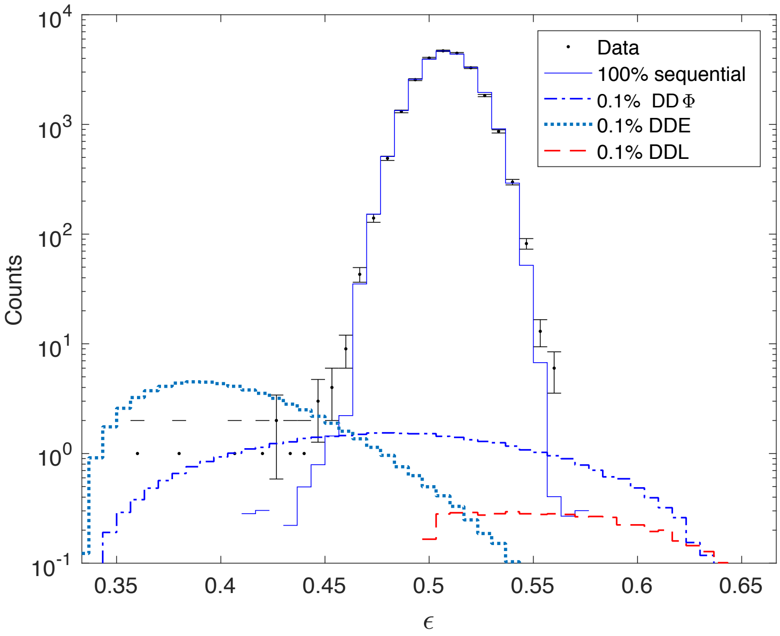

Figure 5.61: One-dimensional projection of the Dalitz plot, corresponding to when each α-particle strikes a separate DSSD. The sequential decay profile has a 100% branching ratio. The three direct decay profiles are shown at the level of 0.1%.

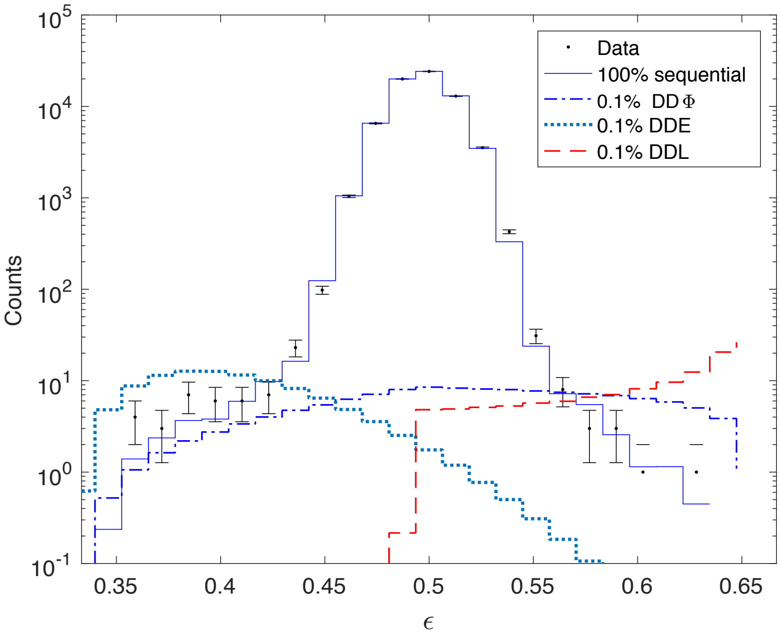

Figure 5.62: One-dimensional projection of the Dalitz plot, corresponding to where two α-particles strike the same DSSD. The sequential decay profile has a 100% branching ratio. The three direct decay profiles are shown at the level of 0.1%.

5.9.2 Frequentist statistical analysis

For each type of direct decay, a series of branching ratios were chosen and Monte-Carlo data reflecting these branching ratios were simulated. The experimental data and simulations were then compared under the condition of equal counts in the experimental and simulated data sets. For each value of the branching ratio, the likelihood of reproducing the experimental data was evaluated.

Consider the one-dimensional histograms of figure 5.60. Each histogram bin has a number of counts x and the Monte-Carlo simulations have counts in the same bin of λ. Since the experimental data points follow a Poisson distribution, the probability of getting an experimental count x from a model which predicts a count λ is given by the Poisson distribution

$$f(x;\lambda) = \frac{\lambda^x}{x!}e^{-\lambda}. \tag{5.50}$$

The probability, f_i, of obtaining each data point in figures 5.60 a) and b) from the proposed model was calculated. Then the total probability of reproducing the whole data set X across all N data points was obtained by calculating

$$\begin{aligned} \mathcal{L}(BR) &= \prod_{i=1}^{N} f(x_i;\lambda_i) && (5.51) \\ \ln(\mathcal{L}(BR)) &= \sum_{i=1}^{N} \ln(f(x_i;\lambda_i)). && (5.52) \end{aligned}$$

Here, $\mathcal{L}(BR)$ gives the probability of obtaining experimental data X from the Monte-Carlo simulations with a direct decay branching ratio BR. This process was repeated for various branching ratios in small steps between $BR = 0 - 10^{-3}$. This permits the construction of the likelihood functions which track the probability of obtaining the experimental data as a function of the branching ratio parameter. The normalised likelihood functions are shown in figure 5.63 for the DDE/DDP^2 and DDΦ decay models. The DDL decay was very well constrained, due to its localisation on the Dalitz plot, and could not be plotted on the same scale.

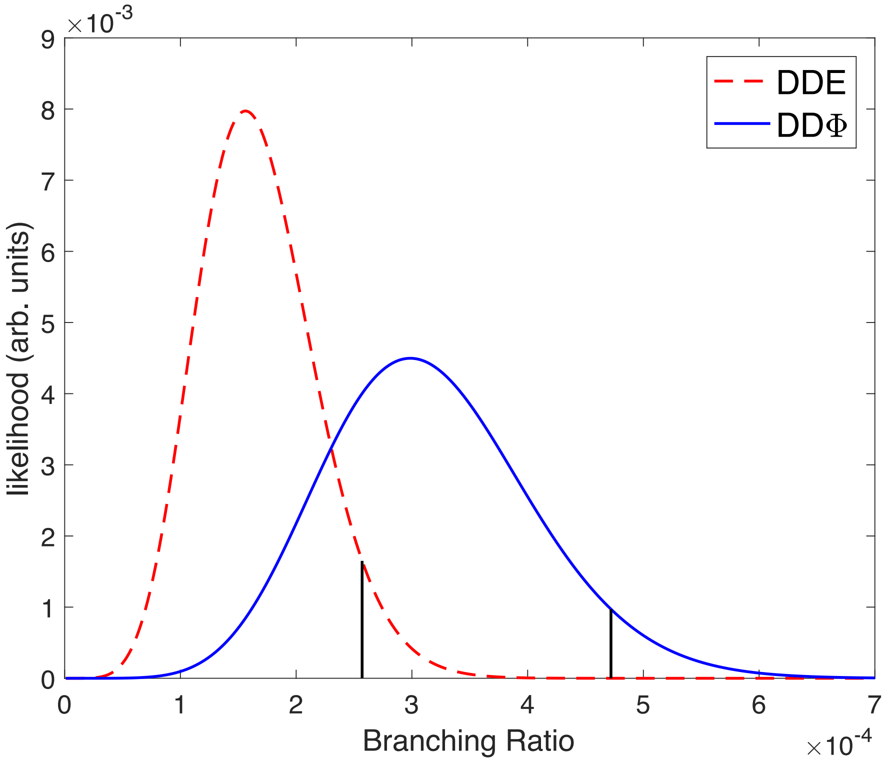

Figure 5.63: The normalised likelihood of reproducing the experimental data as a function of the direct decay branching ratio parameter. The dashed line shows the distribution for a DDE/DDP^2 direct decay contribution and the solid line shows the distribution for the DDΦ decay. The likelihood distribution for the DDL decay was much narrower and could not be plotted on the same scale. Upper limits on the direct decay contributions were calculated by evaluating the 95% confidence intervals of these distributions (P-value = 0.05), and are marked by the vertical lines.

The optimum value of the branching ratio parameter is identified as the point corresponding to the maximum of the likelihood function. Upper limits on the branching ratio for each of the direct decay models were obtained by evaluating the 95% and 99.5% confidence intervals. The 95% confidence intervals are marked by the vertical lines in figure 5.63. The extracted details of the branching ratios for each decay model are summarised in table 5.3.

	BR Optimal	BR limit (95% C.L.)	BR limit (99.5% C.L.)
DDΦ	3.0×10^{-4}	4.7×10^{-4}	5.8×10^{-4}
DDE/DDP^2	1.6×10^{-4}	2.57×10^{-4}	3.2×10^{-4}
DDL	0	3.8×10^{-5}	6.4×10^{-5}

Table 5.3: The values of branching ratio upper limits for each of the direct decay mechanisms.

To visually compare the experimental data with the Monte-Carlo simulations for different values of the direct decay branching ratio, figures 5.64 – 5.66 were produced. These overlay the Monte-Carlo simulations corresponding to different branching ratios on the total experimental data (9.3×10^4 events). For each plot, as the branching ratio parameter increases, the fit to the experimental data worsens.

An alternative, yet equivalent way to determine upper limits to the direct decay contributions is to track the χ^2 fit value as a function of the branching ratio parameter. With zero direct decay contribution, the fit to the experimental data resulted in a χ^2/DoF value close to 1 which lies at the 50% confidence interval in the χ^2 distribution. The value of the branching ratio was increased in steps and the data were refit for each. The values of the branching ratio where the value of χ^2 exceeds the 95% and 99.5% confidence intervals in the χ^2 distribution, were treated as the upper limits for each type of direct decay. The extracted values were similar to those presented in table 5.3. The direct decay can be rejected at these values of the branching ratio at 95% and 99.5% confidence levels.

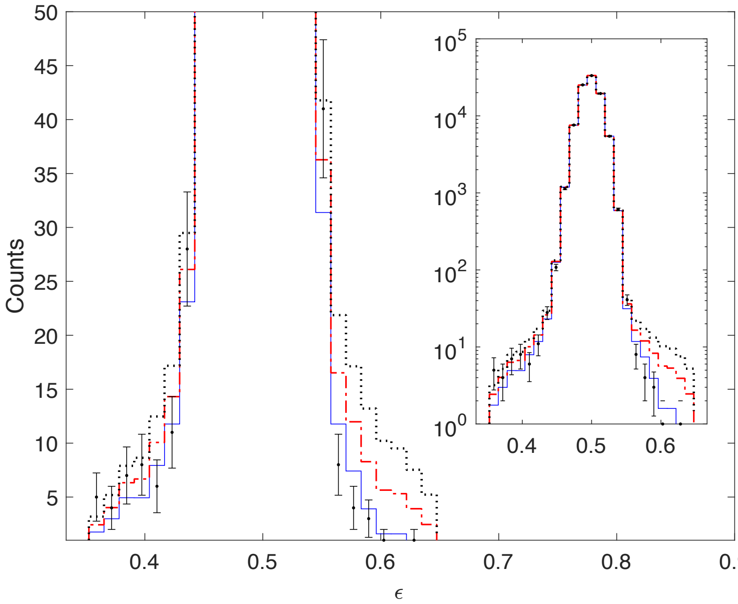

Figure 5.64: DDΦ direct decay mechanism: Fit of Monte-Carlo simulations to the experimental data for DDΦ branching ratios 0% (solid blue line), 0.047% (dot-dashed red line) and 0.1% (dotted black line).

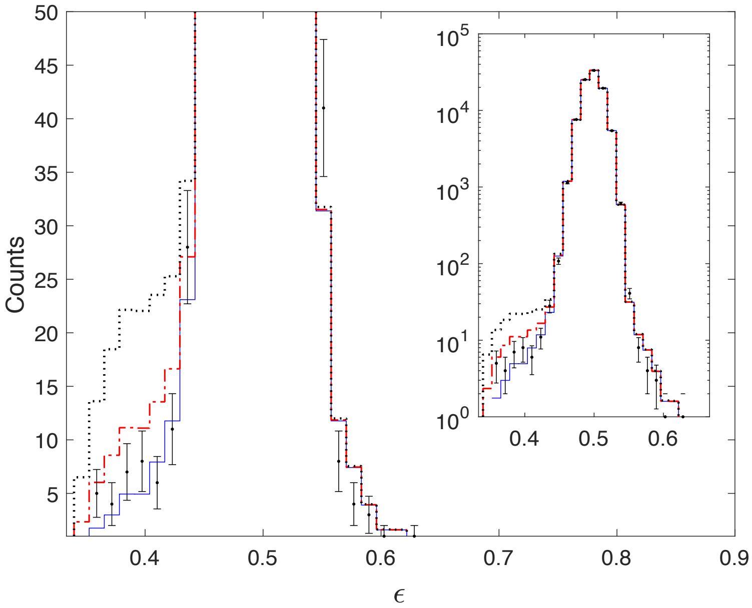

Figure 5.65: DDE/DDP^2 direct decay mechanism: Fit of Monte-Carlo simulations to the experimental data for DDE/DDP^2 branching ratios 0% (solid blue line), 0.035% (dot-dashed red line) and 0.1% (dotted black line).

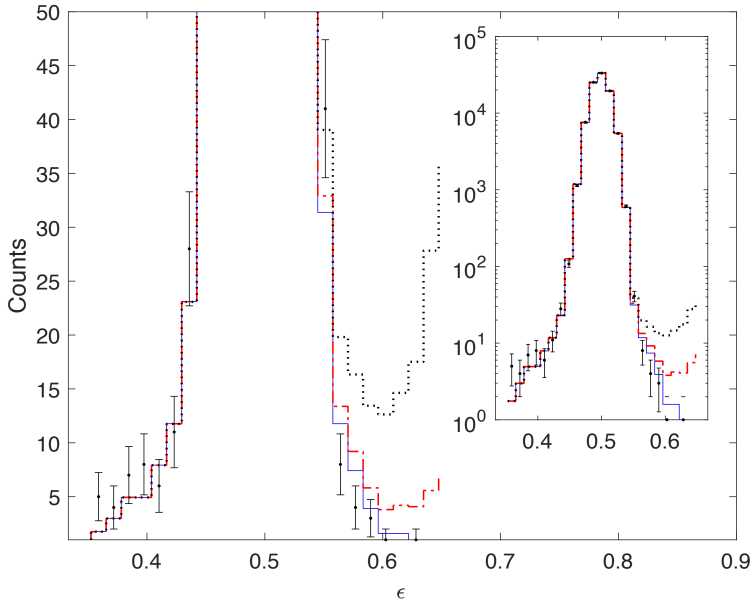

Figure 5.66: DDL direct decay mechanism: Fit of Monte-Carlo simulations to the experimental data for DDL branching ratios 0% (solid blue line), 0.02% (dot-dashed red line) and 0.1% (dotted black line).

Summary

One-dimensional projections of the experimental Dalitz plots were fit with the equivalent plots for the simulated data, with the condition of equal counts in the experimental and simulated spectra. After accounting for the different detection efficiencies, the likelihood of reproducing the experimental spectrum was evaluated for various values of the direct decay branching ratio used in the simulations. The likelihood plots as a function of the branching ratio were used to evaluate the 95% and 99.5% confidence intervals, in order to place an upper limit on the direct decay contribution. The results are summarised in table 5.3. An equivalent analysis, which tracked the value of χ^2 as a function of the branching ratio, gave the same results.

5.9.3 Bayesian statistical analysis

In addition to the frequentist analysis, Bayesian inference was also used to determine an upper limit on the DDΦ direct decay branching ratio of the Hoyle state.

Bayesian statistics is often contrasted with the classical frequentist statistics, which assumes that measured phenomena are generated by a fixed, unknown process. In particular, this classical formulation assumes that parameters are unknown constants, given that a complete knowledge about a system is not available. The concept of probability is then used to describe the outcomes of experimental measurements.

Bayesian statistics, on the other hand, assumes that parameters, although not known exactly, are quantifiable random variables which can be described by probability distributions [201]. Subjective probability distributions of parameters, called *priors*, are constructed based on our experience and reasoning about these parameters. In this context, probability is interpreted as a degree of belief about the values of the parameter under investigation. Once we collect new experimental data, these are combined with the proposed prior distribution to create a new distribution called the *posterior*, which represents our current and updated probability assessment of the parameters. Our new understanding about the parameters value is contained within the posterior.

In the context of the Hoyle state decay, we should not treat the direct decay branching ratio as a completely unknown parameter, since two recent measurements have set upper limits for DDΦ decay of 0.5% [139] and 0.2% [140] with 95% confidence. Therefore, we know with 95% confidence that the branching ratio is less that 0.2%. The idea is to combine these previous results with the present experimental measurements in order to better constrain the direct decay branching ratio. Specifying the prior distribution is a controversial topic, due to the obvious influence it has on the result. However, as shall be seen for the present data, the impact of the prior is diminished as we gather more observations.

Previous experiments have also placed limits on the DDE and DDL decay branching ratios.

However, a standard definition of each of these decay modes was not observed. Therefore, prior information about branching ratios for these processes was not incorporated in the present study. For example, reference [139] assumed that a DDL decay comprised of a collinear decay where two of the α-particles existed in the ^{8}Be ground state resonance. In the present study, we instead permit any collinear decay to belong to the DDL decay model. Similarly, reference [139] assumed that for the DDE decay mechanism all three α-particles have exactly the same energies. The present study and reference [140] assert that there must be must be an uncertainty/ smearing of their energies due to their initial confinement inside the nucleus.

The formulation of Bayesian statistics is summarised by Bayes theorem, which states

$$P(A|X) = \frac{P(X|A)P(A)}{P(X)}, \tag{5.53}$$

where $P(X|A)$ is the probability of measuring experimental data X given a physical model A. The prior probability distribution (our current knowledge about the model A) is given by $P(A)$. The term, $P(X)$, is a normalising constant to ensure that the total probability is 1. This allows us to calculate the important quantity $P(A|X)$, which is the probability of model A being true, given the experimental data X. In a frequentist analysis, one basically assumes that $P(X|A) = P(A|X)$ without inferring anything from the prior.

In a simple example consider a medical test which searches for a condition A and gives a positive result X or a negative result Y. The test has an accuracy of 0.9; the probability of a positive result X if you have the condition A is 90% and the probability of a negative result Y if you do not have the condition A is also 90%. Therefore, in the frequentist approach, if you get a positive test result, there is a 90% chance you have the condition. However, the Bayesian result is different. The quantity that we actually require is $P(A|X)$, the probability of having the condition A, given the test result X. If the condition has a prevalence so that on average 10% of the population have it, $P(A) = 0.1$. In order to use Bayes theorem to calculate $P(A|X)$, we also need to calculate $P(X)$, which is the total probability of measuring X regardless of the state of the patient.

$$P(X)_{\text{total}} = P(X) \times P(A) + P(Y) \times (1 - P(A)) \quad (5.54)$$

$$P(X) = (0.9 \times 0.1) + (0.1 \times 0.9) = 0.18 \quad (5.55)$$

Substituting the relevant values into equation 5.53 you calculate

$$P(A|X) = \frac{P(X|A)P(A)}{P(X)} \quad (5.56)$$

$$P(A|X) = \frac{0.9 \times 0.1}{0.18} = 0.5. \quad (5.57)$$

Therefore, perhaps surprisingly, if you measure a positive test result, the probability of the patient having the condition is actually only 50%. The frequentist misses some important information, and the prior knowledge that only 10% of the population have the medical condition is crucial to obtain a meaningful probability. In a similar way, in the present analysis, it is possible to test for direct decay while bearing in mind that an upper limit on its existence has already been calculated at the level of 0.2% (95% confidence interval).

To apply Bayes theorem to the present experimental data, the alternative to null hypothesis testing presented in reference [202] was used. Here, the branching ratio for direct decay, BR, is treated as a model parameter, and our knowledge about the value of this parameter is treated as a probability distribution. The prior knowledge about the parameter comes from reference [140], which concludes that for DDΦ decays, there is a 95% probability that BR $\leq 2 \times 10^{-3}$. A number of prior probability distributions reflecting this result are shown in figure 5.67 and were used in the calculation. For each of these distributions, 95% of their areas lie below the branching ratio 2×10^{-3}.

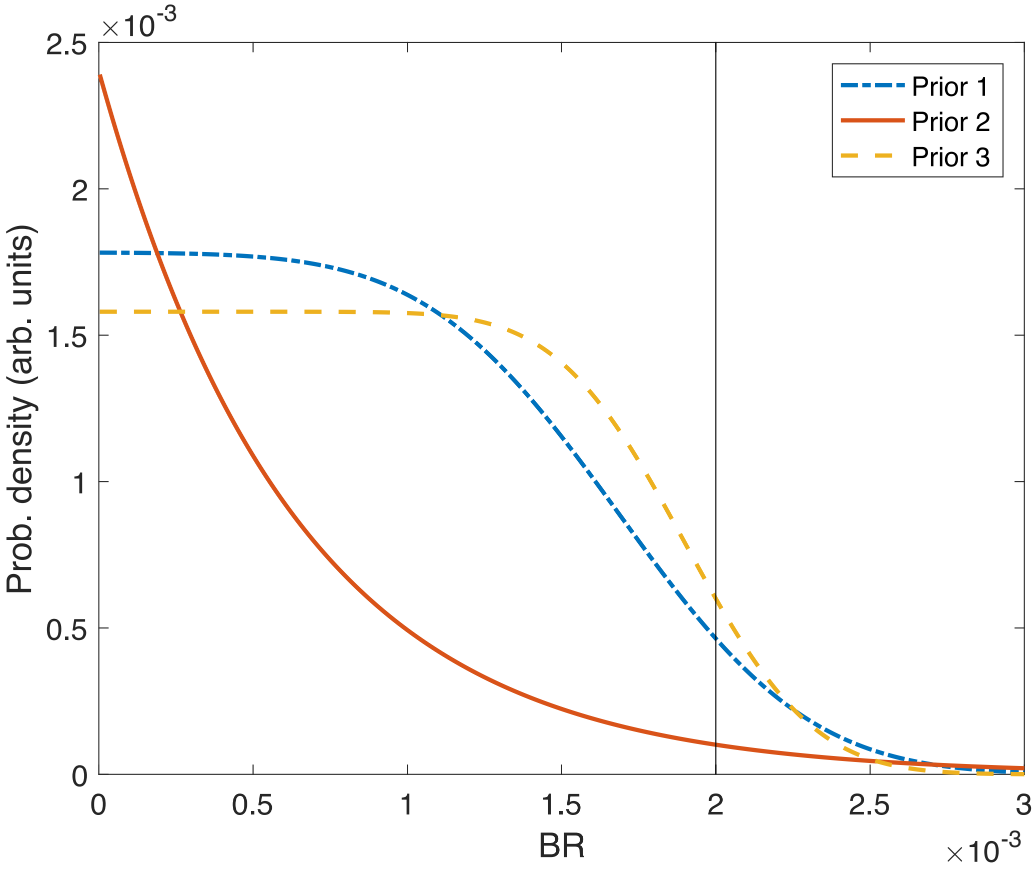

Figure 5.67: Three prior distributions chosen to reflect the present experimental knowledge about the direct decay branching ratio. The vertical line marks the known upper limit on the branching ratio (2σ confidence) from reference [140].

Branching ratios from BR $= 0$ up to BR $= 10^{-3}$ were chosen in small, equal increments. Monte-Carlo simulations were then used to generated Dalitz plots (and their 1D projections) corresponding to these branching ratios, which were then compared with the experimental data. Assuming the data points followed a Poisson distribution, the probability of generating the experimental data $P(X|BR)$ was calculated for each BR value. This results in the normalised likelihood distributions shown by figure 5.63 in section 5.9.2. At this point, no prior knowledge has been incorporated. Therefore, by examining the areas beneath the two likelihood functions, the 95% and 99.5% confidence intervals were calculated and are presented in table 5.3.

The prior distributions in figure 5.67 were then folded into these likelihood functions, producing $P(X|BR) \times P(BR)$. These distributions were normalised to provide the required posterior distribution $P(BR|X) = {}^{P(X|BR)P(BR)}/_{P(X)}$. The normalised posterior distributions were then used to evaluate the 95% credible intervals. The posterior distributions are not plotted, because the effect of the prior distributions on the likelihood functions were minimal. As such, their effect on the 95% credible intervals, and the corresponding branching ratio limits are small. The mean branching ratio limit was calculated across the different prior distributions, and any difference due to the choice of prior is incorporated as a systematic uncertainty. The results are summarised in table 5.4.

	BR upper lim. (95% C.I.)	BR upper lim. (99.5% C.I.)
DDΦ	$(4.65 \pm 0.05) \times 10^{-4}$	$(5.67 \pm 0.1) \times 10^{-4}$

Table 5.4: The values of the DDΦ branching ratio limits to 95% and 99.5% credible intervals based on the Bayesian analysis. Uncertainties are systematic due to the choice of prior.

Summary

In addition to the frequentist analysis, a Bayesian alternative to null-hypothesis significance testing was performed for the DDΦ direct decay fits. A number of prior distributions were used, each reflecting what was known about the value of the direct decay branching ratio before the present experiment was performed. Due to the significantly improved sensitivity of this experiment compared with previous efforts, the effect of the prior distributions on the results were very small. The results are summarised in table 5.4.

5.9.4 Summary of results

By comparing the experimental Dalitz plots to Monte-Carlo simulations of the sequential and direct decay processes, improved upper limits were placed on the value of the direct 3α decay branching ratio of the Hoyle state. The results are summarised in table 5.5.

BR upper limit	95% C.L.	99.5% C.L.	95% C.L. (Bayesian)	99.5% C.L. (Bayesian)
DDΦ	4.7×10^{-4}	5.8×10^{-4}	$(4.65 \pm 0.05) \times 10^{-4}$	$(5.67 \pm 0.1) \times 10^{-4}$
DDE/DDP^2	2.57×10^{-4}	3.2×10^{-4}	–	–
DDL	3.8×10^{-5}	6.4×10^{-5}	–	–

Table 5.5: The values of branching ratio upper limits for each of the direct decay mechanisms. The left columns of data correspond to the frequentist analysis and the right columns correspond to the Bayesian analysis. The quoted systematic uncertainties are due to the choice of prior distribution in the Bayesian analysis.

5.10 Interpretation of Results

The present experimental results build on numerous measurements of the direct decay of the Hoyle state in the past [137–140]. The current experiment is unique in that it possessed the sensitivity required to compare the experimental result with current theoretical predictions, covered in sections 5.4.3, 5.4.2 and 5.5. Notably, the result allows us to comment on the possible α-condensate nature of the Hoyle state.

In section 5.4.3, it was argued that for the decay of an α-condensed state into a number of α-condensed sub-systems, the branching ratio for each possibility should depend only on the decay transmission probability and the available phase space. This was then estimated using WKB Coulomb barrier penetrability calculations and found to be around 0.06%. The present results $\underline{\text{reject}}$ the direct decay of the Hoyle state at the levels

$$\mathrm{DD}\Phi > 0.047\%, \quad \mathrm{DDE/DDP}^2 > 0.026\% \quad \text{and} \quad \mathrm{DDL} > 0.004\%.$$

The upper limits for each proposed direct decay model are below the calculated phase space limit. An enhancement of the ^{8}Be + α channel compared with this limit indicates that the α-condensate model may not be a good approximation of the Hoyle state. A dominant ^{8}Be + α structure, such as that predicted by AMD and FMD calculations [146, 153] seems more likely.

Furthermore, in 2014, Ishikawa performed a theoretical study into the decay of the Hoyle state, using a full three-body quantum mechanical formulation [178]. In that work, the Hoyle state is considered to be a system of three bosonic α-particles. The decay amplitude was evaluated as a function of the momenta of the emitted α-particles and hence, the form of the Dalitz plot was calculated. Ishikawa concluded that the number of events lying on a triangular locus in the Dalitz plot, which are interpreted as sequential decay, would amount to 99.9% of the total. No previous experiment has had the sensitivity to confirm or reject this proposed 0.1% direct decay contribution. The present experimental measurements reject a direct decay contribution $> 0.047\%$, which is a factor of two lower than Ishikawa's theoretical prediction. More specifically, the calculations predict

$$\text{Total} \approx 0.1\%, \quad \text{DDE} = 0.005\% \quad \text{and} \quad \text{DDL} = 0.03\%.$$

This disagreement with the experimental data indicates that the theoretical treatment of the three α-particle constituents of the Hoyle state as bosons is an incorrect approach, casting doubts on the BEC interpretation. The current experiment has rejected a DDL contribution below this level, but did not have the sensitivity to test the proposed DDE contribution.

5.11 Outlook

The present experiment worked at the limits of a typical charged-particle spectroscopy measurement in terms of experimental resolution and realistic beam times. In order to measure a lower direct decay branch, or to examine the nature of the resulting α energy distributions, another approach is needed. Rather than distinguishing between direct and sequential decays using the energies of the emitted α-particles, an approach such as that adopted by Zimmerman *et al.*, which used an optical time projection chamber (O-TPC) detector, could be taken [203]. Here, the α-particles resulting from ^{12}C photodisintegration were tracked by the O-TPC and their relative separation directions during the decay were imaged. A decay of ^{12}C into three α-particles imaged by the O-TPC is shown in figure 5.68 from reference [203].

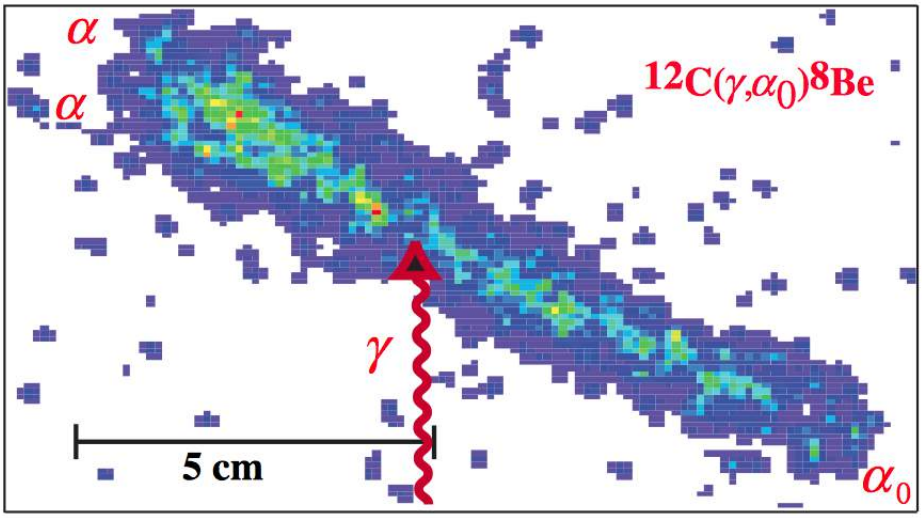

Figure 5.68: A O-TPC image of the ^{12}C(γ,α)^{8}Be reaction from reference [203].

With an improved directional resolution, this technique could provide a way to unambiguously differentiate between a sequential and direct decay process. An image of a direct decay, where the three α-particles separate with similar energies, is easily distinguished from the sequential decay process shown in figure 5.68.

A full, experimentally-measured direct decay profile would be useful for theoretical developments. Since the 3α decay is largely dominated by barrier penetration, the exact distribution of the final-state α-particles will be quite sensitive to the $\alpha - \alpha$ interactions used in calculations. Therefore, reproducibility of the direct decay profile could form an excellent test for realistic interaction potentials. In terms of theoretical input, more calculations of the direct decay branching ratios, based on various models, would be welcome.

Chapter 6

Resistive strip detector improvements

The two experiments presented in this thesis both detected charged particles using double-sided silicon strip detectors. These consist of vertical front strips and horizontal rear strips. The energy collected by a single front and single rear strip should be the same when a particle is stopped in the detector. Therefore, by matching the energies collected by the front and rear strips, the crossing point provides the position of the hit. The direction of the detected particle can then be inferred. However, when there is a high multiplicity of particles, or the particles have similar energies, it is possible to mis-assign their hit positions, as discussed in section 5.7. In these instances, it may be advantageous to use a different type of detector called a *resistive charge division strip detector.* These detectors have strips running only in one direction, but have electrical contacts at each end of the strip. The strip itself carries a large resistance, meaning that the signal, measured at each end of the strip, is proportional to the position of the hit along the strip. Although these detectors have their advantages for certain applications, they also have some major downfalls, such as being more susceptible to electronic noise. The following paper, which will be submitted to *Nuclear Instruments and Methods A* in the near future, aims to address some of these problems using novel techniques in the hardware and in post-processing.

Chapter 7

Summary

At the end of this thesis, which details several different experiments, it is useful to reflect on how these elements all fit together, and the overall contribution that this work has made towards the field of nuclear physics.

Carbon-12

Foremost, the question of whether Bose-Einstein condensates can manifest in atomic nuclei is something that has been speculated for a number of years, and has strongly influenced the treatment of near-threshold states in α-conjugate nuclei. Due to its large radius, the Hoyle state in ^{12}C has long been seen as the ideal candidate nuclear state for this phenomenon to occur. However, despite the fact that this theory very successfully predicts some properties of this state, such as the charge form factor for inelastic electron excitation from the ground state to the Hoyle state, this is not a unique description, and an unambiguous test of this structure had not been performed.

The work presented in chapter 5 has unambiguously indicated that the interpretation of Hoyle state as an α-condensate is problematic. In order to achieve this, a challenging, high precision measurement of the direct 3α decay of this state was required. Under the assumption of an α-condensed state, the direct 3α decay branching ratio should lie at 0.06%, given that the branching ratio should depend only on the phase space and barrier penetrability for the decay. The previous best measurement of this quantity was only able to place an upper limit on the branching ratio at 0.2% [140]. The present work has set an upper limit at 0.047% or 0.026%, depending on the type of direct decay that was considered.

Several improvements in the experimental method and analysis were required in order to come to these conclusions. First of all, a novel detector geometry was implemented in order to reduce the dominant experimental background. Implementing a quadrant array of DSSDs to detect the three break-up α-particles permitted each to strike a separate DSSD, and remove the ambiguity regarding their hit positions, which is a problem when multiple particles hit the same detector. Utilising a large number of detectors and placing them further away from the target also improved the angular granularity of the detectors. This is the dominant contribution towards the resolution of the Dalitz plot, and hence, the sensitivity to direct decay. A large number of decays were measured in order to collect the statistics required to reject the direct decay at the quoted levels. To achieve this, a long experimental run of over 60 cumulative hours was performed on the in-house Birmingham MC40 cyclotron.

Regarding the experimental analysis, the present study has been the first to link the absolute value of the direct decay branching ratio with a signature for an α-condensate structure. Reference [180] noted that for an α-condensate state, a break-up into any set of α-condensed subsystems should be equally probable, as a reflection of the common wave functions of the α-particles in the initial state. In the case of the Hoyle state, the propensity for decays through the ^{8}Be ground state and the rare direct 3α decay channel, should dictated purely by the phase space for the decay and the relative transmission probabilities through the Coulomb barrier. By considering these factors, it was calculated in section 5.5 that the break-up branching ratio for direct 3α decay should be ≈0.06%. The present experiment has rejected the direct decay at levels consistently below this value, indicating that there is a problem with the α-condensate interpretation of the Hoyle state. A full quantum mechanical three-body calculation for the decay of the Hoyle state has also been performed in the past, and found that a total direct decay contribution of ≈0.1% is expected [178]. This calculation treated the α-particles as bosons; its disagreement with the current experimental data indicates that this may not be the correct approach.

Previous experimental studies used a phenomenological DDΦ direct decay profile as the standard for searching for direct decays [138–140]. In this model, equal probabilities for direct decays to anywhere in the available phase space are considered. However, this simple model does not account for the significant changes in the transmission probability through the Coulomb barrier, depending on the relative orientations of the three α-particles. For example, a decay where the α-particles emerge with the same energies has a much lower Coulomb barrier than the case where one α-particle remains at rest. Therefore, there is a higher probability of the former situation occurring. By utilising WKB calculations in hyperspherical coordinates, the present study has developed a new direct decay profile, DDP^2, which quantifies this effect. Its manifestation was found to be almost identical to that of the DDE profile used in the present study and in reference [140]. It is this modified direct decay profile that should be considered in future studies, since it more accurately describes the decaying system.

Beryllium-9

The Beryllium-9 nucleus has been long thought to possess a molecular structure. In this picture, the two α-particles of the highly-clustered, unbound ^{8}Be, are thought to become bound by the exchange of a neutron. The valence neutron may occupy a number of different molecular orbitals about the two α-particle cores; these are expected to have different angular momenta and parities, and correspond to different amounts of deformation in the nucleon density. For example, the π-binding configuration has a more compact geometry than the σ-binding configuration. Since the ^{9}Be system is deformed, the nucleus can rotate collectively, leading to rotational bands, which are built on top of the different intrinsic molecular configurations. Until this study, evidence has been found for three rotational bands in ^{9}Be, corresponding to the collective rotations of the π-binding, σ-binding and σ-antibinding molecular states.

The present experiment has identified a previously unmeasured level in the ^{9}Be spectrum at 3.8 MeV, which may correspond to the π-antibinding molecular configuration. By comparing with a newly-measured level in the mirror nucleus, ^{9}B, and assuming that the reduced widths for $^8\text{Be}_{\text{g.s.}} + n$ decay are the same for the two states, a firm limit on its angular momentum was placed at $J < 7/2$. This leaves the possibility that the level does correspond to the hitherto unmeasured π-antibinding state. More work is needed to explore this possibility and future experimental work has been proposed.

Since the unbound resonances of ^{9}Be are very broad, they strongly overlap and make analysing the states populated during an experiment difficult. To overcome this, very high statistics measurements were performed; data were collected for over 30 hours and a thick target was utilised. A novel method for reducing the energy losses in the thick target was developed. Data were also acquired at two different beam energies, to ensure that any new features that were identified were part of the ^{9}Be spectrum, rather than manifestations of the many background reactions taking place.

Detector improvements

This investigation, which aimed to improve the performance of resistive charge division strip detectors (RSDs), was in part motivated by the experimental challenges of measuring the direct decay of the Hoyle state, detailed in this thesis. Since double-sided silicon strip detectors (DSSDs) do not perform well for high multiplicity events where the detected particles have similar energies, it was proposed that RSDs may provide a better alternative. However, although the ambiguity in particle hit positions is not a problem when using RSDs, further issues are encountered. Due to the charge division mechanism, the detectors are susceptible to noise, meaning that they possess worse energy resolution and require higher discriminator thresholds than DSSDs. Since there are fewer detector channels, RSDs also suffer from more pile-up.

Two methods of reducing these backgrounds were developed. The first method utilised the normally-unused rear contact of the RSD, which covers the whole of the detector area. By ensuring that the sum of the energies detected by the front detector strips equalled that collected by the rear detector contact, events where pile-up on a single strip or where a strip triggered on noise could be omitted. This led to an improvement in the signal-to-background ratio by around a factor of 4.

A second method was developed, which further improved the situation, by considering the timing of the detections at each end of a detector strip. In a standard timing set-up, constant fraction discriminators (CFDs) can be used to accurately measure the time of all of the detections in an event, with respect to a reference time. All detections associated with a single event should fall within the same small time window. Placing a software gate on this time window improves the signal-to-background ratio. However, in the absence of expensive CFDs, if leading edge discriminators (LEDs) are used, timing information is smeared out due to time walk. The present study showed that LEDs can be used for timing when using RSDs. If the time of the pulses measured at each end of a detector strip are taken, due to the charge division, there should be a fixed amount of time walk. By comparing the amount of time walk with the charge division, detections falling within a correct time window could be identified and selected, leading to an improvement in the signal-to-background ratio by a factor of around 3.5.

These methods can be utilised for any detector that uses resistive charge division in one dimension. The TIARA array, presently located at one of the cyclotrons at Texas A&M, uses Micron X1 resistive strip detectors, so the present methods could be applied there [204]. Due to its ease of implementation in the hardware and in post-processing, the method of matching the energies on front and rear detector contacts is most highly recommended at the present time.

Appendices

References

[1] R. Machleidt. “The nuclear force in the third millennium”. In: *Nucl. Phys. A* 689 (2001), pp. 11 –22. ISSN: 0375-9474. DOI: http://dx.doi.org/10.1016/S0375-9474(01)00814-4. URL: http://www.sciencedirect.com/science/article/pii/S0375947401008144.

[2] H. D. Politzer. “Asymptotic freedom: An approach to strong interactions”. In: *Phys. Rep.* 14 (1974), pp. 129 –180. ISSN: 0370-1573. DOI: http://dx.doi.org/10.1016/0370-1573(74)90014-3. URL: http://www.sciencedirect.com/science/article/pii/0370157374900143.

[3] A. Ekström, G. Baardsen, C. Forssén, G. Hagen, M. Hjorth-Jensen, G. R. Jansen, R. Machleidt, W. Nazarewicz, T. Papenbrock, J. Sarich, and S. M. Wild. “Optimized Chiral Nucleon-Nucleon Interaction at Next-to-Next-to-Leading Order”. In: *Phys. Rev. Lett.* 110 (2013), p. 192502. DOI: 10.1103/PhysRevLett.110.192502. URL: https://link.aps.org/doi/10.1103/PhysRevLett.110.192502.

[4] G. F. Knoll. *Radiation detection and measurement*. John Wiley & Sons, 2010.

[5] L. R. Hafstad and E. Teller. “The Alpha-Particle Model of the Nucleus”. In: *Phys. Rev.* 54 (1938), pp. 681–692. DOI: 10.1103/PhysRev.54.681. URL: https://link.aps.org/doi/10.1103/PhysRev.54.681.

[6] M. Freer. “The clustered nucleus: cluster structures in stable and unstable nuclei”. In: *Rep. Prog. Phys.* 70 (2007), p. 2149. URL: http://stacks.iop.org/0034-4885/70/i=12/a=R03.

[7] J.-P. Ebran, E. Khan, T. Nikšić, and D. Vretenar. “How atomic nuclei cluster”. In: *Nature* 487 (2012), pp. 341–344.

[8] C. F. v. Weizsäcker. “Zur Theorie der Kernmassen”. In: *Z. Phys. A Hadron Nucl.* 96 (1935), pp. 431–458. ISSN: 0044-3328. DOI: 10.1007/BF01337700. URL: http://dx.doi.org/10.1007/BF01337700.

[9] J. Breithaupt. *New understanding physics for advanced Level.* IOP Publishing, 2000, p. 162.

[10] N. Bohr and J. A. Wheeler. “The Mechanism of Nuclear Fission”. In: *Phys. Rev.* 56 (1939), pp. 426–450. DOI: 10.1103/PhysRev.56.426. URL: https://link.aps.org/doi/10.1103/PhysRev.56.426.

[11] B. Cameron Reed. “Simple derivation of the Bohr–Wheeler spontaneous fission limit”. In: *Am. J. Phys.* 71 (2003), pp. 258–260.

[12] J. Watterson. *The Liquid Drop Model lecture slides.* https://indico.cern.ch/event/145296/contributions/1381141/attachments/136909/194250/lecture17.pdf. Accessed: 24-05-2017.

[13] W. Demtröder. *Atoms, molecules and photons.* Springer, 2006.

[14] M. G. Mayer. “On Closed Shells in Nuclei”. In: *Phys. Rev.* 74 (1948), pp. 235–239. DOI: 10.1103/PhysRev.74.235. URL: https://link.aps.org/doi/10.1103/PhysRev.74.235.

[15] R. D. Woods and D. S. Saxon. “Diffuse Surface Optical Model for Nucleon-Nuclei Scattering”. In: *Phys. Rev.* 95 (1954), pp. 577–578. DOI: 10.1103/PhysRev.95.577. URL: https://link.aps.org/doi/10.1103/PhysRev.95.577.

[16] O. Haxel, J. H. D. Jensen, and H. E. Suess. “On the ”Magic Numbers” in Nuclear Structure”. In: *Phys. Rev.* 75 (1949), pp. 1766–1766. DOI: 10.1103/PhysRev.75.1766.2. URL: https://link.aps.org/doi/10.1103/PhysRev.75.1766.2.

[17] R. Lawson. *Theory of the nuclear shell model.* Clarendon Press Oxford, 1980.

[18] A. Bohr and B. R. Mottelson. *Nuclear structure.* Vol. 1. World Scientific, 1998.

[19] *Nuclear Deformation.* http://www.wheldon.talktalk.net/thesis/thesis/node10.html. Accessed: 20/08/2014.

[20] *Nuclear Deformation Diagrams.* http://creativecommons.org/licenses/by-sa/3.0/http://en.wikipedia.org/wiki/Spheroid. Accessed: 22/09/2014.

[21] B. R. Mottelson and S. G. Nilsson. “Classification of the Nucleonic States in Deformed Nuclei”. In: *Phys. Rev.* 99 (1955), pp. 1615–1617. DOI: `10.1103/PhysRev.99.1615`. URL: `http://link.aps.org/doi/10.1103/PhysRev.99.1615`.

[22] R Casten. *Nuclear structure from a simple perspective.* Vol. 6. Oxford University Press Oxford, 2000.

[23] J. M. Brown and A. Carrington. *Rotational spectroscopy of diatomic molecules.* Cambridge University Press, 2003.

[24] F. S. Stephens. “Coriolis effects and rotation alignment in nuclei”. In: *Rev. Mod. Phys.* 47 (1975), pp. 43–65. DOI: `10.1103/RevModPhys.47.43`. URL: `https://link.aps.org/doi/10.1103/RevModPhys.47.43`.

[25] S. Kumar, J. Singh, J. K. Sharma, and S. Singh. “Coriolis Effects in Atomic Nuclei”. In: *International Journal of Computer Science and Communication Engineering IJCSCE Special issue on “Emerging Trends in Engineering” ICETIE 2012* ().

[26] D. J. Rowe. *Nuclear collective motion: models and theory.* World Scientific, 2010, pp. 86–87.

[27] *Coriolis Force: an artefact of the earth’s rotation.* `http://ww2010.atmos.uiuc.edu/(Gh)/guides/mtr/fw/crls.rxml`. Accessed: 27/05/2017.

[28] W. von Oertzen, M. Freer, and Y. Kanada-En’yo. “Nuclear clusters and nuclear molecules”. In: *Phys. Rep.* 432 (2006), pp. 43 –113. ISSN: 0370-1573. DOI: `https://doi.org/10.1016/j.physrep.2006.07.001`. URL: `http://www.sciencedirect.com/science/article/pii/S0370157306002626`.

[29] J. A. Peacock, S. Cole, P. Norberg, C. M. Baugh, J. Bland-Hawthorn, T. Bridges, R. D. Cannon, M. Colless, C. Collins, W. Couch, et al. “A measurement of the cosmological mass density from clustering in the 2dF Galaxy Redshift Survey”. In: *Nature* 410 (2001), pp. 169–173.

[30] *OS MACKEREL CONTRA O MUNDO.* `https://www.ideafixa.com/oldbutgold/os-mackerel-contra-o-mundo`. Accessed: 30/05/2017.

[31] K. Ikeda, N. Takigawa, and H. Horiuchi. "The systematic structure-change into the molecule-like structures in the self-conjugate 4n nuclei". In: *Prog. Theor. Phys. Suppl.* 68 (1968), pp. 464–475.

[32] K. Giovanetti. *Matter Sources.* `http://csma31.csm.jmu.edu/physics/courses/163/older/bigbang2.htm`. Accessed: 30/05/2017.

[33] M. Freer, R. R. Betts, and A. H. Wuosmaa. "Relationship between the deformed harmonic oscillator and clustering in light nuclei". In: *Nucl. Phys. A* 587 (1995), pp. 36 –54. ISSN: 0375-9474. DOI: `http://dx.doi.org/10.1016/0375-9474(94)00820-D`. URL: `http://www.sciencedirect.com/science/article/pii/037594749400820D`.

[34] O. R. Frisch, G. Hevesy, and H. A. C. McKay. "Selective Absorption of Neutrons by Gold". In: *Nature* 137 (1936), pp. 149–150.

[35] E. Amaldi and E. Fermi. "On the Absorption and the Diffusion of Slow Neutrons". In: *Phys. Rev.* 50 (1936), pp. 899–928. DOI: `10.1103/PhysRev.50.899`. URL: `https://link.aps.org/doi/10.1103/PhysRev.50.899`.

[36] G. Breit and E. Wigner. "Capture of Slow Neutrons". In: *Phys. Rev.* 49 (1936), pp. 519–531. DOI: `10.1103/PhysRev.49.519`. URL: `https://link.aps.org/doi/10.1103/PhysRev.49.519`.

[37] K. S. Krane and D. Halliday. *Introductory nuclear physics.* Vol. 465. Wiley New York, 1988.

[38] *What is Nuclear Resonance – Compound Nucleus.* `http://www.nuclear-power.net/nuclear-power/reactor-physics/nuclear-engineering-fundamentals/neutron-nuclear-reactions/compound-nucleus-reactions/what-is-nuclear-resonance-compound-nucleus/prettyPhoto`. Accessed: 15-05-2017.

[39] J. Refsgaard. "Resonances, R-Matrix – Rotations in ^{12}C?" PhD thesis. Institut for Fysik go Astromomi Aarhus Universitet, 2016.

[40] A. M. Lane and R. G. Thomas. "R-Matrix Theory of Nuclear Reactions". In: *Rev. Mod. Phys.* 30 (1958), pp. 257–353. DOI: `10.1103/RevModPhys.30.257`. URL: `https://link.aps.org/doi/10.1103/RevModPhys.30.257`.

[41] P. Descouvemont and D. Baye. “The R-matrix theory”. In: *Rep. Prog. Phys.* 73 (2010), p. 036301. URL: http://stacks.iop.org/0034-4885/73/i=3/a=036301.

[42] T. Teichmann and E. P. Wigner. “Sum Rules in the Dispersion Theory of Nuclear Reactions”. In: *Phys. Rev.* 87 (1952), pp. 123–135. DOI: 10.1103/PhysRev.87.123. URL: http://link.aps.org/doi/10.1103/PhysRev.87.123.

[43] C. Simenel, B. Avez, and D. Lacroix. “Microscopic approaches for nuclear Many-Body dynamics: applications to nuclear reactions”. In: *arXiv preprint arXiv:0806.2714* (2008).

[44] I. J. Thompson and F. M. Nunes. *Nuclear reactions for astrophysics: principles, calculation and applications of low-energy reactions*. Cambridge University Press, 2009, p. 347.

[45] F. C. Barker and P. B. Treacy. “Nuclear levels near thresholds”. In: *Nucl. Phys.* 38 (1962), pp. 33 –49. ISSN: 0029-5582. DOI: http://dx.doi.org/10.1016/0029-5582(62)91014-3. URL: http://www.sciencedirect.com/science/article/pii/0029558262910143.

[46] F. C. Barker, H. J. Hay, and P. B Treacy. “0^+ States of ^{8}Be”. In: *Austr. J. Phys.* 21 (1968), pp. 239 –258.

[47] C. A. Diget, F. C. Barker, M. J. G. Borge, R. Boutami, P. Dendooven, T. Eronen, S. P. Fox, B. R. Fulton, H. O. U. Fynbo, J. Huikari, S. Hyldegaard, H. B. Jeppesen, A. Jokinen, B. Jonson, A. Kankainen, I. Moore, A. Nieminen, G. Nyman, H. Penttilä, V. F. E. Pucknell, K. Riisager, S. Rinta-Antila, O. Tengblad, Y. Wang, K. Wilhelmsen, and J. Äystö. “Breakup channels for ^{12}C triple-α continuum states”. In: *Phys. Rev. C* 80 (2009), p. 034316. DOI: 10.1103/PhysRevC.80.034316. URL: https://link.aps.org/doi/10.1103/PhysRevC.80.034316.

[48] F. D. Becchetti, C. A. Fields, R. S. Raymond, H. C. Bhang, and D. Overway. “Ghost anomaly in ^{8}Be studied with ^{9}Be(p,d) at E_p = 14.3 and 26.2 MeV”. In: *Phys. Rev. C* 24 (1981), pp. 2401–2408. DOI: 10.1103/PhysRevC.24.2401. URL: http://link.aps.org/doi/10.1103/PhysRevC.24.2401.

[49] A. Szczurek, K. Bodek, L. Jarczyk, and J. K. et. al. “Ghost anomaly and first excited state of ^{8}Be in the ^{9}Be(d,t)^{4}He reaction at 7 MeV”. In: *Nucl. Phys. A* 531 (1991), pp. 77 –92. ISSN: 0375-9474. DOI: http://dx.doi.org/10.1016/0375-9474(91)

90569-R. URL: http://www.sciencedirect.com/science/article/pii/037594749190569R.

[50] E. H. Berkowitz, G. L. Marolt, A. A. Rollefson, and C. P. Browne. “Survey of the ^{8}Be Ghost Anomaly”. In: *Phys. Rev. C* 4 (1971), pp. 1564–1570. DOI: 10.1103/PhysRevC.4.1564. URL: https://link.aps.org/doi/10.1103/PhysRevC.4.1564.

[51] *AZURE2 R-Matrix Program*. https://azure.nd.edu/login.php. Accessed: 22-05-2017.

[52] D. Tilley, J. Kelley, J. Godwin, D. Millener, J. Purcell, C. Sheu, and H. Weller. “Energy levels of light nuclei A=8,9,10”. In: *Nucl. Phys. A* 745 (2004), pp. 155 –362. ISSN: 0375-9474. DOI: http://dx.doi.org/10.1016/j.nuclphysa.2004.09.059. URL: http://www.sciencedirect.com/science/article/pii/S0375947404010267.

[53] M. Freer. “Molecules in nuclei”. In: *C. R. Phys.* 4 (2003), pp. 475–487.

[54] D. Scharnweber, W. Greiner, and U. Mosel. “The two-center shell model”. In: *Nucl. Phys. A* 164 (1971), pp. 257–278.

[55] W. von Oertzen. “Two-center molecular states in ^{9}B, ^{9}Be, ^{10}Be, and ^{10}B”. In: *Z. Phys. A Hadron Nucl.* 354 (1996), pp. 37–43. ISSN: 0939-7922. DOI: 10.1007/s002180050010. URL: http://dx.doi.org/10.1007/s002180050010.

[56] F. Barker and C. Woods. “States of ^{5}He and ^{5}Li”. In: *Austr. J. Phys.* 38 (1985), pp. 563–576.

[57] S. Okabe, Y. Abe, and H. Tanaka. “The Structure of ^{9}Be Nucleus by a Molecular Model. I)”. In: *Prog. Theor. Phys.* 57 (1977), p. 866. DOI: 10.1143/PTP.57.866. eprint: /oup/backfile/content_public/journal/ptp/57/3/10.1143/ptp.57.866/2/57-3-866.pdf. URL: http://dx.doi.org/10.1143/PTP.57.866.

[58] S. Okabe, Y. Abe, and H. Tanaka. “The Structure of ^{9}Be by a Molecular Model. II”. In: *Prog. Theor. Phys.* 61 (1979), p. 1049. DOI: 10.1143/PTP.61.1049. eprint: /oup/backfile/content_public/journal/ptp/61/4/10.1143/ptp.61.1049/2/61-4-1049.pdf. URL: +http://dx.doi.org/10.1143/PTP.61.1049.

[59] C. Adler, T. Corcoran, and C. Mast. “The application of the Su(3) shell model to ^{9}Be”. In: *Nucl. Phys.* 88 (1966), pp. 145 –168. ISSN: 0029-5582. DOI: `http://dx.doi.org/10.1016/0029-5582(66)90457-3`. URL: `http://www.sciencedirect.com/science/article/pii/0029558266904573`.

[60] A. G. Slight, T. E. Drake, and G. R. Bishop. “Inelastic electron scattering and the electromagnetic properties of ^{9}Be”. In: *Nucl. Phys. A* 208 (1973), pp. 157 –195. ISSN: 0375-9474. DOI: `http://dx.doi.org/10.1016/0375-9474(73)90740-9`. URL: `http://www.sciencedirect.com/science/article/pii/0375947473907409`.

[61] M. A. Caprio, P. Maris, and J. Vary. “Emergence of rotational bands in ab initio no-core configuration interaction calculations of light nuclei”. In: *Phys. Lett. B* 719 (2013), pp. 179 –184. ISSN: 0370-2693. DOI: `https://doi.org/10.1016/j.physletb.2012.12.064`. URL: `http://www.sciencedirect.com/science/article/pii/S0370269313000026`.

[62] M. A. Caprio, P. Maris, J. P. Vary, and R. Smith. “Collective rotation from ab initio theory”. In: *Int. J. Mod. Phys. E* 24 (2015), p. 1541002.

[63] P. Maris and J. P. Vary. “Ab initio nuclear structure calculations of p-shell nuclei with JISP16”. In: *Int. J. Mod. Phys. E* 22 (2013), p. 1330016.

[64] R. C. Cockrell. “Ab initio nuclear structure calculations for light nuclei”. PhD thesis. Iowa State University, 2012.

[65] H. Akimune, M. Fujimura, M. Fujiwara, K. Hara, T. Ishikawa, T. Kawabata, H. Utsunomiya, T. Yamagata, K. Yamasaki, and M. Yosoi. “Evidence for a 3.8 MeV state in ^{9}B”. In: *Phys. Rev. C* 64 (2001), p. 041305. DOI: `10.1103/PhysRevC.64.041305`. URL: `https://link.aps.org/doi/10.1103/PhysRevC.64.041305`.

[66] C. Scholl, Y. Fujita, T. Adachi, P. von Brentano, H. Fujita, M. Górska, H. Hashimoto, K. Hatanaka, H. Matsubara, K. Nakanishi, T. Ohta, Y. Sakemi, Y. Shimbara, Y. Shimizu, Y. Tameshige, A. Tamii, M. Yosoi, and R. G. T. Zegers. “High-resolution study of the ^{9}Be(^{3}He,t)^{9}B reaction up to the ^{9}B triton threshold”. In: *Phys. Rev. C* 84 (2011), p. 014308. DOI: `10.1103/PhysRevC.84.014308`. URL: `https://link.aps.org/doi/10.1103/PhysRevC.84.014308`.

[67] C. Forssén, P. Navrátil, W. E. Ormand, and E. Caurier. “Large basis *ab initio* shell model investigation of ^{9}Be and ^{11}Be”. In: *Phys. Rev. C* 71 (4 2005), p. 044312. DOI: 10.1103/PhysRevC.71.044312. URL: https://link.aps.org/doi/10.1103/PhysRevC.71.044312.

[68] R. Machleidt. “High-precision, charge-dependent Bonn nucleon-nucleon potential”. In: *Phys. Rev. C* 63 (2 2001), p. 024001. DOI: 10.1103/PhysRevC.63.024001. URL: https://link.aps.org/doi/10.1103/PhysRevC.63.024001.

[69] S. M. Lenzi. “Coulomb energy differences in mirror nuclei”. In: *J. Phys. Conf. Ser.* Vol. 49. IOP Publishing. 2006, p. 85.

[70] B. Agrawal, T. Sil, S. Samaddar, J. De, and S. Shlomo. “Coulomb energy differences in mirror nuclei revisited”. In: *Phys. Rev. C* 64 (2001), p. 024305.

[71] F. Zijderhand, R. Makkus, and C. V. D. Leun. “Investigation of ^{41}Sc by proton capture in ^{40}Ca”. In: *Nucl. Phys. A* 466 (1987), pp. 280 –294. ISSN: 0375-9474. DOI: http://dx.doi.org/10.1016/0375-9474(87)90442-8. URL: http://www.sciencedirect.com/science/article/pii/0375947487904428.

[72] C. Wheldon, T. Kokalova, M. Freer, J. Walshe, R. Hertenberger, H.-F. Wirth, N. I. Ashwood, M. Barr, N. Curtis, T. Faestermann, R. Lutter, J. D. Malcolm, and D. J. Marín-Lámbarri. “Spectroscopy of ^{9}B via high-resolution ejectile-tagged recoil break-up”. In: *Phys. Rev. C* 91 (2015), p. 024308. DOI: 10.1103/PhysRevC.91.024308. URL: https://link.aps.org/doi/10.1103/PhysRevC.91.024308.

[73] M. A. Bentley and S. M. Lenzi. “Coulomb energy differences between high-spin states in isobaric multiplets”. In: *Prog. Part. Nucl. Phys.* 59.2 (2007), pp. 497 –561. ISSN: 0146-6410. DOI: https://doi.org/10.1016/j.ppnp.2006.10.001. URL: http://www.sciencedirect.com/science/article/pii/S0146641006000743.

[74] R. Smith, C. Wheldon, M. Freer, N. Curtis, T. Kokalova, S. Almaraz-Calderon, A. Aprahamian, N. I. Ashwood, M. Barr, B. Bucher, P. Copp, M. Couder, X. Fang, G. Goldring, F. Jung, S. R. Lesher, W. Lu, J. D. Malcolm, A. Roberts, W. P. Tan, and V. A. Ziman. “Evidence for a 3.8 MeV state in ^{9}Be”. In: *Phys. Rev. C* 94 (2016), p. 014320. DOI: 10.1103/PhysRevC.94.014320. URL: https://link.aps.org/doi/10.1103/PhysRevC.94.014320.

[75] F. C. Barker and N. Ferdous. "The Low-lying Levels of ^{13}C and ^{13}N". In: *Australian Journal of Physics* 33.4 (1980), pp. 691–718.

[76] R. G. Thomas. "An Analysis of the Energy Levels of the Mirror Nuclei, C^{13} and N^{13}". In: *Phys. Rev.* 88 (5 1952), pp. 1109–1125. DOI: 10.1103/PhysRev.88.1109. URL: https://link.aps.org/doi/10.1103/PhysRev.88.1109.

[77] J. B. Ehrman. "On the Displacement of Corresponding Energy Levels of C^{13} and N^{13}". In: *Phys. Rev.* 81 (3 1951), pp. 412–416. DOI: 10.1103/PhysRev.81.412. URL: https://link.aps.org/doi/10.1103/PhysRev.81.412.

[78] H. T. Fortune and R. Sherr. "Proton and alpha spectroscopic factors for states at 6.4˘7.5 MeV in ^{19}Ne". In: *Phys. Rev. C* 73 (2006), p. 024302. DOI: 10.1103/PhysRevC.73.024302. URL: https://link.aps.org/doi/10.1103/PhysRevC.73.024302.

[79] *Institute for Nuclear Structure and Astrophysics (ISNAP) Accelerators.* http://isnap.nd.edu/research/facility/accelerator/. Accessed: 21-04-2017.

[80] *Van de Graaff generator dictionary definition.* http://www.yourdictionary.com/van-de-graaff-generator. Accessed: 20-07-2017.

[81] L. Lamm. *FN Tandem Van de Graaff Accelerator at Notre Dame.* http://www.jinaweb.org/outreach/PIXE-PAN09/docs/Accelerator%20Presentation_June2009.pdf. Accessed: 21-04-2017.

[82] N Curtis. *Accelerators and Detectors.* Lecture. 2014.

[83] H. Liebl. *Applied charged particle optics.* Vol. 2012. Springer, 2008, p. 39.

[84] *DC Coupled Double Sided.* http://www.micronsemiconductor.co.uk/products-strip.asp?productsubcatID=2. Accessed: 20-12-2012.

[85] W. R. Leo. "Techniques for Nuclear and Particle Physics Experiments; A How-to Approach". In: 48 (1993), p. 271.

[86] G. Knoll and D. Mcgregor. "Fundamentals of Semiconductor Detectors for Ionizing Radiation". In: *MRS Proceedings* 302 (1993). DOI: 10.1557/PROC-302-3.

[87] K. Shah, J. Lund, and F. Olschner. "Charge collection efficiency in a semiconductor radiation detector with a non-constant electric field". In: *IEEE Trans. Nucl. Sci.* 37 (1990), pp. 183–186.

[88] G. Lindström. “Radiation damage in silicon detectors”. In: *Nucl. Instrum. Methods Phys. Res. A* 512 (2003), pp. 30–43.

[89] G. Casse. “The effect of hadron irradiation on the electrical properties of particle detectors made from various silicon materials”. PhD thesis. Universite Joseph Fourier - Grenoble, Sept. 1998.

[90] R. Smith. *Investigating Clustered States in ^{9}Be through Inelastic Alpha Particle Scattering*. http://undergraduatelibrary.org/2013/mathematics-physics/investigating-clustered-states-9be-nucleus-through-inelastic-alpha-particle. Accessed: 24/09/2014.

[91] P. Busa. “Understanding Design and Operation of Successive Approximation Register”. In: (2008). URL: http://cmosedu.com/jbaker/courses/ece614/s08/lec23_ece614.pdf.

[92] *Multi Instance Data Acquisition System*. http://npg.dl.ac.uk/MIDAS/. Accessed: 22-05-2017.

[93] S. M. Singer. *Sunsort reference manual*. http://npg.dl.ac.uk/MIDAS/manual/SunSort/index.html. Accessed: 2017.

[94] R. Smith, M. Freer, C. Wheldon, N. Curtis, S. Almaraz-Calderon, A. Aprahamian, N. I. Ashwood, M. Barr, B. Bucher, P. Copp, et al. “Breakup branches of Borromean beryllium-9”. In: *AIP Conference Proceedings*. Vol. 1681. AIP Publishing. 2015, p. 060003.

[95] T. W. Armstrong and K. C. Chandler. *A Fortran program for computing stopping powers and ranges for muons, charged pions, protons, and heavy ions*. ORNL-4869, Oak Ridge National Laboratory. Accessed: 27-04-2017. 1973.

[96] T. Armstrong and K. Chandler. “SPAR, a FORTRAN program for computing stopping powers and ranges for muons, charged pions, protons, and heavy ions”. In: *ORNL-4869, Oak Ridge National Laboratory* (1973).

[97] H. Bethe and J. Ashkin. *Nuclear structure from a simple perspective*. J Wiley, New York, 1953, p. 253.

[98] J. Lindhard, M. Scharff, and H. E. Schiøtt. *Range concepts and heavy ion ranges*. Munksgaard Copenhagen, 1963.

[99] P. Papka, T. A. D. Brown, B. R. Fulton, D. L. Watson, S. P. Fox, D. Groombridge, M. Freer, N. M. Clarke, N. I. Ashwood, N. Curtis, V. Ziman, P. McEwan, S. Ahmed, W. N. Catford, D. Mahboub, C. N. Timis, T. D. Baldwin, and D. C. Weisser. "Decay path measurements for the 2.429 MeV state in ^{9}Be: Implications for the astrophysical $\alpha+\alpha+n$ reaction". In: *Phys. Rev. C* 75 (2007), p. 045803. DOI: 10.1103/PhysRevC.75.045803. URL: https://link.aps.org/doi/10.1103/PhysRevC.75.045803.

[100] T. A. D. Brown, P. Papka, B. R. Fulton, D. L. Watson, S. P. Fox, D. Groombridge, M. Freer, N. M. Clarke, N. I. Ashwood, N. Curtis, V. Ziman, P. McEwan, S. Ahmed, W. N. Catford, D. Mahboub, C. N. Timis, T. D. Baldwin, and D. C. Weisser. "Decay studies for states in ^{9}Be up to 11 MeV: Insights into the n+^{8}Be and α+^{5}He cluster structure". In: *Phys. Rev. C* 76 (2007), p. 054605. DOI: 10.1103/PhysRevC.76.054605. URL: https://link.aps.org/doi/10.1103/PhysRevC.76.054605.

[101] N. Curtis, N. M. Clarke, B. R. Fulton, S. J. Hall, M. J. Leddy, A. S. J. Murphy, J. S. Pople, R. P. Ward, W. N. Catford, G. J. Gyapong, S. M. Singer, S. P. G. Chappell, S. P. Fox, C. D. Jones, D. L. Watson, W. D. M. Rae, and P. M. Simmons. ""Association of the ^{12}C+^{12}C breakup states in ^{24}Mg with the quasimolecular resonances"". In: *Phys. Rev. C* 51 (1995), pp. 1554–1557. DOI: 10.1103/PhysRevC.51.1554. URL: http://link.aps.org/doi/10.1103/PhysRevC.51.1554.

[102] N. Curtis, A. S. J. Murphy, N. M. Clarke, M. Freer, B. R. Fulton, S. J. Hall, M. J. Leddy, J. S. Pople, G. Tungate, R. P. Ward, W. N. Catford, G. J. Gyapong, S. M. Singer, S. P. G. Chappell, S. P. Fox, C. D. Jones, D. L. Watson, W. D. M. Rae, P. M. Simmons, and P. H. Regan. "Evidence for a highly deformed band in ^{16}O+^{16}O breakup of ^{32}S". In: *Phys. Rev. C* 53 (1996), pp. 1804–1810. DOI: 10.1103/PhysRevC.53.1804. URL: http://link.aps.org/doi/10.1103/PhysRevC.53.1804.

[103] N. Curtis. PhD thesis. University of Birmingham, 1995.

[104] M. A. Tiede, K. W. Kemper, N. R. Fletcher, D. Robson, D. D. Caussyn, S. J. Bennett, J. D. Brown, W. N. Catford, C. D. Jones, D. L. Watson, and W. D. M. Rae. "Measurement of low-lying states in ^{9}B". In: *Phys. Rev. C* 52 (1995), pp. 1315–1325. DOI: 10.1103/PhysRevC.52.1315. URL: https://link.aps.org/doi/10.1103/PhysRevC.52.1315.

[105] R. E. Azuma, E. Uberseder, E. C. Simpson, C. R. Brune, H. Costantini, R. J. de Boer, J. Görres, M. Heil, P. J. LeBlanc, C. Ugalde, and M. Wiescher. "AZURE: An R-matrix code for nuclear astrophysics". In: *Phys. Rev. C* 81 (2010), p. 045805. DOI: 10.1103/PhysRevC.81.045805. URL: https://link.aps.org/doi/10.1103/PhysRevC.81.045805.

[106] R. Smith. *Tracey Peaker version 1.0 peak fitting code.* Matlab File Exchange, 57125. Accessed: 12-05-2016.

[107] F. Ajzenberg-Selove. "Energy levels of light nuclei A = 1112". In: *Nucl. Phys. A* 506 (1990), pp. 1 –158. ISSN: 0375-9474. DOI: http://dx.doi.org/10.1016/0375-9474(90)90271-M. URL: http://www.sciencedirect.com/science/article/pii/037594749090271M.

[108] N. I. Ashwood, M. Freer, D. J. Millener, N. A. Orr, F. Carstoiu, S. Ahmed, J. C. Angélique, V. Bouchat, W. N. Catford, N. M. Clarke, N. Curtis, F. Hanappe, M. Horoi, Y. Kerckx, J. L. Lecouey, F. M. Marqués, T. Materna, G. Normand, S. Pain, N. Soi ć, C. Timis, A. Unshakova, and V. A. Ziman. "High-energy two-neutron removal from ^{10}Be". In: *Phys. Rev. C* 72 (2005), p. 024314. DOI: 10.1103/PhysRevC.72.024314. URL: https://link.aps.org/doi/10.1103/PhysRevC.72.024314.

[109] B. P. Flannery, S. A. Teukolsky, and W. T. Vetterling. *Radiation detection and measurement.* Cambridge University Press, 1992.

[110] E. Gete, L. Buchmann, R. E. Azuma, D. Anthony, N. Bateman, J. C. Chow, J. M. D'Auria, M. Dombsky, U. Giesen, C. Iliadis, K. P. Jackson, J. D. King, D. F. Measday, and A. C. Morton. "β-delayed particle decay of ^{9}C and the A=9, T=1/2 nuclear system: Experiment, data, and phenomenological analysis". In: *Phys. Rev. C* 61 (2000), p. 064310. DOI: 10.1103/PhysRevC.61.064310. URL: https://link.aps.org/doi/10.1103/PhysRevC.61.064310.

[111] C. Wheldon. *ckin 2-body kinematics code.* http://www.np.ph.bham.ac.uk/research_resources/programs/. Accessed: 29-09-2014.

[112] I. McLaren. *Wclbes.f subroutine.* http://cernlib.sourcearchive.com/documentation/2006.dfsg.2/wclbes_8F_source.html. Accessed: 08-03-2016.

[113] I. J. Thompson and B. A. R. "COULCC: A continued-fraction algorithm for Coulomb functions of complex order with complex arguments". In: *Computer Physics Communications* 36 (1985), pp. 363 –372. ISSN: 0010-4655. DOI: http://dx.doi.org/10.1016/0010-4655(85)90025-6. URL: http://www.sciencedirect.com/science/article/pii/0010465585900256.

[114] R. Smith. *Spectroscopy of the Borromean ^{9}Be and ^{9}B Mirror Nuclei.* Paper presented at the 11th International Conference on Clustering Aspects of Nuclear Reactions and Dynamics. Accessed: 20-07-2017.

[115] N. Curtis, S. Almaraz-Calderon, A. Aprahamian, N. I. Ashwood, M. Barr, B. Bucher, P. Copp, M. Couder, X. Fang, M. Freer, G. Goldring, F. Jung, S. R. Lesher, W. Lu, J. D. Malcolm, A. Roberts, W. P. Tan, C. Wheldon, and V. A. Ziman. "^{8}Be + ^{8}Be". In: *Phys. Rev. C* 94 (2016), p. 034313. DOI: 10.1103/PhysRevC.94.034313. URL: https://link.aps.org/doi/10.1103/PhysRevC.94.034313.

[116] H. Hart, C. M. Hadad, L. E. Craine, and D. J. Hart. *Organic chemistry: a short course.* Cengage Learning, 2011.

[117] A. Dalila, A. B. Suriani, M. Rosmi, R Rosazley, J. Rosli, and M Rusop. "Carbon Nanotubes: A Brief Outlook on History, Synthesis Methods and Various Bio-Hydrocarbon Sources". In: *Advanced Materials Research.* Vol. 832. Trans. Tech. Publ. 2014, pp. 792–797.

[118] E. P. Randviir, D. A. Brownson, and C. E. Banks. "A decade of graphene research: production, applications and outlook". In: *Mater. Today* 17 (2014), pp. 426–432.

[119] *Carbon Chemistry: An Introduction.* http://www.visionlearning.com/en/library/Chemistry/1/Carbon-Chemistry/60. Accessed: 20-07-2017.

[120] D. Jenkins and O. S. Kirsebom. "The secret of life". In: *Phys. World* 26 (2013), p. 23.

[121] R. H. Cyburt, B. D. Fields, K. A. Olive, and T.-H. Yeh. "Big bang nucleosynthesis: Present status". In: *Rev. Mod. Phys.* 88 (2016), p. 015004. DOI: 10.1103/RevModPhys.88.015004. URL: https://link.aps.org/doi/10.1103/RevModPhys.88.015004.

[122] *Scheme of nuclear reaction chains for Big Bang nucleosynthesis*. `https://upload.wikimedia.org/wikipedia/commons/5/5f/Scheme_of_nuclear_reaction_chains_for_Big_Bang_nucleosynthesis.svg`. Accessed: 20-07-2017.

[123] E. J. Öpik. “Stellar Models with Variable Composition. II. Sequences of Models with Energy Generation Proportional to the Fifteenth Power of Temperature”. In: *Proceedings of the Royal Irish Academy. Section A: Mathematical and Physical Sciences*. JSTOR. 1951, pp. 49–77.

[124] E. E. Salpeter. “Nuclear reactions in stars without hydrogen.” In: *Astrophys. J* 115 (1952), pp. 326–328.

[125] M. Milin, M. Zadro, S Cherubini, T Davinson, A Di Pietro, P Figuera, . Miljanić, A Musumarra, A Ninane, A. Ostrowski, et al. “Sequential decay reactions induced by a 18 MeV ^{6}He beam on ^{6}Li and ^{7}Li”. In: *Nucl. Phys. A* 753 (2005), pp. 263–287.

[126] F. Hoyle, D. N. F. Dunbar, W. A. Wenzel, and W. Whaling. “A state in C-12 predicted from astrophysical evidence”. In: *Phys. Rev.* Vol. 92. AMERICAN PHYSICAL SOC ONE PHYSICS ELLIPSE, COLLEGE PK, MD 20740-3844 USA. 1953, pp. 1095–1095.

[127] F Hoyle. “Resonances and nuclear molecular configurations in heavy-ion reactions”. In: *Astrophys. J. (Suppl.)* 1 (1954), p. 12.

[128] D. N. F. Dunbar, R. E. Pixley, W. A. Wenzel, and W. Whaling. “The 7.68-Mev state in C^{12}”. In: *Phys. Rev.* 92 (1953), p. 649.

[129] C. W. Cook, W. A. Fowler, C. C. Lauritsen, and T. Lauritsen. “B 12, C 12, and the red giants”. In: *Phys. Rev.* 107 (1957), p. 508.

[130] M. Holloway and B. Moore. “The disintegration of N 14 and N 15 by deuterons”. In: *Phys. Rev.* 58 (1940), p. 847.

[131] M. Livio, D. Hollowell, A. Weiss, and J. W. Truran. “The anthropic significance of the existence of an excited state of ^{12}C”. In: *Nature* 340 (1989), pp. 281–284.

[132] H. Kragh. “An anthropic myth: Fred Hoyle’s carbon-12 resonance level”. In: *Arch. Hist. Exact Sci.* 64 (2010), pp. 721–751.

[133] H Morinaga. “Interpretation of Some of the Excited States of 4 n Self-Conjugate Nuclei”. In: *Phys. Rev.* 101 (1956), p. 254.

[134] E. E. Salpeter. “Nuclear reactions in stars without hydrogen.” In: *Astrophys. J* 115 (1952), pp. 326–328.

[135] A. Ray. “Massive stars as thermonuclear reactors and their explosions following core collapse”. In: *Principles and Perspectives in Cosmochemistry: Lecture Notes of the Kodai School on 'Synthesis of Elements in Stars' held at Kodaikanal Observatory, India, April 29 - May 13, 2008*. Ed. by A. Goswami and B. E. Reddy. Berlin, Heidelberg: Springer Berlin Heidelberg, 2010, pp. 209–275. ISBN: 978-3-642-10352-0. DOI: `10.1007/978-3-642-10352-0_5`. URL: `http://dx.doi.org/10.1007/978-3-642-10352-0_5`.

[136] K. Ogata, M. Kan, and M. Kamimura. “Quantum three-body calculation of the non-resonant triple-α reaction rate at low temperatures”. In: *Prog. Theor. Phys.* 122 (2009), pp. 1055–1064.

[137] A. R. Raduta, B. Borderie, E. Geraci, N. L. Neindre, P. Napolitani, M. Rivet, R. Alba, F. Amorini, G. Cardella, M. Chatterjee, E. D. Filippo, D. Guinet, P. Lautesse, E. L. Guidara, G. Lanzalone, G. Lanzano, I. Lombardo, O. Lopez, C. Maiolino, A. Pagano, S. Pirrone, G. Politi, F. Porto, F. Rizzo, P. Russotto, and J. Wieleczko. “Evidence for α-particle condensation in nuclei from the Hoyle state deexcitation”. In: *Phys. Lett. B* 705 (2011), pp. 65 –70. ISSN: 0370-2693. DOI: `http://dx.doi.org/10.1016/j.physletb.2011.10.008`. URL: `http://www.sciencedirect.com/science/article/pii/S0370269311012408`.

[138] M. Freer, A. H. Wuosmaa, R. R. Betts, D. J. Henderson, P. Wilt, R. W. Zurmühle, D. P. Balamuth, S. Barrow, D. Benton, Q. Li, Z. Liu, and Y. Miao. “Limits for the 3α branching ratio of the decay of the 7.65 MeV, 0_2^+ state in ^{12}C”. In: *Phys. Rev. C* 49 (1994), R1751–R1754. DOI: `10.1103/PhysRevC.49.R1751`. URL: `http://link.aps.org/doi/10.1103/PhysRevC.49.R1751`.

[139] O. S. Kirsebom, M. Alcorta, M. J. G. Borge, M. Cubero, C. A. Diget, L. M. Fraile, B. R. Fulton, H. O. U. Fynbo, D. Galaviz, B. Jonson, M. Madurga, T. Nilsson, G. Nyman, K. Riisager, O. Tengblad, and M. Turrión. “Improved Limit on Direct α Decay of the Hoyle State”. In: *Phys. Rev. Lett.* 108 (2012), p. 202501. DOI: `10.1103/PhysRevLett.108.202501`. URL: `http://link.aps.org/doi/10.1103/PhysRevLett.108.202501`.

[140] M. Itoh, S. Ando, T. Aoki, H. Arikawa, S. Ezure, K. Harada, T. Hayamizu, T. Inoue, T. Ishikawa, K. Kato, H. Kawamura, Y. Sakemi, and A. Uchiyama. "Further Improvement of the Upper Limit on the Direct 3α Decay from the Hoyle State in ^{12}C". In: *Phys. Rev. Lett.* 113 (2014), p. 102501. DOI: `10.1103/PhysRevLett.113.102501`. URL: `http://link.aps.org/doi/10.1103/PhysRevLett.113.102501`.

[141] S. Karataglidis, P. J. Dortmans, K. Amos, and R. de Swiniarski. "Fully microscopic model of 200 MeV proton$-^{12}$C elastic and inelastic scattering". In: *Phys. Rev. C* 52 (1995), pp. 861–877. DOI: `10.1103/PhysRevC.52.861`. URL: `https://link.aps.org/doi/10.1103/PhysRevC.52.861`.

[142] S. Cohen and D. Kurath. "Effective interactions for the 1p shell". In: *Nucl. Phys.* 73 (1965), pp. 1 –24. ISSN: 0029-5582. DOI: `http://dx.doi.org/10.1016/0029-5582(65)90148-3`. URL: `http://www.sciencedirect.com/science/article/pii/0029558265901483`.

[143] A. C. Dreyfuss, K. D. Launey, T. Dytrych, J. P. Draayer, and C. Bahri. "Hoyle state and rotational features in Carbon-12 within a no-core shell-model framework". In: *Phys. Lett. B* 727 (2013), pp. 511 –515. ISSN: 0370-2693. DOI: `http://doi.org/10.1016/j.physletb.2013.10.048`. URL: `http://www.sciencedirect.com/science/article/pii/S0370269313008551`.

[144] E. Epelbaum, H. Krebs, T. A. Lähde, D. Lee, and U.-G. Meißner. "Structure and Rotations of the Hoyle State". In: *Phys. Rev. Lett.* 109 (2012), p. 252501. DOI: `10.1103/PhysRevLett.109.252501`. URL: `https://link.aps.org/doi/10.1103/PhysRevLett.109.252501`.

[145] Y. Kanada-En'yo and H. Horiuchi. "Structure of light unstable nuclei studied with antisymmetrized molecular dynamics". In: *Prog. Theor. Phys. Suppl.* 142 (2001), pp. 205–263.

[146] Y. Kanada-En'yo. "The structure of ground and excited states of ^{12}C". In: *Prog. Theor. Phys.* 117 (2007), pp. 655–680.

[147] A. Ogloblin, T. Belyaeva, A. Danilov, A. Demyanova, and S. Goncharov. "Radius of ^{12}C in the excited 2^+ Hoyle state". In: *Eur. Phys. J. A* 49 (2013), pp. 1–7.

[148] A. Danilov, T. Belyaeva, A. Demyanova, S. Goncharov, and A. Ogloblin. “Determination of nuclear radii for unstable states in ^{12}C with diffraction inelastic scattering”. In: *Phys. Rev. C* 80 (2009), p. 054603.

[149] I. Sick and J. McCarthy. “Elastic electron scattering from ^{12}C and ^{16}O”. In: *Nucl. Phys. A* 150 (1970), pp. 631 –654. ISSN: 0375-9474. DOI: http://dx.doi.org/10.1016/0375-9474(70)90423-9. URL: http://www.sciencedirect.com/science/article/pii/0375947470904239.

[150] A. Nakada, Y. Torizuka, and Y. Horikawa. “Determination of the Deformation in ^{12}C from Electron Scattering”. In: *Phys. Rev. Lett.* 27 (1971), pp. 745–748. DOI: 10.1103/PhysRevLett.27.745. URL: https://link.aps.org/doi/10.1103/PhysRevLett.27.745.

[151] A. Nakada, Y. Torizuka, and Y. Horikawa. “Determination of the Deformation in ^{12}C from Electron Scattering”. In: *Phys. Rev. Lett.* 27 (1971), pp. 1102–1102. DOI: 10.1103/PhysRevLett.27.1102.2. URL: https://link.aps.org/doi/10.1103/PhysRevLett.27.1102.2.

[152] P. Strehl and T. Schucan. “Study of monopole transitions in ^{12}C, ^{24}Mg, ^{28}Si, ^{32}S and ^{40}Ca by inelastic electron scattering”. In: *Phys. Lett. B* 27 (1968), pp. 641 –643. ISSN: 0370-2693. DOI: http://dx.doi.org/10.1016/0370-2693(68)90303-1. URL: http://www.sciencedirect.com/science/article/pii/0370269368903031.

[153] M. Chernykh, H Feldmeier, T Neff, P von Neumann-Cosel, and A Richter. “Structure of the Hoyle State in ^{12}C”. In: *Phys. Rev. Lett.* 98 (2007), p. 032501.

[154] D. Brink. “Proc. Int. School of Physics Enrico Fermi, Course XXXVI, Varenna, 1966”. In: (1966).

[155] D. Brink and E. Boeker. “Effective interactions for Hartree-Fock calculations”. In: *Nucl. Phys. A* 91 (1967), pp. 1 –26. ISSN: 0375-9474. DOI: http://dx.doi.org/10.1016/0375-9474(67)90446-0. URL: http://www.sciencedirect.com/science/article/pii/0375947467904460.

[156] H. Margenau. “Statistics of Excited Energy States of Nuclei”. In: *Phys. Rev.* 59 (1941), pp. 627–632. DOI: 10.1103/PhysRev.59.627. URL: https://link.aps.org/doi/10.1103/PhysRev.59.627.

[157] R. Bijker and F. Iachello. “Cluster states in nuclei as representations of a U(ν+1) group”. In: *Phys. Rev. C* 61 (2000), p. 067305. DOI: 10.1103/PhysRevC.61.067305. URL: https://link.aps.org/doi/10.1103/PhysRevC.61.067305.

[158] D. J. Marín-Lámbarri, R. Bijker, M. Freer, M. Gai, T. Kokalova, D. J. Parker, and C. Wheldon. “Evidence for Triangular $\mathcal{D}_{3h}$ Symmetry in ^{12}C”. In: *Phys. Rev. Lett.* 113 (2014), p. 012502. DOI: 10.1103/PhysRevLett.113.012502. URL: https://link.aps.org/doi/10.1103/PhysRevLett.113.012502.

[159] M. H. Anderson, J. R. Ensher, M. R. Matthews, C. E. Wieman, and E. A. Cornell. “Observation of Bose-Einstein condensation in a dilute atomic vapor”. In: *Science* 269 (1995), p. 198.

[160] A Tohsaki, H Horiuchi, P Schuck, and G Röpke. “Alpha Cluster Condensation in ^{12}C and ^{16}O”. In: *Phys. Rev. Lett.* 87 (2001), p. 192501.

[161] G. Röpke, A. Schnell, P. Schuck, and P. Nozières. “Four-Particle Condensate in Strongly Coupled Fermion Systems”. In: *Phys. Rev. Lett.* 80 (1998), pp. 3177–3180. DOI: 10.1103/PhysRevLett.80.3177. URL: https://link.aps.org/doi/10.1103/PhysRevLett.80.3177.

[162] M Beyer, S. Sofianos, C Kuhrts, G Röpke, and P Schuck. “The α-particle in nuclear matter”. In: *Phys. Lett. B* 488 (2000), pp. 247–253.

[163] Y. Funaki, A. Tohsaki, H. Horiuchi, P. Schuck, and G. Röpke. “Analysis of previous microscopic calculations for the second 0^+ state in ^{12}C in terms of $3-\alpha$ particle Bose-condensed state”. In: *Phys. Rev. C* 67 (2003), p. 051306. DOI: 10.1103/PhysRevC.67.051306. URL: https://link.aps.org/doi/10.1103/PhysRevC.67.051306.

[164] T. Yamada and P. Schuck. “Dilute multi-α cluster states in nuclei”. In: *Phys. Rev. C* 69 (2004), p. 024309. DOI: 10.1103/PhysRevC.69.024309. URL: https://link.aps.org/doi/10.1103/PhysRevC.69.024309.

[165] A. Tohsaki. "New effective internucleon forces in microscopic α-cluster model". In: *Phys. Rev. C* 49 (1994), p. 1814.

[166] J. Nuñez, C. Esebbag, M. T. Martin, L. Rebollo, and A. Plastino. "A generalized Hill-Wheeler ansatz". In: *Z. Phys. A Hadron Nucl.* 318 (1984), pp. 223–229. ISSN: 0939-7922. DOI: 10.1007/BF01413473. URL: http://dx.doi.org/10.1007/BF01413473.

[167] Y. Funaki, A. Tohsaki, H. Horiuchi, P. Schuck, and G. Röpke. "Inelastic form factors to alpha-particle condensate states in ^{12}C and ^{16}O: What can we learn?" In: *Eur. Phys. J. A* 28 (2006), pp. 259–263. ISSN: 1434-601X. DOI: 10.1140/epja/i2006-10061-5. URL: http://dx.doi.org/10.1140/epja/i2006-10061-5.

[168] Y. Funaki, H. Horiuchi, W. von Oertzen, G. Röpke, P. Schuck, A. Tohsaki, and T. Yamada. "Concepts of nuclear α-particle condensation". In: *Phys. Rev. C* 80 (2009), p. 064326. DOI: 10.1103/PhysRevC.80.064326. URL: https://link.aps.org/doi/10.1103/PhysRevC.80.064326.

[169] D. H. Boal, C.-K. Gelbke, and B. K. Jennings. "Intensity interferometry in subatomic physics". In: *Rev. Mod. Phys.* 62 (1990), pp. 553–602. DOI: 10.1103/RevModPhys.62.553. URL: https://link.aps.org/doi/10.1103/RevModPhys.62.553.

[170] M Freer. "Can $\alpha\alpha$ correlations be used to measure the size of ^{12}C excited states?" In: *J. Phys. G Nucl. Partic.* 34 (2007), p. 789. URL: http://stacks.iop.org/0954-3899/34/i=5/a=001.

[171] V. Olkhovsky and A. Zaichenko. "About the influence of space-time separations between sources of α-particle emission in the reaction p+^{11}B $\rightarrow 3\alpha$ on interference phenomena in their spectra". In: *Phys. Lett. B* 272 (1991), pp. 183 –185. ISSN: 0370-2693. DOI: http://dx.doi.org/10.1016/0370-2693(91)91816-E. URL: http://www.sciencedirect.com/science/article/pii/037026939191816E.

[172] H. O. U. Fynbo, Y. Prezado, U. C. Bergmann, M. J. G. Borge, P. Dendooven, W. X. Huang, J. Huikari, H. Jeppesen, P. Jones, B. Jonson, M. Meister, G. Nyman, K. Riisager, O. Tengblad, I. S. Vogelius, Y. Wang, L. Weissman, K. W. Rolander, and J. Äystö. "Clarification of the Three-Body Decay of ^{12}C (12.71 MeV)". In: *Phys. Rev. Lett.* 91 (2003), p. 082502. DOI: 10.1103/PhysRevLett.91.082502. URL: https://link.aps.org/doi/10.1103/PhysRevLett.91.082502.

[173] O. S. Kirsebom, M. Alcorta, M. J. G. Borge, M. Cubero, C. A. Diget, R. Dominguez-Reyes, L. M. Fraile, B. R. Fulton, H. O. U. Fynbo, S. Hyldegaard, B. Jonson, M. Madurga, A. Muñoz Martin, T. Nilsson, G. Nyman, A. Perea, K. Riisager, and O. Tengblad. "Breakup of ^{12}C resonances into three α particles". In: *Phys. Rev. C* 81 (2010), p. 064313. DOI: `10.1103/PhysRevC.81.064313`. URL: `https://link.aps.org/doi/10.1103/PhysRevC.81.064313`.

[174] A. Umar, J. Maruhn, N Itagaki, and V. Oberacker. "Microscopic study of the triple-α reaction". In: *Phys. Rev. Lett.* 104 (2010), p. 212503.

[175] P. H. C. Lau and N. S. Manton. "States of Carbon-12 in the Skyrme Model". In: *Phys. Rev. Lett.* 113 (2014), p. 232503. DOI: `10.1103/PhysRevLett.113.232503`. URL: `https://link.aps.org/doi/10.1103/PhysRevLett.113.232503`.

[176] R. Álvarez-Rodríguez, A. S. Jensen, D. V. Fedorov, H. O. U. Fynbo, and E. Garrido. "Energy Distributions from Three-Body Decaying Many-Body Resonances". In: *Phys. Rev. Lett.* 99 (2007), p. 072503. DOI: `10.1103/PhysRevLett.99.072503`. URL: `https://link.aps.org/doi/10.1103/PhysRevLett.99.072503`.

[177] E. Nielsen, D. Fedorov, A. Jensen, and E. Garrido. "The three-body problem with short-range interactions". In: *Phys. Rep.* 347 (2001), pp. 373 –459. ISSN: 0370-1573. DOI: `http://doi.org/10.1016/S0370-1573(00)00107-1`. URL: `http://www.sciencedirect.com/science/article/pii/S0370157300001071`.

[178] S. Ishikawa. "Decay and structure of the Hoyle state". In: *Phys. Rev. C* 90 (2014), p. 061604. DOI: `10.1103/PhysRevC.90.061604`. URL: `https://link.aps.org/doi/10.1103/PhysRevC.90.061604`.

[179] L. Faddeev. "Scattering theory for a three particle system". In: *Sov. Phys. JETP* 12 (1961), p. 1014.

[180] T. Kokalova, N. Itagaki, W. von Oertzen, and C. Wheldon. "Signatures for Multi-α-Condensed States". In: *Phys. Rev. Lett.* 96 (2006), p. 192502. DOI: `10.1103/PhysRevLett.96.192502`. URL: `http://link.aps.org/doi/10.1103/PhysRevLett.96.192502`.

[181] P. Schuck, Y. Funaki, H. Horiuchi, G. Röpke, A. Tohsaki, and T. Yamada. “Alpha particle clusters and their condensation in nuclear systems”. In: *Phys. Scripta* 91 (2016), p. 123001.

[182] E. Garrido, D. Fedorov, A. Jensen, and H. Fynbo. “Anatomy of three-body decay I: schematic models”. In: *Nucl. Phys. A* 748 (2005), pp. 27 –38. ISSN: 0375-9474. DOI: http://dx.doi.org/10.1016/j.nuclphysa.2004.10.014. URL: http://www.sciencedirect.com/science/article/pii/S0375947404011042.

[183] A. T. Fromhold Jr and D. Adler. *Quantum Mechanics for Applied Physics and Engineering*. 1983.

[184] M. Chernykh, H. Feldmeier, T. Neff, P. von Neumann-Cosel, and A. Richter. “Structure of the Hoyle State in ^{12}C”. In: *Phys. Rev. Lett.* 98 (2007), p. 032501. DOI: 10.1103/PhysRevLett.98.032501. URL: http://link.aps.org/doi/10.1103/PhysRevLett.98.032501.

[185] Y. Kanada-En’yo. “The Structure of Ground and Excited States of 12C”. In: *Prog. Theor. Phys.* 117 (2007), p. 655. DOI: 10.1143/PTP.117.655. eprint: /oup/backfile/Content_public/Journal/ptp/117/4/10.1143/PTP.117.655/2/117-4-655.pdf. URL: +http://dx.doi.org/10.1143/PTP.117.655.

[186] R. Smith. *WKB two and three body Coulomb barrier decay transmission*. Matlab File Exchange, 63777. Accessed: 18-07-2017.

[187] E. Garrido, D. Fedorov, A. Jensen, and H. Fynbo. “Anatomy of three-body decay II: decay mechanism and resonance structure”. In: *Nucl. Phys. A* 748 (2005), pp. 39 –58. ISSN: 0375-9474. DOI: http://dx.doi.org/10.1016/j.nuclphysa.2004.11.008. URL: http://www.sciencedirect.com/science/article/pii/S0375947404011819.

[188] D. Fedorov and A. Jensen. “The three-body continuum Coulomb problem and the 3 structure of 12C”. In: *Phys. Lett. B* 389 (1996), pp. 631 –636. ISSN: 0370-2693. DOI: http://dx.doi.org/10.1016/S0370-2693(96)80001-3. URL: http://www.sciencedirect.com/science/article/pii/S0370269396800013.

[189] T. Myo, K. Kat ō, S. Aoyama, and K. Ikeda. “Analysis of ^{6}He Coulomb breakup in the complex scaling method”. In: *Phys. Rev. C* 63 (2001), p. 054313. DOI: 10.1103/PhysRevC.63.054313. URL: http://link.aps.org/doi/10.1103/PhysRevC.63.054313.

[190] F. Ajzenberg-Selove. “Energy levels of light nuclei A = 1112”. In: *Nucl. Phys. A* 506 (1990), pp. 1 –158. ISSN: 0375-9474. DOI: http://dx.doi.org/10.1016/0375-9474(90)90271-M. URL: http://www.sciencedirect.com/science/article/pii/037594749090271M.

[191] *Geant4 10.3 Physics Reference Manual*. http://geant4.web.cern.ch. Accessed: 14-03-2017.

[192] E. G. B. V. S. Barashenkov B. N. Barbashov. In: *Nuovo Cimento* 7 (1958), p. 117.

[193] S. Bailey. *‘Investigating the Energy Levels of ^{18}F through the Study of the Resonant Reaction $^{14}N + \alpha$’*. Unpublished, Final year report, University of Birmingham. 2012.

[194] *Hyperphysics*. http://hyperphysics.phy-astr.gsu.edu/HBASE/magnetic/cyclot.html. Accessed: 24-09-2014.

[195] *Positron Imaging Centre*. http://www.np.ph.bham.ac.uk/pic/cyclotron. Accessed: 20-09-2014.

[196] D. R. H. “On the analysis of τ-meson data and the nature of the τ-meson”. In: *Lond. Edinb. Dubl. Phil. Mag.* 44 (1953), pp. 1068–1080. DOI: 10.1080/14786441008520365. eprint: http://dx.doi.org/10.1080/14786441008520365. URL: http://dx.doi.org/10.1080/14786441008520365.

[197] W. D. R. F. *Ternary Equilibrium Diagrams 2nd Revised Edition*. Chapman and Hall, London, 1982, p. 3.

[198] R. Smith, C. Wheldon, M. Freer, N. Curtis, T. Kokalova, S. Almaraz-Calderon, A. Aprahamian, N. I. Ashwood, M. Barr, B. Bucher, P. Copp, M. Couder, X. Fang, G. Goldring, F. Jung, S. R. Lesher, W. Lu, J. D. Malcolm, A. Roberts, W. P. Tan, and V. A Ziman. “Disentangling unclear nuclear breakup channels of beryllium-9 using the three-axis Dalitz plot”. In: *Proceedings of 11th International Conference on Clustering Aspects of Nuclear Structure and Dynamics*. EDP Sciences. 2017. DOI: 10.1051/epjconf/20146602026. URL: http://dx.doi.org/10.1051/epjconf/20146602026.

[199] Y. Liang, H. Rang-Lin, L. Wei-Guo, B. Jian-Ming, F. Cheng-Dong, H. Bin, L. Ying, L. Qi-Wen, N. Fei-Peng, S. Sheng-Sen, X. Min, Z. Jian-Yong, and Z. Yong-Sheng. “Lagrange multiplier method used in BESIII kinematic fitting”. In: *Chin. Phys. C* 34 (2010), p. 204. URL: http://stacks.iop.org/1674-1137/34/i=2/a=009.

[200] R. Smith. *Fast Universal Kinematic Fitting code*. https://sourceforge.net/projects/funk-fit/. Accessed: 22-05-2017.

[201] J. L. Puga, M. Krzywinski, and N. Altman. “Points of Significance: Bayes’ theorem”. In: *Nat. Methods* 12 (2015), pp. 277–278.

[202] J. L. Puga, M. Krzywinski, and N. Altman. “Points of Significance: Bayesian statistics”. In: *Nat. Methods* 12 (2015), pp. 377–378.

[203] W. R. Zimmerman, M. W. Ahmed, B. Bromberger, S. C. Stave, A. Breskin, V. Dangendorf, T. Delbar, M. Gai, S. S. Henshaw, J. M. Mueller, C. Sun, K. Tittelmeier, H. R. Weller, and Y. K. Wu. “Unambiguous Identification of the Second 2^+ State in $^{12}\mathbf{C}$ and the Structure of the Hoyle State”. In: *Phys. Rev. Lett.* 110 (2013), p. 152502. DOI: 10.1103/PhysRevLett.110.152502. URL: https://link.aps.org/doi/10.1103/PhysRevLett.110.152502.

[204] M. Labiche, W. Catford, R. Lemmon, C. Timis, R. Chapman, N. Orr, B. Fernndez-Domnguez, G. Moores, N. Achouri, N. Amzal, S. Appleton, N. Ashwood, T. Baldwin, M. Burns, L. Caballero, J. Cacitti, J. Casadjian, M. Chartier, N. Curtis, K. Faiz, G. de France, M. Freer, J. Gautier, W. Gelletly, G. Iltis, B. Lecornu, X. Liang, C. Marry, Y. Merrer, L. Olivier, S. Pain, V. Pucknell, B. Raine, M. Rejmund, B. Rubio, F. Saillant, H. Savajols, O. Sorlin, K. Spohr, C. Theisen, G. Voltolini, and D. Warner. “TIARA: A large solid angle silicon array for direct reaction studies with radioactive beams”. In: *Nucl. Instrum. Methods Phys. Res. A* 614 (2010), pp. 439–448. ISSN: 0168-9002. DOI: http://dx.doi.org/10.1016/j.nima.2010.01.009. URL: http://www.sciencedirect.com/science/article/pii/S0168900210000379.

[205] D. Sahoo. “Investigating Violations of some fundamental symmetries of nature via Dalitz plots and Dalitz prisms”. PhD thesis. Homi Bhabha National Institute, 2015.

[206] P. Avery. “Applied fitting theory I: General least squares theory”. In: *CLEO Note CBX* (1991), pp. 91–72.